

## Abstract

Title of Dissertation: Signal Corrections and Calibrations of the  
LUX Dark Matter Detector  
Richard Knoche, Doctor of Philosophy, 2016

Dissertation directed by: Professor Carter Hall, Department of Physics  
Department of Physics

# Signal Corrections and Calibrations of the LUX Dark Matter Detector

by

Richard Knoche

Dissertation submitted to the Faculty of the Graduate School of the  
University of Maryland, College Park in partial fulfillment  
of the requirements for the degree of  
Doctor of Philosophy

2016

## Advisory Committee:

Professor Carter Hall, Chair/Adviser

Professor Person One

Professor Person Two

Professor Person Three

Professor Person Four

## Acknowledgments

# Contents

<b>1</b>	<b>Introduction to Dark Matter</b>	<b>1</b>
1.1	Evidence for Dark Matter . . . . .	2
1.1.1	Mass Measurements from Galactic Rotation Curves . . . . .	2
1.1.2	Mass Measurements from x-ray Gases . . . . .	5
1.1.3	Gravitational Lensing . . . . .	7
1.1.4	Cosmological Evidence . . . . .	17
1.2	Dark Matter Candidates . . . . .	23
1.2.1	The $\Lambda$ CDM Model . . . . .	23
1.2.2	Nonbaryonic Dark Matter . . . . .	26
1.2.3	WIMPs and SUSY . . . . .	28
1.2.4	Axions and Axinos . . . . .	30
1.2.5	Gravitons and Gravitinos . . . . .	31
1.2.6	WIMPzillas . . . . .	31
<b>2</b>	<b>Searching for WIMPs</b>	<b>32</b>
2.1	Indirect Detection Experiments . . . . .	32
2.1.1	Gamma-Ray Experiments . . . . .	33
2.1.2	Neutrino Experiments . . . . .	34
2.1.3	Positron Experiments . . . . .	35
2.2	WIMP creation in Colliders . . . . .	36
2.3	Direct Detection Experiments . . . . .	36
2.3.1	The Canonical Halo Model . . . . .	37
2.3.2	The WIMP Recoil Spectrum . . . . .	38
2.3.3	Backgrounds in Direct Detection Experiments . . . . .	44
2.3.4	Direct Detection Methods . . . . .	47
<b>3</b>	<b>The LUX Detector</b>	<b>51</b>
3.1	Detector Internals . . . . .	54
3.1.1	Cryostats . . . . .	54
3.1.2	PMT Arrays, PTFE Structure, and Electric Field Cage . . . . .	55
3.1.3	Cryogenics . . . . .	57
3.1.4	Instrumentation . . . . .	58
3.2	External Support Systems . . . . .	59
3.2.1	Gas Circulation and Purification System . . . . .	59
3.2.2	Gas Sampling System . . . . .	61
3.2.3	Water Tank and Muon Veto System . . . . .	62
3.2.4	Calibration Systems . . . . .	63
3.3	Detector Electronics . . . . .	65
3.4	Science Results . . . . .	67

<b>4</b>	<b>Tritium as a Calibration Source</b>	<b>67</b>
4.1	Tritiated Methane Injection System . . . . .	69
4.2	Triated Methane Removal . . . . .	72
4.2.1	Gas Phase Experiments . . . . .	72
4.2.2	Liquid Phase Experiments . . . . .	75
4.2.3	Outgassing Experiements . . . . .	78
4.2.4	Simulating Outgassing in LUX . . . . .	83
4.3	ER Band Calibration of the LUX Detector . . . . .	90
<b>5</b>	<b>Signal Corrections in the LUX Detector</b>	<b>96</b>
5.1	Use of $^{83m}\text{Kr}$ in Signal Corrections . . . . .	99
5.2	S1 Corrections . . . . .	100
5.3	S2 Corrections . . . . .	104
5.4	Radon as a measure of Electron Lifetime . . . . .	108
5.5	A PMT-by-PMT approach to S1 Corrections . . . . .	112
<b>6</b>	<b>Energy Scale Calibrations</b>	<b>115</b>
6.1	Combined Energy Model . . . . .	116
6.2	Doke Plot Analysis of $g_1$ and $g_2$ . . . . .	120
6.2.1	Doke Plot Systematic Errors . . . . .	123
6.2.2	Doke Plot Results . . . . .	126
6.2.3	Recombination Fluctuations from Doke Plot Data . . . . .	129
6.2.4	Light Yield from Doke Plot Data . . . . .	131
6.3	Tritium $\chi^2$ Analysis of $g_1$ and $g_2$ . . . . .	132
<b>7</b>	<b>Calibration of the LUX Detector in a nonuniform Field</b>	<b>134</b>
7.1	Description of the Nonuniform Electric Field . . . . .	135
7.1.1	Measuring the Run04 Electric Field . . . . .	135
7.1.2	Complications Arising from the Run04 Electric Field . . . . .	137
7.1.3	The Goal of KrypCal in Run04 . . . . .	140
7.2	Measuring Electric Field Effects in $^{83m}\text{Kr}$ Data . . . . .	141
7.2.1	General Strategy for Measuring the Field Effect . . . . .	141
7.2.2	Measuring Detector Inefficiency Corrections with $\text{CH}_3\text{T}$ . . . . .	143
7.2.3	Measuring Field Effects in $^{83m}\text{Kr}$ Data . . . . .	150
7.2.4	Measuring the S1a and S1b Pulse Areas in $^{83m}\text{Kr}$ data . . . . .	154
7.2.5	Relating the S1a/S1b Ratio to S2 Field Effects . . . . .	156
7.2.6	Measuring the S1a/S1b Ratio to S1 Field Effect Relationship with Recombination Physics . . . . .	160
7.2.7	Measuring the S1a/S1b Ratio to S1 Field Effect Relationship with the S1a Signal . . . . .	164
7.2.8	Expectation for G1 . . . . .	169

7.2.9	Measuring the S1a/S1b Ratio to S1 Field Effect Relationship with $\chi^2$ Fitting Methods . . . . .	170
7.2.10	Summary of S1a/S1b Ratio to Field Effect Measurements . . . . .	175
7.3	Producing Detector Inefficiency Corrections in KrypCal . . . . .	176
7.3.1	Mapping S1a/S1b . . . . .	177
7.3.2	Removing the field effect from $^{83m}\text{Kr}$ Data . . . . .	178
7.3.3	Measuring Detector Inefficiencies . . . . .	179
7.3.4	Additional Output from KrypCal: Electron Lifetime . . . . .	183
7.3.5	Additional Output from KrypCal: Single Electron Size . . . . .	185
7.3.6	Additional Output from KrypCal: Electric Field Maps . . . . .	187
7.4	Results of the KrypCal Corrections . . . . .	188
7.4.1	Energy Spectra . . . . .	188
7.4.2	Energy Threshold . . . . .	192
7.4.3	G1 and EE . . . . .	194
7.4.4	Lifetime Estimates . . . . .	195
7.4.5	Energy Resolution . . . . .	196
7.4.6	Nuclear Recoil Band . . . . .	198
7.4.7	Electron Recoil Band . . . . .	198
7.5	Conclusions . . . . .	202

## List of Tables

1	$\text{CH}_3\text{T}$ purification efficiencies in liquid xenon. . . . .	80
2	Table of sources used in the Doke plot analysis. . . . .	121
3	Extracted fluctuations from Doke plot data in units of quanta. . . . .	129
4	Extracted fluctuations from Doke plot data in units of quanta when using the bottom array only. . . . .	131
5	Light yield measurements from Doke plot data. . . . .	132
6	The energy threshold calculated from the $\text{CH}_3\text{T}$ spectrum on dif- ferent dates. . . . .	192
7	The mean, width, and energy resolution of Gaussian fits to the the $\text{DD}$ and $^{83m}\text{Kr}$ energy peaks based on a version of KrypCal which does not account for field effects properly. . . . .	197
8	The mean, width, and energy resolution of Gaussian fits to the the $\text{DD}$ and $^{83m}\text{Kr}$ energy peaks based on a version of KrypCal which does account for field effects properly. . . . .	197

# List of Figures

1	Rotation curve of galaxy NGC 6503. The dotted line indicates the contribution of baryonic gas, the dashed line indicates the contribution of visible matter in the disk, and the dash-dotted line indicates the contribution of dark matter. In the absence of dark matter the total velocity curve would fall off in a manner similar to the dotted line.[16]	3
2	A source emits light at position S. The light is deflected by a massive lens at L, and causes the image seen by the observer to appear at an angle $\theta$ . $D_{LS}$ , $D_L$ , $\theta$ , and $\beta$ are, respectively, the distance from the lens plane to the source plane, the distance from the lens plane to the observer, the angle of the image relative to the observer, and the angle of the source relative to the observer. [21]	13
3	An illustration of how positive and negative $\gamma_1$ and $\gamma_2$ distort an object with initial ellipticity of zero. [55]	16
4	X-ray image of the baryonic mass in the Bullet cluster, overlayed with mass contours derived from weak lensing measurements. The separation of the dominant mass component from the baryonic matter indicates the presence of dark matter. [26]	17
5	The latest measurement of the CMB temperature anisotropies from Planck data. [28]	18
6	The power spectrum of temperature fluctuations from the CMB based on data from Planck. [28]	20
7	A depiction of the effect of baryons on the oscillating plasma during BAO. The mass of the baryons loads down the plasma, producing an asymmetry in the oscillations in which the plasma compresses further toward the minimum of the potential well. Since the CMB power spectrum does not care about the sign of the fluctuation, we see that the odd numbered peaks become enhanced over the even numbered peaks. [40]	22
8	The two hierarchies of neutrino mass states. Black, teal, and red indicated the three flavors of neutrinos, while one, two, and three indicated the three mass states. [49]	27
9	Calculated differential spectrum in evts/keV/kg/d (solid lines) and the integrated event rate in evts/kg/d (dashed lines) for $^{131}\text{Xe}$ , $^{73}\text{Ge}$ , and $^{40}\text{Ar}$ assuming a 100 GeV WIMP with spin-independent cross section for a WIMP-nucleon of $\sigma = 5 \times 10^{-43} \text{cm}^2$ .	43

10	A depiction of a recoil event in LUX. The response of the top PMT array to the S2 light is used for xy position reconstruction, while the timing between the S1 and S2 signals is used for the depth measurement. . . . .	52
11	Simulated gamma ray backgrounds in the LUX detector after removing multiscatter events. The black dashed lines indicate the fiducial volume used in the first LUX WIMP search results. . . . .	53
12	Cross section of the LUX cryostats and internal detector components.[10]	54
13	Depiction of the LUX PMT supports, PTFE panels, and field cage.[10]	57
14	Depiction of the LUX sampling system. Xenon enters the sampling system through various sampling ports in the main circulation path. These sampling ports are shown in the top left of the diagram. The xenon then passes through one of three leak valves (indicated by red triangles) into a U-shaped cold trap, where it is analyzed by an RGA on the output of the cold trap. A secondary set of vacuum pumps is included so that the system can be evacuated independently of the RGA space. . . . .	62
15	Cross section of the LUX water tank which surrounds the cryostat.	63
16	Rendering of the six external source tubes which surround the LUX cryostat. . . . .	64
17	Plumbing diagram of the LUX tritium injection system. Blue labels indicate valves, red labels indicate equipment, and green labels indicate the size of individual expansion volumes when all valves are closed. . . . .	71
18	Diagram of the gaseous xenon system at UMD. THe three section of the system are distinguished by green lines. Circles labeled PG and MG are pressure gauges, and the hourglass shaped symbols represent hand valves. . . . .	73
19	Single pass inefficiency of the purifier when removing CH <sub>3</sub> T. Red and blue points indicate data taken by different students, while the black points indicate data for which procedures were intentionally altered. . . . .	74
20	Time-separated clusters of purification have an upward trend in purification inefficiency. . . . .	75
21	The tritium injection system for the liquid phase experiments at UMD. The red box indicates the CH <sub>3</sub> T storage bottle and methane purifier area, the green box indicated the expansion volumes, and the box indicates the cryopumping and xenon flow through area. . .	76

22	The liquid xenon system at UMD. (A) The xenon condenser consists of a helical coil cooled by a pulse tube refrigerator. (B) The liquid xenon storage vessel houses two PMTs to observe tritium decay. . . . .	77
23	Left: Overlay of CH <sub>3</sub> T spectra seen by PMTs in the liquid xenon detector. The blue spectrum is what is seen prior to injecting tritium, the red spectrum is what is seen after injecting tritium, and the green spectrum is what is seen by after purifying the xenon to remove any injected CH <sub>3</sub> T. Right: The difference between the before injection and after purification spectra. . . . .	79
24	Residual background rates over time in the UMD detector after purifying the CH <sub>3</sub> T out of the xenon. Blue data points are data sets in which no plastic curtains were used inside of the detector, red data points are data sets in which teflon curtains were used inside of the detector, and green data points are data sets in which polyethylene curtains were used inside of the detector. . . . .	79
25	A time histogram of the CH <sub>3</sub> T rate in our system. The third red line indicates when our purifier was bypassed. . . . .	81
26	An overlay of three spectra from a step in CH <sub>3</sub> T after bypassing our purifier. The blue spectrum was collected prior to a step occurring, the red spectrum was collected while a step was occurring, and the green spectrum was collected after the step had reached a plateau. . . . .	82
27	The event rate of a <sup>137</sup> Cs source placed outside the xenon storage vessel. The flatness of the rate over time indicates that the PMT gains are mostly constant. . . . .	83
28	Fits of the integral of the flux of CH <sub>3</sub> T out of plastic over time to the outgassing data collected in Maryland's liquid xenon system assuming that the step features are due to diffusion. The model does not perfectly describe the data, so a range of $G$ values is shown. These fits are used to set an upper limit on $G$ . Bottom: Fits of the integral of the flux of CH <sub>3</sub> T out of plastic over time to the same data, assuming that the step features are not due to diffusion. These fits are used to set a lower limit on $G$ . . . . .	87
29	The results of simulating the CH <sub>3</sub> T activity in LUX after a 10 Bq injection. In the first week the amount of residual CH <sub>3</sub> T is dominated by the purification time constant, while the out gassing time constant determines the amount of activity later times. . . . .	89
30	Sampling system results from the 0.375 gram natural methane injection which was used to constraint the value of $G$ . [13] . . . . .	90

31	Rate of CH <sub>3</sub> T events after the first small injection into LUX. The 6.9 hour time constant is consistent with expectations from the natural methane sampling campaign prior to this injection. . . . .	91
32	The location of events during the initial LUX CH <sub>3</sub> T injection. The solid black like indicates the fiducial volume used for the first LUX Run03 results paper. . . . .	92
33	Top: The combined energy spectrum from a high statistics CH <sub>3</sub> T calibration in LUX. Data is shown in black, and a model of the expected tritium beta spectrum is shown in red. Bottom: The residual differences between the data and model for each bin, in units of $\sigma$ . . . . .	94
34	The ratio of the tritium data to expectations. An error function fit used to determine the energy threshold is shown in blue. . . . .	94
35	The electron recoil calibration of LUX resulting from 170,000 CH <sub>3</sub> T events at 180 V/cm. The Gaussian means of each S1 bin, as well as power law fits to those means and the 10% and 90% contours of the ER band are shown in black. The power law fits to the mean, 10%, and 90% countours of the NR band are shown in red. . . . .	96
36	The leakage fraction and discrimination versus S1 in the LUX detector at 180 V/cm. . . . .	96
37	The energy level diagram of the <sup>83</sup> Rb and <sup>83m</sup> Kr decays. . . . .	99
38	(Left) Density of <sup>83m</sup> Kr events in the X-Y plane 10-30 minutes after a <sup>83m</sup> Kr injection. (Right) Density of <sup>83m</sup> Kr events in the R <sup>2</sup> -Z plane 10-30 minutes after a <sup>83m</sup> Kr injection. . . . .	100
39	(Left) Gaussian distribution fits to <sup>83m</sup> Kr S1 data that are used to determine the drift time dependence of the S1 pulse area. (Right) The z dependence of the S1 pulse area. Black points indicate the maximum of Gaussian distribution fits for each drift time bin, and red points indicate the polynomial fit to that data. . . . .	101
40	(Left) Two dimensional map of the XY dependence in <sup>83m</sup> Kr S1 data determined by fitting a Gaussian distribution to XY bins of the data and tracking the mean of each fit.(Right) Two dimensional map of the XY correction factor which is applied to z-corrected S1 data. . . . .	102
41	The <sup>83m</sup> Kr S1 spectrum with no corrections applied (blue), z dependent corrections applied (red), and xyz dependent corrections applied (green). . . . .	104

42	The corrected $^{83m}\text{Kr}$ S1 mean over the duration of LUX’s Run03 data taking campaign. The dashed blue line indicates the mean of the corrected $^{83m}\text{Kr}$ S1 spectrum over time, and the grey band indicates one standard deviation around the mean. . . . .	104
43	(Left) Gaussian distribution fits to $^{83m}\text{Kr}$ S2 data that are used to determine the drift time dependence of the S2 pulse area. (Right) The z dependence of the S2 pulse area. Black points indicate the maximum of Gaussian distribution fits for each drift time bin, and red points indicate the exponential fit to that data. . . . .	105
44	(Left) Two dimensional map of the XY dependence in $^{83m}\text{Kr}$ S2 data determined by fitting a Gaussian distribution to XY bins of the data and tracking the mean of each fit.(Right) Two dimensional map of the XY correction factor which is applied to z-corrected S2 data. . . . .	106
45	The $^{83m}\text{Kr}$ S2 spectrum with no corrections applied (blue), z dependent corrections applied (red), and xyz dependent corrections applied (green). . . . .	108
46	The corrected $^{83m}\text{Kr}$ S2 mean over the duration of LUX’s Run03 data taking campaign. The dashed blue line indicates the mean of the corrected $^{83m}\text{Kr}$ S2 spectrum over time, and the grey band indicates one standard deviation around the mean. . . . .	109
47	Selection of radon events from a week of WIMP search data. Black points include data from all alpha sources, and the blue lines indicate the box cut that is used to select $^{222}\text{Rn}$ data (shown in red). . . . .	110
48	A comparison of the calculated electron lifetimes based on the maximum likelihood method with an attenuated Gaussian PDF (in blue) and corrected Gaussian PDF (in red). The electron lifetime measured from $^{83m}\text{Kr}$ calibrations is shown in black. . . . .	112
49	The $^{83m}\text{Kr}$ corrected S1 spectrum after applying the PMT-by-PMT method (in red) and after applying the standard correction method from Section 5.2 (in black). The events within the fiducial volume are shown on the left, and all of the events are shown on the right. . . . .	116
50	Depiction of particle interaction and the production of xenon excitons, ionized xenon, electron, photons, and heat. [52] . . . . .	117
51	S1 versus S2 density plot for all data that was used in Run03 Doke plot analysis. . . . .	123
52	Single electron sizes for all $^{83m}\text{Kr}$ data sets over the course of LUX’s Run03 data taking campaign. . . . .	124

53	Corrected S1 peaks for all $^{83m}\text{Kr}$ data sets at 170 V/cm field strength. The step near data set 20 is due to an update of the S1 XYZ corrections map. This effect is accounted for in our systematic errors .	125
54	Corrected S2 peaks for all $^{83m}\text{Kr}$ data sets at 170 V/cm field strength.	125
55	The Doke plot from this analysis. The red faded red lines indicate the result of each MCMC trial, while the dark red line indicates the best fit result. The energy of each source is indicated by the point's color. . . . .	127
56	A triangle plot showing the correlation between the fit parameters during the MCMC process. A projection of the fit results onto each axis is shown above and next to the triangle plot. . . . .	127
57	The energy spectrum of LUX's Run03 data after using the $g_1$ and $g_2$ values from the Doke plot analysis . . . . .	128
58	Measured values of $\sigma_R$ , $\sigma_{n_{\gamma}Det}$ , and $\sigma_{n_eDet}$ versus energy. . . . .	130
59	Measured values of $\sigma_R$ , $\sigma_{n_{\gamma}Det}$ , and $\sigma_{n_eDet}$ versus photons, electrons, and ions, respectively. . . . .	130
60	The results of Scott's September 2014 RvZ field map.[39] . . . . .	136
61	The reconstructed distribution of events resulting from the field map in Figure 60. Each point in the figure was placed on a uniform grid and allowed to drift to the liquid surface, where the final radius is measured. The color of each point indicates the strength of the electric field in this "uncorrected" XY coordinate system. This simulation reproduces the distribution of events seen in data from September 2014. [39] . . . . .	139
62	Predictions from NEST for the light yield (top row) and charge yield (bottom row) of electron recoil event from gamma ray interaction (left column) and beta particle interaction (right column). Field values are indicated by the colored lines. Light yield and charge yield have less dependence on the field strength for lower energy events. [64] . . . . .	140
63	Density plot of uncorrected S1 versus uncorrected S2 from the September 2015 CH <sub>3</sub> T calibration. The red lines indicate the box cut used to select CH <sub>3</sub> T events. The dense population to the right of the box cut is $^{83m}\text{Kr}$ which is present in the data set and excluded from the box cut. . . . .	144
64	Two dimensional map of the recombination probability for a 2.5 keV ER based on Scott's September 2015 electric field map and NEST. .	145

65	(Left) Landau distribution fits to the $S2_F$ data that are used to determine the drift time dependence of the $S2_F$ pulse area. For illustrative purposes, a drift time bin width of 60 $\mu$ seconds was chosen for this plot. (Right) The Z dependence of the $S2_F$ pulse area after field effects are removed. Black points indicate the maximum of Landau distribution fits for each drift time bin, and red points indicate the interpolation and extrapolation of that data. . . . .	148
66	Two dimensional map of the XY dependence in $CH_3T$ $S2_F$ data determine by fitting a Landau distribution to XY bins of the data and tracking the maximum of each fit. . . . .	149
67	A histogram of uncorrected S1 data from the $CH_3T$ calibration in September 2015. The maximum of the distribution falls below threshold and can not be used for detector inefficiency corrections. . .	150
68	The S2 field effect versus drift time relationship in September 2015. The relationship was measured using both PMT arrays, and the bottom-only PMT array, and found to agree with both methods. . .	151
69	(Left) Gaussian distribution fits to the $^{83m}Kr$ $S2_E$ data that are used to determine the drift time dependence of the $S2_E$ pulse area. For illustrative purposes, a drift time bin width of 60 $\mu$ seconds was chosen for this plot. (Right) The Z dependence of the $^{83m}Kr$ $S2_E$ pulse area after detector inefficiency effects are removed. Black points indicate the mean of Gaussian distribution fits for each drift time bin, and red points indicate the interpolation and extrapolation of that data. . . . .	152
70	Two dimensional map of the XY dependence in $^{83m}Kr$ $S2_E$ data determine by fitting a Gaussian distribution to XY bins of the data and tracking the mean of each fit. . . . .	153
71	Sumpod versus time for a $^{83m}Kr$ in which a distinct S1a and S1b peak have been observed. In this case, the fit finds an S1a area of 174 phe, an S1b area of 64.5 phe, and a separation in time of 35 samples. . . . .	155
72	(Left) The output of the S1a/S1b fitting module as a function of time separation between the two decays. The red line indicate the minimum separation between the S1a and S1b events required by our cut in this analysis. (Right) A scatter plot of all S1a and S1b pulse areas measured by the fitting module (black) compared to the S1a and S1b pulse areas that are left after our selection cut. (red) .	156

73	(Left) Gaussian distribution fits to the $^{83m}\text{Kr}$ S1a data that are used to determine the drift time dependence of the S1a/S1b ratio. For illustrative purposes, a drift time bin width of 60 $\mu\text{seconds}$ was chosen for this plot. Similar fits are performed on the S1b pulse area data. (Right) The Z dependence of the $^{83m}\text{Kr}$ S1a/S1b ratio. Black points indicate the S1a/S1b ratio as measured by the Gaussian distribution fits for each drift time bin, and the red line indicates the polynomial fit to this data. . . . .	157
74	The XY dependence of the $^{83m}\text{Kr}$ S1a/S1b ratio determined by fitting a Gaussian distribution to XY bins of the S1a and S1b data and tracking the mean of each fit. The map does not extend to $r=25$ cm due to the squeezing effect of the nonuniform electric field. . . . .	158
75	The XY relationship of the $^{83m}\text{Kr}$ S1a/S1b ratio to the $^{83m}\text{Kr}$ $S_{2E}$ field effect. No significant correlation is found in this data. . . . .	159
76	The Z (dark red) and three dimensional (light red) relationship of the $^{83m}\text{Kr}$ S1a/S1b ratio to the $^{83m}\text{Kr}$ $S_{2E}$ field effect. . . . .	160
77	The Z (black) and three dimensional (grey) relationship of the $^{83m}\text{Kr}$ S1a/S1b ratio to the $^{83m}\text{Kr}$ S1 field effect. The black and grey data points are not measured, but instead inferred from the Z (dark red) and three dimensional (light right) relationship of the $^{83m}\text{Kr}$ S1a/S1b ratio to the $^{83m}\text{Kr}$ $S_{2E}$ field effect. . . . .	163
78	The energy spectrum of the efficiency corrected $\text{CH}_3\text{T}$ data (red) after utilizing the S1 field effect measurements from this section in September 2015 (left) and February 2016 (right). The expected energy spectrum is shown in black. . . . .	164
79	(Left) The energy spectrum of efficiency corrected $^{83m}\text{Kr}$ data in September 2015 (red) and February 2016(blue) after utilizing the S1 field effect measurements from this section in KrypCal. (Right) The Z dependence of the $^{83m}\text{Kr}$ energy peaks in September 2015 (red) and February 2016 (black) and the expected energy (blue). . . . .	164
80	Relative light yield of the $^{83m}\text{Kr}$ and $^{57}\text{Co}$ decays defined as the light ield at an applied field divided by the light yield at zero field. Historical data for the $^{57}\text{Co}$ relative light yield is shown by the grey diamond points. Dashed lines correspond to fit parameters to the data. . . . .	167
81	The strength of the S1 field effect measured in this section (grey) compared to the strength of the S1 field effect measured in section 7.2.9 (blue). The large error bars on the data are due to systematic uncertainties in the field maps detector inefficiency corrections. . . . .	167

82	The energy spectrum of the efficiency corrected CH <sub>3</sub> T data (red) after utilizing the S1 field effect measurements from this section and the S2 field effect measurements from section 7.2.5 in September 2015 (left) and February 2016 (right). The expected energy spectrum is shown in black. . . . .	169
83	(Left) The energy spectrum of efficiency corrected <sup>83m</sup> Kr data in February 2016 (red) and September 2015(blue) after utilizing the S1 field effect measurements from this section and the S2 field effect measurements from section 7.2.5 in KrypCal. (Right) The Z dependence of the <sup>83m</sup> Kr energy peaks in September 2015 (red) and February 2016 (black). . . . .	169
84	(Left) The energy spectrum of <sup>83m</sup> Kr data in February 2016 (red) and September 2015(blue) after determining the S1 field effect to S1a/S1b relationship from the version 2.22 reduced $\chi^2$ method. The energy spectrum is expected to be a Gaussian distribution centered around the black line. (Right) The Z dependence of the <sup>83m</sup> Kr energy peaks in September 2015 (red) and February 2016 (black). . . . .	174
85	(Left) The energy spectrum of CH <sub>3</sub> T data in September 2015 (left) and February 2016 (right) after determining the S1 field effect to S1a/S1b relationship from the reduced $\chi^2$ method. The expected CH <sub>3</sub> T energy spectrum for each data set is shown in black. . . . .	175
86	The S1a/S1b to field effect relationships measured in this work. The method to measure each line is indicated by the color in the legend. Red shades indicate measurements of the strength of the field effect in <sup>83m</sup> Kr S1 data, and blue shades indicate the strength of the field effect in <sup>83m</sup> Kr S2 data. Solid lines represent measurements that are used in KrypCal, and dashed lines represent measurements that are supplementary cross checks. . . . .	176
87	The three dimensional field effect in <sup>83m</sup> Kr S2 (black) and S1(red) data versus drift time. The wide regions are areas in which the three dimensional S1a/S1b maps are interpolated with a spline function, and the narrow regions are areas in which the three dimensional S1a/S1b maps are extrapolated based on the S1a/S1b Z dependence map. . . . .	178

88	(Left) Gaussian distribution fits to the field corrected $S2_F$ data that are used to determine the drift time dependence of the $S2_F$ pulse area. For illustrative purposes, a drift time bin width of 60 $\mu$ seconds was chosen for this plot. (Right) The Z dependence of the $S2_F$ pulse area after field effects are removed. Black points indicate the maximum of Gaussian distribution fits for each drift time bin, and red points indicate the interpolation and extrapolation of that data.	180
89	(Left) Gaussian distribution fits to the field corrected $S1_F$ data that are used to determine the drift time dependence of the $S1_F$ pulse area. For illustrative purposes, a drift time bin width of 60 $\mu$ seconds was chosen for this plot. (Right) The Z dependence of the $S1_F$ pulse area after field effects are removed. Black points indicate the maximum of Gaussian distribution fits for each drift time bin, and red points indicate the polynomial fit to that data.	181
90	(Left) Two dimensional map of the XY dependence in $^{83m}\text{Kr}$ $S2_F$ data determine by fitting a Gaussian distribution to XY bins of the data and tracking the mean of each fit.(Right) Two dimensional map of the XY dependence in $^{83m}\text{Kr}$ $S1_F$ data determine by fitting a Gaussian distribution to XY bins of the data and tracking the mean of each fit.	182
91	(Left) A reasonable exponential fit to the $S2_F$ Z dependence in September 2014 (Right) A poor exponential fit to the $S2_F$ Z dependence in January 2016. The higher field variation leads to a worse fit due to the drift velocity dependence of the absorption cross section.	184
92	The electron lifetime over Run04 found by fitting an exponential to the $S2_F$ Z dependence. Red areas indicate circulation outages. At high lifetimes the $S2_F$ Z dependence is less exponential, leading to larger errors on the measurement.	184
93	The result of our first approach for measuring the single electron size at the center of the detector. We perform this measurement for every $^{83m}\text{Kr}$ data set. In this particular example from September 03, 2014 the single electron size is found to be $27.23 \pm 0.044$ .	186
94	The XY dependence of the single electron size used in our second approach for measuring the single electron size at the center of the detector. We perform this measurement for every $^{83m}\text{Kr}$ data set. In this particular example from September 03, 2014 the single electron size is found to be $27.40 \pm 0.31$ .	186
95	The $S1a/S1b$ to field strength relationship measured in September 2014 (red) and September 2015 (black).	187

96	(Left) R <sup>2</sup> vZ map of the electric field on September 03, 2014 as measured by KrypCal (Right) R <sup>2</sup> vZ map of the systematic error in the electric field measurement on September 03, 2014. . . . .	188
97	(Left) The energy spectrum of <sup>83m</sup> Kr data in September 2014 (red) and September 2015(blue) after determining the S1 field effect to S1a/S1b relationship from the version 2.22 reduced $\chi^2$ method. The energy spectrum is expected to be a Gaussian distribution centered around the black line. (Right) The Z dependence of the <sup>83m</sup> Kr energy peaks in September 2014 (red) and September 2015 (black). . . . .	189
98	The September 2014, November 2014, February 2015, September 2015, and February 2016 CH <sub>3</sub> T energy spectra resulting from KrypCal 2.22 corrections. . . . .	190
99	(Left) The energy spectrum of <sup>83m</sup> Kr data in February 2016 (red) and September 2015(blue) using a version of KrypCal that does no properly account for field effects. The energy spectrum is expected to be a Gaussian distribution centered around the black line. (Right) The Z dependence of the <sup>83m</sup> Kr energy peaks in September 2015 (red) and February 2016 (black) using the same version of KrypCal. . . . .	191
100	(Left) The energy spectrum of CH <sub>3</sub> T data in September 2015 (left) and February 2016 (right) using a version of KrypCal that does no properly account for field effects. The expected CH <sub>3</sub> T energy spectrum for each data set is shown in black. . . . .	192
101	The September 2014, November 2014, February 2015, and September 2015 energy thresholds resulting from KrypCal 2.22 corrections. . . . .	193
102	The expected extraction efficiency based on Scott's RvZ field map. The expectation is derived from a Guschin curve, and is dependent on the height of the liquid above the gate. The exact liquid level in Run04 is currently unknown, so a range of possible values is depicted. . . . .	194
103	(Left) The electron lifetime measurement for a particular data set when field effects are not properly accounted for. (Right) The electron lifetime measurement for the same data set when field effects are properly separated from detector inefficiency effects. . . . .	195
104	(Left) The xenon activation energy spectra from October 2015 resulting from corrections which do not properly account for field effects. (Right) The xenon activation energy spectra from the same data sets resulting from corrections which do properly account for field effects. . . . .	196

105	(Left) The Z dependence of the NR band mean using a version of KrypCal which does not properly account for field effects. (Right) The Z dependence of the NR band mean from the same datasets using a version of KrypCal which does properly account for field effects. . . . .	198
106	(Left) The spatial variation of the KrypCal 2.22 corrected ER band from September 2015. The black band represents the total, unbinned ER band and the grey bands represent the ER band from each voxel. (Right) The time dependence of the total, unbinned ER band as measured by the KrypCal 2.22 corrected data at four points in time. . . . .	199
107	(Left) The measured relationship between S1a/S1b and the ER band power law exponent. (Right) The measured relationship between S1a/S1b and the ER band power law coefficient. The light blue region indicates one $\sigma$ uncertainties on each fit. . . . .	200
108	Monte Carlo data for the February 2015 ER band generated from S1a/S1b using the relationship found in Figure 107. A fit to the Monte Carlo data is shown in blue, and a fit to the actual calibration data (not shown) is shown in red. . . . .	201
109	Monte Carlo data for the September 2015 ER band generated from S1a/S1b using the relationship found in Figure 107. A fit to the Monte Carlo data is shown in blue, and a fit to the actual calibration data (not shown) is shown in red. . . . .	201
110	Monte Carlo data for the February 2016 ER band generated from S1a/S1b using the relationship found in Figure 107. A fit to the Monte Carlo data is shown in blue, and a fit to the actual calibration data (not shown) is shown in red. . . . .	202

## 1 Introduction to Dark Matter

In recent decades it has been discovered that the luminous matter which scientists have studied for centuries is only a small fraction of the total composition of the universe. There is strong evidence of dark baryonic matter (a few percent), non-baryonic hot dark matter ( $\sim 0.1\%-1.5\%$ ), non baryonic cold dark matter ( $\sim 27\%$ ), and dark energy ( $\sim 68\%$ ) components to the universe, where the percentages are

as a fraction of their total contribution to the universe’s composition. While we know a large amount about the “normal” matter which contributes  $\lesssim 5\%$  of the universe’s total composition, we know very little about these larger components. In particular, while we understand certain characteristics of the cold dark matter component, there is no consensus on its composition. Before examining the experiments which seek to answer this question we will first discuss what is currently known about the nonbaryonic dark matter component.

## 1.1 Evidence for Dark Matter

### 1.1.1 Mass Measurements from Galactic Rotation Curves

In the early 1930’s Fritz Zwicky was the first to use the Virial theorem to determine the total mass of the Coma cluster of galaxies. In his examination, Zwicky found that the velocities at large radii were too high to be consistent with the Newtonian prediction arising from the visible matter alone [72]. This discrepancy was reinforced in the 1970’s, when further data on the rotational velocity of spiral galaxies began to be collected. Instead of the rotational velocity falling off as  $\propto 1/\sqrt{r}$  beyond the radius of visible matter as one would expect, the rotational velocity rises for small radii, then asymptotes to a constant  $v \simeq 100 - 300 \text{ km/s}$  for large radii in most galaxies [51, 35, 22]. The most widely accepted explanation of this phenomenon is that the disk galaxies are immersed in a dark matter (DM) halo such that  $M(r)/r$  remains constant at large radii. Such a halo could form from an isotropic sphere of ideal gas at a uniform temperature.

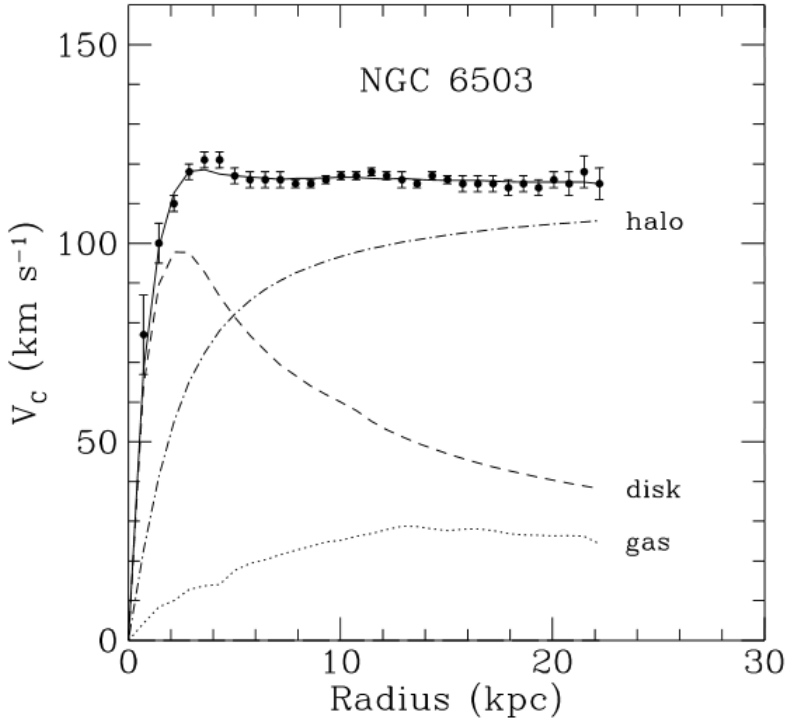


Figure 1: Rotation curve of galaxy NGC 6503. The dotted line indicates the contribution of baryonic gas, the dashed line indicates the contribution of visible matter in the disk, and the dash-dotted line indicates the contribution of dark matter. In the absence of dark matter the total velocity curve would fall off in a manner similar to the dotted line.[16]

Following Zwicky's footsteps, we can use the Virial theorem to calculate the luminous matter's contribution to the total mass of the Coma Cluster. The theorem states that for a system of  $N$  particles

$$\frac{1}{2} \sum_{i=1}^N \langle m_i v_i^2 \rangle = -\frac{1}{2} \sum_{i=1}^N \langle \mathbf{r}_i \cdot \mathbf{F}_i \rangle \quad (1)$$

where  $m_i, v_i$ , and  $\mathbf{r}_i$  are the mass, velocity, and position of the  $i$ th particle in a system of particles, and  $\mathbf{F}_i$  is the force acting on the same particle. Since the total

force on a particle is the sum of all of the forces acting on it

$$\mathbf{F}_i = \sum_{j=1}^N \mathbf{F}_{ji} \quad (2)$$

where  $\mathbf{F}_{ji}$  is the force that particle  $j$  applies on particle  $i$ . Noting that a particle does not apply force to itself, and that Newton's third law of motion states that  $\mathbf{F}_{ji} = -\mathbf{F}_{ij}$  we can rewrite the right hand side of the Virial theorem to be

$$\sum_{i=1}^N \mathbf{F}_i \cdot \mathbf{r}_i = \sum_{i=1}^N \sum_{j < i} \mathbf{F}_{ji} \cdot \mathbf{r}_i + \sum_{i=1}^N \sum_{j > i} \mathbf{F}_{ji} \cdot \mathbf{r}_i = \sum_{i=1}^N \sum_{j < i} \mathbf{F}_{ji} \cdot (\mathbf{r}_i - \mathbf{r}_j). \quad (3)$$

Using the law of gravitation to apply equation 3 to a cluster of galaxies, the Virial theorem becomes

$$\sum_{i=1}^N \langle m_i v_i^2 \rangle = \sum_i^N \sum_{j < i} \left\langle \frac{Gm_i m_j}{r_{ij}} \right\rangle \quad (4)$$

where  $G$  is the gravitational constant. The left hand side of this equation is the total mass,  $M$ , of the cluster of galaxies multiplied by the time and mass averaged squared velocity. The right hand side is approximately equal to  $\frac{GM^2}{R}$ , where  $R$  is the radius of the galaxy cluster. Rearranging equation 4, we arrive at an equation which relates the total mass of the galaxy cluster to the mean square velocity

$$M \approx \frac{\langle v^2 \rangle R}{G} \quad (5)$$

The mean square velocity of a galaxy cluster can be estimated by calculating the one dimensional line of sight velocity via redshift. Under the assumption of spherical symmetry

$$\langle v^2 \rangle = 3 \langle (v_r - c \langle z \rangle)^2 \rangle \quad (6)$$

where  $\langle z \rangle$  is the measured redshift of the galaxy cluster,  $v_r$  is the line of sight velocity, and  $c$  is the speed of light. For the Coma cluster  $\langle z \rangle = 0.0232$ , which produces an estimate of  $\langle v^2 \rangle \approx 2 \times 10^{12} \frac{m^2}{s^2}$ . [57] Using the measured radius of the Comma cluster ( $R \approx 5 \times 10^{22}$ ) the total mass of the system in terms of solar mass ( $M_\odot$ ) is found to be

$$M_{total} \approx 2 \times 10^{15} M_\odot. \quad (7)$$

Comparing this the mass calculated from luminous matter alone we see that these components contribute only a small fraction of the total mass of the system. [57]

$$\frac{M_{lum}}{M_{total}} \approx \frac{2.3 \times 10^{14} M_\odot}{2 \times 10^{15} M_\odot} = 0.11 \quad (8)$$

### 1.1.2 Mass Measurements from x-ray Gases

The total mass of a dynamically relaxed galaxy cluster can be measured from the hydrostatic equilibrium equation, which can be derived from the Tolman-Oppenheimer-Volkoff equation for stellar structure by taking the nonrelativistic limit of  $c \rightarrow \infty$ , such that

$$\frac{dP}{dr} = -\frac{GM(r)}{r^2}\rho \quad (9)$$

where  $P$  is the pressure of the gas in a cluster,  $G$  is the gravitational constant,  $M(r)$  is the mass of the galaxy cluster at a particular radius, and  $\rho$  is the density of the gas in the cluster. From the ideal gas law we know that

$$P = \left( \frac{\rho}{\mu m_H} \right) kT \quad (10)$$

where  $\mu$  is the mean molecular weight ( $\sim 0.6$  for an ionized plasma),  $m_H$  is the mass of the hydrogen atom, and  $k$  is Boltzman's constant. Plugging this into equation 9 yields

$$\frac{k}{\mu m_H} \left( T \frac{d\rho}{dr} + \rho \frac{dT}{dr} \right) = -\frac{GM(r)}{r^2} \rho \quad (11)$$

Solving equation 11 for  $M(r)$  produces a measurement of the cluster's mass from x-ray gas density and temperatures

$$M(r) = -\frac{kT}{\mu m_H G} \left( \frac{d \ln(\rho)}{d \ln(r)} + \frac{d \ln(T)}{d \ln(r)} \right) r \quad (12)$$

where the logarithms were introduced using the fact that

$$\frac{r}{t} \frac{dT}{dr} = \frac{\frac{dT}{T}}{\frac{dr}{r}} = \frac{d \ln T}{d \ln r}. \quad (13)$$

This mass measurement technique is complicated by the fact that the gas density and temperature of a galaxy cluster has spatial variation, as well as the fact that x-ray emission measurements are a two-dimensional projection of a three-dimensional object, which produces complications when integrating x-ray spectra along lines of sight through the cluster. One method for simplifying the mass measurement, called the beta model, is to assume the cluster is made of isothermal, spherically symmetric gas. In this case the density of the gas traces the density of the gravitational mass, such that

$$\rho_{gas}(r) = \rho_0 \left( 1 + \frac{r}{r_c} \right)^{-3\beta/2} \quad (14)$$

where  $r_c$  is the core radius,  $\rho_0$  is the central density, and  $\beta$  is a slope parameter. [70] The core radius  $r_c$  is defined using the intensity of x-ray observations such that  $I(r_c) = \frac{1}{2}I(0)$ , or more generally to be the radius at which  $\frac{d^2 \ln(I)}{d \ln(r)^2}$  is maximized. In this model the mass measurement reduces to a derivation of the spatial density profile by determining the best fit parameters of  $r_c$  and  $\beta$  to the x-ray observations. When this mass measurement technique is compared to mass measurements from luminous matter alone more evidence for dark matter arises. For example, using this technique the Virgo Cluster has been measured to have a total mass (within  $r < 1.8\text{Mpc}$ ) between  $1.5 \times 10^{14} M_\odot$  and  $5.5 \times 10^{14} M_\odot$ . [68] Comparing this to the mass measured from x-ray luminosity yields a ratio of

$$\frac{M_{lum}}{M_{total}} \approx \frac{4.75 \times 10^{13} M_\odot}{3.5 \times 10^{14} M_\odot} = 0.14 \quad (15)$$

### 1.1.3 Gravitational Lensing

Gravitational lensing provides an independent method for measuring the mass of galaxy clusters and other astronomical objects. Gravitational lensing can be divided into two categories – strong lensing and weak lensing. Strong lensing, in which a background light source is distorted into arcs around a massive foreground object, is a rare phenomenon which requires a light source and a very massive lens to be nearly in line with the observer. When such a situation occurs the mass of the lens can be inferred from the angular width of the arc of light which is produced. We turn to general relativity to derive the equation which produces this mass measurement.

The geodesic equation, which describes the path that a free particle travels, is

given by

$$\frac{d}{d\tau} \left( g_{aj} \frac{dx^j}{d\tau} \right) - \frac{1}{2} \frac{\partial g_{ij}}{\partial x^a} \frac{dx^i}{d\tau} \frac{dx^j}{d\tau} = 0 \quad (16)$$

where  $g_{\alpha j}$  is a metric,  $\tau$  is the proper time, and  $x$  is the four dimensional coordinate vector. For a spacetime in a vacuum outside of a spherically symmetric mass the appropriate metric to use is the Schwarzschild metric. With units of  $c = 1$  it is given by

$$ds^2 = - \left( 1 - \frac{2GM}{r} \right) dt^2 + \left( 1 - \frac{2GM}{r} \right)^{-1} dr^2 + r^2 d\theta^2 + r^2 \sin^2 \theta d\phi^2. \quad (17)$$

From the  $t$  component of the geodesic equation we know that

$$\frac{d}{d\tau} \left( g_{tj} \frac{dx^j}{d\tau} \right) - \frac{1}{2} \frac{\partial g_{ij}}{\partial t} \frac{dx^i}{d\tau} \frac{dx^j}{d\tau} = 0. \quad (18)$$

The Schwarzschild metric does not depend on time, and is diagonal, therefore

$$\frac{d}{d\tau} \left( g_{tj} \frac{dx^j}{d\tau} \right) = \frac{d}{d\tau} \left( g_{tt} \frac{dt}{d\tau} \right) = - \frac{d}{d\tau} \left( \left( 1 - \frac{2GM}{r} \right) \frac{dt}{d\tau} \right) = 0. \quad (19)$$

Equation 18 is true if the quantity inside of the derivative is constant, leading us to the first constant of motion

$$E = \left( 1 - \frac{2GM}{r} \right) \frac{dt}{d\tau}. \quad (20)$$

We now turn to the  $\phi$  component of the geodesic equation

$$\frac{d}{d\tau} \left( g_{\phi j} \frac{dx^j}{d\tau} \right) = \frac{d}{d\tau} \left( g_{\phi\phi} \frac{d\phi}{d\tau} \right) = - \frac{d}{d\tau} \left( r^2 \sin^2 \theta \frac{d\phi}{d\tau} \right) = 0 \quad (21)$$

where we have once again used the fact that the metric does not depend on time and is diagonal to simplify the equation. From this we arrive at the second constant of motion

$$l = r^2 \sin^2 \theta \frac{d\phi}{d\tau} \quad (22)$$

Returning to the Schwarzschild metric, for a photon  $ds^2=0$ , and if we assume motion in the equatorial plane  $\theta = \pi/2$  and  $d\theta = 0$ , such that

$$-\left(1 - \frac{2GM}{r}\right) dt^2 + \left(1 - \frac{2GM}{r}\right)^{-1} dr^2 + r^2 d\phi^2 = 0. \quad (23)$$

From the two constants of motion we know that

$$d\phi^2 = \frac{l^2}{r^4 \sin^4 \theta} d\tau^2 \quad (24)$$

and

$$dt^2 = E^2 \left(1 - \frac{2GM}{r}\right)^{-2} d\tau^2 \quad (25)$$

Plugging equations 24 and 25 into equation 23 and simplifying yields

$$dr^2 = \left[ E^2 - \left(1 - \frac{2GM}{r}\right) \frac{l^2}{r^2} \right] d\tau^2 \quad (26)$$

Finally, by dividing equation 26 by 24 we arrive at the equation of motion for light traveling in a Schwarzschild spacetime in polar coordinates

$$\left(\frac{1}{r^2} \frac{dr}{d\phi}\right)^2 = \left(\frac{E}{l}\right)^2 - \left(1 - \frac{2GM}{r}\right) \frac{1}{r^2} \equiv \left(\frac{1}{b}\right)^2 - \left(1 - \frac{2GM}{r}\right) \frac{1}{r^2} \quad (27)$$

The quantity  $b \equiv l/E$  is known as the impact parameter, which represents the

perpendicular distance between the center of attraction and the particle's initial trajectory. To determine the change in the direction of light due to a gravitational field we must integrate  $\frac{d\phi}{dr} dr$  from the minimum distance the light travels by the massive object, denoted as  $R$ , and then multiply by a factor of 2 to account for the symmetrical motion of the particle during its approach to the object. Note that at a distance  $R$  the light is moving tangentially, such that  $\frac{dr}{dt} = 0$  and equation 27 becomes

$$\frac{1}{b^2} = \left(1 - \frac{2GM}{R}\right) \frac{1}{R^2}. \quad (28)$$

Therefore, we can rewrite equation 27 for any value of  $r$  as

$$\left(\frac{1}{r^2} \frac{dr}{d\phi}\right)^2 = \left(1 - \frac{2GM}{R}\right) \frac{1}{R^2} - \left(1 - \frac{2GM}{r}\right) \frac{1}{r^2}. \quad (29)$$

Making the convenient substitution of  $u \equiv R/r$ , where  $0 \leq u \leq 1$  in equation 29 yields

$$\left(\frac{du}{d\phi}\right)^2 = 1 - u^2 - \frac{2GM}{r}(1 - u^3). \quad (30)$$

From this we can find an equation for the infinitesimal variation  $d\phi$  in terms of  $du$

$$d\phi = \frac{(1 - u^2)^{-1/2} du}{\left[1 - \frac{2GM}{R}(1 - u^3)(1 - u^2)^{-1}\right]^{-1/2}}. \quad (31)$$

A further substitution of  $u \equiv \cos(\alpha)$ , where  $0 \leq \alpha \leq \pi/2$ , leads (after some simplification) to the equation

$$d\phi = \left[1 - \frac{2GM}{R} \left(\cos(\alpha) + \frac{1}{1 + \cos(\alpha)}\right)\right]^{-1/2} d\alpha. \quad (32)$$

In most cases, the quantity  $M/R \ll 1$ , so we can use the approximation  $(1+x)^n \approx 1+nx$  for small  $x$  in equation 32 such that

$$d\phi = \left[ 1 + \frac{GM}{R} \left( \cos(\alpha) + \frac{1}{1+\cos(\alpha)} \right) \right] d\alpha. \quad (33)$$

This is known as the "weak field" limit. Integrating this expression from  $0 \leq \alpha \leq \pi/2$  and multiplying by 2 to account for the two symmetrical legs of the light's trajectory provides an expression for the total azimuthal angle of the light.

$$\phi = 2 \int_0^{\pi/2} \left[ 1 + \frac{GM}{R} \left( \cos(\alpha) + \frac{1}{1+\cos(\alpha)} \right) \right] d\alpha = \pi + \frac{4GM}{R}. \quad (34)$$

Noting that the first term,  $\pi$ , is the azimuthal angle of the light if no mass were present, we arrive at an equation that relates the angle of deflection of light to the total mass of the gravitational object.

$$\Delta\phi = \phi - \pi = \frac{4GM}{R}. \quad (35)$$

In practice, we must go one step further to turn astronomical observations of gravitational lensing into a mass measurement. Any observation of a lensed light source involves an observer viewing an image of the object after it passes by a gravitational lens. This situation is depicted in Figure 2. To measure the mass of a lens we seek to relate the source position to the image position. Using the small angle approximation for  $\theta$  and  $\beta$  we can arrive at

$$D_S\theta = D_S\beta + D_{LS}\Delta\phi. \quad (36)$$

where  $D_s = D_L + D_{LS}$  is the distance from the source plane to the observer. Using equation 35, and the fact that  $R \approx \theta D_L$  this becomes

$$\theta = \beta + \frac{4GMD_{LS}}{\theta D_L D_S} \quad (37)$$

This is a quadratic equation with roots

$$\theta = \frac{\beta \pm \sqrt{\beta^2 + 4\theta_E^2}}{2} \quad (38)$$

where  $\theta_E = \left(4GM \frac{D_{LS}}{D_S D_L}\right)^{1/2}$  is the angular size of the "Einstein ring" that forms when the source and lens are perfectly aligned. If the quantities  $D_{LS}$ ,  $D_L$ , and  $\beta$  are known, equation 38 can be used to measuring the mass of the lens by measure the angle of deflection  $\theta$ . [21] In the handful of cases in which this mass measurement has been carried out, it has been found to be consistent with dark matter models.

[71]

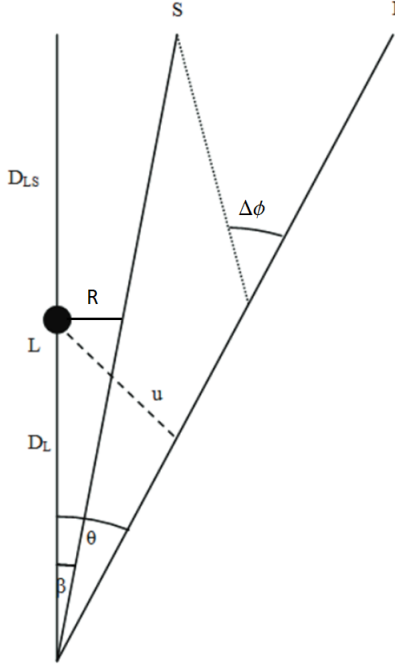


Figure 2: A source emits light at position  $S$ . The light is deflected by a massive lens at  $L$ , and causes the image seen by the observer to appear at an angle  $\theta$ .  $D_{LS}$ ,  $D_L$ ,  $\theta$ , and  $\beta$  are, respectively, the distance from the lens plane to the source plane, the distance from the lens plane to the observer, the angle of the image relative to the observer, and the angle of the source relative to the observer. [21]

Although there are only a few cases in which strong gravitational lensing can be observed, there are numerous cases of weak gravitational lensing. Weak lensing occurs when the lensing mass isn't large enough for strong lensing, or if the source of light is not directly aligned with the lensing mass, resulting in a shear distortion of the image. Measuring the mass of a weak lens is complicated by the fact that each light source has a unique, intrinsic ellipticity which typically dwarfs the magnitude of the image distortion. This intrinsic ellipticity is known as “shape noise” in weak gravitational lensing studies. In cases where many sources are lensed by the same object, the distortion from the lens can be measured by averaging over the many source images, taking advantage of their random intrinsic orientation.

In these cases, the measured shear distortion results from photons being deflected by mass fluctuations along the line of sight. In this case, the two dimensional lens equation (analogous to equation 37) in vector format is

$$\boldsymbol{\beta} = \boldsymbol{\theta} - \frac{D_{LS}}{D_S} \Delta\phi(\boldsymbol{\xi}) \quad (39)$$

where  $\boldsymbol{\xi} = D_S \boldsymbol{\theta}$  is the impact parameter. The deflection angle can be calculated by integrating the 3D gravitational potential,  $\Phi(\mathbf{r})$ , along the line of sight such that

$$\Delta\phi(\boldsymbol{\xi}) = 2 \int \nabla_{\perp} \Phi(\mathbf{r}) dz = \nabla_{\perp} \left( 2 \int \Phi(\mathbf{r}) dz \right) \equiv \nabla_{\perp} V. \quad (40)$$

Assuming the angle between the image and the observer,  $\boldsymbol{\theta}$ , is small equation 39 can be approximated with a first order Taylor series as

$$\beta_i = A_{ij} \theta_j \quad (41)$$

where  $i$  corresponds to the  $i^{th}$  component of the lens plane,  $j$  corresponds to the  $j^{th}$  component of the source plane, and

$$A_{ij} = \frac{\partial \beta_i}{\partial \theta_j} = \delta_{ij} - \frac{\partial \Delta\phi_i(\boldsymbol{\theta})}{\partial \theta_j} = \delta_{ij} - \frac{\partial^2 V(\boldsymbol{\theta})}{\partial \theta_i \partial \theta_j} \quad (42)$$

are the elements of a Jacobian distortion matrix,  $\mathbf{A}$ , which describes the isotropic dilation and anisotropic distortion due to convergence and shear effects. The distortion matrix can be written in terms of the convergence,  $\kappa$ , which increases the size of the image while conserving brightness, and the shear,  $\gamma$ , which distorts

the the image tangentially around the lens.

$$A_{ij} = (1 - \kappa) \begin{pmatrix} 1 & 0 \\ 0 & 1 \end{pmatrix} - \gamma \begin{pmatrix} \cos(2\phi) & \sin(2\phi) \\ \sin(2\phi) & -\cos(2\phi) \end{pmatrix} \quad (43)$$

Equations 42 and 43 offer a relationship between the observable quantities  $\kappa$  and  $\gamma$ , and the gravitational potential  $V$ .

$$\gamma_1 \equiv \gamma \cos 2\phi = \frac{1}{2} \left[ \frac{\partial^2 V(\boldsymbol{\theta})}{\partial \theta_1^2} - \frac{\partial^2 V(\boldsymbol{\theta})}{\partial \theta_2^2} \right] \quad (44)$$

$$\gamma_2 \equiv \gamma \sin(2\phi) = \frac{\partial^2 V(\boldsymbol{\theta})}{\partial \theta_1 \partial \theta_2} \quad (45)$$

$$\kappa = \frac{1}{2} \nabla^2 V(\boldsymbol{\theta}) \quad (46)$$

where equation 44 comes from  $A_{11} - A_{22}$ , equation 45 comes from  $A_{12} - A_{21}$ , and equation 46 comes from  $\text{tr}(A)$ . Since  $\kappa$  is equal to half the laplacian of the projected gravitational potential,  $V$ , it is directly proportional to the mass density of the lens. The shear component  $\gamma_1$  corresponds to elongation and compression along the  $x$  and  $y$  directions, and the component  $\gamma_2$  describes elongation and compression along the diagonal  $x = y$  and  $x = -y$  directions. In the case of weak lensing, the mass measurement then reduces to a measurement of the shear and convergence produced by the lens. [54]. As with strong gravitational lensing, weak gravitational lensing mass measurements have been found to be consistent with dark matter models. [71]

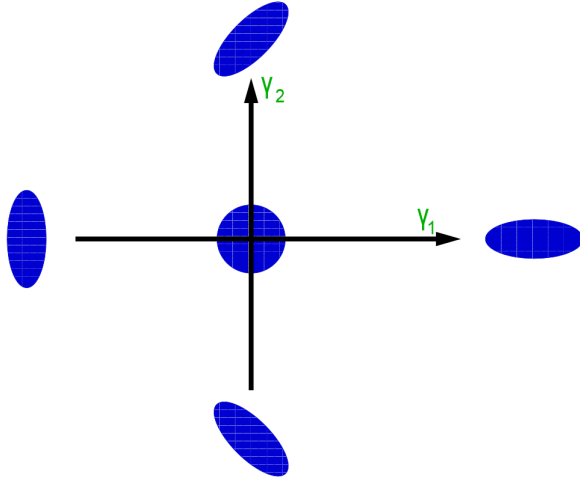


Figure 3: An illustration of how positive and negative  $\gamma_1$  and  $\gamma_2$  distort an object with initial ellipticity of zero. [55]

One of the most famous instances of weak lensing evidence for dark matter is a collision of two galaxies clusters known as the Bullet Cluster. The baryonic matter in each galaxy cluster is predominantly in the form of hot gas. Electromagnetic interaction causes the gas to slow down and concentrate in the center of the collision. In the absence of dark matter gravitational lensing measurements should be correlated with the hot gas, since it is the dominant luminous mass in the system. However, if dark matter was a dominant mass component in the Bullet Cluster it would not be slowed by electromagnetic interactions and would pass through the collision without significant perturbation. Indeed, weak gravitational lensing observations show that the majority of the mass in the Bullet Cluster passed through the collision rather than concentrating at the center like the luminous matter, suggesting that dark matter is present in abundance over the baryonic matter of the two galaxy clusters. [26]

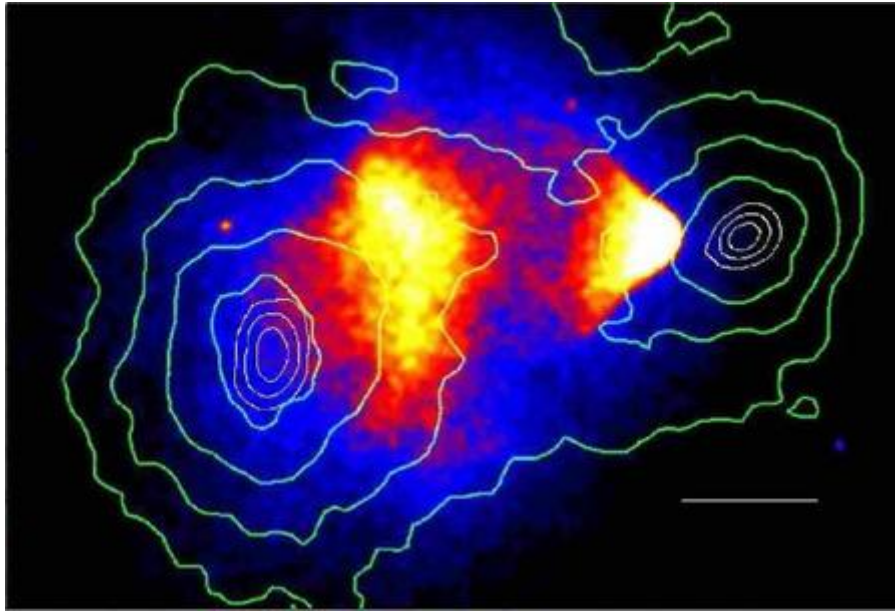


Figure 4: X-ray image of the baryonic mass in the Bullet cluster, overlayed with mass contours derived from weak lensing measurements. The separation of the dominant mass component from the baryonic matter indicates the presence of dark matter. [26]

#### 1.1.4 Cosmological Evidence

The early universe was filled with a hot, dense plasma of electrons and baryons. At this time photons scattered off of the free electrons, restricting their movement across the universe. As the universe cooled below the binding energy of hydrogen (13.6 eV) protons and electrons began to combine, forming neutral hydrogen atoms. At this point in time, known as the recombination epoch, photons and electrons decoupled and the photons began traveling with a mean free path the size of the universe. These photons produce the Cosmic Microwave Background (CMB) that we see today. (Figure 5) The radiation is extremely isotropic and exhibits a black-body spectrum at a red shifted temperature of 2.72 K. The frequency spectrum, temperature fluctuations, and polarization of the CMB all contain a vast amount

of information about the formation of the universe. Here, we focus on just one of these properties.

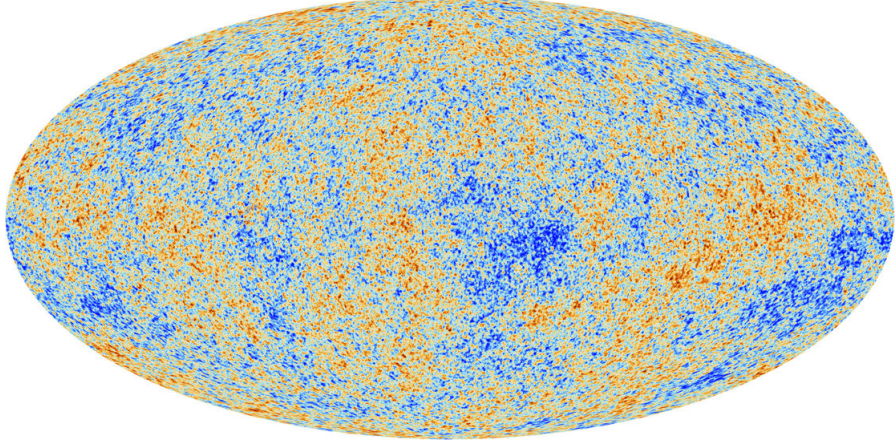


Figure 5: The latest measurement of the CMB temperature anisotropies from Planck data. [28]

In 2003 the WMAP satellite observed small (1 part in 10,000) fluctuations in the average temperature of the CMB. We see these temperature fluctuations projected on a 2D spherical surface, so it is typical to expand them in terms of spherical harmonics defined by

$$Y_{lm} = \sqrt{\frac{2l+1}{4\pi} \frac{(l-m)!}{(l+m)!}} P_l^m(\cos \theta) e^{im\phi} \quad (47)$$

where  $l = 0, \dots, \infty$ ,  $-l \leq m \leq l$ , and  $P_l^m$  are associated Legendre polynomials. The temperature fluctuations can then be written as

$$f(\theta, \phi) \equiv \frac{\delta T(\theta, \phi)}{T_0} = \sum_{l=0}^{l=\infty} \sum_{m=-l}^{m=l} a_{lm} Y_{lm}(\theta, \phi) \quad (48)$$

where  $T_0$  is the average temperature of the CMB and  $a_{lm}$  are the coefficients of

expansion. Since the spherical harmonics are orthonormal

$$a_{lm} = \int_{\theta=-\pi}^{\pi} \int_{\phi=0}^{2\pi} f(\theta, \phi) Y_{lm}^*(\theta, \phi) d\Omega \quad (49)$$

and since  $a_{lm}$  are independent random variables

$$\langle a_{lm} a_{l'm'}^* \rangle = \delta_{ll'} \delta_{mm'} \langle |a_{lm}|^2 \rangle. \quad (50)$$

The temperature fluctuations are isotropic and therefore independent of  $m$ , so

$$\langle |a_{lm}|^2 \rangle = \frac{1}{2l+1} \sum_m \langle |a_{lm}^2| \rangle \equiv C_l. \quad (51)$$

where the function  $C_l$  is referred to as the angular power spectrum of the temperature fluctuations. The angular power spectrum is related to contribution of the multipole  $l$  to the temperature variance by

$$\begin{aligned} \left\langle \left( \frac{\delta T(\theta, \phi)}{T_0} \right)^2 \right\rangle &= \left\langle \sum_{lm} a_{lm} Y_{lm}(\theta, \phi) \sum_{l'm'} a_{l'm'}^* Y_{l'm'}^*(\theta, \phi) \right\rangle \\ &= \sum_{ll'} \sum_{mm'} Y_{lm}(\theta, \phi) Y_{l'm'}^*(\theta, \phi) \langle a_{lm} a_{l'm'}^* \rangle \\ &= \sum_l C_l \sum_m |Y_{lm}(\theta, \phi)|^2 = \sum_l \frac{2l+1}{4\pi} C_l \end{aligned} \quad (52)$$

where we have used the closure relation

$$\sum_m |Y_{lm}(\theta, \phi)|^2 = \frac{2l+1}{4\pi} \quad (53)$$

in the last step of equation 52. [46]

Cosmological models predict the variance of the  $a_{lm}$  expansion coefficients, and therefore predict the angular power spectrum and the contribution of each multipole to the temperature variance. By measuring the angular power spectrum of the CMB and comparing to the  $C_l$  values predicted by each model we can learn about the composition of the universe. The temperature fluctuations of the CMB are typically plotted in terms of  $D_l \equiv l(l+1)C_l/(2\pi)$  with units of  $\mu K^2$  versus the multipoles  $l$  as shown in Figure 6.

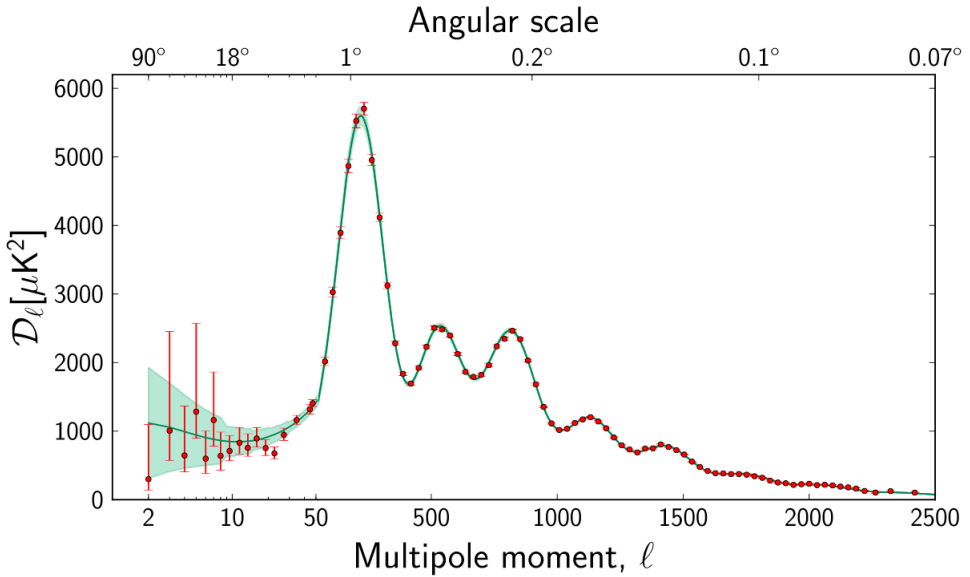


Figure 6: The power spectrum of temperature fluctuations from the CMB based on data from Planck. [28]

To understand the wealth of information present in Figure 6 we must first understand the origin of the temperature fluctuations in the early universe. Prior to recombination the primordial plasma consisted of anisotropic regions of varying density. Overdense regions of matter would gravitationally attract more matter. As this happened, heat from photons scattering off of free electrons would produce an increase in pressure, counteracting the force of gravity and pushing baryonic

matter away from the high density regions. As these two processes competed they produced oscillations in the distribution of baryonic matter, which we refer to as Baryon acoustic oscillations (BAO). After recombination the photons diffused through the baryonic matter, removing the source of pressure, ending the oscillating process, and leaving a shell of overdense baryonic matter at the origin of the anisotropy and at a fixed radius called the sound horizon.

The first peak in Figure 6 details the curvature of the universe. If the universe had positive curvature the light from the CMB would be magnified, shifting the first peak to lower multipole in Figure 6. Likewise, in a negatively curved universe the scale of the temperature fluctuations in the CMB would appear diminished, shifting the first peak to higher multipole. The observed location of the first peak, close to  $l \sim 200$ , turns out to be consistent with a flat universe.

The second peak in Figure 6 details the amount of baryonic matter in the universe. Baryons add mass to the system during the oscillating process described above. This additional inertia forces the primordial plasma to travel farther before recoiling back to the center of the anisotropy, much like adding a mass to the end of a spring. The odd numbered peaks in Figure 6 are associated with how far the plasma compresses during BAO and are enhanced by the presence of additional baryons, as shown in Figure 7. The even numbered peaks are associated with how far the plasma rebounds during BAO and are unaffected by the presence of additional baryons. Therefore, the presence of baryons enhances the size of the odd peaks over the even peaks such that a smaller second peak in Figure 6 corresponds to a larger amount of baryonic matter in the universe. The latest results from Planck indicate that baryonic matter makes up 4.9% of the universe.

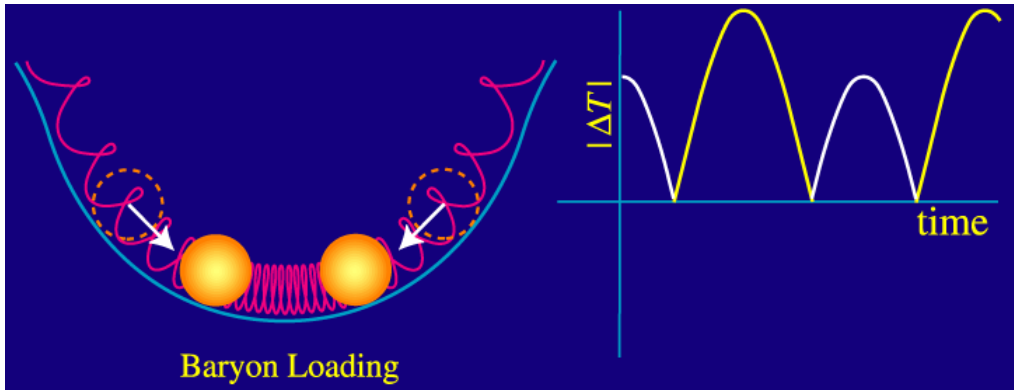


Figure 7: A depiction of the effect of baryons on the oscillating plasma during BAO. The mass of the baryons loads down the plasma, producing an asymmetry in the oscillations in which the plasma compresses further toward the minimum of the potential well. Since the CMB power spectrum does not care about the sign of the fluctuation, we see that the odd numbered peaks become enhanced over the even numbered peaks. [40]

The third peak in Figure 6 details the amount of dark matter in the universe. Since the very early universe was dominated by photon-baryon interactions, the outward pressure caused the gravitational potential of the BAO system to decay in such a way that it drove the amplitude of oscillations higher. With higher dark matter density this driving effect is diminished and the overall magnitude of the peaks becomes smaller. Although this effects all of the peaks in Figure 6 it is only distinguishable in the third peak. Furthermore, as with ordinary matter, dark matter was gravitational attracted to areas with higher density. Since dark matter does not interact through the electromagnetic force it was unaffected by the increasing photon pressure which produced acoustic oscillations in baryons. As a result, a higher density of dark matter corresponded to a larger gravitational potential well for baryons to fall into during their oscillations, increasing the amplification of BAO on the odd numbered peaks. Therefore, the height of the third peak tells us the amount of dark matter that is present in the universe. [40] The

Planck observations indicates that dark matter makes up 26.8% of the universe. The remaining 68.3% of the universe is made up of dark energy. [28]

## 1.2 Dark Matter Candidates

### 1.2.1 The $\Lambda$ CDM Model

To further examine the properties of dark matter it is useful to introduce a quantitative measure for the composition of the universe. Friedmann's equation, which describes the expansion of space in a homogeneous and isotropic universe, is given by

$$\frac{\dot{a}^2 + kc^2}{a^2} = \frac{8\pi G\rho + \Lambda c^2}{3}, \quad (54)$$

where  $a$  is the scale factor of the universe,  $k$  is the spatial curvature of the universe (equivalent to one sixth of the Ricci Scalar) ,  $c$  is the speed of light,  $G$  is the gravitational constant,  $\rho$  is the density of the universe, and  $\Lambda$  is the cosmological constant. Einstein's field equations,

$$G_{\mu\nu} = \frac{8\pi G}{c^4} T_{\mu\nu} \quad (55)$$

provide an expression for the cosmological constant,  $\Lambda$ . We can split the stress energy tensor into two terms, one describing matter and the other describing the vacuum, such that  $T_{\mu\nu} = T_{\mu\nu}^{matter} + T_{\mu\nu}^{vac}$ . Since the stress energy tensor is given by

$$T_{\mu\nu} = (\rho + p)U_\mu U_\nu + pg_{\mu\nu}, \quad (56)$$

and to maintain Lorentz invariance  $p^{vac} = -\rho^{vac}$ , we can write the vacuum component of the stress energy tensor as

$$T_{\mu\nu}^{vac} = -\rho^{vac}g_{\mu\nu}. \quad (57)$$

If we identify the vacuum energy density as

$$\rho^{vac} = \frac{\Lambda c^2}{8\pi G} \quad (58)$$

then Einstein's field equation takes on the familiar form

$$G_{\mu\nu} + g_{\mu\nu}\Lambda = \frac{8\pi G}{c^4} T_{\mu\nu}^{matter}, \quad (59)$$

where  $G_{\mu\nu}$  is the Einstein tensor,  $g_{\mu\nu}$  is the metric tensor,  $G$  is the gravitational constant, and  $\Lambda$  is the cosmological constant. Setting the normalized spatial curvature  $k = 0$  in Friedmann's equation(representing a flat universe), one can find the critical density for which the universe is spatially flat to be

$$\rho_c = \frac{3}{8\pi G} \frac{\dot{a}^2}{a^2}, \quad (60)$$

where  $\rho_c = \rho^{vac} + \rho$ . Recognizing Hubble's constant to be  $H = \frac{\dot{a}}{a}$ , we can rewrite this as

$$\rho_c = \frac{3H^2}{8\pi G} \quad (61)$$

where  $H$  is the present value of the Hubble constant [41]. The current experimental value for  $H$  in the dimensionless units 100 km/s/Mpc is  $h \sim 0.7$  with an uncertainty

of  $\sim 5\%$ . We can then define the density parameter as

$$\Omega = \frac{\rho}{\rho_c} = \frac{8\pi G\rho}{3H_0^2}. \quad (62)$$

If  $\Omega$  is larger than unity the universe is spatially closed, and if  $\Omega$  is less than unity the universe is spatially open. This density parameter can be split into components, such that for a particular component  $x$

$$\Omega_x = \frac{\rho_x}{\rho_c}. \quad (63)$$

Detailed cosmological studies have concluded that all the luminous matter in the universe has a density parameter of  $\Omega_{lum} \lesssim 0.01$ . This information, combined with the fact that analysis of galactic rotational velocities implies  $>90\%$  of the mass in galaxies is dark leads to the conclusion that  $\Omega_{DM} \geq 0.09$ . This is only a lower limit on the dark matter density parameter, since most rotation curves remain flat out to the largest radii at which they can be measured and it can be assumed that the DM halos extend even farther out.

With  $\Omega_{DM} \geq 0.1$  it is possible that baryonic DM alone could be responsible for the dark matter halos. However, other analyses eliminate this possibility. Direct searches for massive compact halo objects (MACHOs) utilizing microlensing have determined that  $<25\%$  of the dark halos could be due to baryonic dark matter within the mass range of  $2 \times 10^{-7} M_{sun} < M < 1 M_{sun}$  at a 95% confidence limit [8, 11]. Furthermore, data from the Hubble Deep Field Space Telescope suggests dark matter halos consist of  $\leq 5\%$  white dwarfs.

With baryonic dark matter being ruled out as the sole component of dark mat-

ter halos we now investigate the other density parameter components. Big Bang nucleosynthesis models constrain the amount of baryonic matter in the universe to  $\Omega_b \approx 0.045$  (where b stands for baryons) [67]. Additionally, analysis of velocity flows, x-ray emissions temperatures, and gravitational lensing in large clusters and superclusters of galaxies suggests that the total matter component of the universe has density parameter  $\Omega_m \approx 0.2 - 0.3$ . One can combine this information, assuming  $h = 0.7$  to find density parameters that are consistent with the Planck observation of

$$\Omega_b = 4.9\%$$

$$\Omega_{nbm} = 26.8\%$$

$$\Omega_\Lambda = 68.3\%$$

where  $\Omega_b$  is the baryonic density of the universe,  $\Omega_{nbm}$  is the nonbaryonic density parameter of the universe, and  $\Omega_\Lambda$  is the dark energy density parameter of the universe [61, 28]. This is known as the  $\Lambda$ -CDM model.

### 1.2.2 Nonbaryonic Dark Matter

With  $\Omega_{nbm} = 26.8\%$  it is intriguing to look at the particles which have been proposed to explain this contribution to the total density parameter. One such particle is the standard-model neutrino. The neutrino is an electrically neutral, weakly interacting particle with a nearly zero mass. Neutrinos exist in three distinct flavors – the electron neutrino ( $\nu_e$ ), the muon neutrino ( $\nu_\mu$ ), and the tau neutrino ( $\nu_\tau$ ). It is known that neutrinos oscillate between these three flavors, with each flavor state being a super position of three neutrino states of definite mass ( $\nu_1, \nu_2$ , and  $\nu_3$ ). Ex-

periments studying solar neutrino oscillations have determined the squared mass difference between what is known as the solar neutrino doublet ( $\nu_1$  and  $\nu_2$ ) to be  $\delta m^2 = (7.66 \pm 0.35) \times 10^{-5} eV^2$ , while experiments studying atmospheric neutrino oscillations have determined the remaining squared mass difference between the solar neutrino doublet and  $\nu_3$  to be  $\pm(2.38 \pm 0.27) \times 10^{-3} eV^2$  up to an unknown sign [56]. This sign ambiguity leads to two possible hierarchies for the neutrino mass states. (Figure 8) If we assume the normal hierarchy to be true, we can set a lower limit on the most massive neutrino state to be  $m_{\nu_3} \gtrsim 0.05$  eV.

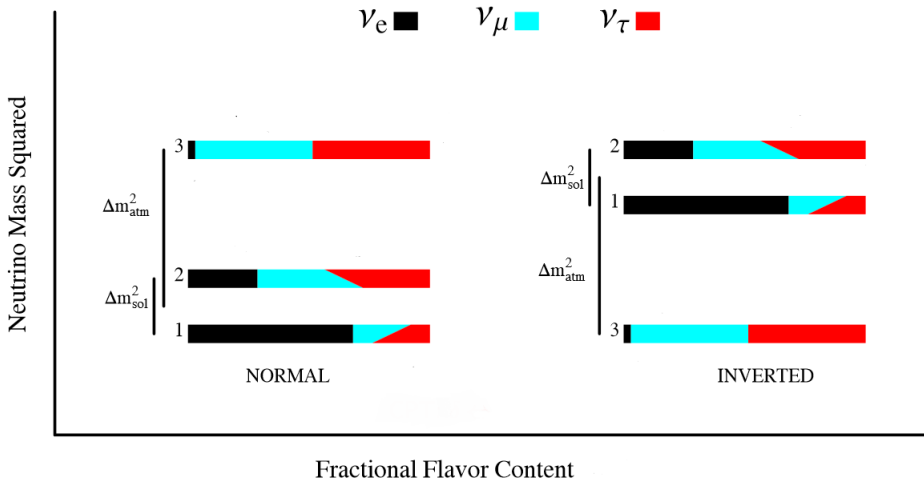


Figure 8: The two hierarchies of neutrino mass states. Black, teal, and red indicated the three flavors of neutrinos, while one, two, and three indicated the three mass states. [49]

The density parameter of neutrinos is given by

$$\Omega_\nu = \frac{\rho_\nu}{\rho_c} = \frac{1}{h^2} \sum_{i=1}^3 \frac{g_i m_i}{90 eV},$$

where  $g_i = 1$  for Majorana neutrinos (own antiparticle) and  $g_i = 2$  for Dirac neutrinos (distinct antiparticles) [50]. Using the lower mass limit of the neutrino

and assuming Majorana neutrinos, this suggests a lower limit on the neutrino density parameter of  $\Omega_\nu \gtrsim 0.00122$ . Thus, neutrinos do provide some contribution to the nonbaryonic dark matter density parameter.

To find an upper limit on the neutrino contribution to the nonbaryonic dark matter density parameter it is necessary to distinguish hot dark matter from cold dark matter. Hot dark matter is composed of particles that have zero or nearly-zero mass. Special relativity requires that the massless particles move at the speed of light, and that the nearly-massless particles move close to the speed of light. As a result hot dark matter forms very hot gases. Cold dark matter is composed of particles that have sufficient mass to travel at sub-relativistic velocities, thus forming colder gases. With their low masses neutrinos fall under the hot dark matter category. A combination of galaxy clustering measurements, CMB observations, and Lyman- $\alpha$  observations give an upper limit on the hot dark matter contribution of  $\Omega_\nu \lesssim 0.0155$ , thus neutrinos and other hot dark matter particles cannot be the primary contribution to the nonbaryonic dark matter density parameter [61].

### 1.2.3 WIMPs and SUSY

If we assume cold dark matter (CDM) particles were in thermal equilibrium with the other standard-model particles during the early stages ( $< 1$  ns) of the universe it is possible to calculate the CDM density parameter. According to Maxwell-Boltzmann statistics, as the temperature,  $T$ , of the universe cools, the particles with masses  $m > T$  will diminish exponentially. Once the temperature of the universe cooled below the CDM mass scale the creation of these particles would have ceased. At this time the CDM particles which still existed would have continued annihilating with one another. As time went on, CDM annihilation became less

and less likely due to their dwindling abundance. Once the expansion rate of the universe, given by Hubble's constant, exceeded the CDM annihilation/creation rate, the CDM particles dropped out of thermal equilibrium and the CDM density became fixed.

The density parameter for CDM is approximately given by

$$\Omega_\chi h^2 \simeq \frac{T_0^3}{M_{Pl} \langle \sigma_A \nu \rangle}$$

where  $\sigma_A$  is the total annihilation cross section of CDM particles,  $\nu$  is the relative velocity of CDM particles,  $T_0$  is the equilibrium temperature,  $M_{Pl}$  is the Planck mass,  $c$  is the speed of light, and  $\langle \dots \rangle$  represents an average over the thermal distribution of CDM particle velocities [45, 42]. Remarkably, for the total density parameter of the universe to equal unity, as required by cosmological models, a cross section on the order of particles interacting on the electroweak scale ( $\sim 10^{-9} GeV^{-2}$ ) is required for CDM particles. This result is the main motivation behind suspecting weakly interacting massive particles (WIMPs) as the dominant contribution to the nonbaryonic dark matter density parameter.

Supersymmetry (SUSY) is a symmetry of space-time which has been proposed in an effort to unify the electroweak, strong, and gravitational forces. This theory offers some insight into the nature of WIMPs. SUSY requires that a supersymmetric partner particle exists for each particle in the standard model. These partners go by the names of sleptons (partners of leptons), squarks (partners of quarks), gauginos (partners of gauge bosons), and higgsinos (partners of Higgs bosons). Sleptons and squarks have spin zero, while gauginos and higgsinos have spin one-half. Since none of these supersymmetric particles have been discovered it is thought they are

far more massive than their standard model counterparts, and thus that supersymmetry is not an explicit symmetry of nature.

Goldberg [38] and Ellis [36] have suggested that neutral gauginos and neutral higgsinos can mix together in a superposition known as the neutralino,  $\chi$ . In most SUSY models, the neutralino is the lightest supersymmetric particle (LSP). In models which conserve R-parity (a new quantum number distinguishing SUSY particles from standard model particles) the LSP is stable, making it a prime candidate particle for dark matter. The expected cross section of neutralinos interacting via inelastic collisions with nucleons is dependent on the allowed regions of parameter space in the SUSY model being used. Results from the WMAP satellite refined this parameter space, concluding that the density parameter of neutralinos would be  $0.192 < \Omega_\chi < 0.263$  [61, 18, 12].

The neutralino is one of many candidate particles suggested for WIMPs, and as previously mentioned, WIMPs are not the only candidate for dark matter. In the following sections we will briefly discuss some of the other candidates before returning to the discussion of WIMPs in Chapter 2.

#### 1.2.4 Axions and Axinos

Quantum chromodynamics (QCD) is a theory describing the strong interaction between quarks and gluons, which make up hadrons. In particle physics there exists a proposed symmetry of nature referred to as charge conjugation parity symmetry (CP-Symmetry). CP-Symmetry postulates that particles should behave the same if they are replaced by their own antiparticle (C symmetry), and then have their parity reversed (P symmetry). Within QCD there is no theoretical reason to assume CP-symmetry exists. However, when a CP-violation term is included

in the QCD lagrangian its coefficient has been experimentally determined to be less than  $10^{-10}$  [15]. This unexpected result is known as the strong CP problem in quantum chromodynamics. To reconcile this, a new symmetry known as the Peccei-Quinn theory has been proposed. This theory postulates the existence of a new pseudoscalar particle called the axion. According to the Peccei-Quinn theory, axions would be electrically neutral, low mass ( $1\mu eV - 1eV$ ) particles that have very low interaction cross sections for the strong and weak forces. The axino arises when SUSY is introduced to the Peccei-Quinn theory, resulting in a supersymmetric partner to the axion known as the axino.

### 1.2.5 Gravitons and Gravitinos

In quantum field theory, the graviton is a hypothetical elementary particle which mediates the gravitational force. As with axions and axinos, when SUSY is introduced to quantum field theory a supersymmetric partner to the graviton is predicted to exist known as the gravitino. In some models, gravitinos are the LSP in SUSY and are thus a candidate particle for dark matter.

### 1.2.6 WIMPzillas

WIMPzillas are supermassive dark matter particles which arise when one considers the possibility that dark matter might be composed of nonthermal supermassive states. These particles would have a mass many orders of magnitude higher than the weak scale [25]. Studies have shown that for stable particles with masses close to  $10^{13} \text{ GeV}$  WIMPzillas would be produced in sufficient abundance to give  $\Omega \approx 1$  for the total density parameter of the universe.

It should be noted that the discussion of this section does not encompass all

of the alternatives to WIMPs. Although these other dark matter candidates offer intriguing explanations to the dark matter problem, the next chapter will focus on the experimental detection of WIMPs.

## 2 Searching for WIMPs

The search for WIMPs can be separated in three categories: indirect detection, direction detection, and WIMP creation. [19] Direct detection experiments search for the scattering of dark matter particles off of atomic nuclei and will be the topic of this thesis from Chapter 3 onward. Indirect detection experiments search for remnants of WIMP interactions such as gamma-rays, positrons, and neutrinos using both space based and ground based detectors. Similarly, high energy particle colliders are used to search for missing energy signals during WIMP that may be produced during their collisions.

### 2.1 Indirect Detection Experiments

In section 1.2.3 we discussed the annihilation of CDM particles such as WIMPs during the early universe. WIMP annihilation can produce gamma-rays, neutrinos, and positrons. Numerous indirect detection experiments search for these annihilation remnants in gravitational wells where the dark matter density is expected to be high, such as the center of the Sun. In the following sections, we will discuss efforts to detect each annihilation product separately.

### 2.1.1 Gamma-Ray Experiments

WIMP annihilation is expected to produce monoenergetic photons with an energy given by

$$E_\gamma = m_\chi \left( 1 - \frac{m_X^2}{4m_\chi^2} \right) \quad (64)$$

where  $m_\chi$  is the mass of the WIMP and  $m_X$  is the mass of the remnant particle. At the GeV energy scale photons interact with matter via electron-positron pair production, leading to an interaction length much shorter than the thickness of Earth's atmosphere. As a result, any experiment seeking to directly detect gamma-ray radiation from WIMP annihilation must be based in space. Satellites such as the Fermi-LAT detect the electron-positron pairs produced by gamma-ray interaction in a detector made of a dense material (in the case of Fermi-LAT, tungsten is used). These space based detectors are hindered by the numerous sources of background radiation present in astrophysical data, and are therefore unable to make significant claim of detection without observing a monoenergetic signal across multiple sources. As of 2012 the Fermi-LAT has observed no such line features or significant gamma-ray flux in its data. [6]

When gamma-rays interact with the atmosphere they produce a cascade of secondary particles. These seconday particles produce Cerenkov radiation as they pass through the atmosphere, allowing ground-based telescopes to search for the gamma-ray product of WIMP annihilation indirectly. Cosmic ray radiation can also induce Cerenkov radiation in the atmosphere, making the it difficult to distinguish gamma-ray sources from the cosmic ray background. Ground based experiments employ numerical simulations of atmospheric showers and require an excess of directional gamma-rays above the isotropic background induced by cosmic rays

to overcome this challenge. [44] As with space based experiments, ground based experiments have yet to observe a gamma-ray flux above background in their data. [4]

### 2.1.2 Neutrino Experiments

Neutrinos from WIMP annihilation can interact with ordinary matter via a charge current interaction or a neutral current interaction. In a charged current interaction, a high energy neutrino transforms into its lepton partner via a process such as inverse beta decay ( $\bar{\nu}_e + p \rightarrow n + e^+$ ). These neutrino interactions are ideal to work with, since the leptons are easy to detect and allow the neutrino to be flavor-tagged. However, if a neutrino has less energy than the mass of its lepton partner it can not interact via a charge current interaction. In a neutral current interaction the neutrino remains as a neutrino but deposits energy and momentum onto a target particle. If the target is light, such as an electron, it can be accelerated above the speed of light in the medium and produce Cerenkov radiation.

Ground based detectors, such as ANTARES and IceCube, search for the neutrinos produced in dark matter annihilation by observing the Cerenkov radiation from muon tracks produced in charged current interactions at the GeV-TeV energy scale. These detectors utilize large photo-multiplier arrays buried deep in a transparent medium, such as the antartic ice, to avoid background from cosmic rays. These experiments have not observed any dark matter annihilation signal from dark matter particles at the center of the Sun or in nearby galaxy clusters, but have set the world's best spin-dependent cross section limits for WIMPs in the process. [2, 3]

### 2.1.3 Positron Experiments

Positrons can be produced with a varying spectrum via direct annihilation of dark matter to positron-electron pairs or by annihilations to ZZ or W<sup>+</sup>W<sup>-</sup>. [24, 43]. These positrons do not travel in straight lines from their source due to galactic magnetic fields. Due to their low mass, electrons and positrons lose energy via inverse Compton scattering and synchrotron radiation as they travel from source to observer. The energy loss increases with the square of the electron energy, such that the power law energy spectrum is steepened at the location of the observer, resulting in an expectation of  $\sim E^{-3}$ . [27] The inelastic collision of cosmic-ray protons and  $\alpha$ -particles produce charged pions, which in turn produce secondary positrons and electrons in roughly equal amounts via the  $\pi - \mu - e$  decay chain. [62] For secondary electrons and positrons, the source spectrum would therefore follow the energy spectrum of ambient protons, which is approximately  $\sim E^{-3.7}$  after radiative loss during transit. If the only source of positrons was from secondary production, and astrophysical sources produced electrons, we would then expect the positron fraction  $e^+/(e^+ + e^-)$  to decrease smoothly with energy. [27] Therefore, experiments which seek to measure a positron signal from dark matter annihilation observe the positron fraction as a function of energy from entire galactic halo and compare their results to astrophysical models of positron production.

Experiments such as FERMI-LAT, PAMELA, and AMS-02 have confirmed a rise in the positron fraction at high energy. [7, 29, 5] However, a very high cross section and leptophilic models are required for these observations to be attributed to dark matter annihilation. Alternative explanations such as local pulsar sources and acceleration of secondary positrons have also been proposed. [58]

## 2.2 WIMP creation in Colliders

Experiments such as ATLAS and CMS are using the Large Hadron Collider (LHC) beneath France and Switzerland to search for the production of WIMPs in high energy particle collisions. The LHC is a proton-proton collider which should have a large production cross section for colored super symmetric particles. The WIMP pair production interaction  $pp(p\bar{p}) \rightarrow \chi\bar{\chi}$  is of no use in these experiments, since it leaves no observable signal in the detector. Instead, these experiments try to observe the higher order  $pp(p\bar{p}) \rightarrow \chi\bar{\chi} + jets$  interaction, with the jets serving as a trigger that an event took place. The dominant background when looking for such an event comes from the electroweak processes where the Z decays into a pair of neutrinos  $pp(p\bar{p}) \rightarrow \nu\bar{\nu} + jets$  or the  $W^\pm$  decays into a neutrino and a lepton  $pp(p\bar{p}) \rightarrow l^-\bar{\nu} + jets$  or  $pp(p\bar{p}) \rightarrow l^+\nu + jets$ . In a WIMP + jets event the WIMP will exit the detector unseen, producing a signature with missing transverse momentum. The magnitude of this missing momentum is typically denoted as  $E_T^{miss}$ . A model independent approach shows that  $E_T^{miss}$  should be detectable at the LHC under the assumption that all new particles mediating the interaction of WIMPs and standard model particles are too heavy to be produced directly. [17] However, no excess of events beyond the standard model processes has been observed at the LHC as of yet. [1]

## 2.3 Direct Detection Experiments

If dark matter interacts through the weak force then it should be possible to observe WIMPs via nuclear recoils in direct detection experiments. During these events a WIMP will scatter off of a target nucleus in the detector, producing a

signal in the range of 1-100 keV. [47] Direct detection experiments typically observe ionization, scintillation, or low temperature phonons produced during the event (or a combination of the three), although more recent experiments have developed an acoustic method of detection based on producing bubbles in a superheated fluid at the site of a recoil. These signals are susceptible to both nuclear recoil and electron recoil backgrounds so detailed *in situ* calibrations are required to characterize the detector's response to each type of event. In this section, we will review the canonical halo model and derive an expression for the WIMP recoil spectrum before discussing different types of direct detection experiments in detail. The following chapter we will be devoted to one particular direct detection experiment, the LUX detector.

### 2.3.1 The Canonical Halo Model

The canonical halo model treats dark matter as an isothermal spherical distribution that behaves as a non-interacting ideal gas. The spherical shape of the distribution implies no rotational movement in the bulk of the distribution, otherwise it would flatten into a disk. The velocity of a WIMP relative to the galactic center,  $v_0$ , can be approximated by the orbital velocity at a given radius from the galactic center. At the location of the sun,  $r \approx 8.5$  kpc, and  $v_0 \approx 220$  km/s. [53]

The local number density of WIMPs is given by

$$n_\chi = \frac{\rho_\chi}{M_\chi} \tag{65}$$

where  $\rho_\chi$  is the density of WIMPs in the local vicinity, and  $M_\chi$  is the mass of a WIMP particle. The local density of the dark matter halo is estimated to be

$0.3 < \rho_\chi < 0.7$  GeV/cm<sup>3</sup> [37]. Assuming the value of  $\rho_\chi = 0.4$  GeV/cm<sup>3</sup> from reference [47] we see that  $n_\chi = 0.004$  per cm<sup>3</sup> for a WIMP mass of 100 GeV. With an average WIMP velocity of  $v_0 = 220$  km/s, this is equivalent to a flux of  $\phi_\chi \approx 10^7 M_\chi s^{-1} cm^{-2}$ , or roughly half a billion WIMPs of  $M_\chi = 100$  GeV passing through your hand every second.

### 2.3.2 The WIMP Recoil Spectrum

Lewin and Smith provide a standard derivation of the expected WIMP recoil spectrum in reference [47]. Their derivation begins with the differential particle density given by

$$dn = \frac{n_0}{k} f(\mathbf{v}, \mathbf{v}_E) d^3\mathbf{v} \quad (66)$$

where  $n_0$  is the mean dark matter particle density,  $\mathbf{v}$  is the velocity of the WIMP relative to the target,  $\mathbf{v}_E$  is the velocity of the earth relative to the WIMP,  $f(\mathbf{v}, \mathbf{v}_E)$  is the WIMP velocity distribution function. The normalization constant  $k$  is given by

$$k = \int_0^{2\pi} \int_{-1}^1 \int_0^{v_{esc}} f(\mathbf{v}, \mathbf{v}_E) v^2 d(\cos\theta) dv \quad (67)$$

where  $v_{esc}$  is the local escape velocity, so that

$$\int_0^{v_{esc}} dn \equiv n_0. \quad (68)$$

Note that an annual modulation is induced in the velocity of the earth relative to the dark matter particles, and subsequently induced in the event rate of WIMPs in terrestrial detectors as well, due to the velocity of earth around the sun. This

modulation is given by

$$v_E = v_0 + 15 \cos\left(2\pi \frac{T - 152.5}{365.25}\right) \quad (69)$$

where  $T$  is measured in days from June 2nd, and  $v_0 \approx 220$  km/s is the velocity of the sun around the galactic center. The DAMA/Libra collaboration has claimed a detection a dark matter signal with annual modulation with  $8.2 \sigma$  significance. However, many dark matter experiments have since ruled this result out, so it is likely due some other unidentified modulating phenomenon in the data.

We treat the dark matter as a non-interacting ideal gas so that we can assume a Maxwellian dark matter velocity distribution given by

$$f(\mathbf{v}, \mathbf{v}_E) = e^{(-v+v_E)^2/v_0^2}. \quad (70)$$

Then for  $v_{esc} = \infty$  we define

$$k_0 \equiv (\pi v_0^2)^{3/2}, \quad (71)$$

and for finite escape velocity  $v_{esc} = |\mathbf{v} + \mathbf{v}_E|$ ,

$$k = k_0 \left[ \operatorname{erf}\left(\frac{v_{esc}}{v_0}\right) - \frac{2}{\sqrt{\pi}} \frac{v_{esc}}{v_0} e^{-v_{esc}^2/v_0^2} \right]. \quad (72)$$

The event rate per unit mass on a target of atomic mass  $A$  (AMU), with cross-section per nucleus  $\sigma$  is given by

$$dR = \frac{N_0}{A} \sigma v dn \quad (73)$$

where  $N_0$  is Avogadro's number ( $6.02 \times 10^{26} mol^{-1}$ ). For constant cross section

$\sigma = \sigma_0$ , the event rate per unit mass is then

$$R = \frac{N_0}{A} \sigma_0 \int v dn \equiv \frac{N_0}{A} \sigma_0 n_0 \langle v \rangle. \quad (74)$$

Substituting  $n_0 = \rho_\chi / M_\chi$  (where  $\rho_\chi$  and  $M_\chi$  are the WIMP density and mass, respectively) we define the event rate per unit mass for  $v_E = 0$  and  $v_{esc} = \infty$  as

$$R_0 = \frac{2N_0\rho_\chi}{\sqrt{\pi}AM_\chi} \sigma_0 v_0 = \frac{2\rho_\chi}{\sqrt{\pi}M_\chi M_T} \sigma_0 v_0 \quad (75)$$

where  $M_T$  is the mass of the WIMP, such that

$$R = R_0 \frac{\sqrt{\pi} \langle v \rangle}{2v_0} = R_0 \frac{k_0}{2\pi v_0^4 k} \int v f(\mathbf{v}, \mathbf{v}_E) d^3 v. \quad (76)$$

In differential form equation 76 becomes

$$dR = R_0 \frac{k_0}{2\pi v_0^4 k} v f(\mathbf{v}, \mathbf{v}_E) d^3 v. \quad (77)$$

The recoil energy (as measured in the lab frame) of a nucleus struck by a WIMP of kinetic energy  $E = \frac{1}{2}M_\chi v^2$  and scattered at an angle  $\theta$  in a center-of-mass frame is given by

$$E_R = \frac{1}{2} M_\chi v^2 \frac{2M_\chi M_T}{(M_\chi + M_T)^2} (1 - \cos \theta). \quad (78)$$

For isotropic scattering recoils are uniformly distributed over a range of  $0 \leq E_R \leq \frac{1}{2}M_\chi v^2 \frac{4M_\chi M_T}{(M_\chi + M_T)^2}$  so

$$\frac{dR}{dE_R} = \int_{E_{min}}^{E_{max}} \frac{(M_\chi + M_T)^2}{4M_\chi M_T E} dR(E) \quad (79)$$

where  $E_{max} = \frac{1}{2}M_\chi v^2 \frac{4M_\chi M_T}{(M_\chi + M_T)^2}$  and  $E_{min}$  is the smallest WIMP energy which can

produce a recoil of energy  $E_R$ . Since  $E = \frac{1}{2}M_\chi v^2$  and  $E_0 = \frac{1}{2}M_\chi v_0^2$ ,  $E = E_0 \frac{v^2}{v_0^2}$  and equation 79 becomes

$$\frac{dR}{dE_R} = \frac{(M_\chi + M_T)^2}{4M_\chi M_T E_0} \int_{v_{min}}^{v_{max}} \frac{v_0^2}{v^2} dR(v) \quad (80)$$

where  $v_{min}$  and  $v_{max}$  is the WIMP velocities corresponding to  $E_{min}$  and  $E_{max}$ . Therefore, using equations 71, 75, and 77 the expected energy recoil spectrum of WIMPs scattering off of a target nucleus is given by

$$\begin{aligned} \frac{dR}{dE_R} &= \frac{(M_\chi + M_T)^2}{4M_\chi M_T} \frac{k_0 R_0}{2\pi E_0 k v_0^2} \int_{v_{min}}^{v_{max}} \frac{f(\mathbf{v}, \mathbf{v}_E)}{v} d^3v \\ &= \frac{(M_\chi + M_T)^2}{2M_\chi^2 M_T^2} \frac{\rho_\chi}{M_\chi} \frac{\sigma_0}{k} \int_{v_{min}}^{v_{max}} \frac{f(\mathbf{v}, \mathbf{v}_E)}{v} d^3v \end{aligned} \quad (81)$$

It is conventional to express  $\sigma_0$  as the product of  $\sigma_0$  at the coherent scattering limit in which the WIMP interacts with the entire nucleus (with momentum transfer  $q = 0$ ) and a nuclear form factor  $F$  which accounts for the loss of coherence with higher momentum transfer. Therefore, using the WIMP-nucleus reduced mass given by  $\mu \equiv \frac{M_\chi M_T}{M_\chi + M_T}$  equation 81 becomes

$$\frac{dR}{dE_R} = \frac{\sigma_0 \rho_\chi}{2\mu^2 M_\chi k} F^2(q) \int_{v_{min}}^{v_{max}} \frac{f(\mathbf{v}, \mathbf{v}_E)}{v} d^3v, \quad (82)$$

where, as a reminder,  $\rho_\chi$  is the local WIMP density,  $f(\mathbf{v}, \mathbf{v}_E)$  is the velocity distribution of WIMPs in the halo,  $v_{min}$  is the minimum WIMP velocity able to generate a recoil of energy  $E_R$ ,  $v_{esc}$  is the escape velocity for WIMPs in the halo,  $\sigma_0$  is the WIMP-nucleus interaction cross sections, and  $F(q)$  is the nuclear form factor describing the scattering amplitude for momentum transfer  $q$ .

The WIMP-nucleus cross section can have both spin-independent (SI) and spin-dependent (SD) components [59]. The SI interaction cross section is given by

$$\sigma_0^{SI} = \frac{4}{\pi} \mu^2 [Z f_p + (A - Z) f_n]^2,$$

where  $Z$  is the atomic number of the target nucleus (the number of protons),  $A$  is the atomic mass number of the target nucleus ( $A - Z$  is therefore the number of neutrons in the nucleus), and  $f_p$  and  $f_n$  are the effective scalar couplings of WIMPs to protons and neutrons, respectively. In this process we must sum over the interactions in each nucleon prior to squaring, since the DeBroglie wavelength associated with the momentum transfer is comparable to, or larger than, the size of the target nuclei, giving rise to a coherence effect across the nucleons. If the scalar couplings of WIMPs with neutrons and protons are approximately equal (which is the case with the LSP of SUSY), then the SI cross section can be simplified to

$$\sigma_0^{SI} \simeq \frac{4}{\pi} \mu^2 A^2 |f_p|^2.$$

The cross section for SD interactions is given by

$$\sigma_0^{SD} = \frac{32}{\pi} G_F^2 \mu^2 \frac{J+1}{J} [\langle S_p \rangle a_p + \langle S_n \rangle a_n]^2,$$

where  $G_F$  is the Fermi constant,  $J$  is the total spin of the target nucleus,  $\langle S_{(p,n)} \rangle$  are the expectation values of the proton and neutron group spins, and  $a_{(p,n)}$  are the effective SD WIMP couplings on protons and neutrons. In SD WIMP-nucleus interactions it is assumed that only unpaired nucleons contribute significantly to the total cross section, since the spins of the nucleons in a nucleus are anti-aligned.

In most cases, the spin independent, coherent term dominates the total WIMP-nucleus cross section due to its  $A^2$  dependence on the atomic mass number of the target nucleus.

A calculation of both the differential and integrated WIMP event rates in single isotope targets of  $^{131}\text{Xe}$ ,  $^{73}\text{Ge}$ , and  $^{40}\text{Ar}$  using a WIMP mass of 100 GeV is included in Figure 4.

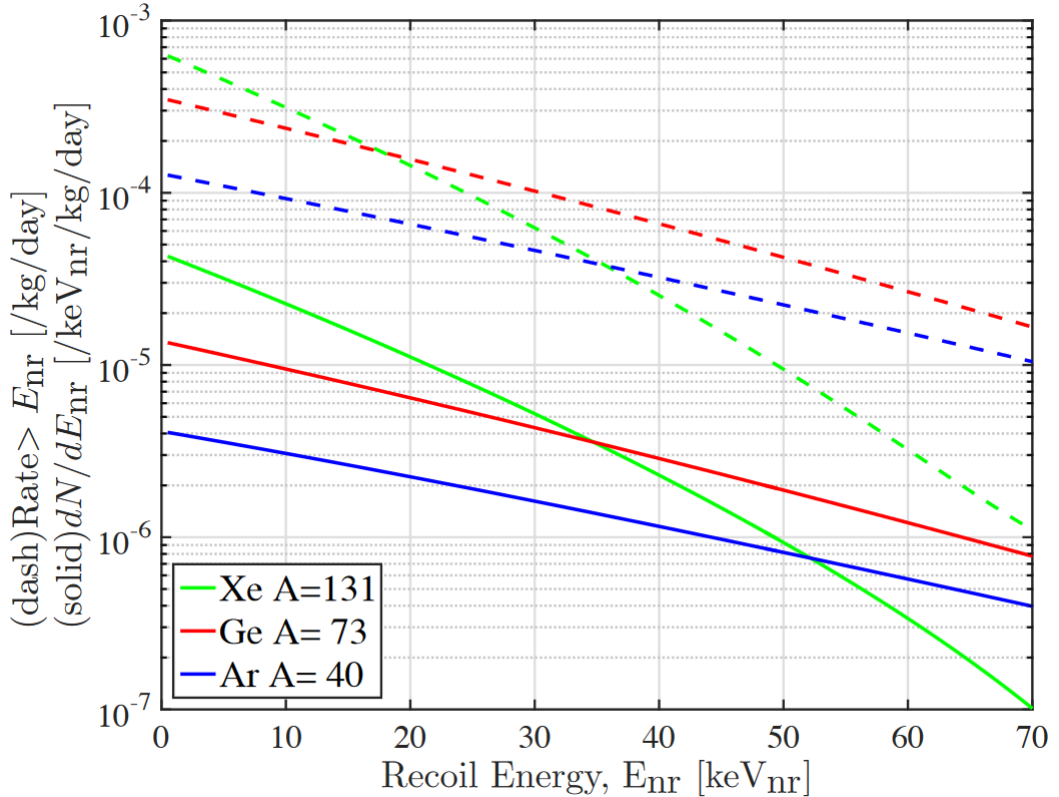


Figure 9: Calculated differential spectrum in evts/keV/kg/d (solid lines) and the integrated event rate in evts/kg/d (dashed lines) for  $^{131}\text{Xe}$ ,  $^{73}\text{Ge}$ , and  $^{40}\text{Ar}$  assuming a 100 GeV WIMP with spin-independent cross section for a WIMP-nucleon of  $\sigma = 5 \times 10^{-43} \text{ cm}^2$ .

Lighter target nuclei will produce lower event rates in a WIMP detector due to their lower cross sections (resulting from lower  $A^2$  contribution in the coherent

SI term) and less effective transfer of energy during nuclear recoil events. While heavier target nuclei produce stronger interaction cross sections, they also result in reduced event rates at high energies due to a loss of coherence from form factor suppression. To maximize efficiency a xenon detector with a low analysis threshold is ideal.

### 2.3.3 Backgrounds in Direct Detection Experiments

Direct detection experiments search for an extremely rare nuclear recoil signal between 1-100 keV. These detectors have a number of internal and external backgrounds which interfere with the WIMP search signal. Therefore, limiting sources of background is critical to maintaining a high discovery potential.

Internal backgrounds can be introduced by radioactive materials present in individual detector components. Naturally occurring radioisotopes such as  $^{232}\text{Th}$ ,  $^{238}\text{U}$ , and  $^{40}\text{K}$  can produce high energy gamma rays which penetrate deep into a detector. In the case of  $^{232}\text{Th}$ , the decay chain produces high energy gamma rays from radioactive daughters such as  $^{228}\text{Ac}$ ,  $^{212}\text{Pb}$ ,  $^{212}\text{Bi}$ , and  $^{208}\text{Tl}$  before reaching stable  $^{208}\text{Pb}$ . Likewise, the  $^{238}\text{U}$  decay chain produce high energy gamma rays from  $^{234}\text{Th}$ ,  $^{234}\text{Pa}$ ,  $^{214}\text{Pb}$ ,  $^{214}\text{Bi}$  before reaching stable  $^{206}\text{Pb}$ . In the case of  $^{40}\text{K}$ , a 1460.85 MeV gamma ray can be produced via electron capture decay to  $^{40}\text{Ar}$ . In addition to the naturally occurring radioisotopes, cosmogenically activated radioisotopes can also be present inside detector components. Neutron activation of copper can produce  $^{60}\text{Co}$ , which produces 1.173 MeV and 1.33 MeV gamma rays when it beta decays into  $^{60}\text{Ni}$  via electron emission with a half life of 5.2714 years. Neutron activation of titanium can produce  $^{46}\text{Sc}$ , which emits 889 keV and 1.12 MeV gamma rays when it beta decays into  $^{46}\text{Ti}$  via electron emission with a half

life of 84 days. Atmospheric radon in the detector introduces the  $^{222}\text{Rn}$  and  $^{220}\text{Rn}$  decay chains as additional backgrounds. While most of the daughters in the radon decay chains produce easily vetoed alpha particles the  $^{222}\text{Rn}$  decay chain includes  $^{214}\text{Pb}$  and  $^{214}\text{Bi}$ .  $^{214}\text{Pb}$  decays into  $^{214}\text{Bi}$  with a half life of 26.8 minutes via beta emission at 1024 keV, and the subsequent  $^{214}\text{Bi}$  decays in  $^{214}\text{Po}$  with a half life of 19.9 minutes via beta emission at 3272 keV. The  $^{220}\text{Rn}$  decay chain includes  $^{212}\text{Pb}$ , which decays into  $^{212}\text{Bi}$  with a half life of 10.64 hours via beta emission at 573.8 keV. The  $^{212}\text{Bi}$  then decays via alpha decay into  $^{208}\text{Tl}$ , which can subsequently decay via beta emission. These beta decays either produce no gamma ray particles (referred to as "naked" beta decays) or high energy gamma rays that can leave the detector without scattering (referred to as "semi-naked" beta decays), resulting in a background which can not be reduced via detection of a high energy gamma-ray component. Internal backgrounds from detector components are mitigated with careful screening of the materials which go into a detector; with simulations being used to predict background events arising from materials which make it through the screening process. [23]

Long lived intrinsic radioisotopes can be present in the detection medium as well. Cosmogenically activated  $^{127}\text{Xe}$  beta decays via electron capture to  $^{127}\text{I}$  with a half life of 26.358 years. The captured electron has an 85% chance of coming from the K shell with an x-ray of 33 keV, a 12% chance of coming from the L shell with an x-ray of 5.2 keV, and a 3% chance of coming from higher shells with x-rays of  $<1.2$  keV. The subsequent  $^{127}\text{I}$  daughter can decay to ground state via high energy gamma emission, with the gamma frequently leaving the detector without scattering. The  $^{127}\text{Xe}$  activity decays away quickly, so this background can be mitigated by moving the detector underground prior to data collection.

$^{39}\text{Ar}$  is generated by cosmic ray interactions with  $^{40}\text{Ar}$  in a (n,2n) process in the atmosphere and can find it's way into a detector's medium. The 565 keV electron emission decay has a half life of 269 years, placing strong constraints on the amount of  $^{39}\text{Ar}$  that can be present in a detector's medium when data is collected.  $^{85}\text{Kr}$  is produced by man made processes, such as nuclear fuel processing. As with  $^{39}\text{Ar}$ , the  $^{85}\text{Kr}$  can make its way into a detector's medium where it will beta decay via electron emission to  $^{85}\text{Rb}$  with a half life of 10.756 years at 687 keV. These long lived radioisotopes which originate from the atmosphere must be purified from the detector medium prior to data collection to reduce background levels in the detector. [23]

Neutrons are particularly dangerous source of background which can mimic the single scatter nuclear recoil present in a WIMP signal. While neutrons can be stopped by a few tens of meter water equivalent shielding, cosmic ray muons can penetrate many kilometers of shielding. Muon interactions in the laboratory can produce "cosmogenic" neutrons at the GeV scale with mean free path much longer than most detectors. These neutrons can be attenuated by rock or shielding and produce keV scale recoils in WIMP detectors. Such events are mitigated by tagging the initial muon with a muon veto system, placing external shielding around the detector, and by placing the detector deep underground to limit the muon flux. Neutrons can also be generated internally via ( $\alpha$ ,n) interactions in construction materials, such as the ( $\alpha + ^{19}\text{F} \rightarrow ^{22}\text{Na} + \text{n}$ ) reaction in fluorine present in PTFE, and from spontaneous fission of  $^{238}\text{U}$  and  $^{232}\text{Th}$ .

The background mitigation techniques discussed in this section can not completely remove backgrounds from a detector. To separate any remaining backgrounds from a WIMP signal, detectors use a technique called nuclear recoil dis-

crimination. Nuclear recoil discrimination does not reduce the total number of background events, but instead seeks to distinguish electron recoil interactions from nuclear recoil interactions and reject the former population. In the next section we discuss a variety of WIMP detection methods, with each of these methods having its own form of nuclear recoil discrimination.

#### 2.3.4 Direct Detection Methods

A WIMP deposits energy in a detect in the form of scintillation light, ionization, and heat. A variety of WIMP detectors have been constructed that each detect one or two of these channels. Scintillation detectors use scintillating crystals or liquid scintillators as a target medium. For instance, the DAMA/LIBRA experiment at the Gran Sasso Laboratory in Italy uses room temperature, thallium doped sodium iodide ( $\text{NaI}(\text{Tl})$ ) scintillating crystals as a target medium. Each crystal is paired with two photomultiplier tubes (PMT) which collect scintillation light from within each crystal. Annual modulation of the WIMP signal due to the motion of the earth around the sun is used to discriminated background events from WIMP events. The XMASS detector uses liquid xenon as a target medium. The scintillation produced in the xenon by recoil events is collected by PMT arrays. Background events from gamma ray sources are attenuated by the liquid xenon's large atomic number ( $Z=54$ ) and high density, leading to a low background fiducial volume. This discrimination technique is referred to as "self shielding." Single phase liquid argon experiments, such as DEAP and CLEAN, can not take advantage of self shield techniques due to the intrinsic background from  $^{39}\text{Ar}$ . Instead, these experiments use a technique called pulse shape discrimination to differentiate signal events from background. Scintillation in liquid noble gases is produced by

the decay of singlet or triplet excimers. The triplet state emits light over a longer period of time, and the light can be suppressed by destructive interactions such as Penning ionization and electron-triplet spin exchange. Nuclear recoils produce higher excitation densities, and therefore more destructive interactions with the triplet excimers, leading to a difference in the pulse shape of nuclear recoil and electron recoil events.

Single phase ionization detectors have also been used in the search for dark matter. The CoGeNT detector in the Soudan Underground Laboratory in Minnesota uses a low input capacitance p-type point contact (PPC) germanium crystal to detect ionization from WIMP interactions. The detector has energy thresholds as low as 500 eV, allowing the collaboration to search for low mass ( $\sim 5$  GeV/c $^2$ ) WIMP particles. Electron recoil background events scatter at multiple events sites in the germanium crystal, while WIMPs scatter at most once. This leads to a longer rise time in pulses from background events which can be used as another form of pulse shape discrimination.

Phonon detectors are the final type of single signal detectors. These type of detectors, such as the Cryogenic Underground Observatory for Rare Events (CUORE) in the Gran Sasso National Laboratory, use low heat capacity crystals as a target medium. In the case of CUORE, tellurium dioxide crystals (TeO<sub>2</sub>) are held at 10 mK to reduce thermal noise. The low heat capacity of the crystals allows particle interactions to raise the temperature of the crystals, which in turn changes the resistance of neutron transmutation doped germanium thermistors which are glued to the top of each crystal. A constant current is applied to the thermistors, and the voltage across each thermistor is used as a detection method. These types of detectors do not have any means of event discrimination, so they rely heavily

on the use of radiopure construction materials and background modeling.

In addition to the single signal detectors, many detectors collect data from two of the three energy deposition channels. The Cryogenic Dark Matter Search (CDMS) in the Soudan mine records signals from both phonons and ionization. The detector uses Ge and Si detectors cooled to  $\sim$ 40mK as a target medium. The low temperature is required to reduce thermal noise in the detector. Ionized particles are drifted to the top of the crystals by an electric field where they are read out using field effect transistors, and the corresponding phonon signal is collected by superconducting transition edge sensors coupled with SQUIDs on the opposite face of each crystal. The ionization yield of a nuclear recoil is lower than an electron recoil, so the ratio of the two signals is used for nuclear recoil discrimination.

The Cryogenic Rare Event Search with Superconducting Thermometers (CRESST) is a phonon and scintillation detector in the Gran Sasso National Laboratory. CRESST uses calcium tungstate ( $\text{CaWO}_4$ ) crystals, which are cooled to 10 mK to lower thermal noise, as a target medium. As with CDMS, transition edge sensors are used to detect phonons originating from particle interactions in the crystals. Scintillation light in the crystals absorbed by a silicon light absorber that converts the scintillation photons to heat, which are then detected by secondary thermometers. A nuclear recoil produces 10-40 times less scintillation light in the  $\text{CaWO}_4$  crystals than an electron recoil does, so the ratio of the phonon and scintillation signal can be used for nuclear recoil discrimination.

The final class of detectors records the scintillation and ionization signals from particle interactions. These detectors, which are known as dual phase time projection chambers, use liquid noble scintillators (typically xenon) as a target medium.

Primary scintillation light is collected by PMT arrays at the top and bottom of the detector. An electric field is used to drift charge from ionized particles to the top of the detector, where the charge produces a secondary source of scintillation light as it accelerates through the gaseous xenon above the liquid. The ratio of the primary and secondary scintillation light can be used for nuclear recoil discrimination. Currently, the most sensitive dark matter detector in the world is a dual phase TPC placed in the Sanford Underground Reasearch Facility in South Dakota. This detector, known as the Large Underground Xenon detector (LUX), will be discussed in depth in Chapter 3.

### 3 The LUX Detector

The Large Underground Xenon detector (LUX) is a dual phase time projection chamber location in the Sanford Underground Research facility in South Dakota. The detector is a dodecagonal structure that uses 300 kg of liquid xenon as a target medium. The commercially bought xenon was distilled to  $\sim 1$  ppm (g/g) of air by the manufacturer before undergoing a krypton removal campaign to lower residual krypton levels to less than 5 parts per trillion (g/g). Particle interactions in the liquid xenon produce ionized and excited state xenon atoms. Some of the electrons released in the ionization process recombine with the xenon ions, forming additional xenon excitons, while the rest are drifted to the liquid surface by an electric field. The xenon excitons return to the ground state with a characteristic time constant of 2.2 ns for the singlet state and 27 ns for the triplet state, producing scintillation light at  $\sim 175$  nm in the processes. This scintillation light is referred to as the S1 signal. Electrons which make it to the liquid surface are accelerated through the gas above the liquid xenon by a stronger electric field, producing electroluminescent light which is referred to as the S2 signal. This process will be discussed in depth in section 6.1 .

Two arrays of 61 PMTs each are used to measure both the S1 and S2 light in the detector. The light response of each PMT in the top array is used to reconstruct the XY position of recoil events based on the intensity of the S2 signal, and the time difference between the S1 and S2 signal is used to reconstruct the depth of the recoil events. In this way, the LUX detector has three dimensional position reconstruction which can be used to construct a low background fiducial volume in the center of the detector.

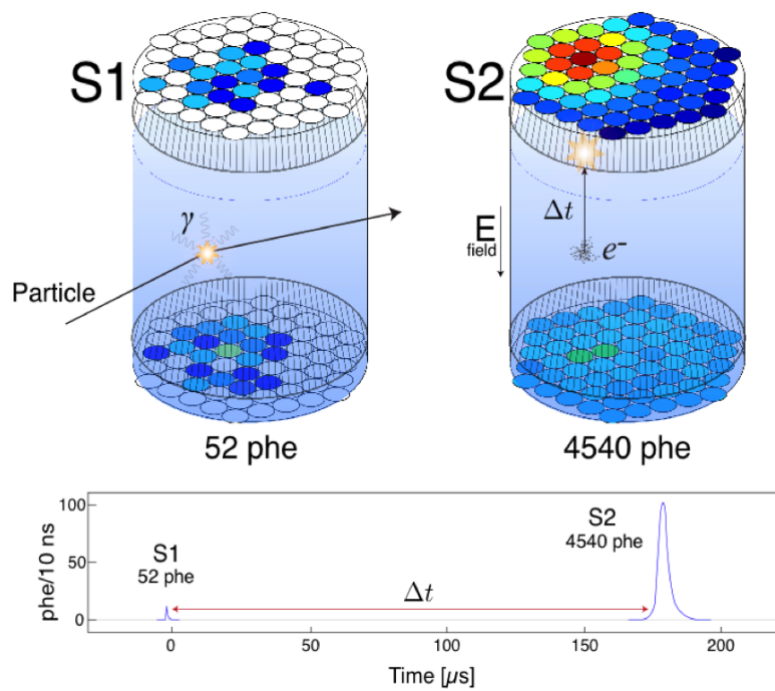


Figure 10: A depiction of a recoil event in LUX. The response of the top PMT array to the S2 light is used for xy position reconstruction, while the timing between the S1 and S2 signals is used for the depth measurement.

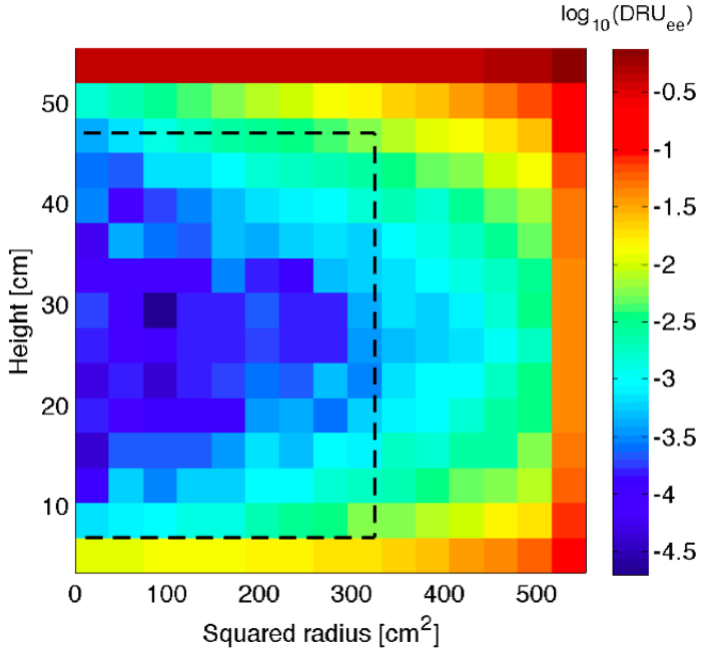


Figure 11: Simulated gamma ray backgrounds in the LUX detector after removing multiscatter events. The black dashed lines indicate the fiducial volume used in the first LUX WIMP search results.

The LUX detector is an extremely low background environment due to the strong self shielding properties of liquid xenon and the lack of naturally occurring xenon radioisotopes. Low energy external backgrounds ( $<50$  keV) can only travel a few millimeters into the liquid xenon volume, while higher energy gamma rays ( $\sim$ MeV range) will produce easily identifiable multiscatter events due to their mean free path of a few centimeters. Any background events which do appear in the fiducial volume are reduced by over 99% by using the ratio of the S1 and S2 signal as a form of nuclear recoil discrimination. Discrimination techniques in the LUX detector will be discussed more in section 4.3. In this section, we will discuss the detector internals, external support system, and the DAQ electronics used to read out the PMT signal.

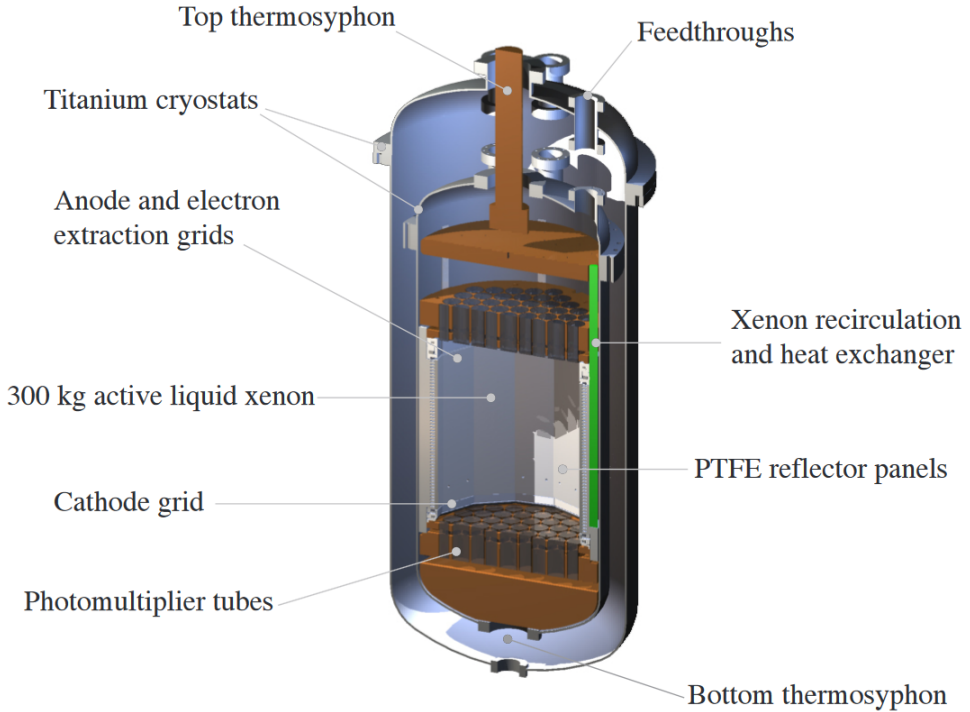


Figure 12: Cross section of the LUX cryostats and internal detector components.[10]

### 3.1 Detector Internals

#### 3.1.1 Cryostats

A cross section of the LUX cryostats and detector internals is shown in figure 12. An outer titanium cryostat is used to maintain a thermally insulating vacuum around the detector. An inner cryostat which houses the liquid xenon and detector internals is attached to the roof of the outer cryostat via three plastic hangers. Instrumentation cables and gas circulation plumbing are fed through flexible conduits at the top of the detector. Flexibility of the feedthroughs is required to deal with thermal contraction of the plastic hangers.

### 3.1.2 PMT Arrays, PTFE Structure, and Electric Field Cage

Inside the inner cryostat, a 5 cm thick copper block with a diameter of 55 cm is mounted directly on to the flange. This copper serves as a radiation shield and a temperature controller during detector operations. A similar copper structure is attached to the bottom of the inner cryostat and is used to displace xenon from the inactive volume in addition to the functions of the top radiation shield.

Two PMT arrays are used to collect light from the S1 and S2 signals in the detector. Each array contains 61 Hamamatsu R8778 PMTs which observe the active volume. These PMTs were specifically designed for operation in liquid xenon, with a typical quantum efficiency of 33% at the 175 nm wavelength of liquid xenon scintillation. The top PMT array is housed in a copper structure which is hung 15 cm below the upper radiation shield by six titanium straps. Reflective polytetrafluoroethylene (PTFE) trifolts cover the inner face of the copper housing to increase light collection efficiency in the detector. A similar structure is placed at the bottom of the detector to house the bottom PMT array.

Twelve PTFE panels hang from the top PMT support and are attached to the bottom PMT support. These panels are used to increase light collection efficiency in the detector, and serve as the support structure for the electric field cage in the detector. The field cage is made of five wire grids. Each grid is made of thin stainless steel wires and are 88-99% transparent at a normal angle of incidence. Stainless steel is known to be 57% reflective at xenon scintillation wavelength, further minimizing the optical footprint of the wire grids. The top grid is located 2 cm below the top PMT array. A stainless steel ring is used to string 50 micron diameter stainless steel wires spaced with a pitch of 1 cm. The voltage on the

top grid is used to zero the electric field at the photocathodes of the top PMTs. The anode is placed 4 cm below the top grid. It is similar in design to the top grid, but uses 30 micro wires with 0.5 mm spacing. The gate grid, which uses 50 micron stainless steel wires with a pitch of 5 mm, is placed 1 cm below the anode grid. The position of the gate grid places it about 5 mm below the liquid xenon surface. These two grids work in tandem to produce a strong extraction field (5-6 kV/cm) that pulls charge out of the liquid xenon and into the gas, producing the S2 signal. The cathode grid is placed about 49.5 cm below the liquid surface. This grid uses 260 micron diameter stainless steel wires with a pitch of 5 mm, and works in tandem with the anode grid to produce a  $\sim$ 180 V/cm electric field which drifts charge from a particle interaction to the liquid surface. The bottom grid is the last of the five wire grids. It is located 4 cm below the cathode grid and 2 cm above the bottom PMT support, and uses 206 micron diameter stainless steel wires with a pitch of 1 cm. The bottom grid serves the similar purpose as the top grid – it is used to zero the field at the photocathodes of the bottom PMT arrays.

Fourty-eight copper field rings are spaced 1 cm apart inside of the PTFE panels to shape the drift field. These rings have thickness of 3.2 mm and a width of 12.7 mm. The spacing and thickness of the rings were chosen to shield the active region from the electric field produced by the cathode high voltage cable. The voltage of the field rings is set by a resistor chain that runs between the gate and the cathode grids. A pair of  $0.875\text{ G}\Omega$  resistors connect the top field ring to the gate grid, while a pair of  $1.25\text{ G}\Omega$  resistors connect the bottom field ring to the cathode grid. A pair of  $1\text{ G}\Omega$  resistors is used to connect each adjacent field ring.

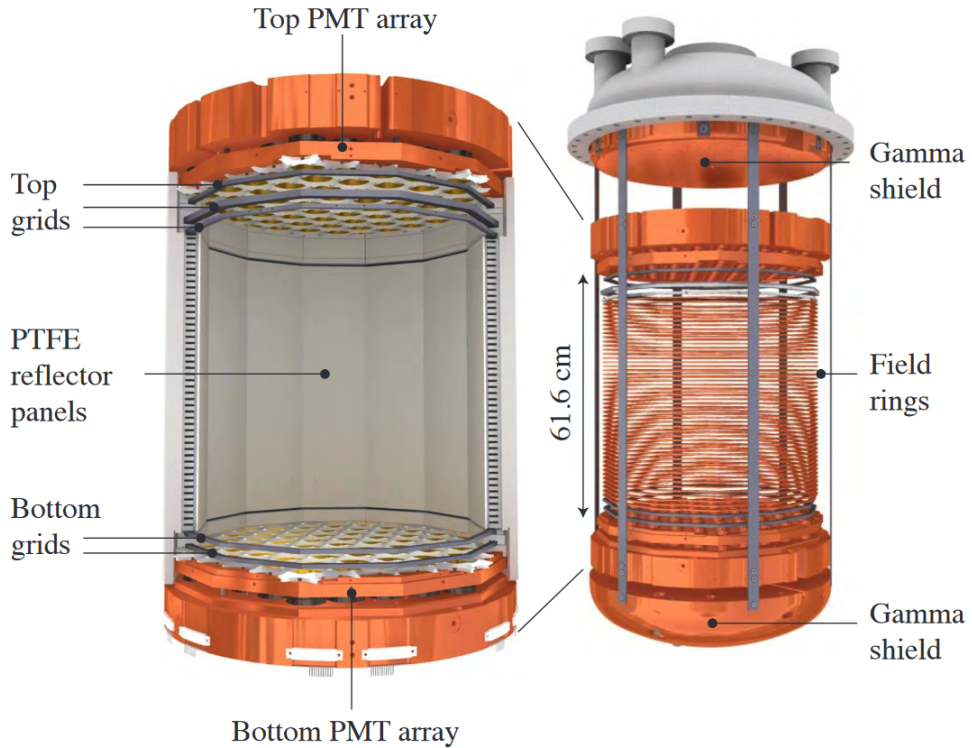


Figure 13: Depiction of the LUX PMT supports, PTFE panels, and field cage.[10]

### 3.1.3 Cryogenics

A thermosyphon system is used to cool the detector internals to liquid xenon temperatures ( $\sim 175\text{K}$ ) during operation. A thermosyphon is a sealed tube filled with a variable amount of gaseous nitrogen ( $\text{N}_2$ ). A condenser which is immersed in a bath of liquid nitrogen is placed at the top of the thermosyphon. As the nitrogen in the thermosyphon tube condenses, gravity causes it to trickle down stainless steel plumbing to copper heat exchangers that are attached to various points in the inner cryostat. The condensed nitrogen evaporates when it hits the copper heat exchanger, removing heat from the detector. The evaporated nitrogen rises back up the stainless steel plumbing where it is once again condensed by

the liquid nitrogen bath. In this way, the thermosyphons act in a continuous loop, transferring heat from the detector to the liquid nitrogen bath which the condenser is immersed in.

Two thermosyphons are attached to the copper radiation shields at the top and bottom of the inner cryostat and are used as the driving force to cool the detector from room temperature to 175K. Two more thermosyphons are attached to copper shielding around the inner inner cryostat and are used to prevent any thermal gradients from building in the detector. Each copper evaporator is fitted with a 50 W heater and a thermometer for fine temperature control. Larger 750 W heaters are attached to the two primary thermosyphons to aid in detector warm up during liquid xenon recovery.

### 3.1.4 Instrumentation

The LUX detectors is fitted with numerous instruments that help monitor and stabilize the conditions within the cryostat. Fourty 100  $\Omega$  thin film platinum resistance temperature detectors (RTDs) are used to monitor the temperature inside the inner cryostat. These instruments are help prevent the formation of thermal gradients which could warp the detector internals. An additional 23 RTDs are used to monitor the temperature inside the outer vacuum space, providing a means to detect leaks from the inner cryostat or outer atmosphere to the insulating vacuum space. Calibration of the RTD readouts was performed prior to installation, as well as in situ at room temperature, with an accuracy of 170 mK for each RTD. Advantech Adam 6015 modules are used to feed the output voltage of the RTDs to a slow control database, where multiple users can monitor the read outs and set automated alarms to notify collaboration members of any temperature fluctuations

in the detector.

A variety of pressure sensors are used throughout the detector. Sensor models include Ashcroft AST4900 sensors, InstruTech Hornet ion and convection gauge, Swagelok PGU-50-PC100-L4FSF manual pressure gauges, and a Setra model 759 capacitance manometer. These instruments are used to monitor the stability of the inner cryostat, the quality of the outer vacuum, and the pressure in various locations of the gas circulation system. As with the RTDs mentioned above, all of the digital pressure gauges are read out to the slow control database where alarms can be set to notify users of potential leaks in the circulation system or out of control warming and cooling effects in the detector.

Six parallel wire sensors are used to monitor the liquid level in the inner cryostat, the weir, dual-phase heat exchanger, and the liquid return line. The later detectors mentioned here will be discussed in section 3.2.1. The capacitance of each wire pair depends on the length of wire submerged in the liquid, allowing the overall height of the liquid to be determined. Additionally, three parallel plate sensors are placed 120 degrees apart between the gate and anode grids. These sensors ensure the liquid surface is uniform and without any tilt.

## 3.2 External Support Systems

### 3.2.1 Gas Circulation and Purification System

The xenon used in the LUX detector needs to be free of electronegative and molecular impurities that could attenuate charge and light from particle interactions. To achieve this goal LUX circulates the detector's xenon through a gas system which includes a heated zirconium getter made by SAES. The getter removes nearly all

non-nobel gas impurities with an efficiency of 99.9%, but requires the xenon to be in gaseous form when operating.

The process of evaporating the liquid xenon, flowing the gaseous xenon to the SAES getter, and recondensing the xenon before returning it to the inner cryostat is handled by the LUX gas system. Within the inner cryostat excess liquid spills over the lip of a weir into a reservoir, where it enters the evaporator side of a two phase heat exchanger. In this side of the heat exchanger, xenon is pumped on by the external circulation system until it evaporates. The cooling effect of the evaporation is used to recondense xenon which is returning to the detector on the other side of the heat exchanger, reducing the heat load of the process by 90%.  
(??)

The gaseous xenon leaving the evaporator side of the heat exchanger passes through a concentric-tube heat exchanger which warms it to room temperature before circulating to the SAES getter. After passing through the SAES getter, the purified xenon continues on to a second concentric-tube heat exchanger where it is cooled before entering the condenser side of the two phase heat exchanger. After condensing in the two phase heat exchanger the, now liquid, xenon enters the inner cryostat through the bottom radiation shield to ensure its temperature is consistent with the detector internals.

A diaphragm pump which is capable of 50 SLPM (420 kg/day) is used to maintain a constant flow of xenon through the circulation system. In practice, the flow is limited to  $\sim$ 27 SLPM (227 kg/day) by the output pressure of the circulation pumps.

### 3.2.2 Gas Sampling System

Five xenon sampling ports are included in the gas circulation system. These ports allow xenon from the two phase heat exchanger, getter input, getter output, conduit purge lines, or circulation pump inlet to be diverted to a xenon assay system. The assay system makes use of a cryogenic cold trap to separate impurities from the xenon. During use, a xenon sample flows through the cold trap, where it is frozen through contact with a liquid nitrogen bath. The frozen xenon sets the vapor pressure of the system at 1.8 mTorr. Most impurities have a vapor pressure higher than 1.8mTorr, allowing them to pass through the cold trap and separate from the bulk of the xenon. The remaining impurities flow at high leak rates to a commercial Residual Gas Analyzer (RGA) made by SRS, where the absolute level of impurities in the bulk xenon is deduced by comparing to a calibration data set. After sampling, xenon can be discarded with the use of vacuum pumps in the sampling system, or recovered to high pressure cryogenic storage and recovery vessel (SRV) for potential reuse later. While we are most concerned with the krypton concentration due to the background producing radioisotope  $^{85}\text{Kr}$ , it is important to assay the other impurities as well. Argon can produce radioactive backgrounds in the detector, helium can diffuse through PMT faces and damage the vacuum behind them, and nitrogen and oxygen can serve as an indicator for air leaks. This assaying technique results in sensitivity to krypton below 1 ppt (1e-12) g/g, a factor of 10,000 better than measurements performed without a cold trap.

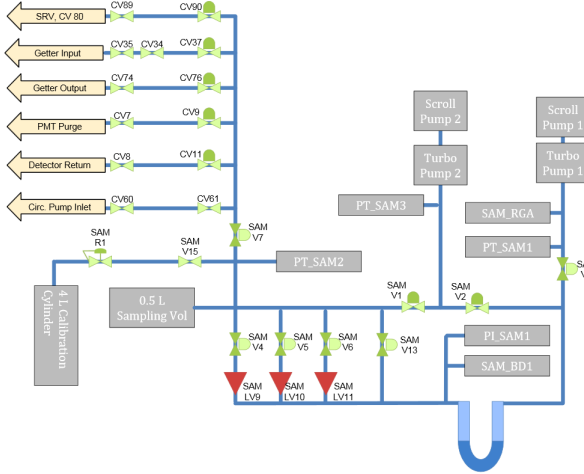


Figure 14: Depiction of the LUX sampling system. Xenon enters the sampling system through various sampling ports in the main circulation path. These sampling ports are shown in the top left of the diagram. The xenon then passes through one of three leak valves (indicated by red triangles) into a U-shaped cold trap, where it is analyzed by an RGA on the output of the cold trap. A secondary set of vacuum pumps is included so that the system can be evacuated independently of the RGA space.

### 3.2.3 Water Tank and Muon Veto System

The LUX cryostat is enclosed in a 7.6 meter diameter, 5.1 meter high water tank. The water tank holds 8 tons of water that is continuously circulated through an industrial purifying system to reduce detector backgrounds originating from the water tank itself. The concentration of uranium, thorium, and potassium are held more than six orders of magnitude lower than the rock surrounding the laboratory (2 ppt, 3ppt, and 4 ppb respectively). The water tank provides 2.75 m of shielding to the top of the detector, and 3.5 m of shielding to the sides, that reduces backgrounds originating in the laboratory environment. The tank is also outfitted with 20 Hamamatsu R7081 PMTs which can be used as an active veto for events which coincide with muons passing through the detector.

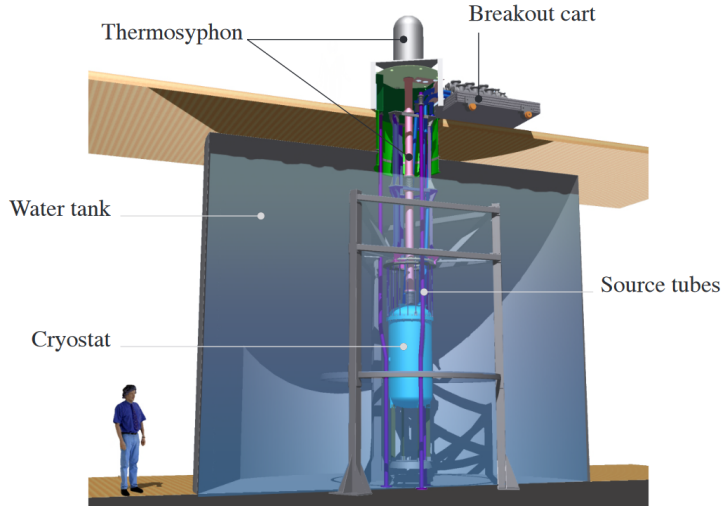


Figure 15: Cross section of the LUX water tank which surrounds the cryostat.

### 3.2.4 Calibration Systems

LUX utilizes multiple internal and external calibration sources to measure the detector's S1 and S2 response to recoil events. Six source tubes surround the cryostat in the water tank. A system of pulleys is used to temporarily deploy radioactive sources in each tube. A collimator is used for directional control of the particle interactions from the external sources. AmBe and  $^{252}\text{Cf}$  are placed in the source tubes to calibrate the detectors nuclear recoil response. High energy  $^{137}\text{Cs}$  gamma ray sources are placed in the tubes to calibrate the detector's electron recoil response, and to illuminate the detector walls for position reconstruction and background modeling studies. Other gamma ray sources, such as  $^{22}\text{Na}$  and  $^{208}\text{Tl}$  are available for electron recoil response calibration as well. High energy gamma rays from external sources only penetrate the outermost centimeters of the liquid xenon volume due the same self shielding properties that reduce unwanted external backgrounds, making it difficult to calibrate the entire fiducial volume

with external sources.

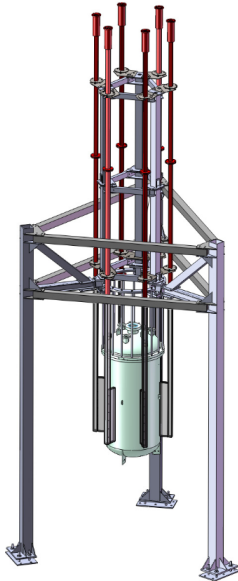


Figure 16: Rendering of the six external source tubes which surround the LUX cryostat.

In addition to the source tubes mentioned above, a 377 cm long horizontal air filled conduit can be lowered into the water tank by a pulley system. This conduit serves to displace water from the tank, opening a collimation path for an Adelphi Technologies, Inc. DD108 deuterium-deuterium neutron generator which is located outside of the water tank. The neutron generator is operated at a 5% duty cycle using  $100 \mu\text{s}$  neutron pulses to produce mono-energetic 2.45 MeV neutrons at a rate of 500 Hz. The resulting neutrons scatter multiple times in the fiducial volume, and are used to calibrate the detector's nuclear recoil response from 0.7 to 24.2 keV<sub>nr</sub>.

LUX also employs two internal calibrations sources which are injected directly into the gas circulation system.  $^{83}\text{Rb}$  soaked charcoal is used to inject  $^{83m}\text{Kr}$  directly into the circulation system on a weekly basis.  $^{83}\text{Rb}$  decays into  $^{83m}\text{Kr}$  with

an 86.2 day half life. The resulting  $^{83m}\text{Kr}$  daughter decays via internal conversion at 9.4 keV and 32.1 keV with a half life of 1.86 hours. Once injected into the gas system, the  $^{83m}\text{Kr}$  quickly makes its way into the fiducial volume, where it uniformly disperses throughout the entire detector. The spatial uniformity and intrinsic nature of this source makes it extremely useful when measuring the spatial dependence of the detector’s S1 and S2 signals, which we will be discuss in depth in Chapter 5. After a calibration has finished, the  $^{83m}\text{Kr}$  is removed from the detector in a short amount of time due to its 1.86 hour half life.

Tritiated methane ( $\text{CH}_3\text{T}$ ) is the second internal calibration source used in LUX.  $\text{CH}_3\text{T}$  is a beta source with a peak at 2.5 keV and a mean energy of 5.6 keV. The wide, low energy spectrum of  $\text{CH}_3\text{T}$  is used to calibrate the detector’s electron recoil response across the entire energy range of interest for WIMP events.  $\text{CH}_3\text{T}$  has a half life of 12.3 years, so unlike the  $^{83m}\text{Kr}$  it must be actively removed from the detector by the SAES getter in the circulation system. The unprecedented  $\text{CH}_3\text{T}$  source was designed specifically for LUX, and is discussed in detail in Chapter 4.

### 3.3 Detector Electronics

The photons collected by the two PMT arrays are amplified by the PMT dynode chains to mV scale voltage signals. The rise time for an S1 pulse is limited to  $\sim$ 6 ns by the response of the PMTs, and the 29 ns effective time constant of the xenon excimer relaxation defines the S1 pulses’ decay constant. The pulse width of and S2 event varies with depth due to diffusion of the electron cloud as it drifts through the detector.

The LUX data acquisition (DAQ) system is designed to distinguish  $>95\%$  of

single photoelectron pulses at 5 sigma above baseline noise fluctuations, and to prevent saturation of events with energies  $< 100 \text{ keV}_{ee}$  at any stage in the electronics. To achieve this, the analog chain must put the peak of single photoelectron distribution at 30 ADC counts. In the analog chain, the mV scale signals from the PMTs are sent to a x5 amplitude preamplifier before passing to a post amplifier in the DAQ electronics rack. The multichannel post amplifier produces a gain of 1.5x that is sent to sixteen 8-channel ADC modules, and a gain of 2.8x to a DDC-8 trigger system.

The ADC modules digitize the signals at 100 MHz (10 ns/sample) with a resolution of 14 bits. Each ADC board is connected to a VME bus that is subsequently connected to the DAQ computer by fiber optic cables. Data is downloaded to the DAQ computer with speeds of up to 80 MB/s. Each ADC board is controlled by four field programmable gate arrays (FPGAs) that operate in a space saving "pulse only digitization" (POD) mode. In POD mode, PMT channels are paired and data is only saved to the DAQ computer if either member of the PMT pairing rises above threshold. A valid pulse trigger gate (VPTG) mechanism further reduces memory space demands. The VPTG is implemented using CAEN V814 discriminators which require two fold coincidence between PMT channels. Valid pulses are expected to occur in more than one channel, so the VPTG reduces unwanted triggers from various sources of noise.

The DAQ trigger system uses two 8 channel digital signal processors (DDC-8DSP). Top and bottom PMTs are summed into 16 groups (8 groups per array), and the analog sum of each group is produced with a Lecroy 628 Linear Fan-In/Fan-Out module. A trigger builder is connected to the DDC-8's and takes  $< 1 \mu\text{second}$  to generate a final trigger signal to send to the DAQ. The trigger builder

is capable of distinguishing S1 and S2 pulses, and can therefore operate in S1-only, S2-only, or S1 and S2 trigger mode. The DAQ can operate with a maximum trigger rate of 1.5 kHz before incurring deadtime.

### 3.4 Science Results

PUT RUN04 RESULT IF (OR RUN03 IF RUN04 ISNT AVAILABLE)

## 4 Tritium as a Calibration Source

In two phase (liquid and gas) xenon detectors recoil events will produce a scintillation signal (referred to as S1) and ionization. The electrons produced by the ionization process can be drifted to an anode located in the gas phase of the detector. Once the electrons are accelerating toward the anode in the xenon gas they will create a secondary scintillation signal (referred to as S2). Nuclear recoil events have higher ionization density, leading to a higher probability that electron will recombine at the site of the initial recoil event, resulting in a higher S1 yield and lower S2 yield than electron recoil events of the same energy. Therefore, the ratio of the S1 and S2 signals can be used to distinguish electron recoil backgrounds from WIMP-like nuclear recoil events. This background discrimination technique is referred to as nuclear recoil discrimination.

A detector's response to both nuclear recoil and electron recoil events must be well understood to take advantage of nuclear recoil discrimination. Typically, an external beta emitter such as  $^{137}\text{Cs}$  is used to calibrate the detector's electron recoil response. However, the xenon in LUX has a strong self-shielding characteristic at UV wavelengths. While this is convenient for eliminating background radiation

from external sources, it makes calibrating the innermost regions of the detector difficult with external calibration sources.

To overcome this problem the LUX collaboration is making use of internal calibration sources. An ideal internal calibration source would need to be a single beta emitter in the energy range of interest ( $< 15$  keV) which can be dissolved into the liquid xenon in the detector. Furthermore, the source must be made of a material with low electronegativity so that it will not diminish the drift length of charge in the detector. Similarly the source cannot attenuate the UV scintillation light produced by events in the detector. To achieve a reliable calibration in all regions of the detector the source would need to have a long enough life time to diffuse throughout the entire detector (a few hours). Finally, there must be a method for removing the source once the calibration has finished. This could simply mean waiting for the source to decay if its half life is short, or actively purifying the source out of the detector if its half life is long

Tritium meets several of these requirements. It is a beta emitter with a Q-value of 18 keV, a mean energy of 5.6 keV, and a mode 3 keV that produces a broad spectrum over the entire energy range of interest. Its 12.3 year half life means that the source will have plenty of time to dissolve uniformly throughout the detector. However, this long half life is potentially dangerous, since one can not simply wait for it to decay away it must be actively removed from the detector when the calibration is completed. To complicate this matter bare tritium sticks to most surfaces, including materials like teflon, polyethylene, and steel which make up the majority of most xenon detectors. To make tritium removal more feasible we have made use of tritiated methane( $\text{CH}_3\text{T}$ ). Methane is highly inert due to its fully saturated carbon-hydrogen bonds. It has a diffusion constant in polyethylene

that is 10 times smaller than hydrogen, and it does not capture electrons that will be drifting through the detector. By replacing one of the hydrogen atoms in a methane molecule with tritium we combine the strength of both of these materials, resulting in the ideal internal calibration source.

## 4.1 Tritiated Methane Injection System

The design of our triated methane calibration technique can be separated into three parts: the injection system, the tritiated methane source bottle, the zirconium getter.

The tritiated methane source bottle was prepared in three steps. First, we prepared a xenon bottle that had similar pressure and purity to the LUX system. We filled a 2250 cc stainless steel bottle with 1590 torr of xenon from the same dekryptonation and purity program which the LUX xenon came from. The purpose of this xenon was to serve as a carrier gas for the tritiated methane. The next step was to prepare a small amount of tritiated methane to mix with this dekryptonated xenon. A reservoir of tritiated methane with an activity of 204 Bq/torr-cc was purchased from Moravek Biochemical. The reservoir was frozen with liquid nitrogen, resulting in a vapor pressure of  $10.4 \pm 0.05$  torr. We then opened the frozen tritiated methane reservoir to a 1/4" VCR cross which was sealed with swagelok valves on each side. This first expansion space had a total volume of  $5.2 \pm 0.9$  cc. Next, we isolated the VCR cross from the tritiated methane reservoir and then opened it to a  $501 \pm 0.2$  cc expansion volume. We isolated the VCR cross a second time and then opened it up to a  $53.2 \pm 3.4$  cc expansion volume. The VCR cross was then isolated for a third time before opening it to a  $10.5 \pm 0.5$  cc

expansion volume. After this final expansion the VCR cross was isolated and the remaining  $0.016 \pm 0.006$  torr-cc of tritiated methane left within was mixed with the dekryptonated xenon inside the 2250 cc bottle via cryopumping. The final result was a tritiated methane source which had an activity of  $9.1\text{e-}7 \pm 3.4\text{e-}7$  Bq/torr-cc. After the success of the initial  $\text{CH}_3\text{T}$  calibrations in LUX, a similar procedure was used to produce stronger source bottles for higher statistics calibrations.

The injection system for our tritiated methane calibration technique consists of a series of expansion volumes which are used to fine tune the amount of  $\text{CH}_3\text{T}$  that is injected. Once the  $\text{CH}_3\text{T}$  source bottle is opened it flows through a methane gas purifier (SAES MC1-905F) to remove any sources of potential contamination, such as bare tritium. The  $\text{CH}_3\text{T}$  then flows into the expansions volumes set by the user. We use expansion volumes of  $9.8 \pm 0.4$  cc,  $13.3 \pm 0.4$  cc,  $26.0 \pm 0.5$  cc,  $82.7 \pm 0.5$  cc,  $12.0 \pm 0.6$  cc, and  $132.7 \pm 0.6$  cc in setup, which provide over an order of magnitude control in the strength of an injection. Note that each injection will lower the total activity in the  $\text{CH}_3\text{T}$  source bottle via volume sharing, results in a smaller, yet calculable, injection activity with subsequent injections. Once the expansion volumes have filled, the flow of xenon in the gas system is diverted through the expansion volumes to sweep the  $\text{CH}_3\text{T}$  into the detector. We continue to flow through the expansion volumes for one hour at 1 SLPM, which is equivalent to flushing out the full 384.5 cc of the expansion volumes roughly 75 times. Two pump out ports allow various parts of the injection system to be evacuated in preparation for each use. A pressure gauge (PT-T1) is included above the tritiated methane source bottle so that this drop in activity can be measured. The final component of the injection system is a particle filter (Mott Corp. GSP3752FF11) which prevents particles contaminants from entering the LUX detector.

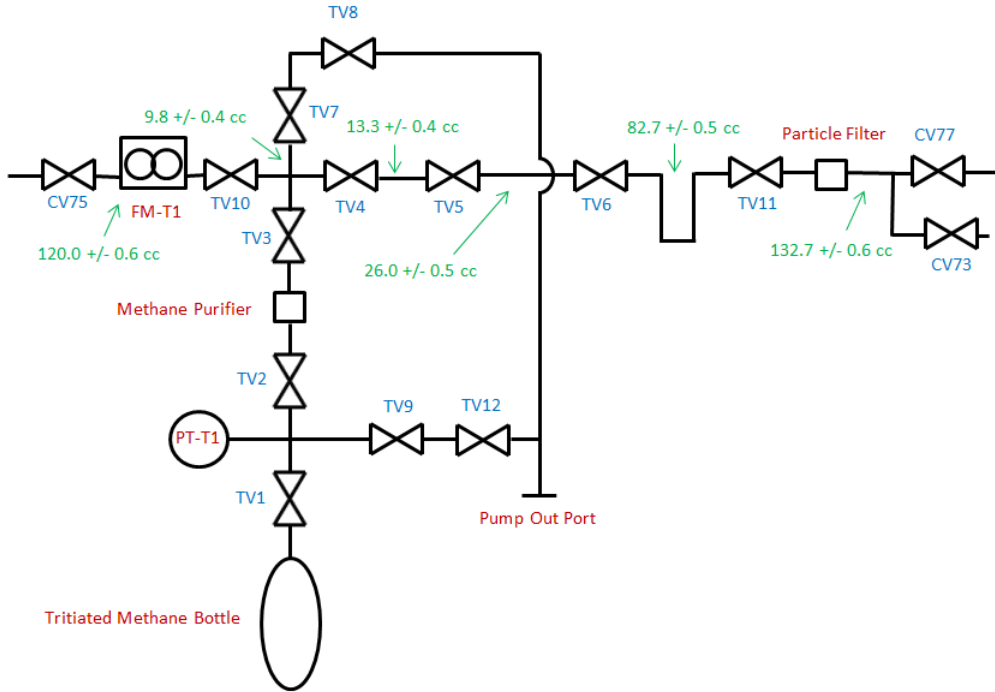


Figure 17: Plumbing diagram of the LUX tritium injection system. Blue labels indicate valves, red labels indicate equipment, and green labels indicate the size of individual expansion volumes when all valves are closed.

Once the CH<sub>3</sub>T has been injected in the LUX gas system it flows into the liquid xenon inside of the LUX cryostat, where it diffuses uniformly throughout the fiducial volume. The CH<sub>3</sub> inside of the cryostat beta decays, producing electron recoil events over a wide range of energies throughout the entire detector.

Since the xenon gas in LUX is constantly circulating, the remaining CH<sub>3</sub>T is swept out of inner cryostat with the circulating xenon. The LUX gas system uses a hot zirconium getter (SAES ??) downstream of the cryostat to remove CH<sub>3</sub>T and other impurities from the xenon. Extensive R&D was conducted using a smaller zirconium getter (SAES pcf4c3r1) at the University of Maryland to learn about the CH<sub>3</sub>T removal efficiency of these purifiers. Details of these studies is

discussed in section 4.2.

## 4.2 Triated Methane Removal

To study the CH<sub>3</sub>T removal efficiency of zirconium getters the University of Maryland built two separate systems to inject tritiated methane into a gaseous xenon and a liquid xenon environment. Both of these systems used zirconium getters to remove any CH<sub>3</sub>T that was injected into them.

### 4.2.1 Gas Phase Experiments

The gaseous xenon system consists of three sections. The first section, the xenon space, contains a hot zirconium getter to remove CH<sub>3</sub>T from the system, two xenon storage bottles used to move xenon through the system via cryopumping, and a proportional tube used to detect activity within the xenon space. The second section is a small transfer system which is used to inject consistent amounts of CH<sub>3</sub>T into the xenon space with each injection. The final section consists of a CH<sub>3</sub>T storage bottle used as the source of injections and a SAES MC1-905F methane purifier to remove unwanted contaminates prior to entering the xenon space.

The primary goal of this experiment was to determine the purification efficiency of the zirconium getter and study residual contamination. We found that the flow rate through the getter and the amount of time between injections had the largest impact of purification efficiency. High flow rates through the purifier can cool the zirconium inside, while inadequate rest time between subsequent purifications can lead to build up of methane on the surface of the zirconium beads. Both of these

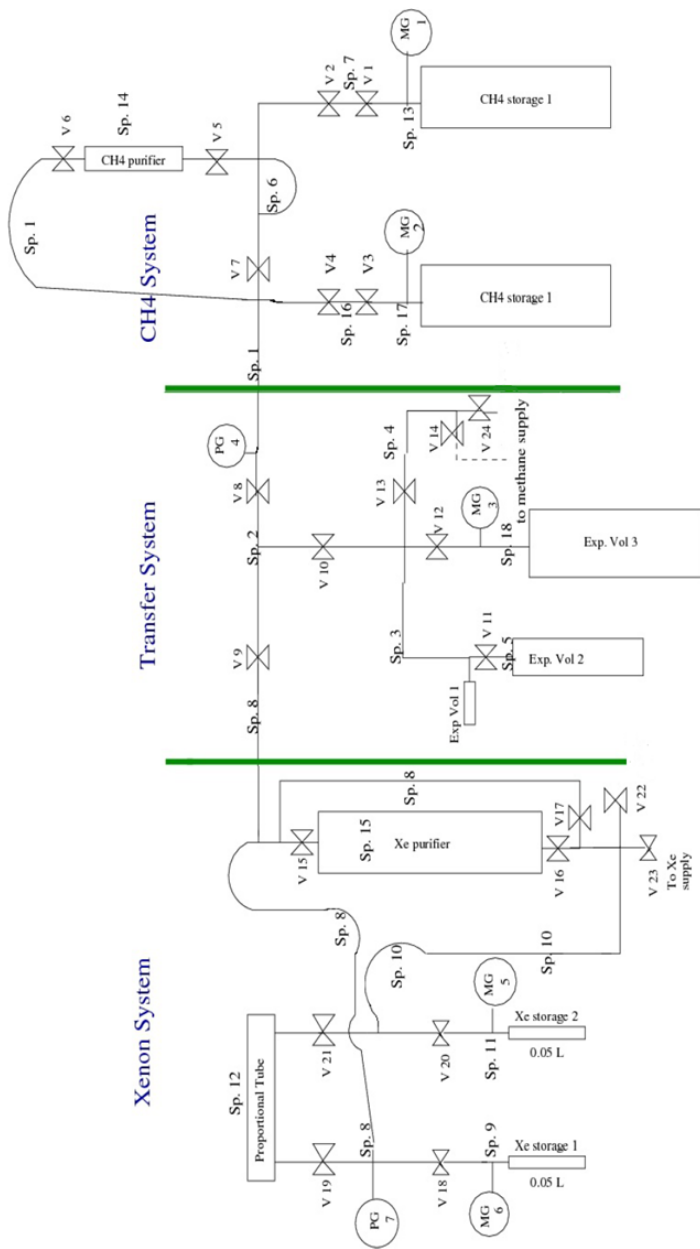


Figure 18: Diagram of the gaseous xenon system at UMD. The three sections of the system are distinguished by green lines. Circles labeled PG and MG are pressure gauges, and the hourglass shaped symbols represent hand valves.

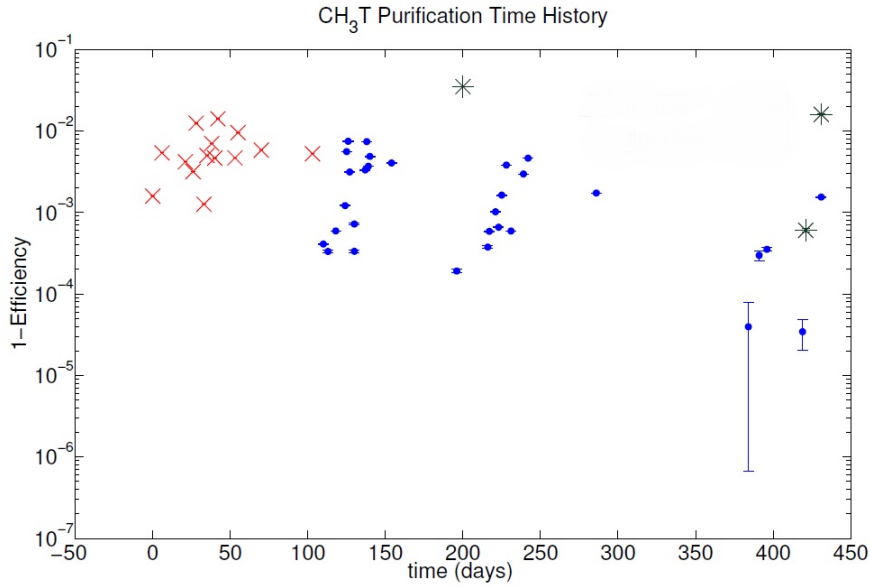


Figure 19: Single pass inefficiency of the purifier when removing CH<sub>3</sub>T. Red and blue points indicate data taken by different students, while the black points indicate data for which procedures were intentionally altered.

situations lead to a decrease in purifier efficiency. The first black data point in Figure 19 is our worst purification efficiency, ( $96\% \pm 1\%$ ) corresponding to our highest flow rate. (8 SLPM compared to the typical 0.3 SLPM) While we were unable to control the flow through rate as much as we desired, we are at least able to conclude that exceeding the maximum flow rate suggested for the purifier does significantly decrease purification efficiency. We also found that allowing ample rest time between subsequent purifications significantly increases purification efficiency. Our best purifications were the first data points in each cluster in Figure 20. We were able to obtain efficiencies of 99.99% when the purifier was resting for three weeks or longer, and obtained efficiencies ranging from 99.00% to 99.90% when the purifier was used on a daily basis.

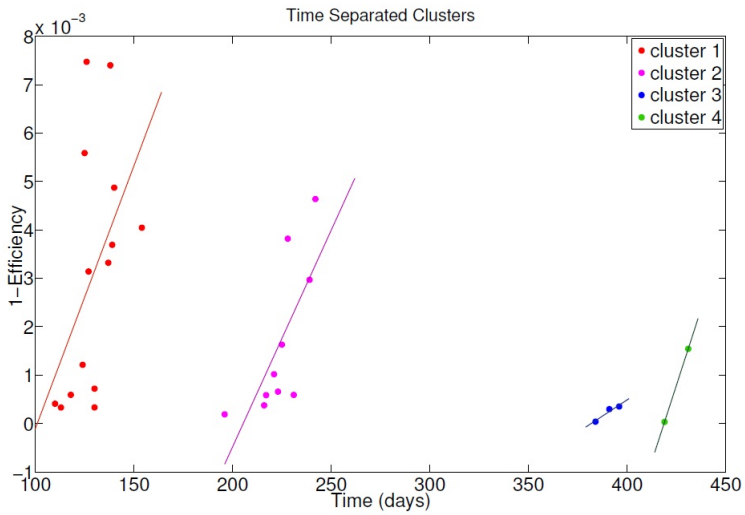


Figure 20: Time-separated clusters of purification have an upward trend in purification inefficiency.

#### 4.2.2 Liquid Phase Experiments

We have also tested tritium removal from liquid xenon. Our liquid xenon system consists of three main sections, the  $\text{CH}_3\text{T}$  injection system, the xenon circulation system, and the liquid xenon cryostat. We will first discuss the set up of the tritium injection system, pictured below. The injection system begins at the  $\text{CH}_3\text{T}$  storage bottle. This bottle is double valved for safety reasons. As with the gaseous experiments, we have a SAES MC1-905F methane purifier in series with the storage bottle. Following the methane purifier there is a series of injection volumes branching out to the left. These injection volumes are designed to inject the desired amount of  $\text{CH}_3\text{T}$  into the xenon system. The last component of the injection system is located above the injection volumes. This plumbing is used to collect all of the  $\text{CH}_3\text{T}$  from the injection volume via cyropumping. After the plumbing has warmed, the xenon circulating outside of the injection system is

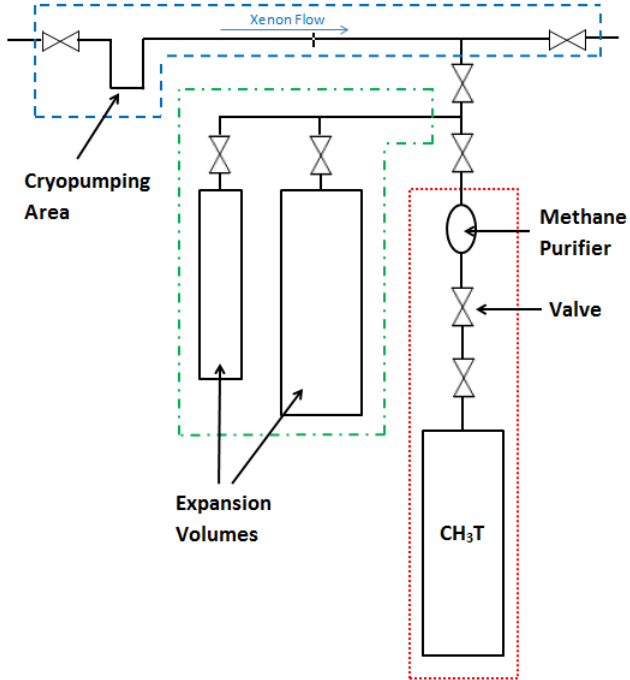


Figure 21: The tritium injection system for the liquid phase experiments at UMD. The red box indicates the  $\text{CH}_3\text{T}$  storage bottle and methane purifier area, the green box indicated the expansion volumes, and the box indicates the cryopumping and xenon flow through area.

rerouted through the cryopump plumbing to sweep all of the  $\text{CH}_3\text{T}$  into the xenon circulation system.

In the xenon circulation system, a small diaphragm pump circulates gaseous xenon in a close circuit. A zirconium getter (SAES pcf4c3r1) is positioned in between the  $\text{CH}_3\text{T}$  injection system and the liquid xenon cryostat. A bypass around the zirconium getter is present to allow control of when  $\text{CH}_3\text{T}$  removal occurs.

The final section of our system, the liquid xenon cryostat, is pictured in Figure 22. In the liquid xenon system, a pulse tube refrigerator cools a xenon gas

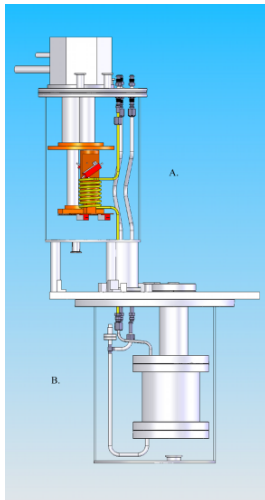


Figure 22: The liquid xenon system at UMD. (A) The xenon condenser consists of a helical coil cooled by a pulse tube refrigerator. (B) The liquid xenon storage vessel houses two PMTs to observe tritium decay.

condenser consisting of a helical coil of copper tubing. The condensed xenon drips into a liquid xenon storage vessel. Two PMTs are placed inside of the storage vessel to observe scintillation light produce by CH<sub>3</sub>T decays in the liquid xenon. Once the vessel is filled both of these PMTs are submerged in the liquid xenon. Note that this means the system at UMD is a single phase detector, rather than a dual phase detector like LUX. Polyethylene and teflon curtains were installed in the inner cryostat to surround the PMTs during some of our data sets. These curtains of plastic were used to study outgassing effects in our detector.

During our liquid phase experiments, our experimental procedure consisted of taking an adequate amount of background data, injecting CH<sub>3</sub>T into the liquid xenon, waiting for the CH<sub>3</sub>T event rate to plateau, and then purifying the CH<sub>3</sub>T out of the xenon. During the data sets in which teflon or polyethylene curtains were installed around our PMTs we bypassed our purifier after initially purifying away the CH<sub>3</sub>T so that outgassing effects could be studied. Injection activities

for our liquid phase experiment ranged from  $1487 \pm 35.06$  Bq to  $12164 \pm 1028.11$  Bq. A detailed list of our purification efficiency measurements in liquid xenon is included in Table 1. Note that the rise in background rate during our polyethylene runs is due to a change in PMT gain. Using the lessons learned from the gaseous xenon experiments we were able to achieve an average purification efficiency of 99.999% in our liquid experiments, where we define our purification efficiency to be

$$\text{Purification Efficiency} = 1 - \frac{A - B}{I - B}, \quad (83)$$

where A is the background event rate after injecting  $\text{CH}_3\text{T}$ , B is the background event rate before to injecting  $\text{CH}_3\text{T}$ , and I is the injected  $\text{CH}_3\text{T}$  activity as observed by out PMTs. We find that the addition of plastic curtains around our PMTs does not impair our ability to remove  $\text{CH}_3\text{T}$  at  $> 99.998\%$  levels. To illustrate the effectiveness of  $\text{CH}_3\text{T}$  removal, an overlay of injected and purified  $\text{CH}_3\text{T}$  spectra is included in Figure 23. Cumulatively, we have injected over 68,000 observed becquerel of  $\text{CH}_3\text{T}$  into our liquid xenon. Although systematic errors lead to a fluctuation of our residual background rates, we see no upward trend in our data set as the cumulative observed injection activity rises.(Figure 24)

#### 4.2.3 Outgassing Experiments

To more accurately model the LUX detector we surrounded our PMTs with polyethylene or teflon panels during some of our data sets. The experimental procedure for these data sets was to collect an adequate amount of background data, inject  $\text{CH}_3\text{T}$  into the liquid xenon, wait for the  $\text{CH}_3\text{T}$  event rate to plateau, purify the  $\text{CH}_3\text{T}$

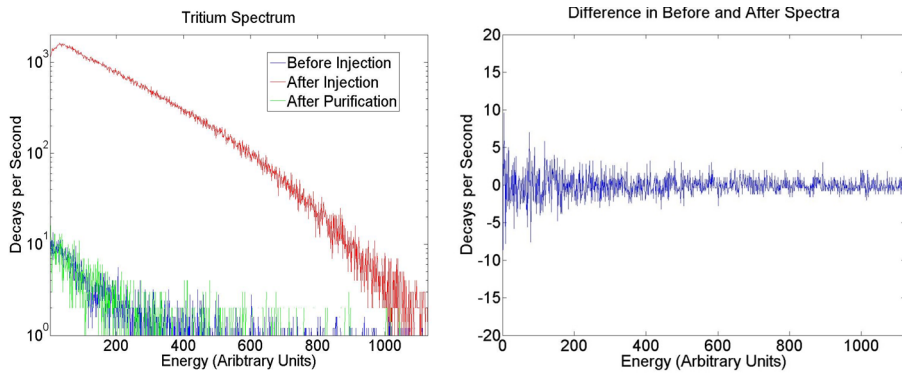


Figure 23: Left: Overlay of  $\text{CH}_3\text{T}$  spectra seen by PMTs in the liquid xenon detector. The blue spectrum is what is seen prior to injecting tritium, the red spectrum is what is seen after injecting tritium, and the green spectrum is what is seen by after purifying the xenon to remove any injected  $\text{CH}_3\text{T}$ . Right: The difference between the before injection and after purification spectra.

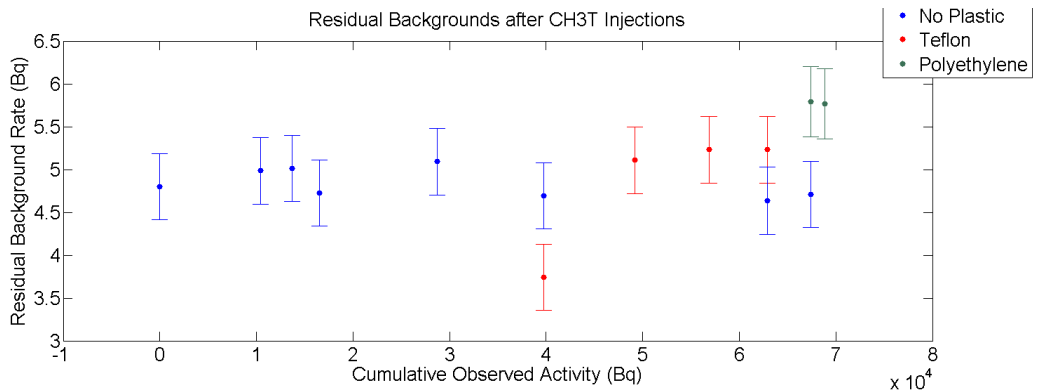


Figure 24: Residual background rates over time in the UMD detector after purifying the  $\text{CH}_3\text{T}$  out of the xenon. Blue data points are data sets in which no plastic curtains were used inside of the detector, red data points are data sets in which teflon curtains were used inside of the detector, and green data points are data sets in which polyethylene curtains were used inside of the detector.

Observed Injection Activity (Bq)	Background Before Injection (Bq)	Background After Injection (Bq)	Purification Efficiency	Type of Plastic
10415.84 ± 140.89	4.78 ± 0.38	4.99 ± 0.39	0.99998 ± 0.000054	No Plastic
3295.15 ± 46.28	4.99 ± 0.39	5.01 ± 0.39	0.99999 ± 0.00017	No Plastic
2836.67 ± 22.35	5.01 ± 0.39	4.76 ± 0.39	1.00009 ± 0.00020	No Plastic
12164.29 ± 1028.11	4.72 ± 0.39	5.09 ± 0.39	0.99997 ± 0.000082	No Plastic
11033.62 ± 1766.87	5.09 ± 0.39	4.69 ± 0.38	1.00004 ± 0.00015	No Plastic
9435.13 ± 180.13	3.74 ± 0.38	5.32 ± 0.39	0.99983 ± 0.000061	Teflon
7666.08 ± 226.67	5.11 ± 0.39	5.23 ± 0.39	0.99998 ± 0.000082	Teflon
6043.72 ± 446.80	5.23 ± 0.39	5.23 ± 0.39	1.00000 ± 0.00016	Teflon
4504.81 ± 220.89	4.64 ± 0.39	4.71 ± 0.40	0.99998 ± 0.00016	No Plastic
1487.09 ± 35.06	5.79 ± 0.41	5.76 ± 0.41	1.00002 ± 0.00043	Polyethylene

Table 1: CH<sub>3</sub>T purification efficiencies in liquid xenon.

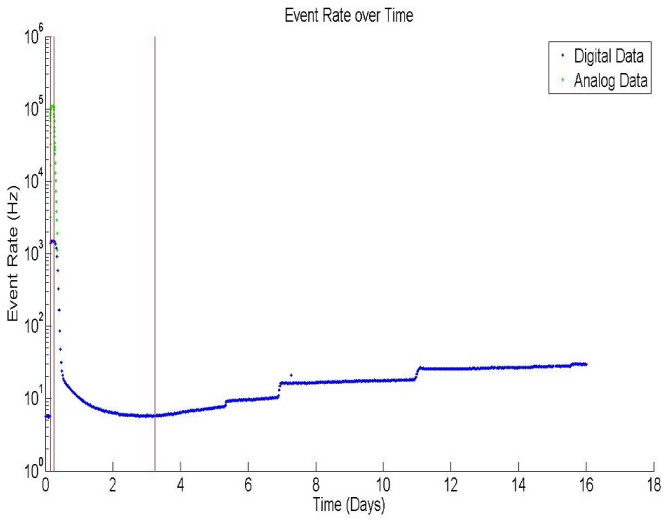


Figure 25: A time histogram of the  $\text{CH}_3\text{T}$  rate in our system. The third red line indicates when our purifier was bypassed.

away until we reached the initial background event rate, then bypass the purifier on our system to study outgassing effects. Once the purifier had been bypassed we discovered two sources of residual  $\text{CH}_3\text{T}$  contamination. We see a gradual rise in  $\text{CH}_3\text{T}$  activity after bypassing our purifier due to outgassing of  $\text{CH}_3\text{T}$  from the plastic panels. This outgassing effect will be discussed in detail in Section 4.2.4. In addition to this steady rise, we see large steps in  $\text{CH}_3\text{T}$  activity at random intervals. (Figure 25) These step features occur every 3 days on average. The longest period of time without a step occurring was 5.08 days. To examine these step features more closely, we analyzed the spectra from one of these events. We found that the integral of the spectra rose from  $8833 \pm 93.98$  to  $17190 \pm 131.11$  during the event, an increase of 194.6%. (Figure 26)

Such an increase in  $\text{CH}_3\text{T}$  activity can be produced through two mechanisms: a drift in PMT gain which would shift the  $\text{CH}_3\text{T}$  spectrum horizontally, or an increase in  $\text{CH}_3\text{T}$  activity shifting the  $\text{CH}_3\text{T}$  spectrum vertically. To determine if

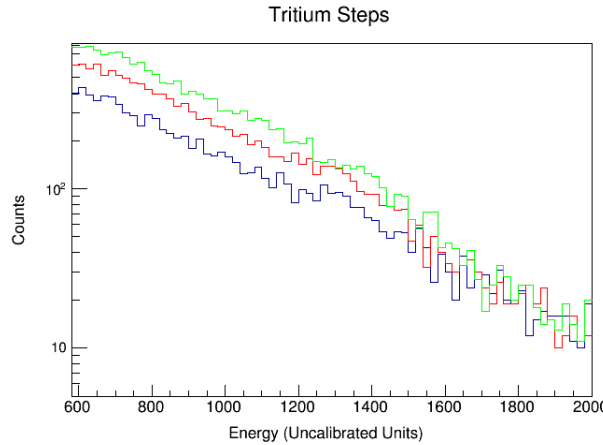


Figure 26: An overlay of three spectra from a step in  $\text{CH}_3\text{T}$  after bypassing our purifier. The blue spectrum was collected prior to a step occurring, the red spectrum was collected while a step was occurring, and the green spectrum was collected after the step had reached a plateau.

our PMT gain was shifting during our  $\text{CH}_3\text{T}$  data sets we used an external  $^{137}\text{Cs}$  source. Over eight days the  $^{137}\text{Cs}$  event rate remained flat, with an initial event rate of  $120255 \pm 346.778$  observed Bq and a final event rate of  $115469 \pm 339.807$  observed Bq. A linear fit to the  $^{137}\text{Cs}$  data results in a nearly zero slope of 0.0026 Bq per day. (Figure 27) We conclude that the rise in tritium rate during the step events can not be due to our PMT gain drifting, and must therefore be a result of an increase in the amount of  $\text{CH}_3\text{T}$  in the fiducial region of our detector. We suspect this increase in  $\text{CH}_3\text{T}$  is due to pockets of stagnant gas slowly moving into the detector's fiducial region. To avoid such a source of residual  $\text{CH}_3\text{T}$  contamination, a detector wishing to use tritiated methane as an internal calibration source must be designed such that no areas of stagnant gas exist within its system.

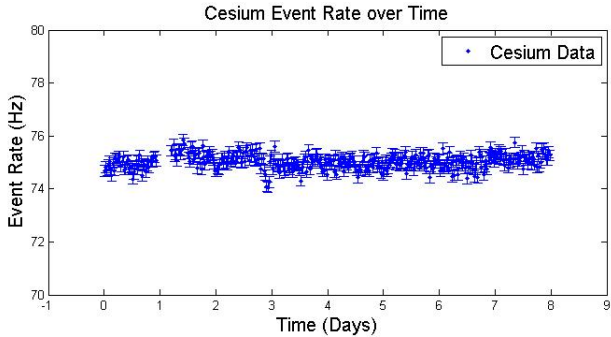


Figure 27: The event rate of a  $^{137}\text{Cs}$  source placed outside the xenon storage vessel. The flatness of the rate over time indicates that the PMT gains are mostly constant.

#### 4.2.4 Simulating Outgassing in LUX

The outgassing effects seen in UMD’s small scale liquid xenon experiment places an upper limit on the  $\text{CH}_3\text{T}$  activity that can be injected into low background detectors such as LUX. In the LUX collaboration we chose to define the tolerable  $\text{CH}_3\text{T}$  activity after a calibration to be 5% of the nominal background rate in LUX, setting a limit on the residual  $\text{CH}_3\text{T}$  activity of  $0.33 \mu\text{Bq}$ . This upper limit is extremely conservative, and guarantees that any electron recoil backgrounds introduced by a  $\text{CH}_3\text{T}$  calibration will be negligible.

With the above constraints in mind, we can determine an upper limit on the amount of  $\text{CH}_3\text{T}$  that can be injected for internal calibrations of the LUX detector. The diffusion process is governed by two different equations known as Fick’s laws. Fick’s first law describes the flux of a material through a surface. Its general form is given by

$$J = -D \frac{d\phi(r, t)}{dr}. \quad (84)$$

Combining Fick's first law with the continuity equation given by

$$\frac{\delta\phi}{\delta t} + \nabla \cdot J = 0, \quad (85)$$

which states that a change in density in any part of the system is due to inflow and outflow of material results in Fick's second law,

$$\frac{\delta\phi}{\delta t} = D\nabla^2\phi, \quad (86)$$

which describes the transport of a material by diffusion.

To implement these diffusion laws into our model we must determine the diffusion coefficient of CH<sub>3</sub>T in the plastics of LUX. At room temperature, the diffusion coefficient of methane in teflon is measured to be  $2.3 \times 10^{-7} \frac{cm^2}{sec}$ . [?]. The temperature dependence of this diffusion constant is modeled by the Arrhenius equation,

$$D = Ae^{\frac{-E_a}{RT}} \quad (87)$$

where  $E_a$  is the activation energy,  $R$  is the gas constant, and  $T$  is the temperature. This suggests than an adjustment factor to the diffusion constant of  $10^6$  at liquid xenon temperature. This adjustment factor is equivalent to increasing the thickness of the plastic in our model by a factor of 1,000. For this reason we are motivated to use half-infinite line boundary conditions in our diffusion model.

The analytic solution to Fick's second law using half-finite line boundary con-

ditions is

$$\phi(x, t) = KC_{out} - \int_0^t \operatorname{erf}\left(\frac{x}{\sqrt{4D(t-\tau)}}\right) KC_{out}(\tau) d\tau - KC_{out}(0) \operatorname{erf}\left(\frac{x}{\sqrt{4Dt}}\right) \quad (88)$$

where  $K$  is the solubility of the material and  $C_{out}$  is the outside concentration of the material. [?] For the outgassing process we are only interest in the flux of the material out of the plastic. This is given by Fick's first law evaluated at  $x = 0$ ,

$$J_{out}(t) = -K \sqrt{\frac{D}{\pi}} \left( \int_0^t \frac{\dot{C}_{out}(\tau)}{\sqrt{t-\tau}} d\tau + \frac{C_{out}(t)}{\sqrt{t}} \right), \quad (89)$$

where the sign has been flipped since the flux of material is outward. We see that it is no longer possible to evaluate  $K$  and  $D$  separately, since the diffusion in and out of the plastic is completely determined by the time-dependent concentration outside of the plastic. To simplify our model, we define a new constant

$$G = K \sqrt{\frac{D}{\pi}} \quad (90)$$

We can fit the integral of our equation for the flux out of the plastic over time to the outgassing data collected in Maryland's liquid xenon system to extract a value for the constant  $G$ . Since the outgassing data includes step features from stagnant pockets of unpurified  $\text{CH}_3\text{T}$ , we can set an upper limit on  $G$  by assuming the step features are a result of outgassing itself, and a lower limit on  $G$  by removing the steps from our data, treating them as if they have no connection to outgassing at all. With this method we loosely constrain  $0.0001 \frac{\text{cm}}{\sqrt{\text{day}}} \leq G \leq 0.0075 \frac{\text{cm}}{\sqrt{\text{day}}}$ . (Figure 28) The value of  $G$  was further constrained to  $G \leq 0.0002 \frac{\text{cm}}{\sqrt{\text{day}}}$  by injecting natu-

ral methane into LUX and observing the effects of outgassing with the sampling system.

With a constraint on G taken from the analytic solution to Fick's second law, we turn to numerical simulation to answer the question of how much initial CH<sub>3</sub>T activity to inject into LUX to meet our calibration conditions. Several assumptions are made to simplify the numerical model. First, we approximate the diffusion into plastic as being a one dimensional process. In cylindrical coordinates, Fick's laws become

$$J = -D \left( \frac{\delta\phi}{\delta r} \hat{\mathbf{r}} + \frac{1}{r} \frac{\delta\phi}{\delta\theta} \hat{\boldsymbol{\theta}} + \frac{\delta\phi}{\delta z} \hat{\mathbf{z}} \right) \quad (91)$$

$$\frac{\delta\phi}{\delta t} = D \left( \frac{\delta^2\phi}{\delta r^2} + \frac{1}{r} \frac{\delta\phi}{\delta r} + \frac{1}{r^2} \frac{\delta^2\phi}{\delta\theta^2} + \frac{\delta^2\phi}{\delta z^2} \right). \quad (92)$$

Since the plastic in our detector at Maryland and in LUX can be approximated by a cylindrical shell, there is no dependence on the azimuthal or z coordinates. Since  $r$  is large compared to the thickness of the plastic shell,  $\frac{\delta^2\phi}{\delta r^2} \gg \frac{1}{r} \frac{\delta\phi}{\delta r}$ , so we can make the approximations

$$J = -D \frac{\delta\phi}{\delta r} \hat{\mathbf{r}} \quad (93)$$

$$\frac{\delta\phi}{\delta t} = D \frac{\delta^2\phi}{\delta r^2} \quad (94)$$

We assume the concentration of CH<sub>3</sub>T in LUX is uniform throughout its volume. This assumption is justified, since the design of LUX creates currents which stirs the liquid xenon. With perfect mixing the effect of the purifier can be modeled by adding an exponential time dependence to the outer volume. The time constant of this decay is equal to the time it takes xenon to recirculate through the LUX detector. We use a simple implementation of the first order Euler method

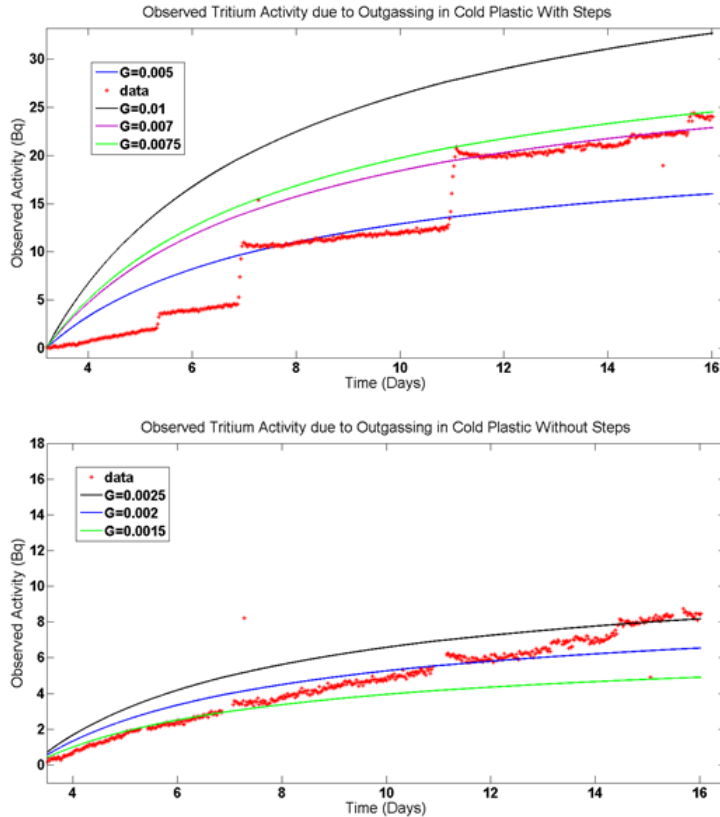


Figure 28: Fits of the integral of the flux of  $\text{CH}_3\text{T}$  out of plastic over time to the outgassing data collected in Maryland's liquid xenon system assuming that the step features are due to diffusion. The model does not perfectly describe the data, so a range of  $G$  values is shown. These fits are used to set an upper limit on  $G$ . Bottom: Fits of the integral of the flux of  $\text{CH}_3\text{T}$  out of plastic over time to the same data, assuming that the step features are not due to diffusion. These fits are used to set a lower limit on  $G$ .

for our numerical simulations. The finite difference approximations of Fick's two laws in one dimension are

$$J_{i,j} = -D \frac{\phi_{i+1,j} - \phi_{i,j}}{\Delta x} \quad (95)$$

$$\phi_{i,j+1} = \phi_{i,j} + \Delta t \left( \frac{\phi_{i+1,j} - 2\phi_{i,j} + \phi_{i-1,j}}{\Delta x^2} \right) \quad (96)$$

where  $i$  is the spacial index and  $j$  is the time index. To avoid divergence solutions we need

$$D \frac{\Delta t}{\Delta x^2} \leq \frac{1}{2}. \quad (97)$$

For effects to be propagated across  $N$  spacial bins,  $N$  time steps are required. Therefore, the effective time resolution is

$$\Delta t_{\text{effective}} = \Delta t \times N_x. \quad (98)$$

The diffusion is simulated by setting the concentration at the boundary of the piece equal to  $KC_{out}$ , where  $C_{out}$  is the concentration of CH<sub>3</sub>T in the xenon. This concentration is dependent on time according to

$$\frac{\delta C_{out}}{\delta t} = J_{out} \frac{A_{\text{plastic}}}{V_{\text{xenon}}} - \frac{C_{out}}{\tau} \quad (99)$$

where  $A_{\text{plastic}}$  is the surface area of the plastic cylinder,  $V_{\text{xenon}}$  is the total volume of xenon in the fiducial region, and  $\tau$  is the time it takes for one full purification cycle. It was originally assumed that  $\tau$  would equal the turn over time of the xenon circulation system in LUX ( $\sim 1.3$  days), but was later found that  $\tau$  was much shorter than expected ( $\sim 6$  hours). The first term on the right of this equation

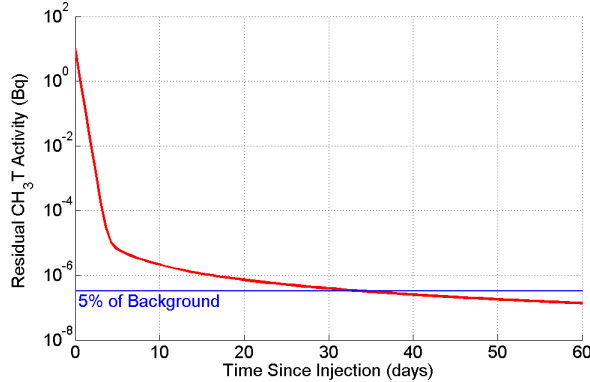


Figure 29: The results of simulating the  $\text{CH}_3\text{T}$  activity in LUX after a 10 Bq injection. In the first week the amount of residual  $\text{CH}_3\text{T}$  is dominated by the purification time constant, while the out gassing time constant determines the amount of activity later times.

models outgassing of  $\text{CH}_3\text{T}$  from the plastic cylinder, while the second term models removal of  $\text{CH}_3\text{T}$  through purification. Using the first order Euler method, we arrive at an expression for  $C_{out}$  given by

$$C_{j+1} = C_j + \Delta t \left[ (J_{1,j} - J_{N_x,j}) \frac{A_{\text{plastic}}}{V_{\text{xenon}}} - \frac{C_j}{\tau} \right]. \quad (100)$$

The initial concentration is defined by dividing the desired injection activity by the volume of the fiducial region. We choose  $D = 2.3 \times 10^{-9} \frac{\text{cm}^2}{\text{sec}}$  such that the half-infinite boundary conditions in our diffusion model is valid, and combine this with our allowed range of values for  $G$  to extract a value for  $K$ . We find that an initial injection activity of 10 Bq results in the background rate returning to  $< 5\%$  of its initial value in one month. [14] (Figure 29)

### 4.3 ER Band Calibration of the LUX Detector

The LUX collaboration took many precautions to ensure a safe and successful tritium injection. Prior to injecting any tritiated methane into the detector, a natural methane injection was performed to measure the purification time constant in LUX and constrain the value of  $G$  further. Twenty milligrams of natural methane were injected into LUX using the  $\text{CH}_3\text{T}$  injection system. The sampling system was used to measure the concentration of methane in the detector over the next few days, and a purification time constant of  $5.90 \pm 0.07$  hours was measured. The first natural methane injection was not large enough to observe outgassing from the detector, but a larger natural methane injection of 0.375 grams was able to constrain  $G \leq 0.0002 \frac{\text{cm}}{\sqrt{\text{day}}}$  at a later date.

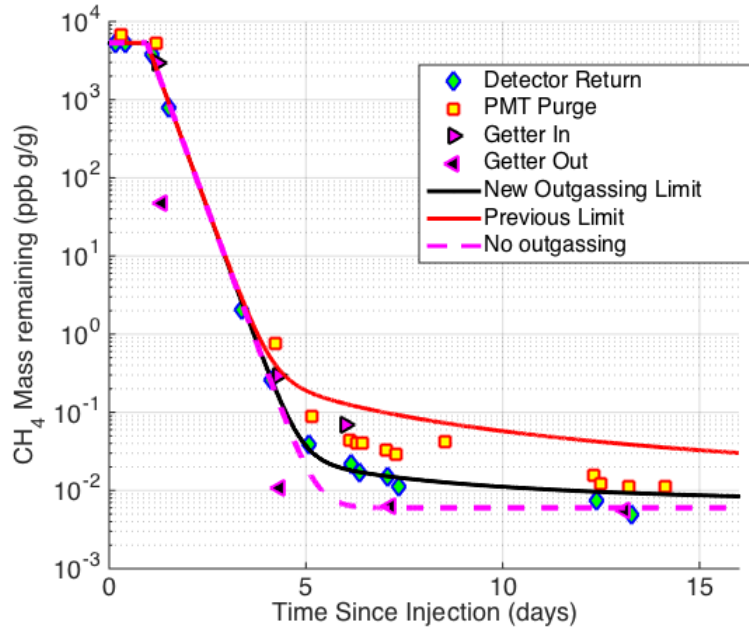


Figure 30: Sampling system results from the 0.375 gram natural methane injection which was used to constraint the value of  $G$ . [13]

After the natural methane campaign a small amount of tritium was injected into LUX to confirm the purification time constant from above, and to confirm the mixing of the source throughout the detector. A fiducial volume containing 125 kg of xenon between drift times of 30 to 320  $\mu$ sec, with radius <17.5 cm was defined for the analysis. The first 23 hours of data show that the initial injection activity in the fiducial volume was  $24.2 \pm 0.3$  mBq, while the initial injection activity in the entire detector was  $44.9 \pm 0.5$  mBq. The ratio of the fiducial volume activity to the total volume activity is  $0.539 \pm 0.009$ , which is close to the expected ratio of 0.5 for a perfectly uniform distribution of  $\text{CH}_3\text{T}$  events. The  $\text{CH}_3\text{T}$  activity fell with a purification time constant of  $6.9 \pm 0.4$  hours within the fiducial volume, confirming the  $\sim 6$  hour time constant measurement from phase one.

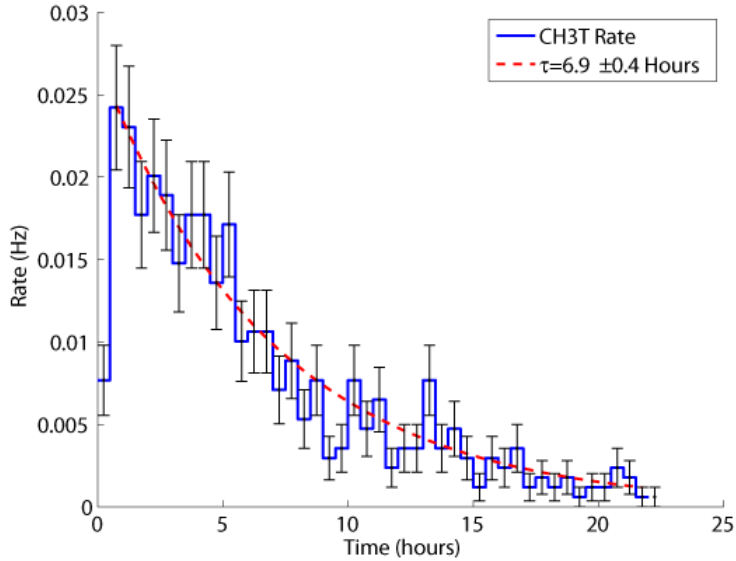


Figure 31: Rate of  $\text{CH}_3\text{T}$  events after the first small injection into LUX. The 6.9 hour time constant is consistent with expectations from the natural methane sampling campaign prior to this injection.

After confirming the purification time constant LUX approved the use of  $\text{CH}_3\text{T}$  as an internal calibration source. The initial  $\text{CH}_3\text{T}$  calibration was limited to 0.3

Hz due to the uncertainty in the value of the the diffusion constant  $G$ , but injections ranging from 2-10 Hz have been done every 3-4 months after the value of  $G$  was constrained further. The location of events from the first  $\text{CH}_3\text{T}$  calibration is shown in Figure 32. As expected, the  $\text{CH}_3\text{T}$  source diffuses uniformly throughout the detector.

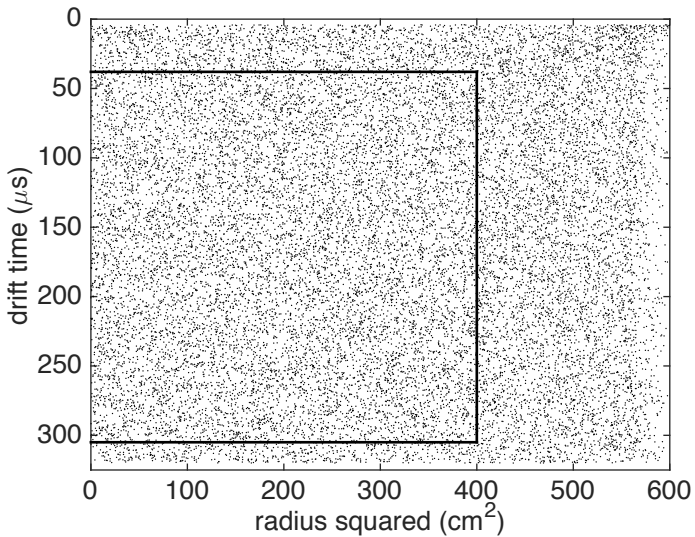


Figure 32: The location of events during the initial LUX  $\text{CH}_3\text{T}$  injection. The solid black like indicates the fiducial volume used for the first LUX Run03 results paper.

The combined energy spectrum for a high statistics  $\text{CH}_3\text{T}$  calibration is shown in Figure 33. A model of the expected tritium beta spectrum which includes detector resolution effects is shown in red. The data agrees very close with expectations above the detector's energy threshold, with a p-value of 0.70 from 3 to 18 keV. The consistency of the energy spectrum across a wide range of energies provides strong support for the combined energy model presented in Section 6. The ratio of the  $\text{CH}_3\text{T}$  data to expectations was used to determine the energy threshold of the LUX detector. A error function fit was used to determine a 50% energy threshold

of  $1.24 \pm 0.026$  keV for electron recoil events.

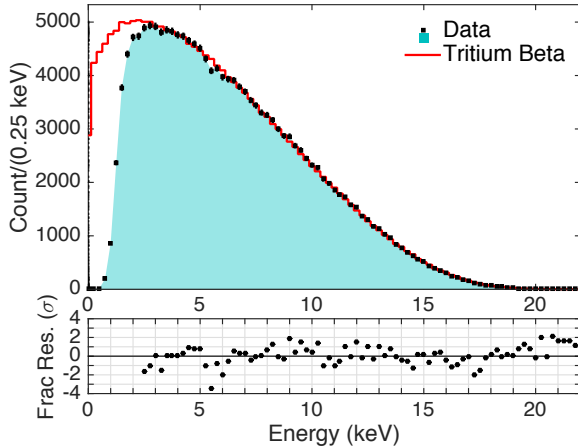


Figure 33: Top: The combined energy spectrum from a high statistics  $\text{CH}_3\text{T}$  calibration in LUX. Data is shown in black, and a model of the expected tritium beta spectrum is shown in red. Bottom: The residual differences between the data and model for each bin, in units of  $\sigma$ .

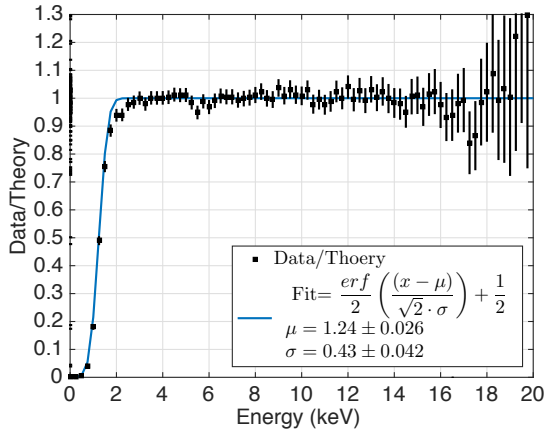


Figure 34: The ratio of the tritium data to expectations. An error function fit used to determine the energy threshold is shown in blue.

The main purpose of the  $\text{CH}_3\text{T}$  calibration source is to measure the detector's electron recoil response. This calibration is crucial when determining the "leakage fraction" of electron recoil backgrounds that fall below the nuclear recoil band mean. Alternatively, a "discrimination" factor can be defined as the fraction of

electron recoil backgrounds that do not fall below the nuclear recoil band mean. The electron recoil band from a high statistics CH<sub>3</sub>T calibration is shown in Figure 35. The nuclear recoil band calibration from LUX’s neutron generator calibration source is also included in Figure 35. These two results have allowed the LUX collaboration to measure the detector’s discrimination with unprecedented accuracy. An average discrimination ( $1-f$ ) for the LUX Run03 result was found to be 99.81%  $\pm$  0.02%.

In addition to the calibration results mentioned in this section, the CH<sub>3</sub>T calibration source has allowed the LUX collaboration to measure fundamental properties of liquid xenon to high accuracy. These results are discussed in reference [9]. The calibration source is also an integral part of producing signal corrections in a detector with a nonuniform electric field, a topic which is discussed in chapter 7.

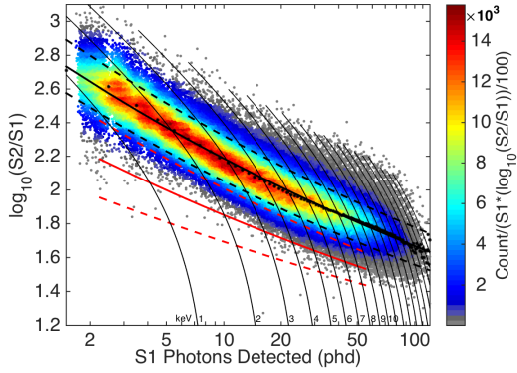


Figure 35: The electron recoil calibration of LUX resulting from 170,000 CH<sub>3</sub>T events at 180 V/cm. The Gaussian means of each S1 bin, as well as power law fits to those means and the 10% and 90% contours of the ER band are shown in black. The power law fits to the mean, 10%, and 90% contours of the NR band are shown in red.

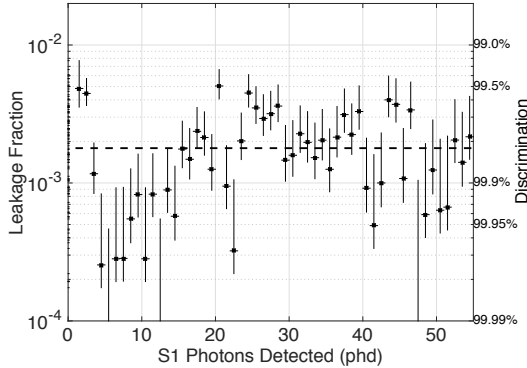


Figure 36: The leakage fraction and discrimination versus S1 in the LUX detector at 180 V/cm.

## 5 Signal Corrections in the LUX Detector

In this chapter, we discuss the need for position dependent corrections to the S1 and S2 signals in LUX. Position dependence in the S1 signal can be introduced by a number of effects. As photons travel from an interaction site to the PMT arrays

they are reflected by teflon panels surrounding the active volume. The reflectivity of the teflon varies based on the proximity of the interaction site, the angle of incidence of the light, and the surface properties of the teflon. Photons are also reflected at the liquid xenon surface, causing about two thirds of the S1 signal to be collected in the bottom PMT array. Events which are closer to the bottom PMT array have more solid angle covered by the PMT array, leading to a larger S1 signal for events toward the bottom of the detector. A z-dependence of the light collection efficiency can also be introduced by light quenching impurities present in the liquid xenon, although this effect is negligible at the liquid xenon purity levels found in LUX.

As electrons travel from the interaction site to the liquid surface they are absorbed by electronegative impurities in the liquid xenon. This attenuation of charge leads to a smaller S2 signal from events originating deeper in the detector. Since the purity of the liquid xenon changes on a weekly basis there is a significant time dependence in the strength of this effect. Small fluctuations in the X-Y plane of the extraction field or the liquid surface level can lead to a position dependence in both the efficiency at which electrons are extracted from the liquid xenon and the number of photoelectrons which are produced per extracted electrons. Both of these effects are reflected in the size of the S2 signal. Furthermore, while the individual PMTs are gain matched with LED calibrations, the variation in quantum efficiency between PMTs can lead to an X-Y position dependence in both the S1 and S2 signals.

In the final data analysis, we wish to know the absolute number of photons and electrons produced by recoil interactions, as well as the nuclear recoil discrimination factor at all locations and times in the detector. It is possible to define

position dependent gain factors which convert the S1 signals and S2 signals to number of photons and number of electrons, respectively, but it is more convenient to normalize the S1 and S2 signals to one location in the detector. Likewise, one could define position and time dependent ER and NR bands to track discrimination over time, but it is more convenient to normalize the data such that the ER band and NR bands are constant at all times and all locations in the detector. In LUX we choose to normalize the S1 signal to the center of the detector, and the S2 signal to the top of the detector. The choice to normalize the S1 signal to the center of the detector is arbitrary since the position dependence of the S1 signal has little time dependence, while the choice to normalize the S2 signal to the top of the detector is convenient for circumventing the time dependence inherent at deeper locations in the detector due to varying amount of electron absorbing impurities in the liquid xenon. Once the S1 and S2 signals are uniform throughout the detector we can define one position independent gain factor for each of the detector signals. Removing the position dependence of the S1 and S2 signals also results in increased resolution of the S1 and S2 spectra, as well as a narrowing of the ER and NR band widths.

Note that a nonuniform drift field can also introduce position dependence to the S1 and S2 signals. However, this effect changes the actual number of photons and electrons produced during a recoil interaction, rather than the detector's efficiency of collecting those photons and electrons. In this chapter we will assume a uniform drift field is present in the detector, and discuss corrections for a detector with a nonuniform electric field in Chapter 7.

## 5.1 Use of $^{83m}\text{Kr}$ in Signal Corrections

The LUX detector's  $^{83m}\text{Kr}$  calibration source is an ideal tool to measure corrections for the S1 and S2 signals. A  $^{83}\text{Rb}$  soaked charcoal source is used to inject its  $^{83m}\text{Kr}$  daughter directly into the LUX circulation system. In the active volume the  $^{83m}\text{Kr}$  decays via internal conversion at 32.1 keV and 9.4 keV with a half life of 1.86 hours. The half life of the 9.4 keV decay is only 154 ns, causing the two decays to merge into one 41.55 keV pulse in the LUX detector. Note that it is possible to modify the LUX pulse finder to separate the two S1 signals when desired, but it is nearly impossible to separate the two S2 signals due to diffusion of the electron clouds as they drift to the liquid surface.

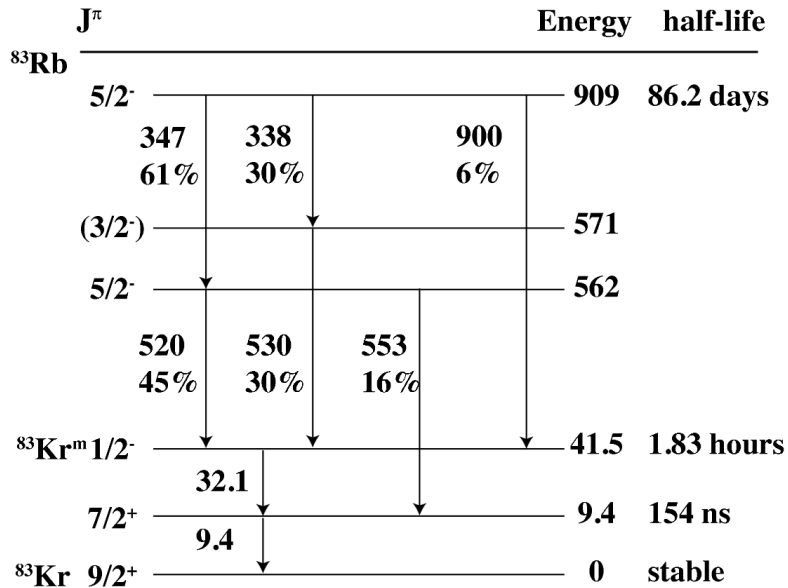


Figure 37: The energy level diagram of the  $^{83}\text{Rb}$  and  $^{83m}\text{Kr}$  decays.

Once injected, the  $^{83m}\text{Kr}$  mixes uniformly throughout the active volume in a matter of minutes. The monoenergetic peak of the  $^{83m}\text{Kr}$  events can be measured at any point in the detector to determine the position dependence of the S1 and

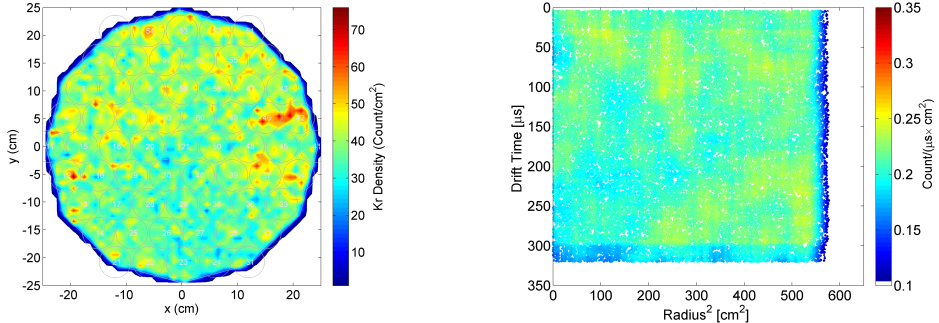


Figure 38: (Left) Density of  $^{83m}\text{Kr}$  events in the X-Y plane 10-30 minutes after a  $^{83m}\text{Kr}$  injection. (Right) Density of  $^{83m}\text{Kr}$  events in the  $R^2$ -Z plane 10-30 minutes after a  $^{83m}\text{Kr}$  injection.

S2 signals.

The short half life causes the calibration source to be removed from the LUX detector in a matter of hours, allowing for calibration of the S1 and S2 signals on a weekly basis. This is a crucial property of the calibration source, since the purity of the liquid xenon, and therefore the z-dependence of the S2 signal, changes on a weekly basis. It is also important that the  $^{83m}\text{Kr}$  is an inert noble gas, a property which prevents temporary attenuation of the S1 and S2 signals during injection of the calibration source.

## 5.2 S1 Corrections

We first measure the Z dependence of the  $^{83m}\text{Kr}$  S1 pulse areas by slicing the detector into drift time bins with widths defined such that each bin has roughly 300 events. A Gaussian distribution is fit to the S1 spectra of each bin to determine the location of the spectra means. A second order polynomial is used to determine the S1 Z dependence between and outside of each drift time bin. A detector inefficiency correction for the Z direction is defined by taking the ratio of the S1

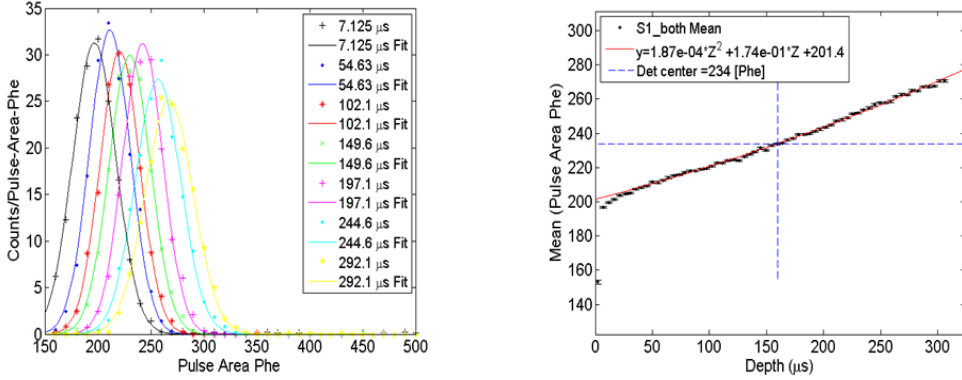


Figure 39: (Left) Gaussian distribution fits to  $^{83m}\text{Kr}$  S1 data that are used to determine the drift time dependence of the S1 pulse area. (Right) The z dependence of the S1 pulse area. Black points indicate the maximum of Gaussian distribution fits for each drift time bin, and red points indicate the polynomial fit to that data.

pulse area at the center of the detector (defined as  $z_c$ ) to the S1 pulse area as a function of Z as described in the equation

$$S1_{z\text{-efficiency-correction}} = \frac{S1(z_c)}{S1(z)}. \quad (101)$$

The XY dependence of the S1 signal is found by dividing the z-corrected ( $S1 \times S1_{z\text{-efficiency-correction}}$ ) data into two dimensional XY bins with lengths defined such that each bin has roughly 300 events, and then fitting Gaussian distributions to the data of each bin. The mean of the Gaussian distribution from each bin is used to construct S1 XY dependence maps, with a spline interpolation and extrapolation being used to determine the XY dependence between and outside of the bins. (Figure 90) A detector inefficiency correction for the XY direction is defined by taking the ratio of the z-corrected S1 pulse area at the center of the detector to the z-corrected S1 pulse area as a function of XY in cm, as shown

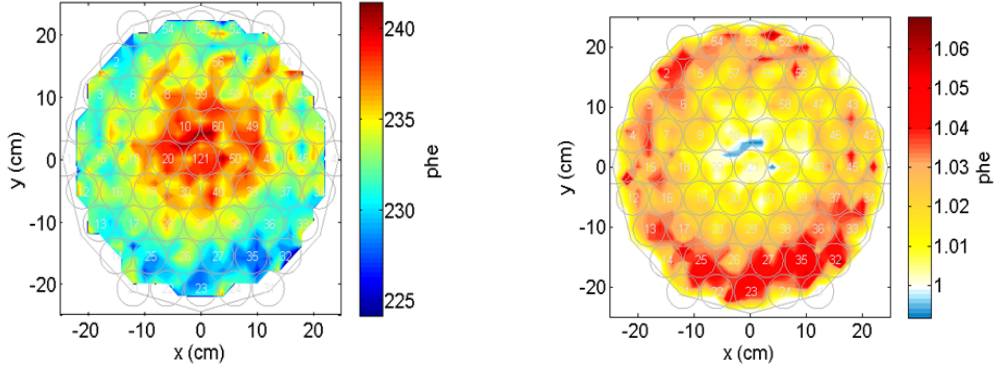


Figure 40: (Left) Two dimensional map of the XY dependence in  $^{83m}\text{Kr}$  S1 data determined by fitting a Gaussian distribution to XY bins of the data and tracking the mean of each fit.(Right) Two dimensional map of the XY correction factor which is applied to z-corrected S1 data.

below

$$S1_{\text{xy-efficiency-correction}} = \frac{S1_{\text{z-efficiency-correction}} \times S1(x_c, y_c, z)}{S2_{\text{z-efficiency-correction}} \times S1(xyz)}. \quad (102)$$

where  $x_c$  and  $y_c$  are the x and y center of the detector in uncorrected position coordinates. The corrected S1 pulse areas are produced by multiplying the raw, uncorrected S1 pulse areas by the XY and Z correction factors

$$S1_{\text{corrected}} = S1_{\text{raw}} \left( S1_{\text{z-efficiency-correction}} \right) \left( S1_{\text{xy-efficiency-correction}} \right). \quad (103)$$

When enough stats are present in a  $^{83m}\text{Kr}$  calibration data set, a three dimensional S1 corrections map is favored over the two step (Z, then XY) corrections described above. In this case, the uncorrected S1 data is divided into three dimensional XYZ voxels with volumes defined such that each bin has roughly 300 events. A Gaussian distribution is fit to the data of each voxel, and the mean of

the Gaussian distribution is used to construct three dimensional S1 dependence maps, with a spline interpolation and extrapolation being used to determine the XYZ dependence between and outside of the voxels. A three dimensional detector inefficiency correction is then defined by taking the ratio of the uncorrected S1 pulse area at the center of the detector to uncorrected S1 pulse area as a function of X,Y, and drift time, as shown below

$$S1_{\text{xyz-efficiency-correction}} = \frac{S1(x_c, y_c, z_c)}{S1(xyz)}. \quad (104)$$

In this case, the corrected S1 pulse areas are produced by multiplying the raw, uncorrected S1 pulse areas by the XYZ correction factor.

$$S1_{\text{corrected}} = S1_{\text{raw}} \left( S1_{\text{xyz-efficiency-correction}} \right). \quad (105)$$

The detector inefficiency effects in the S1 signal are all due to the unchanging internal geometry of the detector. Therefore, the S1 correction maps vary by only a few percent over time and a single high stats three dimensional correction map can be applied to data over a long period of time.

Figure 41 show the  $^{83m}\text{Kr}$  S1 spectrum from one particular data set before and after pulse area corrections are applied. In this data set the corrections improve the S1 resolution resolution by 35%, and shifts the mean by 2%. Similar improvements in resolution are seen in all  $^{83m}\text{Kr}$  data sets. The corrected S1 pulse areas are also found to be extremely uniform over time, with the corrected  $^{83m}\text{Kr}$  S1 varying by less than 0.6% over the course of the LUX detector's Run03 data taking campaign.

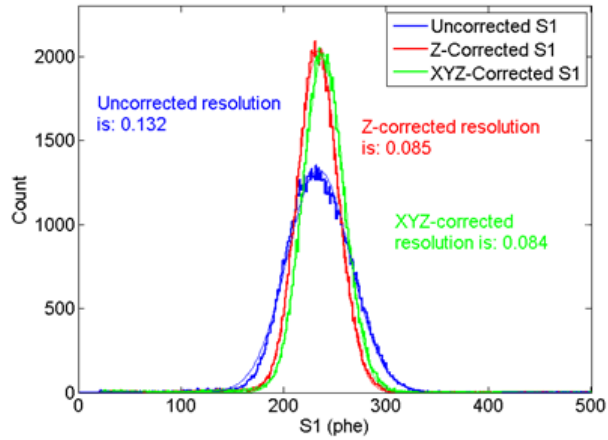


Figure 41: The  $^{83m}\text{Kr}$  S1 spectrum with no corrections applied (blue), z dependent corrections applied (red), and xyz dependent corrections applied (green).

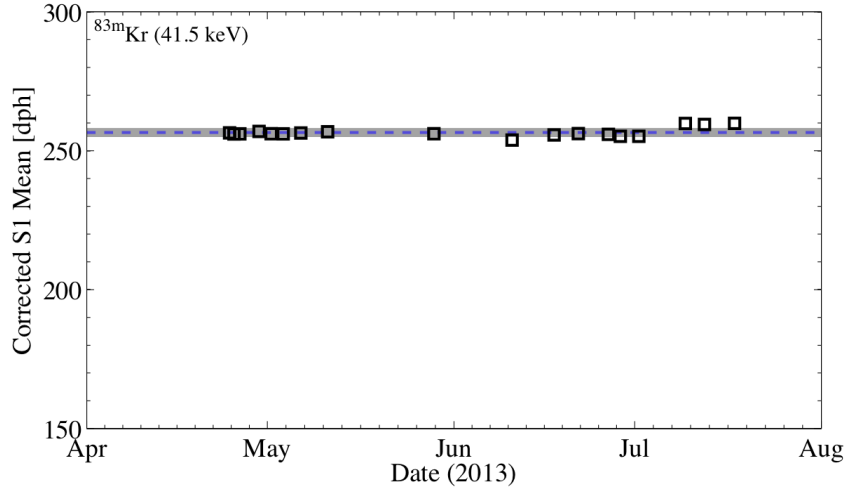


Figure 42: The corrected  $^{83m}\text{Kr}$  S1 mean over the duration of LUX’s Run03 data taking campaign. The dashed blue line indicates the mean of the corrected  $^{83m}\text{Kr}$  S1 spectrum over time, and the grey band indicates one standard deviation around the mean.

### 5.3 S2 Corrections

As with the S1 signal, we measure the Z dependence of the  $^{83m}\text{Kr}$  S2 pulse areas by slicing the detector into drift time bins with widths defined such that each bin

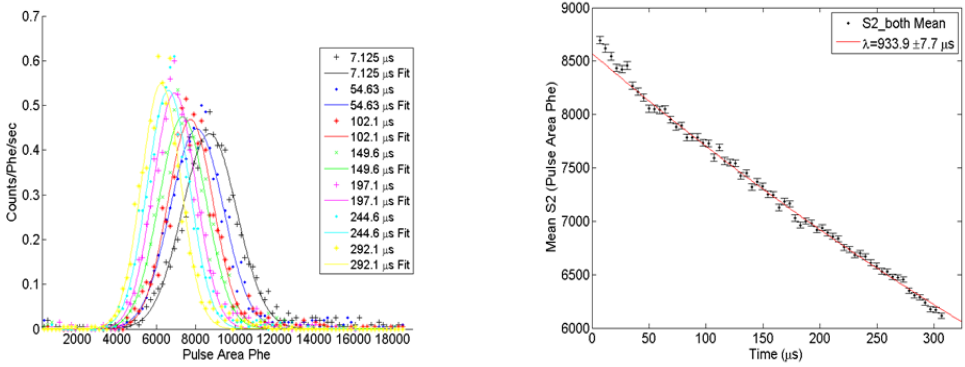


Figure 43: (Left) Gaussian distribution fits to  $^{83m}\text{Kr}$  S2 data that are used to determine the drift time dependence of the S2 pulse area. (Right) The z dependence of the S2 pulse area. Black points indicate the maximum of Gaussian distribution fits for each drift time bin, and red points indicate the exponential fit to that data.

has roughly 300 events. An exponential decay is fit to the drift time dependence of the mean of each  $^{83m}\text{Kr}$  S2 distribution. A detector inefficiency correction for the Z direction is defined by taking the ratio of the S2 pulse area just below the liquid surface to the S2 pulse area as a function of Z as described in the equation

$$S2_{z\text{-efficiency-correction}} = \frac{S2(z=0)}{S2(z)}. \quad (106)$$

The process of measuring the XY dependence of the S2 signal is identical to the process of measuring the XY dependence of the S1 signal. The z-corrected ( $S2 \times S2_{z\text{-efficiency-correction}}$ ) S2 data is divided into two dimensional XY bins with lengths defined such that each bin has roughly 300 events, and a Gaussian distribution is fit to the data of each bin. The mean of the Gaussian distribution from each bin is used to construct S2 XY dependence maps, with a spline interpolation and extrapolation being used to determine the XY dependence between and outside of the bins. (Figure 90) A detector inefficiency correction for the XY

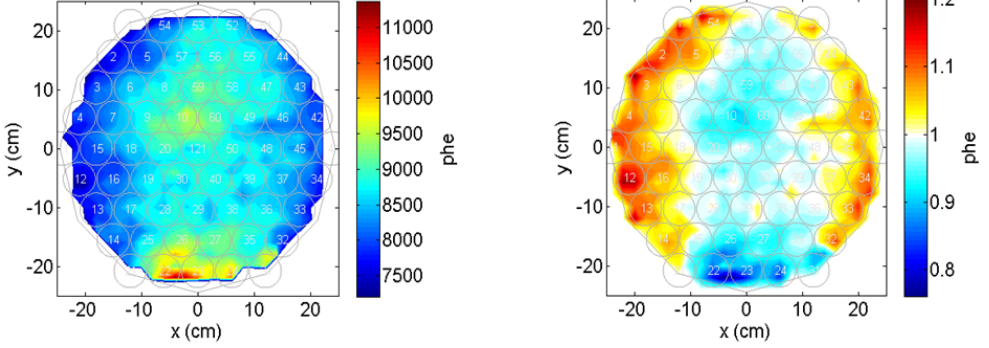


Figure 44: (Left) Two dimensional map of the XY dependence in  $^{83m}\text{Kr}$  S2 data determined by fitting a Gaussian distribution to XY bins of the data and tracking the mean of each fit.(Right) Two dimensional map of the XY correction factor which is applied to z-corrected S2 data.

direction is defined by taking the ratio of the z-corrected S2 pulse area at the center of the detector to the z-corrected S2 pulse area as a function of XY in cm, as shown below

$$S2_{\text{xy-efficiency-correction}} = \frac{S2_{\text{z-efficiency-correction}} \times S2(x_c, y_c, z)}{S2_{\text{z-efficiency-correction}} \times S2(xyz)}. \quad (107)$$

where  $x_c$  and  $y_c$  are the x and y center of the detector in uncorrected position coordinates. The corrected S2 pulse areas are produced by multiplying the raw, uncorrected S2 pulse areas by the XY and Z correction factors

$$S2_{\text{corrected}} = S2_{\text{raw}} \left( S2_{\text{z-efficiency-correction}} \right) \left( S2_{\text{xy-efficiency-correction}} \right). \quad (108)$$

The z-dependence of the S2 signal is a function of the liquid xenon purity, which is in turn a function of the detector's purification efficiency, the detector's flow rate, and the emanation rate of impurities from detector components. Note that

circulation outages have an immediate impact on the purity of the liquid xenon, since the zirconium getter is unable to counteract the emanation of impurities and since the sudden shock to the detector can release impurities from otherwise harmless locations such as the weir reservoir. As a result, the S2 correction maps vary significantly over time and must be remeasured on a weekly basis.

Figure 45 shows the  $^{83m}\text{Kr}$  S2 spectrum from one particular data set before and after pulse area corrections are applied. In this data set the corrections improve the S2 resolution by 22%, and shifts the mean by 21%. The large shift in the  $^{83m}\text{Kr}$  S2 mean is a result of the corrections "adding in" the electrons which were absorbed by impurities in the liquid xenon as they traveled to the surface. Note that the resolution improvement and the shift of the mean are larger in data sets which have worse xenon purity. As with the corrected S1 signal, the corrected S2 pulse areas are found to be extremely uniform over time, with the corrected  $^{83m}\text{Kr}$  S2 varying by less than 2% over the course of the LUX detector's Run03 data taking campaign.

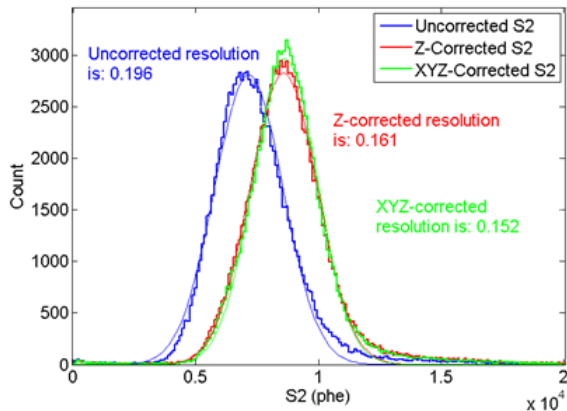


Figure 45: The  $^{83m}\text{Kr}$  S2 spectrum with no corrections applied (blue), z dependent corrections applied (red), and xyz dependent corrections applied (green).

## 5.4 Radon as a measure of Electron Lifetime

The method of extracting electron lifetimes described in Section 5.3 requires high statistics  $^{83m}\text{Kr}$  data sets for calibration. While this method is reliable, data between an electron lifetime changing event, such as a circulation stop, and a  $^{83m}\text{Kr}$

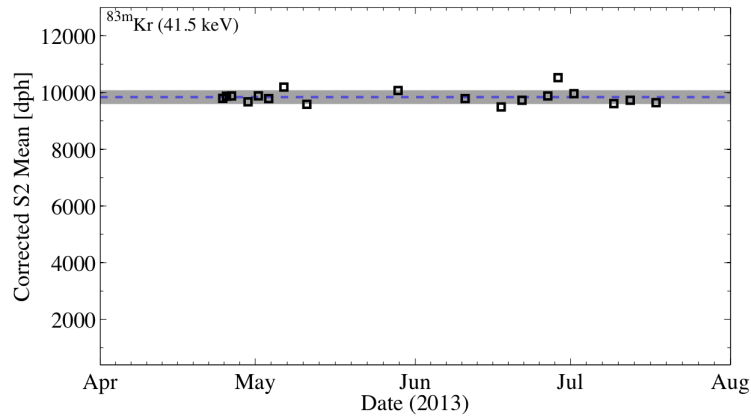


Figure 46: The corrected  $^{83m}\text{Kr}$  S2 mean over the duration of LUX’s Run03 data taking campaign. The dashed blue line indicates the mean of the corrected  $^{83m}\text{Kr}$  S2 spectrum over time, and the grey band indicates one standard deviation around the mean.

calibration data set is unusable due to the lack of an electron lifetime measurement. In this section we will discuss using  $^{222}\text{Rn}$  backgrounds to recover electron lifetime measurements from individual WIMP search data sets so that signals corrections can be applied even if a  $^{83m}\text{Kr}$  calibration is not available.

Radon-222 appears in every data set taken in the LUX detector. While it is an unwanted background in the data, the Radon-222 alpha peak is useful for continuous monitoring of our electron lifetime. Radon events are selected using a box cut on the raw S1 pulse areas. (Figure 47) An upper limit of 240  $\mu\text{seconds}$  is placed on the drift time of the selected events since the S1 signal saturates above this point, causing the radon data to become indistinguishable from the other alpha bands. The S1 pulse areas do not have a time dependence, so the same box cut is applicable to data at any point in time. An additional constraint of  $S2_{\text{bottom}}(z) < S2_{\text{bottom}}(z = 0)$  since the S2 size anywhere in the detector should never exceed the maximum size of a  $^{222}\text{Rn}$  S2 at the top of the detector. To ensure

we are using clean radon data we only use the S2 signal from the bottoms PMT array to avoid PMT saturation. After selection cuts are applied there are not enough radon events in a single data set to slice the detector into drift time bins as we did during  $^{83m}\text{Kr}$  calibrations. Instead, we turn to a maximum likelihood approach to extract the electron lifetime from the limited amount of radon data.

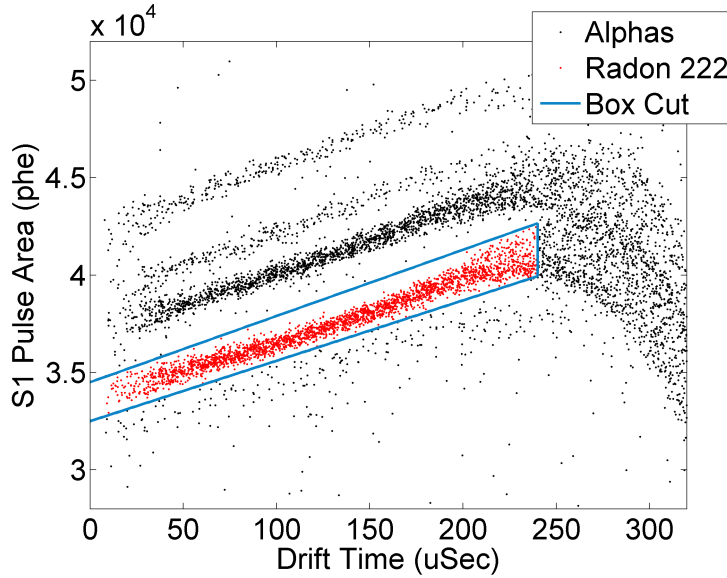


Figure 47: Selection of radon events from a week of WIMP search data. Black points include data from all alpha sources, and the blue lines indicate the box cut that is used to select  $^{222}\text{Rn}$  data (shown in red).

In the maximum likelihood analysis, a probability distribution function is used to determine the probability that an S2 of a given size and drift time will be measured, assuming some value for the electron lifetime. There are two possible probability distribution functions which we can use. The first PDF fits an attenuated Gaussian model to the attenuated S2 data, and is given by

$$F(x_i, z_i | \mu, \sigma, \lambda) = \frac{1}{\sqrt{2\pi}\sigma} e^{\frac{(-x_i - \mu e^{-\frac{-z_i}{\lambda}})^2}{(2\sigma)^2}}, \quad (109)$$

where  $\sigma$  and  $\mu$  are the Gaussian sigma and mean of the corrected radon peak based on the most recent krypton calibration data set,  $x_i$  and  $z_i$  are the signal and depth of the  $i$ th event in the data set, and  $\lambda$  represents the unknown electron lifetime for the data set. The second PDF fits a true Gaussian to the corrected S2 data, and is given by

$$F(x_i, z_i | \mu, \sigma, \lambda) = \frac{1}{\sqrt{2\pi}\sigma} e^{\frac{(-x_i e^{\frac{z_i}{\lambda}} - \mu)^2}{(2\sigma)^2}}. \quad (110)$$

In either case, the PDF is measured on an event by event basis. The likelihood of observing all of the events in a data set, for some value of  $\mu$ ,  $\sigma$ , and  $\lambda$  is then given by the likelihood function

$$\mathcal{L}(\mu, \sigma, \lambda; x_i, z_i) = \prod_{i=1}^n F(x_i, z_i | \mu, \sigma, \lambda) \quad (111)$$

We wish to determine the electron lifetime value which has the highest likelihood of producing the observed data. For convenience, we choose to minimize the negative of the log of the likelihood function with respect to  $\lambda$ , since it is less computational expensive to minimize a summation than it is to maximize a product.

After running the maximum likelihood method on all of the LUX detector's Run03 data sets we see that the attenuated Gaussian PDF is in better agreement with the z-slice method from Section 5.3. (Figure 48) In either case, the results of the maximum likelihood fit from Radon data fall within one sigma of the results from  $^{83m}\text{Kr}$  calibrations.

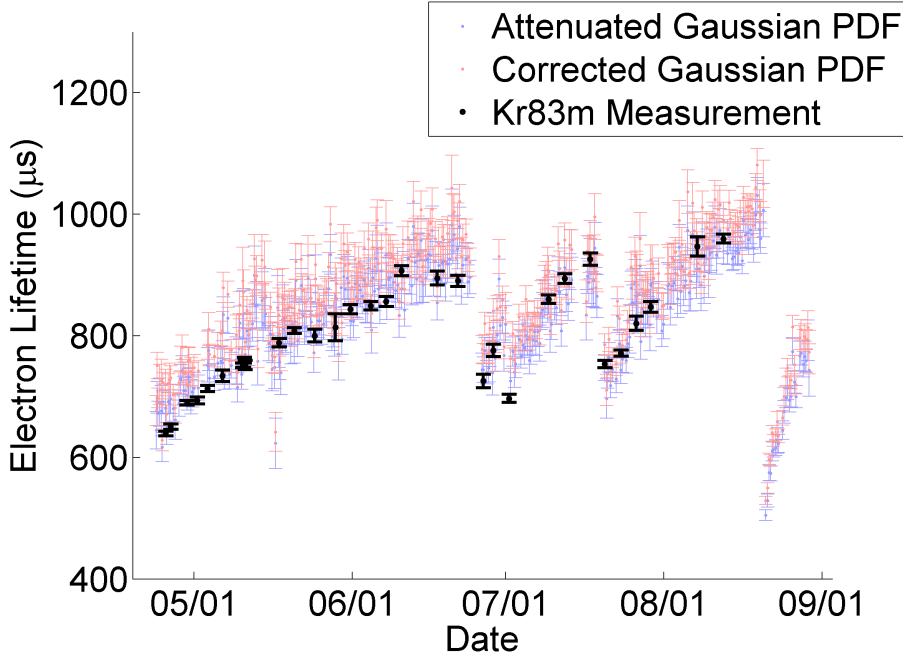


Figure 48: A comparison of the calculated electron lifetimes based on the maximum likelihood method with an attenuated Gaussian PDF (in blue) and corrected Gaussian PDF (in red). The electron lifetime measured from  $^{83m}\text{Kr}$  calibrations is shown in black.

## 5.5 A PMT-by-PMT approach to S1 Corrections

The S1 correction method presented in Section 5.2 improves the detector's resolution by normalizing the summed S1 signal to the center of the detector. While this method is used in the final LUX data analysis, it is possible to improve the detector's S1 resolution further by defining a light collection map on a PMT-by-PMT basis. For each S1 event we define the position corrected S1 signal using the weighted arithmetic mean of each PMT's spatially normalized S1 measurement, given by

$$S1_{\text{corrected}} = \frac{\sum_{j=1}^{j=122} S1'_j W_j}{\sum_{j=1}^{j=122} W_j}, \quad (112)$$

where  $S1'_j$  is the spatially normalized S1 signal of the  $j$ th PMT and  $W_j$  is the weight given to  $j$ th PMT's measurement.

Since we want the corrected S1 signal to be spatially uniform, the spatially normalized S1 signal for each PMT is given by

$$S1'_j = S1_{\text{sc}} \frac{S1_j}{\langle S1 \rangle_j} \quad (113)$$

where  $S1_{\text{sc}}$  is the summed  $^{83m}\text{Kr}$  S1 signal at the center of the detector,  $S1_j$  is the S1 signal of the  $j$ th PMT, and  $\langle S1 \rangle_j$  is the average  $^{83m}\text{Kr}$  S1 signal recorded in the vicinity of the S1 event by the  $j$ th PMT. It is useful to think of the  $\frac{S1_j}{\langle S1 \rangle_j}$  term as measuring the strength of the  $S1_j$  signal as a fraction of the average  $^{83m}\text{Kr}$   $S1_j$  signal, and the  $S1_{\text{sc}}$  term as a normalization constant which scales the fractional signal to the equivalent S1 size at the center of the detector.

The weights of the arithmetic mean are given by relative variance of each PMT's measurement,

$$W_j = \frac{\langle S1 \rangle_j^2}{\sigma_j^2}, \quad (114)$$

where  $\sigma_j^2$  is the variance of the S1 signal in  $j$ th PMT in the vicinity of the event. It is important to use the relative variance of each PMT for the weights, since the absolute variance grows larger with the size of the S1 signal and would therefore give lower weight to PMTs which observe a stronger S1 signal. Equation 112 then becomes

$$S1_{\text{corrected}} = S1_{\text{sc}} \frac{\sum_{j=1}^{j=122} \frac{S1_j}{\langle S1 \rangle_j} \frac{\langle S1 \rangle_j^2}{\sigma_j^2}}{\sum_{j=1}^{j=122} \frac{\langle S1 \rangle_j^2}{\sigma_j^2}}. \quad (115)$$

It is difficult to measure the relative variance of the  $j$ th PMT at all points in the detector, since doing so involves interpolating small values from two different

three dimensional maps of  $\sigma_j^2$  and  $\langle S1 \rangle_j$ . Instead, we can achieve the same result by normalizing the  $S1_j$  signal to the value of  $S1_{\text{sc}}$  prior to calculating the arithmetic mean. In this case, the normalized  $S1_{N,j}$  signal is calculated by scaling the raw  $S1_j$  signal by a normalization factor

$$S1_{N,j} = \frac{S1_{\text{sc}}}{\langle S1 \rangle_j} S1_j. \quad (116)$$

Consequently, the standard deviation and mean of the  $S1_j$  signal are scaled by the same factor, such that

$$\sigma_{N,j} = \frac{S1_{\text{sc}}}{\langle S1 \rangle_j} \sigma_j \quad (117)$$

$$\langle S1 \rangle_{N,j} = \frac{S1_{\text{sc}}}{\langle S1 \rangle_j} \langle S1 \rangle_j = S1_{\text{sc}}. \quad (118)$$

Using the normalized  $S1_{N,j}$  signal, equation 115 becomes

$$S1_{\text{corrected}} = S1_{\text{sc}} \frac{\sum_{j=1}^{j=122} \frac{S1_{N,j}}{\langle S1_{N,j} \rangle} \frac{1}{\sigma_{N,j}^2}}{\sum_{j=1}^{j=122} \frac{1}{\sigma_{N,j}^2}} \quad (119)$$

In practice, Equation 119 is easier to implement and more accurate than Equation 115, since it requires fewer interpolations of the mean and variance maps from the  $^{83m}\text{Kr}$  data.

It is worth noting that if the  $S1_j$  distributions are Poissonian, Equation 115 (and Equation 119) reduces to the S1 correction method described in Section 5.2. In this case

$$\sigma_j^2 = \langle S1 \rangle_j \quad (120)$$

so Equation 115 becomes

$$S1_{\text{corrected}} = S1_{\text{sc}} \frac{\sum_{j=1}^{j=122} S1_j}{\sum_{j=1}^{j=122} \langle S1 \rangle_j} = S1_{\text{sc}} \frac{S1}{\langle S1 \rangle} \quad (121)$$

Where  $S1$  is the sum of all of the PMT signals for the event and  $\langle S1 \rangle$  is the average of the sum of the PMT signals for  ${}^{83m}\text{Kr}$  events. Therefore, this PMT-by-PMT method is only beneficial if significant non-Poissonian noise is present in the PMT signals.

Figure 49 shows the result of applying the PMT-by-PMT method to a  ${}^{83m}\text{Kr}$  data set in the LUX detector. Within the fiducial volume the resolution of the  $S1$  signal improves by 13% over the standard correction method from section 5.2. Outside of the fiducial volume, the interpolations of the variance and mean maps become extrapolations. This leads to significant inaccuracies in the weighted mean measurement, causing non-Gaussian tails to appear in the  $S1$  distribution. Therefore, for events within the fiducial volume the PMT-by-PMT method is an improvement over the standard correction method, but for events outside of the fiducial volume the less complex standard correction method is ideal.

## 6 Energy Scale Calibrations

The correction methods discussed in Chapter 5 allow us to use two spatially independent gain factors to convert the  $S1$  and  $S2$  signals into the number of photons and the number of electrons produced by an event anywhere in the detector. In this chapter, we will present a combined energy model which uses the number of photons and electrons produced to determine the energy deposited during an event

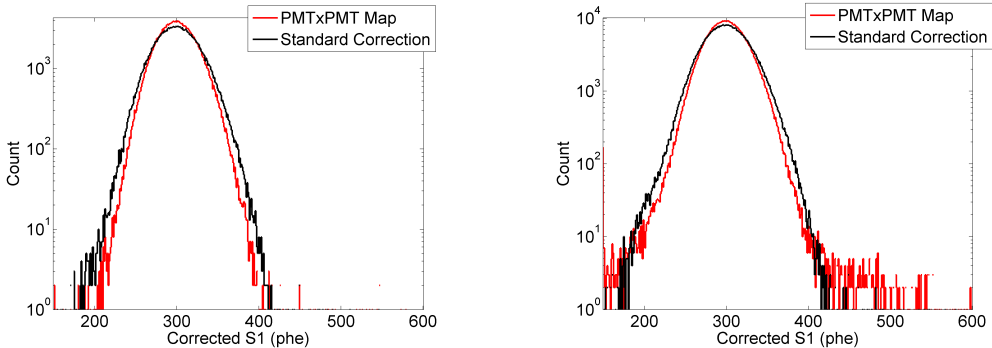


Figure 49: The  $^{83m}\text{Kr}$  corrected S1 spectrum after applying the PMT-by-PMT method (in red) and after applying the standard correction method from Section 5.2 (in black). The events within the fiducial volume are shown on the left, and all of the events are shown on the right.

before discussing methods to measure the individual gain factors.

## 6.1 Combined Energy Model

Energy from a particle interaction produces excited xenon atoms ( $\text{Xe}^*$ ), ionized xenon atoms ( $\text{Xe}^+$ ), and heat. The heat released in the interaction is not observed in LUX. For electron recoil events this lost energy is negligible, but for nuclear recoil it is not.

The excited xenon atoms combine with ground state xenon atoms to form xenon dimers ( $\text{Xe}_2^*$ ). These xenon dimers relax to two ground state xenon atoms, producing a 178 nm VUV photon. This scintillation light is the first component of the S1 signal observed in the LUX detector. The ionization of xenon atoms releases free electrons. These free electrons have a chance to recombine with the positively charged xenon ions, producing additional excitons which contribute to the S1 signal. Therefore, with the probability of an ion recombining represented as  $R$ , the number of photons produced in an interaction is given by the initial

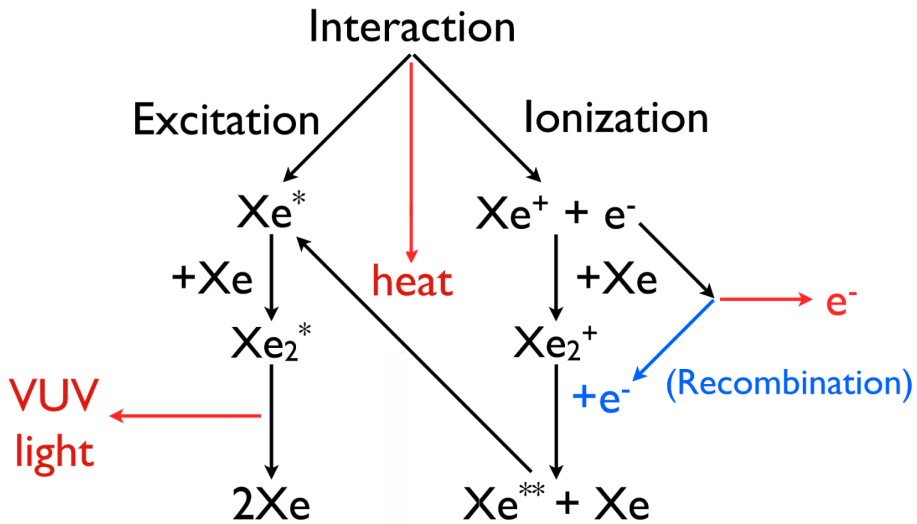


Figure 50: Depiction of particle interaction and the production of xenon excitons, ionized xenon, electron, photons, and heat. [52]

number of excitons produced plus the number of ions which recombine,

$$N_\gamma = N_{ex} + RN_i = N_i(\alpha + R). \quad (122)$$

where  $N_\gamma$  is the number of photons,  $N_{ex}$  is the number of excitons,  $N_i$  is the number of ions, and  $\alpha \equiv \frac{N_{ex}}{N_i}$  is the exciton to ion ratio.

Free electrons which do not recombine drift to the liquid surface where they accelerate through the extraction field and produce the S2 signal. The number of electrons produced in an interaction is given by the fraction of ions which do not recombine,

$$N_e = N_i(1 - R). \quad (123)$$

Nuclear recoils are more densely ionizing than electron recoils, leading to more recombination, and therefore more S1 and less S2 signal. This distinction enables

the discrimination method discussed in section 4.3. Note that in addition to the dependence on the type of recoil, the probability of recombination depends on the electric field and the energy of an interaction, a property which is significant for the work in Chapter 7.

The total energy deposited by an interaction is given by

$$E = \mathcal{L}^{-1}W(N_{ex} + N_i) \quad (124)$$

where where  $E$  is energy in keV,  $\mathcal{L}$  is the Lindhard factor which compensates for heat loss, and  $W$  and is work function for the creation of excitons and ions in liquid xenon. The work function has been measured to be  $W=13.7 \pm 0.2$  eV/quanta [30].

In terms of the atomic mass ( $A$ ), the atomic number ( $Z$ ), and energy of the nuclear recoil ( $E_{nr}$ ), the Lindhard factor is given by

$$\mathcal{L} = \frac{kg(\epsilon)}{1 + kg(\epsilon)} \quad (125)$$

where

$$k = 0.133 \times Z^{2/3} \times A^{1/2} \quad (126)$$

$$g(\epsilon) = 3\epsilon^{0.15} + 0.7\epsilon^{0.6} + \epsilon \quad (127)$$

$$\epsilon = 11.5 \times E_{nr} \times Z^{-7/3}, \quad (128)$$

. For ER events,  $L$  equals one, for NR events  $L$  ranges between 0.1 and 0.2.

Sometimes, experiments use the effective Lindhard factor  $L_{eff}$  (also known as relative scintillation efficiency), defined as the ratio of zero-field light yields of ER

and NR events

$$L_{eff} = \frac{N_{\gamma,NR}E_{ER}}{N_{\gamma,ER}E_{ER}} \quad (129)$$

where the energy is typically chosen to be a 122 keV gamma.

From Equation 124 we see that the same number of electron and photons can produce different energy reconstruction depending on the type of recoil interaction. To avoid ambiguity, the energy of an event is typically referred to in units of kilo electron-volts electron recoil equivalent (keVee) or kilo electron-volts nuclear recoil equivalent. All of the data presented in this thesis is a product of electron recoil calibration sources, so it should be assumed that we are using units of electron-volts electron recoil equivalent unless otherwise stated.

To make use of our combined energy model, we need to convert the S1 and S2 observables from units of photons detected (phd) to the number of photons and electrons produced by the interaction. We do so by defining two gain factors. The gain factor for the S1 signal is referred to as  $g_1$ , and is given by the ratio of the average numbers of photons produced by an interaction to the observed S1 signal,

$$\langle n_{\gamma} \rangle = \frac{\langle S1 \rangle}{g_1}. \quad (130)$$

Note that the  $g_1$  gain factor allows the S1 signal to be written in terms of the number of photons produced

$$S1 = g_1 n_{\gamma} = g_1 (N_{ex} + RN_i) = g_1 * (\alpha + R) N_i \quad (131)$$

The size of  $g_1$  is dependent on the light collection efficiency in the detector, and can be thought of as the probability of a photon from an interaction striking a

PMT and producing a photo electron.

The gain factor for the S2 signal is referred to as  $g_2$ , and is given by the ratio of the average numbers of electrons produced by an interaction to the observed S2 signal.

$$\langle n_e \rangle = \frac{\langle S2 \rangle}{g_2} \quad (132)$$

As with the S1 signal,  $g_2$  allows us to write the S2 signal in terms of the number of electrons produced by an interaction,

$$S2 = g2n_e = g2(1 - R)N_i \quad (133)$$

The size of  $g_2$  is dependent on the efficiency at which electrons are extracted from the liquid xenon at the surface (the extraction efficiency), and the number of photo electrons detected per extracted electron (the single electron size).

## 6.2 Doke Plot Analysis of $g_1$ and $g_2$

The gain factors  $g_1$  and  $g_2$  can be calculated by requiring that the combined energy model reproduce the true energy of two or more electron recoil sources that produce different light and charge yields. In electron recoil events, the light yield and charge yield is a dependent on both the energy of an event, and the strength of the electric field in which the event occurred. Therefore the same electron recoil source taken at two different drift field settings can be used to determine the value of  $g_1$  and  $g_2$  alone. Table 2 lists the eight sources which were selected to measure  $g_1$  and  $g_2$  in LUX’s Run03 campaign.

Source	Energy [keV]	Decay Type	Data
$^{127}\text{Xe}$	5.3	L shell x-ray	Run03 Data
$^{83m}\text{Kr}$	41.55	IC	Run03 Calibrations
$^{131}\text{Xe}$	163.9	IC	Early Run03 Data
$^{127}\text{Xe}$	208.3 (203 $\gamma$ and 5.3 x-ray)	$\gamma$ -emission	Run03 Data
$^{129}\text{Xe}$	236.1	IC	Early Run03 Data
$^{127}\text{Xe}$	409 (375 $\gamma$ + 33.8 x-ray)	$\gamma$ -emission	Run03 Data
$^{214}\text{Bi}$	609	$\gamma$ -emission	Detector Background
$^{137}\text{Cs}$	661.6	$\gamma$ -emission	Run03 Calibrations

Table 2: Table of sources used in the Doke plot analysis..

We use a Doke plot technique to ensure the combined energy model reproduces the true energy of all eight sources. [34, 32] Solving equation 124 for  $\frac{S1}{E}$ , we find

$$\frac{S1}{E} = \frac{g_1}{W} - \frac{S2 g_1}{E g_2} \quad (134)$$

which is the equation of a line with

$$y = \frac{S1}{E}, \quad x = \frac{S2}{E} \quad (135a)$$

$$b = \frac{g_1}{W} \quad (135b)$$

$$m = \frac{g_1}{g_2} = \frac{b \times W}{g_2} \quad (135c)$$

This motivates the creation of a "Doke Plot" in which we plot the mean light yield,

$\frac{S_1}{E}$ , versus the mean charge yield,  $\frac{S_2}{E}$ , for each line source to find the best fit for

$$g_1 = b \times W \quad (136a)$$

$$g_2 = \frac{b \times W}{m} \quad (136b)$$

Diagonal cuts chosen by eye were used for initial event selection of the sources in Table 2. Next, we fit a rotated two dimensional Gaussian distribution to the corrected S1 and S2 spectra of each source to determine the mean and sigma of the S1 and S2 populations. Once the standard deviation of each population is determined, we refit the data using only events within  $\pm 2\sigma$  of the S1 and S2 Gaussians means to eliminate tails caused by backgrounds. A linear fit of  $\frac{\langle S_1 \rangle}{E} = m \frac{\langle S_2 \rangle}{E} + b$  is performed using the refit Gaussian means. Once an initial best fit for  $g_1$  and  $g_2$  is found, we can produce a combined energy scale using equation 124. This combined energy spectrum has significantly better resolution than the individual S1 and S2 spectra, and allows us to improve our initial event selection by placing a  $\pm 2\sigma$  cut around the energy peaks. We then refit S1 and S2 spectra once more with the improved event selection, and find new values for the best fit of  $g_1$  and  $g_2$ . This process of producing an energy spectrum to improve event selection is iterated five times, but quickly converges after the second iteration.

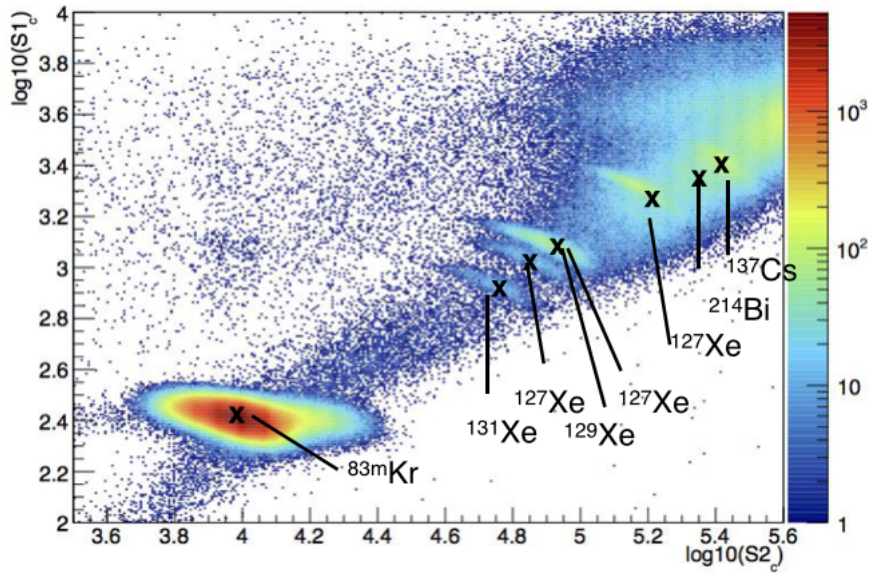


Figure 51: S1 versus S2 density plot for all data that was used in Run03 Doke plot analysis.

### 6.2.1 Doke Plot Systematic Errors

There are a number of systematic errors on the S1 and S2 signals that must be considered when constructing the Doke plot. One such error comes from the variation in single electron size over time, shown in Figure 52. The Doke plot uses data from many sources taken at different points in time, and therefore each point on the plot has a different single electron size. Since we seek one value of  $g_2$  which describes the all of the data, and since  $g_2$  is equal to the extraction efficiency times the single electron size, the variation in single electron size must be included in the S2 error bars.

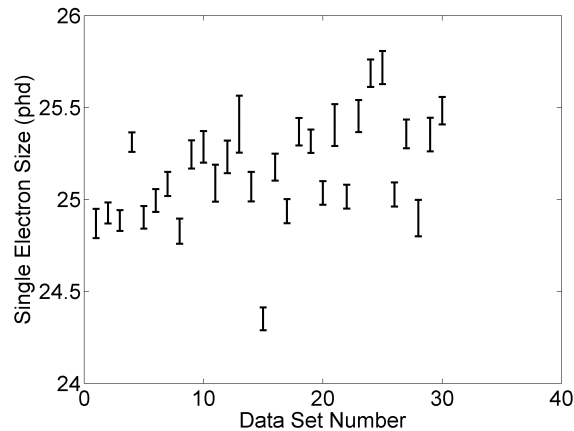


Figure 52: Single electron sizes for all  $^{83m}\text{Kr}$  data sets over the course of LUX’s Run03 data taking campaign.

Another source of error is introduced by variations in the position dependent pulse area corrections. Systematic variations in the correction maps lead to variation in the corrected S1 and S2 signals over time. This adds a systematic error to all of our data points in the Doke plot which can be measured using the standard deviation of the corrected  $^{83m}\text{Kr}$  S1 and S2 peaks over time. We assume that the size of this systematic error scales linearly with S1 and S2 size for the non- $^{83m}\text{Kr}$  data points.

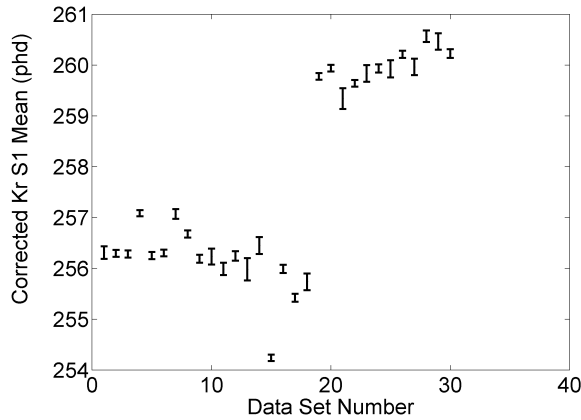


Figure 53: Corrected S1 peaks for all  $^{83m}\text{Kr}$  data sets at 170 V/cm field strength. The step near data set 20 is due to an update of the S1 XYZ corrections map. This effect is accounted for in our systematic errors

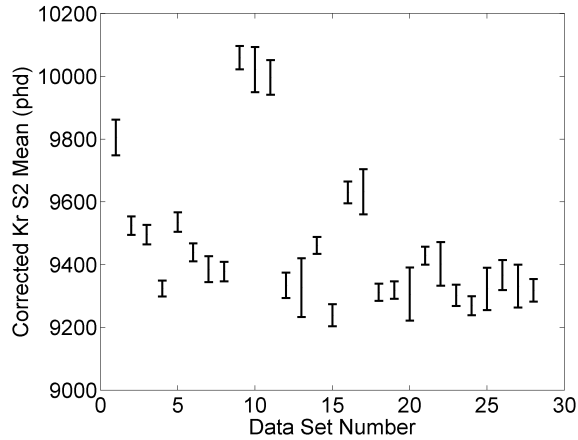


Figure 54: Corrected S2 peaks for all  $^{83m}\text{Kr}$  data sets at 170 V/cm field strength.

Additionally, there is a small difference in the measurement of  $n_e = \frac{S_2}{SE}$  for each Doke plot point when using both PMT arrays or using the bottom PMT array only. The number of electrons produced by a particle interaction is independent of how many PMTs observe the interaction, so this discrepancy can only be due to systematic errors which are likely produced by the PMT arrays saturating at

high energies. The size of this discrepancy is also included in the systematic error of each point.

### 6.2.2 Doke Plot Results

The Doke plot produced by the analysis described in the preceding sections is shown in Figure 55. The best fit parameters for the Doke plot are highly correlated. To account for this the errors on the fit are calculated using a Markov chain Monte Carlo. The covariance matrix produced after five thousand trials is used as for error measurement on each parameter. We get a best fit of  $g_1 = 0.117 \pm 0.003$  and  $g_2 = 12.1 \pm 0.8$ . This value of  $g_2$  corresponds to an extraction efficiency of  $EE = 0.491 \pm 0.032$ .

In Figure 57 we use the best fit parameters from the Doke plot to produce energy spectra for each line source used in this analysis. Sources that are below the line on the Doke plot have energy peaks that are lower than expected, and sources that are higher than the line on the Doke plot have energy peaks that are higher than expected.

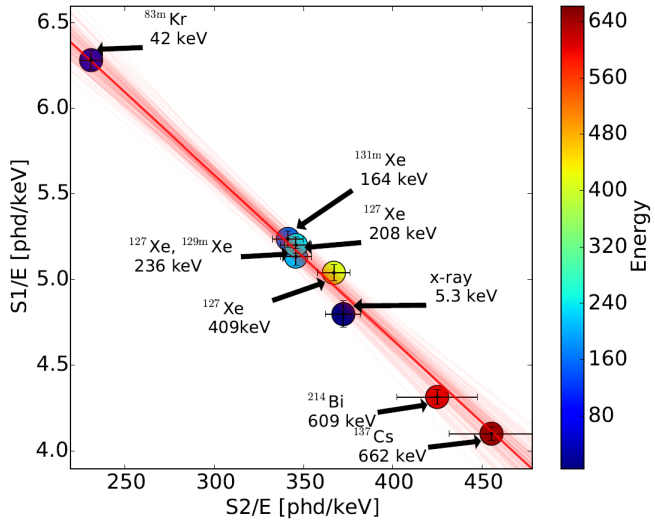


Figure 55: The Doke plot from this analysis. The red faded red lines indicate the result of each MCMC trial, while the dark red line indicates the best fit result. The energy of each source is indicated by the point's color.

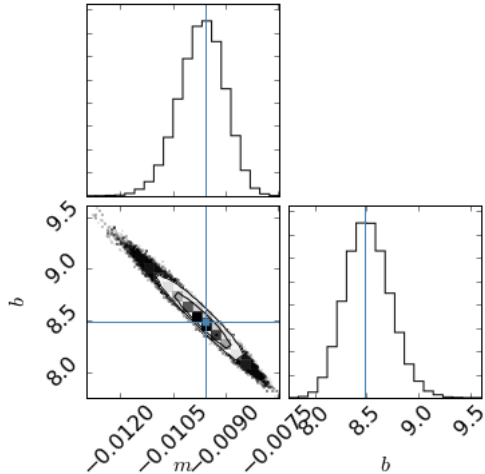


Figure 56: A triangle plot showing the correlation between the fit parameters during the MCMC process. A projection of the fit results onto each axis is shown above and next to the triangle plot.

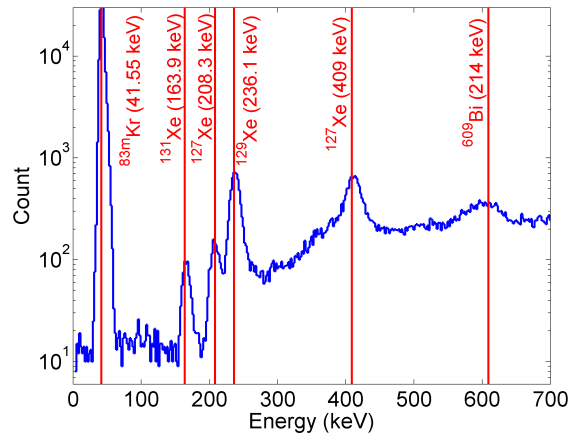


Figure 57: The energy spectrum of LUX's Run03 data after using the  $g_1$  and  $g_2$  values from the Doke plot analysis

### 6.2.3 Recombination Fluctuations from Doke Plot Data

Using the methods from citeDobi and the data from this Doke plot analysis we can determine recombination fluctuations ( $\sigma_R$ ) as well as fluctuations in counting photons ( $\sigma_{n_{\gamma}Det}$ ) and electrons ( $\sigma_{n_eDet}$ ) due to detector resolution. The relevant equations are

$$\begin{aligned}\sigma_R^2 &= \frac{1}{2}(\sigma_{n_{\gamma}Det}^2 + \sigma_{n_eDet}^2 - \frac{\sigma_E^2}{W^2}) = \frac{1}{2}(\frac{\sigma_{S1}^2}{g_1^2} + \frac{\sigma_{S2}^2}{g_2^2} - \frac{\sigma_E^2}{W^2}) \\ \sigma_{n_{\gamma}Det}^2 &= \frac{\sigma_{S1}^2}{g_1^2} - \sigma_R^2 \\ \sigma_{n_eDet}^2 &= \frac{\sigma_{S2}^2}{g_2^2} - \sigma_R^2\end{aligned}$$

where  $\frac{\sigma_{S1}^2}{g_1^2}$ ,  $\frac{\sigma_{S2}^2}{g_2^2}$ , and  $\frac{\sigma_E^2}{W^2}$  can be measured with Gaussian fits to the S1, S2, and energy spectra for each point on the Doke plot. The results of this analysis are shown in table 3. The results included here are the outcome after setting the fitting window by eye in a way which eliminates the most background events while maintaining the majority of each spectrum's peak.

Source	Energy [keV]	$\sigma_R$	$\sigma_{n_{\gamma}Det}$	$\sigma_{n_eDet}$
$^{83m}\text{Kr}$	41.55 (50 V/cm)	$66.59 \pm 2.1$	$151.0 \pm 0.3$	$84.95 \pm 0.4$
$^{83m}\text{Kr}$	41.55 (100 V/cm)	$80.51 \pm 1.6$	$148.7 \pm 0.3$	$82.12 \pm 0.5$
$^{83m}\text{Kr}$	41.55 (170 V/cm)	$104.9 \pm 1.1$	$142.9 \pm 0.3$	$90.71 \pm 0.5$
$^{131}\text{Xe}$	163.9	$355.5 \pm 43$	$260.1 \pm 31$	$354.2 \pm 30$
$^{127}\text{Xe}$	208.3	$662.5 \pm 63$	$489.1 \pm 91$	$167.3 \pm 120$
$^{129}\text{Xe}$	236.1	$540.9 \pm 45$	$416.1 \pm 45$	$477.0 \pm 35$
$^{127}\text{Xe}$	409	$1250 \pm 82$	$894.8 \pm 67$	$1183 \pm 53$
$^{214}\text{Bi}$	609	$1667 \pm 304$	$2147 \pm 100$	$3353 \pm 120$
$^{137}\text{Cs}$	661.6	$1979 \pm 158$	$1248 \pm 82$	$2314 \pm 84$

Table 3: Extracted fluctuations from Doke plot data in units of quanta.

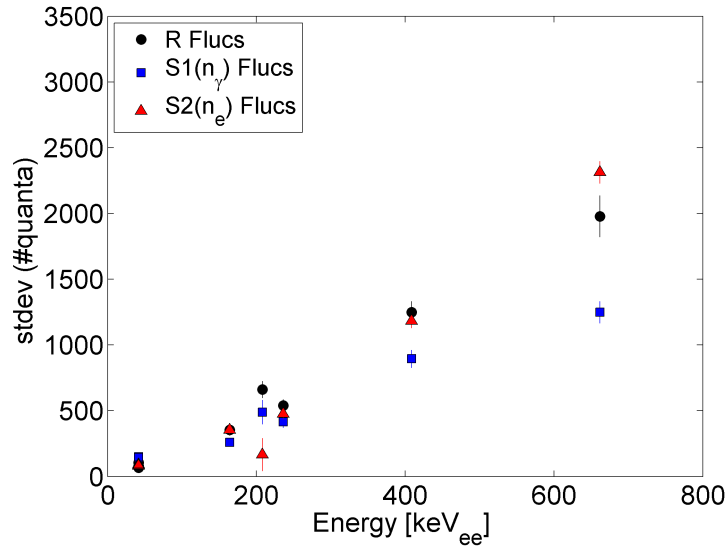


Figure 58: Measured values of  $\sigma_R$ ,  $\sigma_{n_{\gamma}Det}$ , and  $\sigma_{n_eDet}$  versus energy.

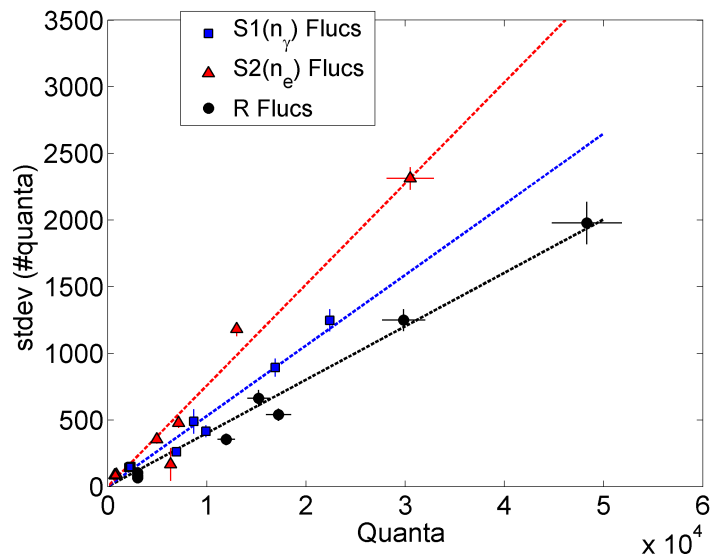


Figure 59: Measured values of  $\sigma_R$ ,  $\sigma_{n_{\gamma}Det}$ , and  $\sigma_{n_eDet}$  versus photons, electrons, and ions, respectively.

This study was repeated using the bottom PMT array only, while keeping both

the cuts and fitting windows exactly the same. The results are shown in table 4. As expected the variance from recombination fluctuations appears independent of which PMTs are used in the analysis. However, the slope of  $\sigma_{n_{\gamma}Det}$  and  $\sigma_{n_eDet}$  versus number of quanta is much more shallow when using the bottom PMT array only. This could represent a systematic error, but it may also suggest that the top array of PMTs is contributing a significant amount of noise, or that the overall variance due to detector resolution is proportional to the number of PMTs which are used.

Source	Energy [keV]	$\sigma_R$	$\sigma_{n_{\gamma}Det}$	$\sigma_{n_eDet}$
$^{83m}\text{Kr}$	41.55 (50 V/cm)	$63.32 \pm 1.2$	$152.6 \pm 0.2$	$79.2 \pm 0.4$
$^{83m}\text{Kr}$	41.55 (100 V/cm)	$82.16 \pm 1.6$	$153.0 \pm 0.3$	$84.5 \pm 0.5$
$^{83m}\text{Kr}$	41.55 (170 V/cm)	$103.4 \pm 1.1$	$149.7 \pm 0.3$	$78.0 \pm 0.5$
$^{131}\text{Xe}$	163.9	$372.0 \pm 27.8$	$249.7 \pm 32$	$313.7 \pm 33$
$^{127}\text{Xe}$	208.3	$696.9 \pm 61$	$400.5 \pm 110$	$306.7 \pm 90$
$^{129}\text{Xe}$	236.1	$595.8 \pm 34$	$348.0 \pm 51$	$412.8 \pm 42$
$^{127}\text{Xe}$	409	$1328 \pm 56$	$790.9 \pm 77$	$874.5 \pm 60$
$^{214}\text{Bi}$	609	$1811 \pm 312$	$2101 \pm 100$	$3253 \pm 180$
$^{137}\text{Cs}$	661.6	$2235 \pm 74.9$	$773.1 \pm 136.5$	$1657 \pm 94$

Table 4: Extracted fluctuations from Doke plot data in units of quanta when using the bottom array only.

#### 6.2.4 Light Yield from Doke Plot Data

The light yield in terms of  $\frac{S1}{keV}$  and  $\frac{photons}{keV}$  for each line source is easily obtainable from the Gaussian fits used in the Doke plot analysis and is included in 5. In the case of  $^{83m}\text{Kr}$  two S1s (32.1 keV and 9.5 keV) are typically merged into one 41.55 keV S1 pulse by the data processing module. The second of the two decays

will occur with varying amounts of recombination depending on the amount of time between the first and second decay. This recombination variation makes the combined 41.55 keV S1 pulse undesirable for measuring light yield. Instead, we search for events where the two S1s occur far enough apart in time that data processing separates them into two S1 pulses. A Gaussian fit is then used to determine the light yield from the 32.1 keV  $^{83m}\text{Kr}$  S1, resulting in  $5.69 \pm 0.03 \frac{\text{S}1}{\text{keV}}$  and  $46.3 \pm 1.16 \frac{\text{photons}}{\text{keV}}$ . Note that the  $^{127}\text{Xe}$  208.3 keV line in 5 is still a result of two decays that are combined in our data processing, and this may affect the LY measurement for that point.

Source	Energy[keV]	$\frac{\text{S}1}{\text{keV}}$	$\frac{\text{photons}}{\text{keV}}$
$^{83m}\text{Kr}$	32.1 (170 V/cm)	$5.69 \pm 0.03 (5.62 \pm 0.36)$	$46.3 \pm 1.16 (45.7 \pm 3.13)$
$^{131}\text{Xe}$	163.9	$5.08 \pm 0.05$	$41.3 \pm 1.1$
$^{127}\text{Xe}$	208.3(203+5.3)	$5.00 \pm 0.07$	$40.7 \pm 1.2$
$^{129}\text{Xe}$	236.1	$5.04 \pm 0.04$	$41.0 \pm 1.1$
$^{127}\text{Xe}$	409	$4.97 \pm 0.04$	$40.4 \pm 1.0$
$^{214}\text{Bi}$	609	$4.21 \pm 0.03$	$34.2 \pm 0.9$
$^{137}\text{Cs}$	661.6	$4.07 \pm 0.03$	$33.1 \pm 0.9$

Table 5: Light yield measurements from Doke plot data.

### 6.3 Tritium $\chi^2$ Analysis of $g_1$ and $g_2$

LUX’s CH<sub>3</sub>T calibration source produces a wide beta spectrum which continuously spans energies from the detector’s threshold up to 18.6 keV. We can take advantage of the wide energy spectrum to measure the  $g_1$  and  $g_2$  gain factors by varying  $g_1$  and  $g_2$  in a two dimensional  $\chi^2$  fit until data matches the expected tritium beta spectrum. References [60, 69, 33] derive an expression for the density of energy

states accessible to the electron in a beta decay. In terms of the kinetic energy of the electron,  $T$ , it is given by

$$\frac{dN(T, Z)}{dT} = C(T^2 + 2Tm_e)^{1/2}(T + m_e)(Q - T)^2 F(T, Z) \quad (137)$$

where  $Q_T = 18.6\text{keV}$  is the maximum kinetic energy of the electron,  $m_e = 511\text{keV}$  is the mass of the electron,  $C$  is a normalization constant,  $Z = 2$  is the nuclear charge for tritium, and

$$F(T, Z) = 2\pi \frac{\alpha}{\left(\frac{\gamma^2 - 1}{\gamma^2}\right)^{1/2}} \quad (138)$$

is the Coulomb correction due to nuclear charge with using  $\alpha = 1/137$  as the fine structure constant, and

$$\gamma = \frac{T + m_e}{m_e} \quad (139)$$

as the energy to rest mass ratio.

Before using equation 137 to produce the expected tritium beta spectrum in the LUX detector, we need to smear the distribution to model effects from the detector's resolution and recombination variation. This is accomplished by drawing the true energy of events from the distribution described by 137 and feeding them into the NEST simulation package. NEST produces simulated S1 and S2 signals for the corresponding energy deposition, which in turn provide a simulated tritium energy spectrum for the LUX detector using equation 124.

Once we have a simulated model for the tritium energy spectrum in LUX we can minimize a two dimensional  $\chi^2$  fit between the data and simulation to find the optimal values of  $g_1$  and  $g_2$ . The optimized  $\text{CH}_3\text{T}$  energy spectrum for the largest  $\text{CH}_3$  calibration in LUX's Run03 data taking campaign is shown in Figure 33. The

result of  $g1 = 0.115 \pm 0.005$  phd/photon,  $g2 = 12.1 \pm 0.9$  phd/electron, and  $EE = 50.9\% \pm 3.8\%$  is in close agreement with the Doke plot results from section 55.

## 7 Calibration of the LUX Detector in a nonuniform Field

KrypCal uses the uncorrected S1 and S2 signals from  $^{83m}\text{Kr}$  data to produce xyz corrections for our detector inefficiencies. These inefficiencies arise from a number of sources. In the S2 signal, a Z dependence is introduced to the data due to impurities absorbing charge as it drifts through the liquid xenon in the detector. An XY variation is also introduced via nonuniform extraction field and liquid level changing the single electron (SE) size in the XY dimensions. The S1 signal can also have a Z dependence introduced to the data at purity levels below 200  $\mu$ second electron lifetime. A more significant XYZ dependence is introduced to the S1 signal via light collection inefficiencies arising from teflon reflectivity, total internal reflection at the liquid xenon surface, and the solid angle covered by each PMT during an event. These sources of spatial dependence in the pulse area will be referred to as "detector inefficiencies" throughout this note.

LUX Run04 data is complicated by a nonuniform electric field in the detector. Although the origin of the radial component of the field is unknown, we suspect it was introduced during our grid conditioning campaign. In this model, UV light produced during grid conditioning broke the bonds of teflon molecules in the detector walls, and the resulting charged particles were separated by the electric field produced by the grids. This accumulation of charge on the detector walls

is believed to be the source of the radial field in the detector. This theory is supported by the sudden appearance of the radial field component shortly after the grid conditioning campaign, as well studies of the effect of UV light on teflon in other fields, such as the space industry. [65, 31] To complicate the matter further, the electric field has been observed to be varying in time as well.

This note will begin by describing the radial component of the electric field and the complications that arise from it. We will then define our goal for KrypCal corrections in the presence of such a field before detailing our efforts to measure and separate the field effects in  $^{83m}\text{Kr}$  Data. We will conclude this note with an evaluation of the current KrypCal method and a look at what complications remain in the Run04 data.

## 7.1 Description of the Nonuniform Electric Field

### 7.1.1 Measuring the Run04 Electric Field

A great deal of effort has been made by both Scott Hertel and Lucie Tvrznikova to measure the electric field at different times in the LUX Run04 data. In Scott's method, the detector is sliced into drift time bins of 25  $\mu\text{second}$  width. An axisymmetric wall radius is defined for each drift time bin based on the XY distribution of events within the bin. A field model including the detector's wire grids and a charge density distribution on the walls is then modified using a "chi-by-eye" fit until a simulated data distribution visually reproduces the RvZ event distribution in data. (Figure 60) [39]

Lucie's field model takes a similar approach to Scott's work. In this method, 43 basis vectors in COMSOL Multiphysics are used to define an electric field model.

One basis vector describe the Run04 grid voltages, and the other 42 basis vectors are used to describe the charge density of 42 tiles placed around the detector's teflon walls. A Metropolis-Hastings algorithm is used to match the three dimensional distribution of events in simulation to Run04 data by varying the charge density on each of the 42 tiles. [66]

Wing To and Tomasz Biesiadzinski have been working to observe the evolution of the electric field in time using  $^{137}\text{Cs}$  and  $^{83m}\text{Kr}$  data. Cesium is useful for this purpose since it does not penetrate the entire fiducial volume and serves to highlight the wall regions around the external source. The results of this analysis have shown significant variation in the electric field over time. The rate of change of this variation has been slowing down over time. [20]

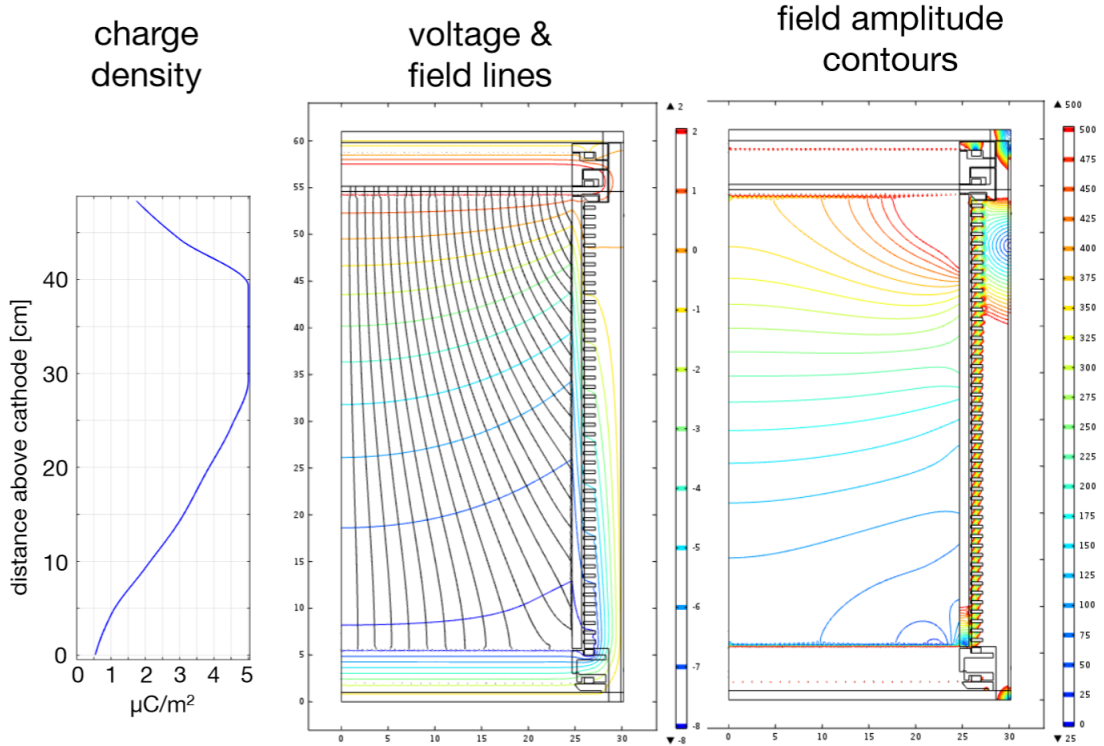


Figure 60: The results of Scott's September 2014 RvZ field map.[39]

### 7.1.2 Complications Arising from the Run04 Electric Field

The nonuniform electric field in Run04 introduces a number of complications to the data. The most obvious of these complications is a radial squeezing in position reconstruction. As charge from an event drifts upward it is pushed toward smaller radii due to the radial component of the electric field. As a result, the XY position of the S2 signal from an event is significantly separated from the XY position of the event itself. Due to their longer drift time, this effect is more pronounced in events from the bottom of the detector. (Figure 61) We hope to use Lucie's field models discussed in section 7.1.1 to reconstruct the position of the events more accurately, but as of this time we are only implementing a smearing model which forces the XYZ distribution of  $^{83m}\text{Kr}$  events to match the physical detector dimensions with uniform density. [63]

The time variation of the electric field complicates the Z position reconstruction of events as well. As the field evolves over time the drift velocity throughout the detector changes. As a result, the mapping of drift time in  $\mu$ seconds to physical position in mm is no longer constant in time or space. Note that in particular this introduces complications when defining the electron lifetime in Run04, since the drift time to mm mapping is no longer one-to-one and the electron capture cross section is dependent on the drift-velocity. As of this time we have no detailed studies of this effect, and the only tools we have developed to deal with it are the uncorrected position to physical position mapping that results from Lucie and Scott's work described in section 7.1.1.

A more subtle complication introduced by the nonuniform electric field lies in the recombination physics that occurs during a recoil event. During a recoil

ionizing radiation produces both ionization and excitation of the xenon atoms. The xenon excimers ( $\text{Xe}_2^*$ ) produce scintillation light as they return to the ground state, which we observe as our S1 signal. Some of the electrons produced during ionization escape the location of the event, drift to the top of our detector, and produce our S2 signal. The electrons that do not escape the event recombine with the ionized xenon atoms in a process called recombination, producing additional xenon excimers that contribute to the S1 signal. Recoil events which occur in a low field region of the detector have a higher chance to recombine, and therefore produce more S1 signal and less S2 signal than an event in a high field region. Complicating this matter further, the strength of this effect is dependent on the energy of the event and whether the event is an electron recoil (ER) or a nuclear recoil (NR). (Figure 62) This source of pulse area variation in space and time will be referred to as "field effects" throughout this note. This means that any pulse area corrections which are based solely on the spatial dependence of  $^{83m}\text{Kr}$  data, as was done in Run03, are no longer valid for ER or NR events in the WIMP search energy range.

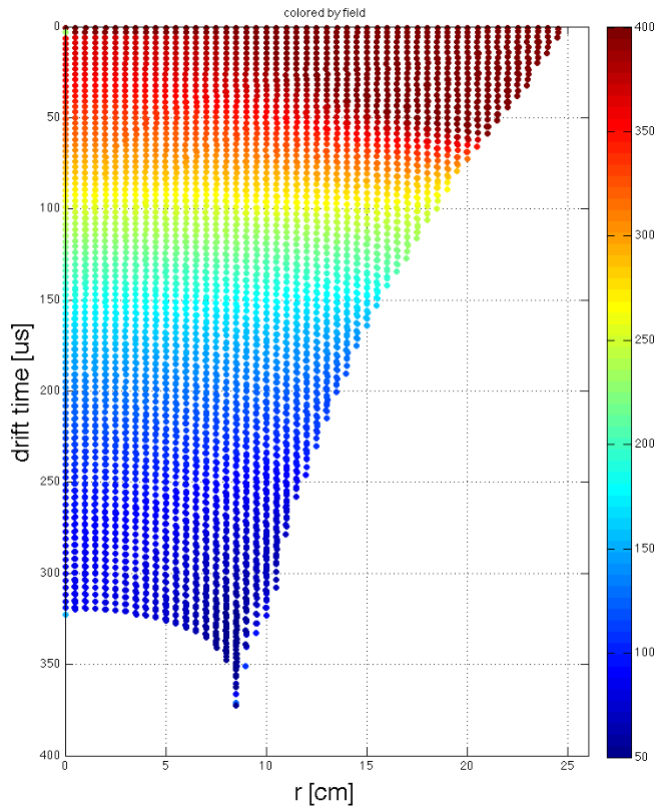


Figure 61: The reconstructed distribution of events resulting from the field map in Figure 60. Each point in the figure was placed on a uniform grid and allowed to drift to the liquid surface, where the final radius is measured. The color of each point indicates the strength of the electric field in this "uncorrected" XY coordinate system. This simulation reproduces the distribution of events seen in data from September 2014. [39]

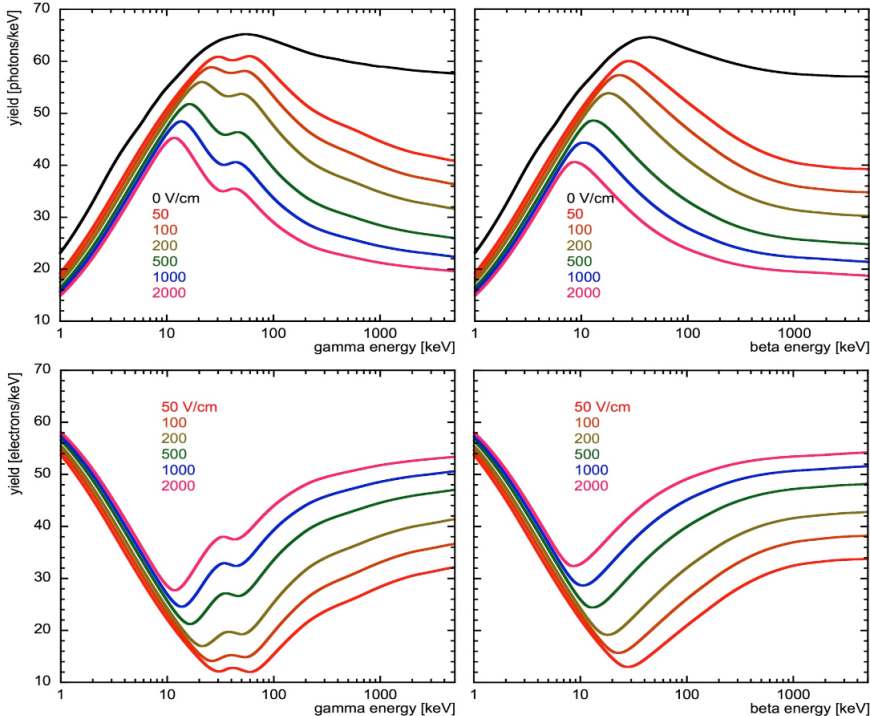


Figure 62: Predictions from NEST for the light yield (top row) and charge yield (bottom row) of electron recoil event from gamma ray interaction (left column) and beta particle interaction (right column). Field values are indicated by the colored lines. Light yield and charge yield have less dependence on the field strength for lower energy events. [64]

### 7.1.3 The Goal of KrypCal in Run04

In Run04 KrypCal must account for field effects as a function of time, space, energy, and recoil type. Since the recoil type of an event in WIMP search data is unknown with exact certainty, and the energy of an event in WIMP search data is unknown prior to KrypCal corrections being applied, it is not possible to remove the spatial and time dependence of the pulse area which is induced by the field effect in our data. Instead, we seek to separate the field effect from the detector inefficiency effects at the known energy and recoil type of  $^{83m}\text{Kr}$ . This separation must be performed at all points in time due to the time dependence of the electric

field. To accomplish this we seek to relate the strength of the field effects in the S1 and S2 pulse areas of  $^{83m}\text{Kr}$  calibration data to the ratio of the two S1 pulses (referred to as S1a and S1b) generated during the  $^{83m}\text{Kr}$  decay. This ratio should be strongly correlated to the strength of the electric field effect, since the two  $^{83m}\text{Kr}$  decays have different energies (32.1 keV for S1a and 9.4 keV for S1b) and are therefore effected by the electric field by different amounts, as discussed in the preceding section. Note that corrections which perfectly separate field effects from detector inefficiency effects in this manner, and only correct for the latter, will have a spatial and time dependence left in the S1 and S2 signals but not in the energy spectra from any source, regardless of energy or recoil type.

## 7.2 Measuring Electric Field Effects in $^{83m}\text{Kr}$ Data

### 7.2.1 General Strategy for Measuring the Field Effect

Before providing detailed descriptions of each step of the KrypCal process, we will first discuss the general strategy for measuring and separating out the electric field effect in  $^{83m}\text{Kr}$  calibrations. First, we measure the electric field in the detector using the methods described in section 7.1.1 at a particular point in time. Due to their high statistics, we choose data sets in September 2015 for this purpose. We would like to use this field map in conjunction with NEST to remove the field effects in the  $^{83m}\text{Kr}$  data directly before measuring detector inefficiency effects. Unfortunately, due to the complicated nature of the  $^{83m}\text{Kr}$  decay (detailed in Section 5.1) NEST does not accurately simulate  $^{83m}\text{Kr}$  data. Instead we turn to CH<sub>3</sub>T data, which NEST has been tuned to simulate extremely well.

After using NEST to determine and remove the strength of the field effects in

$\text{CH}_3\text{T}$  data we measure the residual spatial pulse area variation in the S2 signal and produce corrections for these effects, which, since the field effects have been removed, are due to detector inefficiencies alone. The same process can not be repeated for the S1 signal, since the maximum of the  $\text{CH}_3\text{T}$  S1 spectrum falls below the detector threshold. These S2 corrections are equivalent to the Run03 S2 corrections which were obtained directly from  $^{83m}\text{Kr}$  data when there was no significant field variation. Next, we apply the detector inefficiency corrections to  $^{83m}\text{Kr}$  data taken during the same time as the  $\text{CH}_3\text{T}$  data. At this point, any residual pulse area variation in the S2 signal of the  $^{83m}\text{Kr}$  is due to field effects alone. We measure the strength of the field effects by fitting Gaussian distributions to the inefficiency corrected  $^{83m}\text{Kr}$  S2 signal over a three dimensional map, choosing the ratio  $S2(\text{XYZ})/S2(\text{Center})$  as the figure of merit for the strength of the field effect. At the same time we measure a three dimensional map of the  $^{83m}\text{Kr}$  S1a/S1b ratio. Relating these two maps allows us to determine the strength of the field effect on the S2 pulse area in  $^{83m}\text{Kr}$  taken at any time and any location by simply measuring the  $^{83m}\text{Kr}$  S1a/S1b ratio.

Three approaches have been taken to measure the relationship of the field effect in inefficiency corrected  $^{83m}\text{Kr}$  S1 data, as measured by  $S1(\text{XYZ})/S1(\text{Center})$ , to the  $^{83m}\text{Kr}$  S1a/S1b ratio. The first approach, in section 7.2.6, converts the S2 field effect relationship to an S1 field effect relationship using the physics behind recombination. In section 7.2.7 we use the expected light yield of the  $^{83m}\text{Kr}$  31.2 keV decay as a function of electric field to measure detector inefficiency effects and separate them from the field effect we want to measure. The final approach, in section 7.2.9, takes advantage of the fact that the energy spectrum of any event should remain insensitive to any recombination variation that arises from a

complicated electric field. In this method, we float the  $^{83m}\text{Kr}$  S1(XYZ)/S1(Center) to S1a/S1b relationship in a  $\chi^2$  fit. Within the fit we remove the field effect in both the S1 and S2  $^{83m}\text{Kr}$  data (using the floated relationship for the S1 field effect), produce inefficiency-only corrections from the data, and then evaluate the corrected  $^{83m}\text{Kr}$  and  $\text{CH}_3\text{T}$  energy spectra. The S1(XYZ)/S1(Center) to S1a/S1b relationship which produces the minimum  $\chi^2$  between the observed and expected energy spectra is chosen as the correct relationship.

Once the field induced S2(XYZ)/S2(Center) to S1a/S1b relationship and the field induced S1(XYZ)/S1(Center) to S1a/S1b relationship have been determined they can be used in  $^{83m}\text{Kr}$  data sets from any time to remove the field effects in the  $^{83m}\text{Kr}$  data via mapping the S1a/S1b ratio at the time. Once the field effects are removed the residual S1 and S2 variation in the  $^{83m}\text{Kr}$  can be used to calculate pulse area corrections based on detector inefficienc alone. In the following sections we will describe each step of the process outlined above in more detail.

### 7.2.2 Measuring Detector Inefficiency Corrections with $\text{CH}_3\text{T}$

Before measuring detector inefficiency corrections in  $\text{CH}_3\text{T}$  we must first remove the field effects from the data. We use data from the September 2015  $\text{CH}_3\text{T}$  calibration due to its high statistics. A simple box cut of ( $630 \leq$  uncorrected S2  $\leq 14000$ ) and (uncorrected S1  $\leq 125$ ) is used to select  $\text{CH}_3\text{T}$  events from the data set, as shown in Figure 63. The electric field at the location of each  $\text{CH}_3\text{T}$  event is estimated by interpolating Scott's RvZ field map (described in section 7.1.1) from September 2015. A cubic interpolation is used for events which fall within the bounds of Scott's field map, and a nearest neighbor extrapolation is used for events which fall outside of the bounds. Note that we choose to use Scott's field

maps for this work because interpolating and extrapolating is simplified in a two dimensional map, and because Scott's field map varies more smoothly in space due to the smooth charge density distribution in his field model.

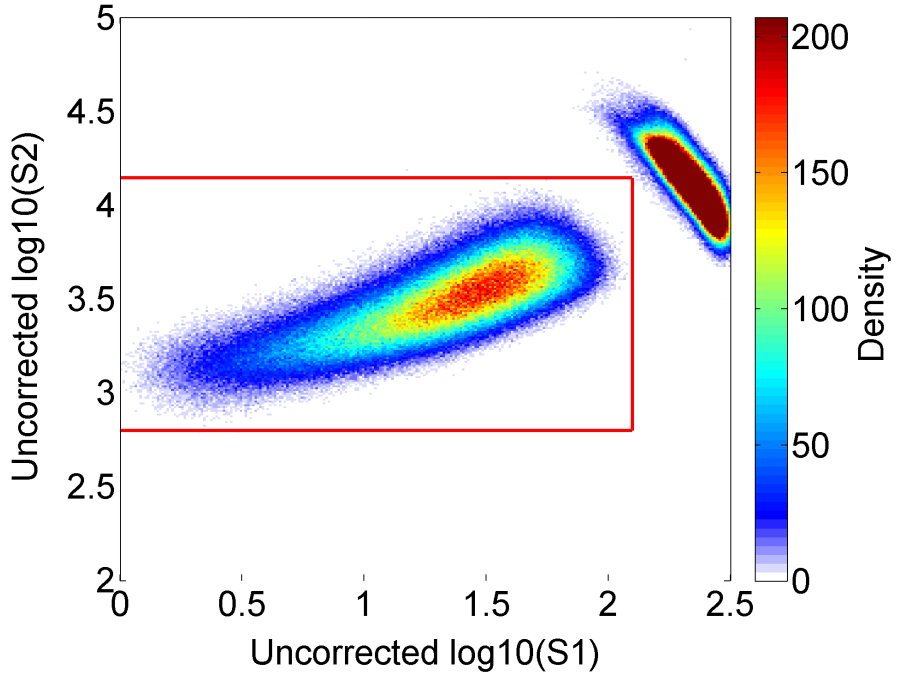


Figure 63: Density plot of uncorrected S1 versus uncorrected S2 from the September 2015 CH<sub>3</sub>T calibration. The red lines indicate the box cut used to select CH<sub>3</sub>T events. The dense population to the right of the box cut is <sup>83m</sup>Kr which is present in the data set and excluded from the box cut.

Once the field strength at the location of a particular event is determined it is converted to a measurement of the recombination for each event using the following equation from NEST. (Figure 64)

$$N_q = \frac{E}{0.0137} \quad (140)$$

$$N_{ion} = \frac{N_q}{1 + \alpha} \quad (141)$$

$$R = 1 - \ln \left( \frac{1 + \left( \frac{TI * N_{ion}}{4} \right)}{\left( \frac{TI * N_{ion}}{4} \right)} \right) \quad (142)$$

where  $E$  is the energy of the event,  $N_q$  is the number of quanta,  $N_{ion}$  is the number of ions,  $\alpha$  is the exciton to ion ratio (assumed to be 0.11),  $TI$  is the Thomas-Imel Box parameter, and  $R$  is the recombination probability. Since we do not know the energy of the event ahead of time (since we do not have working corrections at this point) we assume the most probable energy from the CH<sub>3</sub>T energy spectrum, which is 2.5 keV. We are mainly interested in fitting the maximum of the spectrum when measuring detector inefficiency corrections, so the fact that this recombination estimate for higher energy CH<sub>3</sub>T events may be off by up to a factor of 2.5 is not concerning.

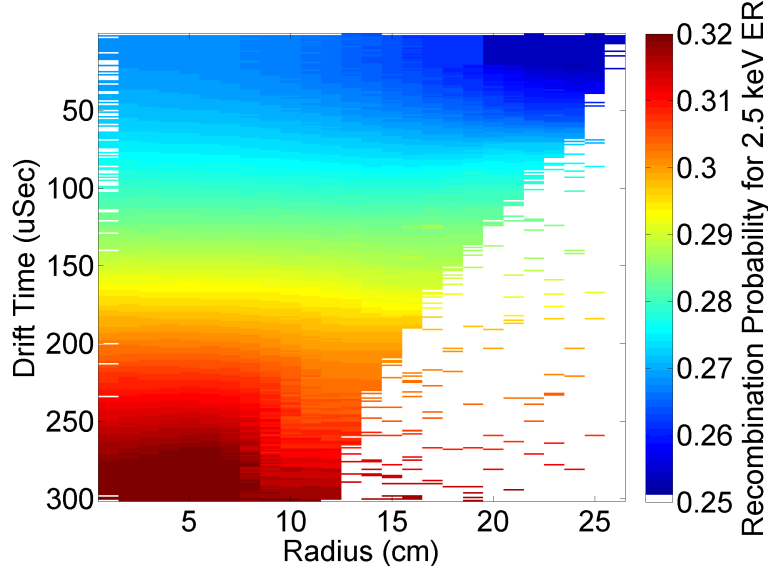


Figure 64: Two dimensional map of the recombination probability for a 2.5 keV ER based on Scott's September 2015 electric field map and NEST.

A normalization factor  $N_{photon-center}/N_{photon}$  for the S1 signal is determined by calculating the number of photons produced in events at the center of the detector, and the number of photons produced in a particular event by using

$$N_{photon} = N_q \frac{\alpha}{1 + \alpha} + N_{ion}R \quad (143)$$

Since we assumed a value of 2.5 keV for all events,  $R$  only has a dependence on the estimated field strength, and therefore the normalization constant only has a dependence on the estimated field strength at each location in the detector as well. Similarly, we determine a normalization factor  $N_{elec-center}/N_{elec}$  for the S2 signal by calculating the number of electrons at the center of the detector and the number of electrons for a particular event by using the equation

$$N_{elec} = N_q - N_{photon} \quad (144)$$

which again is only dependent on the estimated field strength at each location in the detector. We simply multiply the raw S1 and S2 signals by these normalization factors to remove the field effects from the CH<sub>3</sub>T. For clarity, we define the field effect removed S1 and S2 signals as S1<sub>F</sub> and S2<sub>F</sub>, respectively, where the subscript  $F$  stands for "field corrected".

$$S2_F = S2 \left( \frac{N_{elec-center}}{N_{elec}} \right) \quad (145)$$

$$S1_F = S1 \left( \frac{N_{photon-center}}{N_{photon}} \right) \quad (146)$$

Likewise, we define the detector inefficiency corrected S1 and S2 signals (with field effects still present) as S1<sub>E</sub> and S2<sub>E</sub>, where the subscript  $E$  stands for "efficiency corrected", and the detector inefficiency corrected and field effect removed S1 and S2 signals as S1<sub>EF</sub> and S2<sub>EF</sub>, where the subscript  $EF$  stand for "efficiency and field corrected" .

After removing the field effects from the CH<sub>3</sub>T data we are ready to measure the residual spatial pulse area variation due to detector inefficiencies alone. We

first measure the Z dependence of the  $S_{2F}$  pulse area by slicing the detector into drift time bins of 10  $\mu$ second width. A Landau distribution is fit to the  $S_{2F}$  spectrum of each bin to determine the location of the spectra maximums. (Figure 65) Polynomial and skew Gaussian fits have also been used to determine the maximums with consistent results between all three methods. A cubic interpolation is used to determine the  $S_{2F}$  Z dependence between each drift time bin, and a linear extrapolation based on the first and last 20% of Landau distribution data points is used to determine the  $S_{2F}$  Z dependence above and below the span of the drift time bins. A detector inefficiency correction for the Z direction is defined by taking the ratio of the  $S_{2F}$  pulse area at a height of 4  $\mu$ seconds (just below the liquid surface) to the  $S_{2F}$  pulse area as described in the equation

$$S_{2z\text{-efficiency-correction}} = \frac{S_{2F}(z=4)}{S_{2F}(z)}. \quad (147)$$

The XY dependence of the field removed  $S_{2F}$  signal is found by dividing the z inefficiency corrected ( $S_{2F} \times S_{2z\text{-efficiency-correction}}$ ) data into two dimensional XY bins with lengths of 3 cm on each side, and then fitting Landau distributions to the data of each bin. The maximum of the Landau distribution from each bin is used to construct an  $S_{2F}$  XY dependence map, with a spline interpolation and extrapolation being used to determine the XY dependence between and outside of the bins. (Figure 66) A detector inefficiency correction for the XY direction is defined by taking the ratio of the z inefficiency corrected  $S_{2F}$  pulse area at the center of the detector to the z inefficiency corrected  $S_{2F}$  pulse area as a function

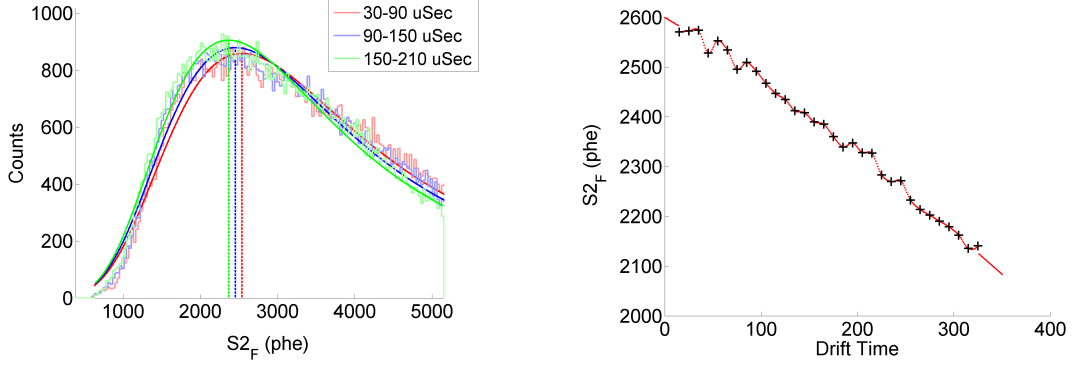


Figure 65: (Left) Landau distribution fits to the  $S2_F$  data that are used to determine the drift time dependence of the  $S2_F$  pulse area. For illustrative purposes, a drift time bin width of 60  $\mu$ seconds was chosen for this plot. (Right) The Z dependence of the  $S2_F$  pulse area after field effects are removed. Black points indicate the maximum of Landau distribution fits for each drift time bin, and red points indicate the interpolation and extrapolation of that data.

of XY in cm, as shown below

$$S2_{xy\text{-efficiency-correction}} = \frac{S2_{z\text{-efficiency-correction}} \times S2_F(x_c, y_c, z)}{S2_{z\text{-efficiency-correction}} \times S2_F(xyz)}. \quad (148)$$

where  $x_c$  and  $y_c$  are the x and y center of the detector in uncorrected coordinates determined by taking the average position of the  $\text{CH}_3\text{T}$  events in each direction.

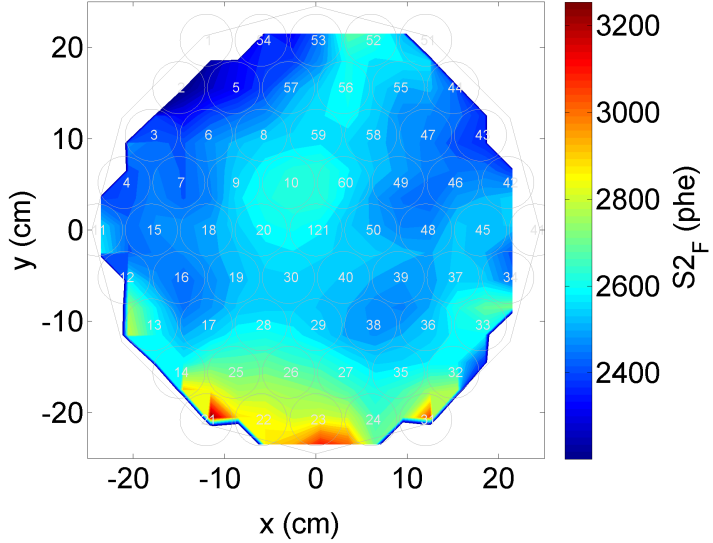


Figure 66: Two dimensional map of the XY dependence in  $\text{CH}_3\text{T}$   $S2_F$  data determine by fitting a Landau distribution to XY bins of the data and tracking the maximum of each fit.

Multiplying the raw  $S2$  signal by both the  $Z$  and the  $XY$  correction factors results in an inefficiency corrected  $S2_E$  signal (with field effects still present), and multiplying the field removed  $S2_F$  signal by the correction factors results in a inefficiency and field corrected  $S2_{EF}$  signal.

$$S2_E = S2 \times S2_{\text{xy-efficiency-correction}} \times S2_{\text{z-efficiency-correction}} \quad (149)$$

$$S2_{EF} = S2_F \times S2_{\text{xy-efficiency-correction}} \times S2_{\text{z-efficiency-correction}} \quad (150)$$

Unfortunately, we are unable to directly measure the detector inefficiency corrections for the  $S1$  signal from  $\text{CH}_3\text{T}$  data, since the maximum of the  $S1$  spectrum falls below the detector threshold and there are no discernible features to fit to. (Figure 67) Instead, we will continue working with the  $S2$  signal of our data and return to the issue of  $S1$  corrections in sections 7.2.6 and 7.2.9.

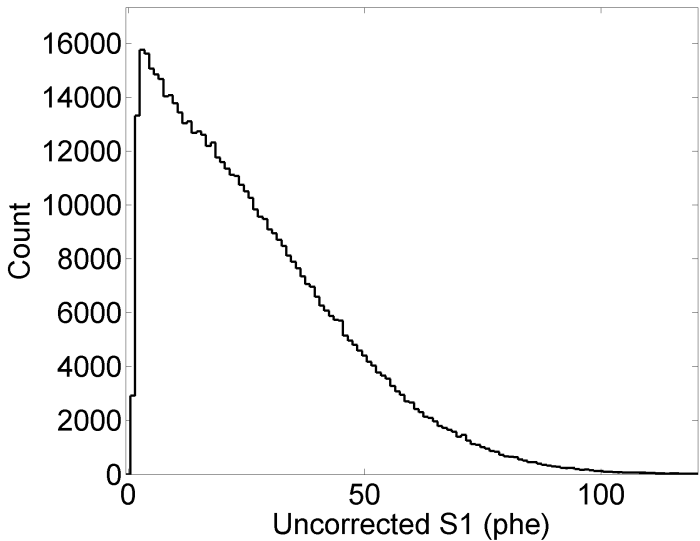


Figure 67: A histogram of uncorrected S1 data from the  $\text{CH}_3\text{T}$  calibration in September 2015. The maximum of the distribution falls below threshold and can not be used for detector inefficiency corrections.

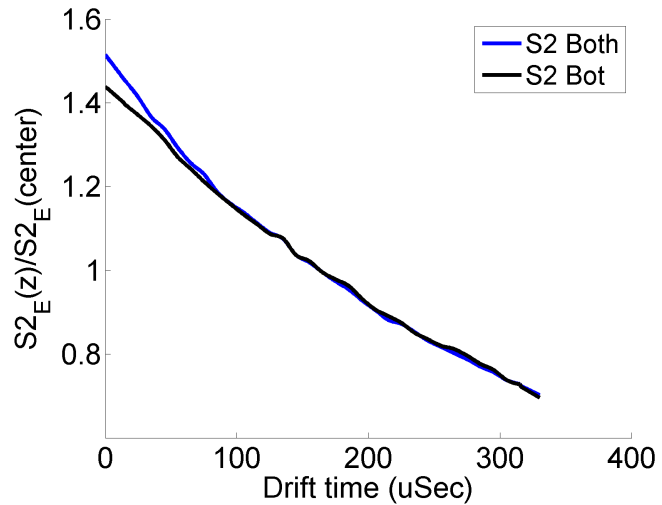
### 7.2.3 Measuring Field Effects in $^{83m}\text{Kr}$ Data

After measuring the S2 detector inefficiency corrections in  $\text{CH}_3\text{T}$  data we have all the tools we need to measure the field effects in the S2 pulse area of  $^{83m}\text{Kr}$  data. We begin by applying the S2 detector inefficiency corrections to the raw, uncorrected  $^{83m}\text{Kr}$  data (taken at the same time as the  $\text{CH}_3\text{T}$  data) by using equation 149. The removal of the detector inefficiency effects from the raw S2 data leave us with an  $\text{S2}_E$  signal which has spatial pulse area variation from field effects alone.

The process for measuring the field effects in the inefficiency corrected  $^{83m}\text{Kr}$   $\text{S2}_E$  data is similar to the process of measuring the detector inefficiency effects in the field effect corrected  $\text{CH}_3\text{T}$   $\text{S2}_F$  data. First, we measure the field induced Z dependence of the  $^{83m}\text{Kr}$   $\text{S2}_E$  pulse area by slicing the detector into drift time bins of 10  $\mu$ second width. A Gaussian distribution is fit to the  $\text{S2}_E$  spectrum of each bin

to determine the mean  $S2_E$  pulse area versus Z. (Figure 69) A cubic interpolation is used to determine the  $S2_E$  Z dependence between each drift time bin, and a linear extrapolation based on the first and last 20% of Gaussian fit data points is used to determine the  $S2_E$  Z dependence above and below the span of the drift time bins. We define the strength of the field effect in the z direction as the ratio of the  $S2_E$  pulse area as a function of Z to the  $S2_E$  pulse area at the center of the detector  $z_c$  (defined by taking the mean drift time value of all  $^{83m}\text{Kr}$  events above 4 microseconds drift time),  $S2_E(z)/S2_E(\text{center})$ . The strength of the field effect in September 2015 is consistent between a measurement with both PMT arrays and a measurement with the bottom-only PMT array. (Figure 68) A field effect correction for the Z direction is defined by taking the inverse of the strength of the field effect, as described in the equation

$$S2_{\text{z-field-correction}} = \frac{S2_E(z = z_c)}{S2_E(z)}. \quad (151)$$



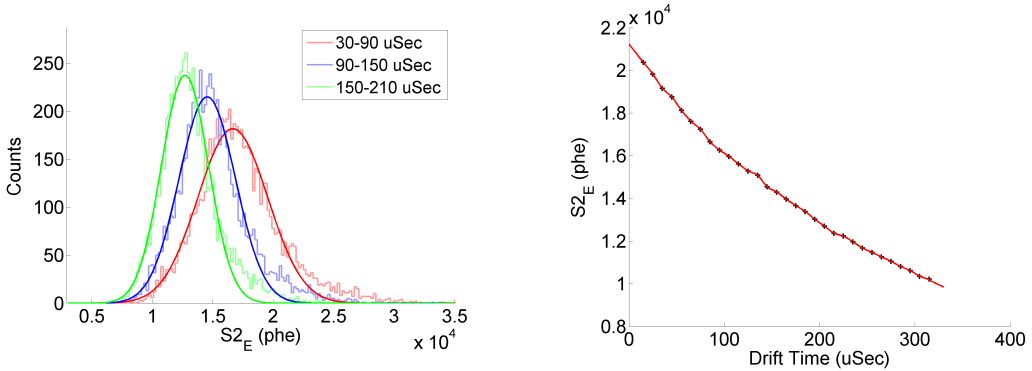


Figure 69: (Left) Gaussian distribution fits to the  $^{83m}\text{Kr}$   $S2_E$  data that are used to determine the drift time dependence of the  $S2_E$  pulse area. For illustrative purposes, a drift time bin width of 60  $\mu$ seconds was chosen for this plot. (Right) The Z dependence of the  $^{83m}\text{Kr}$   $S2_E$  pulse area after detector inefficiency effects are removed. Black points indicate the mean of Gaussian distribution fits for each drift time bin, and red points indicate the interpolation and extrapolation of that data.

Figure 68: The S2 field effect versus drift time relationship in September 2015. The relationship was measured using both PMT arrays, and the bottom-only PMT array, and found to agree with both methods.

The XY dependence of the detector inefficiency corrected  $^{83m}\text{Kr}$   $S2_E$  signal is found by dividing the z field corrected ( $S2_E \times S2_{z\text{-field-correction}}$ ) data into two dimensional XY bins with lengths of 2 cm on each side, and then fitting Gaussian distributions to the data of each bin. The mean of the Gaussian distribution from each bin is used to construct an  $S2_E$  XY dependence map, with a spline interpolation and extrapolation being used to determine the XY dependence between and outside of the bins. (Figure 70) A field effect correction for the XY direction is defined by taking the ratio of the z inefficiency corrected  $S2_E$  pulse area at the center of the detector to the z inefficiency corrected  $S2_E$  pulse area as a function

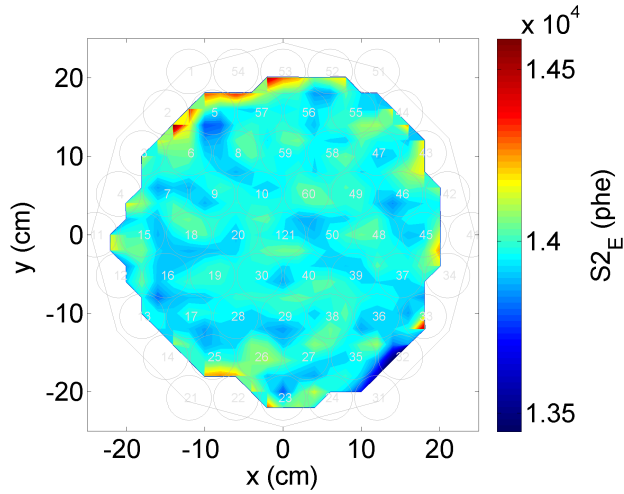


Figure 70: Two dimensional map of the XY dependence in  $^{83m}\text{Kr}$   $S2_E$  data determine by fitting a Gaussian distribution to XY bins of the data and tracking the mean of each fit.

of XY in cm, as shown below

$$S2_{\text{xy-field-correction}} = \frac{S2_{\text{z-field-correction}} \times S2_E(x_c, y_c, z)}{S2_{\text{z-field-correction}} \times S2_E(xyz)}. \quad (152)$$

where  $x_c$  and  $y_c$  are the x and y center of the detector in uncorrected coordinates determined by taking the average position of the  $^{83m}\text{Kr}$  events in each direction.

We also take a separate, three dimensional approach to mapping the field effect in the  $^{83m}\text{Kr}$   $S2_E$  data. In this approach the detector is divided into three dimensional voxels, with X and Y width of 3.5 cm and Z width of 30  $\mu$ seconds. As in the one dimensional (Z) plus two dimensional (XY) case, a three dimensional map of the field induced  $S2_E$  pulse area variation is produced by fitting a Gaussian distribution to the  $^{83m}\text{Kr}$   $S2_E$  data in each voxel. A spline interpolation is used to determine the  $S2_E(\text{xyz})/S2_E(\text{center})$  ratio between the three dimensional voxels, and the  $S2_E(\text{xyz})/S2_E(\text{center})$  Z dependence map is used to extrapolate outside

of the range of the voxels.

#### 7.2.4 Measuring the S1a and S1b Pulse Areas in $^{83m}\text{Kr}$ data

Now that we have measured the field effect in  $^{83m}\text{Kr}$  S2 data from the  $^{83m}\text{Kr}$  S2<sub>E</sub> data at one point in time, we need to develop a method to track the field effect in  $^{83m}\text{Kr}$  S2 data at all points time. To accomplish this we use the uncorrected S1 pules area from the 32.1 keV and 9.4 keV decays within  $^{83m}\text{Kr}$  events, referred to as S1a and S1b respectively. As discussed in section 7.1.2, as the electric field increases the amount of recombination decreases, leading to a smaller S1 signal. The S1a decay is more sensitive to this effect due to its higher energy, leading to a stronger field effect in the S1a data than in the S1b data. Therefore, an inverse relationship exists between the strength of the field and the S1a/S1b ratio.

A matlab module is used to measure the size and location of the S1a and S1b krypton decays. It selects  $^{83m}\text{Kr}$  event with an S2 pulse area pulse area between 2000 to 60000 phe as measured by the bottom PMT array. The module identifies S1 candidates that have pulse area above 10 phe (as measured by both PMT arrays), such that each  $^{83m}\text{Kr}$  event is defined to have exactly one candidate S2 and at least one candidate S1. After the event selection is complete, a region of interest (ROI) beginning at the first candidate S1 and ending at the start of the S2 (or after 150 samples) is defined. The ROI is then used to select sumpod (phd per sample) data from the evt files within the ROI. This data is then fit to a double exponential function which returns the pulse area and maximum fractional area of the S1a and S1b peaks, as well as the time separation between them. (Figure 71) The matlab module does not produce reasonable fit values for events in which the S1a and S1b decays are separated by less than 130 nanoseconds, so a cut requiring

the timing to be greater than this is used to clean up the output of the module.  
(Figure 72)

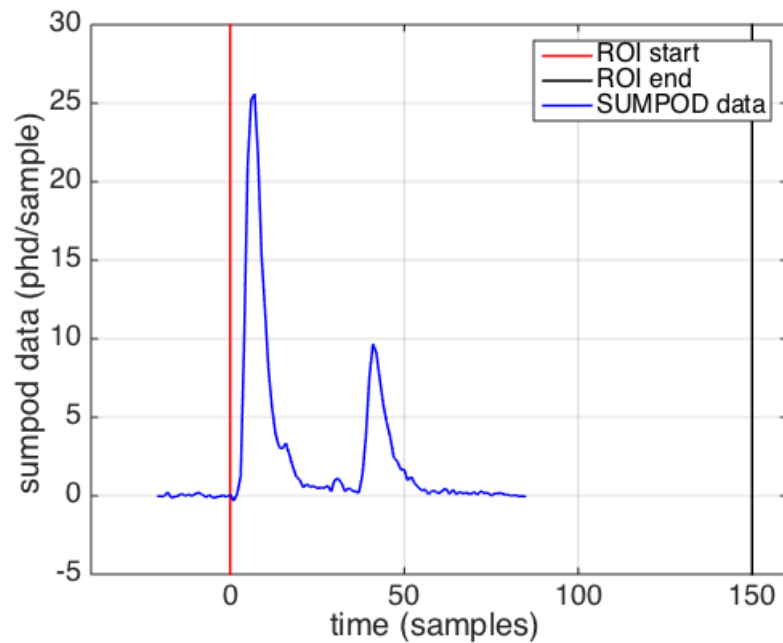


Figure 71: Sumpod versus time for a  $^{83m}\text{Kr}$  in which a distinct S1a and S1b peak have been observed. In this case, the fit finds an S1a area of 174 phe, an S1b area of 64.5 phe, and a separation in time of 35 samples.

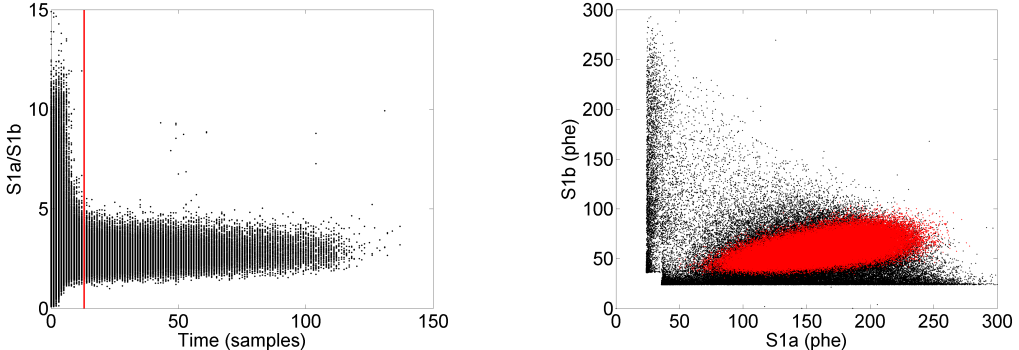


Figure 72: (Left) The output of the S1a/S1b fitting module as a function of time separation between the two decays. The red line indicate the minimum separation between the S1a and S1b events required by our cut in this analysis. (Right) A scatter plot of all S1a and S1b pulse areas measured by the fitting module (black) compared to the S1a and S1b pulse areas that are left after our selection cut. (red)

### 7.2.5 Relating the S1a/S1b Ratio to S2 Field Effects

To relate the S1a/S1b ratio to the S2 field effects measured in section 7.2.3 we begin by measuring the spatial dependence of the S1a/S1b ratio. We first divide the detector into drift time bins of 3  $\mu$ second width. A Gaussian distribution is fit to the S1a and S1b spectrum of each bin to determine the mean pulse areas versus Z. (Figure 73) A second order polynomial is fit to the ratio of the Gaussian means versus Z and is used to determine the S1a/S1b ratio at any drift time in the detector.

The XY dependence  $^{83m}\text{Kr}$  S1a/S1b signal is found in a similar manner. We first remove the z dependence of the S1a/S1b data by normalizing the polynomial fit found above to the detector center (defined by taking the mean drift time value of all  $^{83m}\text{Kr}$  events above 4  $\mu$ seconds drift time). We then divide the detector into two dimensional XY bins with lengths of 3 cm on each side and fit a Gaussian distribution to the S1a and S1b data of each bin. The mean of the Gaussian

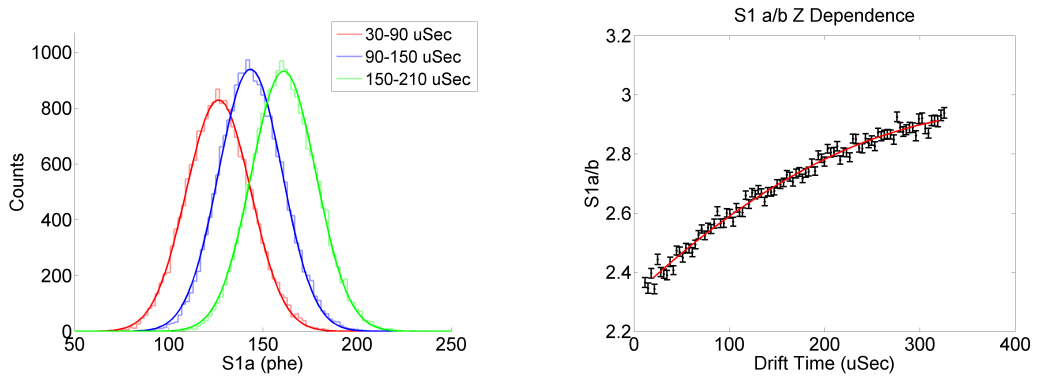


Figure 73: (Left) Gaussian distribution fits to the  $^{83m}\text{Kr}$  S1a data that are used to determine the drift time dependence of the S1a/S1b ratio. For illustrative purposes, a drift time bin width of 60  $\mu$ seconds was chosen for this plot. Similar fits are performed on the S1b pulse area data. (Right) The Z dependence of the  $^{83m}\text{Kr}$  S1a/S1b ratio. Black points indicate the S1a/S1b ratio as measured by the Gaussian distribution fits for each drift time bin, and the red line indicates the polynomial fit to this data.

distribution from each bin is used to construct an S1a/S1b XY dependence map, with a spline interpolation and extrapolation being used to determine the XY dependence between and outside of the bins. (Figure 74)

We also take a separate, three dimensional approach to mapping the  $^{83m}\text{Kr}$  S1a/S1b ratio throughout the detector. In this approach the detector is divided into three dimensional voxels, with X and Y width of 3.5 cm and Z width of 30  $\mu$ seconds. A three dimensional map of S1a/S1b is produced by fitting a Gaussian distribution to the S1a and S1b pulse area spectrum in each voxel. A spline interpolation and extrapolation is used to determine the S1a/S1b ratio between and outside of the three dimensional voxels.

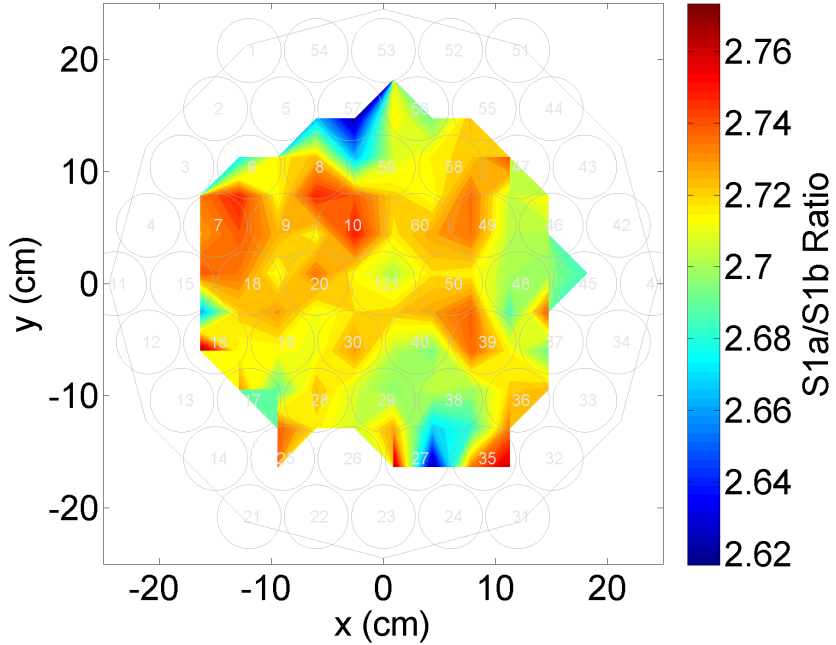


Figure 74: The XY dependence of the  $^{83m}\text{Kr}$  S1a/S1b ratio determined by fitting a Gaussian distribution to XY bins of the S1a and S1b data and tracking the mean of each fit. The map does not extend to  $r=25$  cm due to the squeezing effect of the nonuniform electric field.

Finally, we relate the Z dependence, XY dependence, and three dimensional dependence maps of the S1a/S1b ratio to the Z dependence, XY dependence, and three dimensional dependence maps of the S2 field effect measured in section 7.2.3. We choose to discard the XY dependence maps since no significant relationship is found between them. (Figure 75) This lack of correlation is attributed to the Z dependence of the electric field being much more dominant than the XY dependence of the electric field. A second order polynomial is fit to the spatial dependence of the  $^{83m}\text{Kr}$   $S2_E$  (induced by the field effect) to S1a/S1b relationship. This polynomial will be used in KrypCal to determine the strength of the field effect in  $^{83m}\text{Kr}$  S2 data at all points in time. We find that the Z dependence and three dimen-

sional maps agree closely within the range of measured S1a/S1b ratios, but begin to diverge in the extrapolated regions. (Figure 76) Because the electric field varies more in September 2015 than at earlier times in Run04, and because the time variation of the electric field has significantly slowed at times later than September 2015, we expect the measured range of S1a/S1b ratios in this work will cover the majority of S1a/S1b ratios that will ever be measured in Run04. Therefore, the discrepancy in the extrapolation of each map is not concerning.

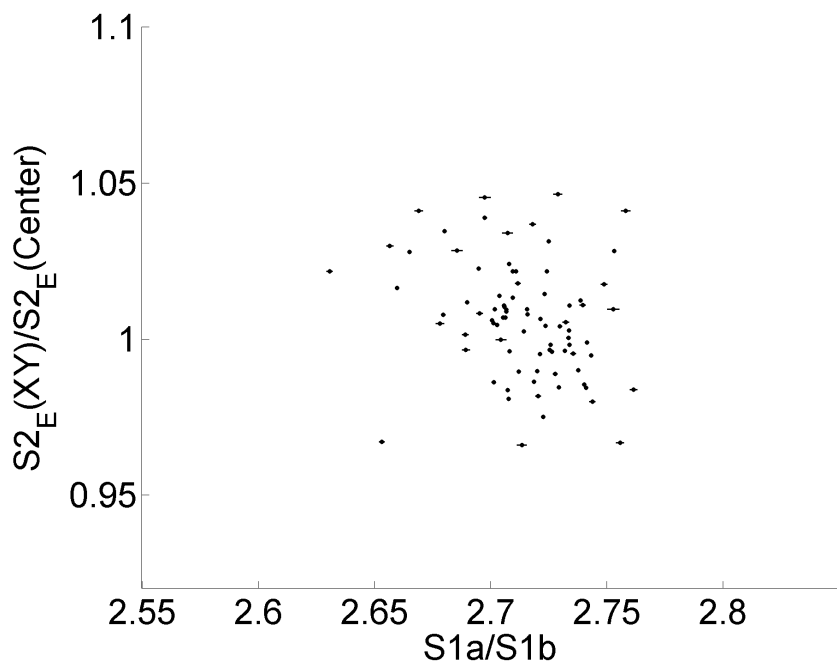


Figure 75: The XY relationship of the  $^{83m}\text{Kr}$  S1a/S1b ratio to the  $^{83m}\text{Kr}$   $S2_E$  field effect. No significant correlation is found in this data.

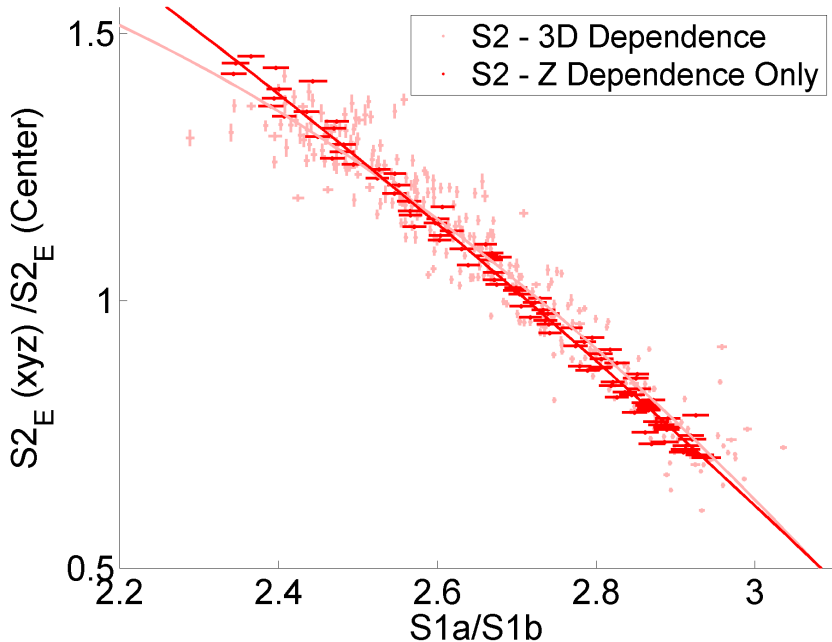


Figure 76: The Z (dark red) and three dimensional (light red) relationship of the  $^{83m}\text{Kr}$  S1a/S1b ratio to the  $^{83m}\text{Kr}$  S2<sub>E</sub> field effect.

### 7.2.6 Measuring the S1a/S1b Ratio to S1 Field Effect Relationship with Recombination Physics

We have successfully measured the strength of the field effect in  $^{83m}\text{Kr}$  S2 data at one point in time, and have related it to the  $^{83m}\text{Kr}$  S1a/S1b ratio such that we can determine the strength of the field effect at any point in time. We are now left with the challenge of measuring the strength of the field effect in  $^{83m}\text{Kr}$  S1 data. Our first approach will turn to the recombination physics that governs particle interaction during a recoil event.

The strength of the field effect (normalized to the detector center) in  $^{83m}\text{Kr}$  S2 data is given by the ratio of the inefficiency corrected S2<sub>E</sub> at a given position to the inefficiency corrected S2<sub>E</sub> at the center of the detector, which was measured

in 7.2.3. This ratio can be written in terms of the recombination during a  $^{83m}\text{Kr}$  event ( $R_{Kr}$ ) as follows

$$\frac{S2_{E,Kr}(xyz)}{S2_{E,Kr}(\text{center})} = \frac{1 - R_{Kr}(xyz)}{1 - R_{Kr}(\text{center})} \quad (153)$$

Note that this can be rewritten as an expression for the recombination during a  $^{83m}\text{Kr}$  as a function of position,

$$R_{Kr}(xyz) = 1 - \frac{S2_{E,Kr}(xyz)}{S2_{E,Kr}(\text{center})}(1 - R_{Kr}(\text{center})). \quad (154)$$

Next, we write the strength of the field effect in  $^{83m}\text{Kr}$  S1 data (normalized to the detector center) as the ratio of the inefficiency corrected  $S1_E$  signal at a given position to the inefficiency corrected  $S1_E$  signal at the center of the detector, which we are unable to measure directly. In terms of the exciton to ion ratio ( $\alpha$ ) and the recombination during a  $^{83m}\text{Kr}$  event ( $R_{Kr}$ ) this is given by

$$\frac{S1_{E,Kr}(xyz)}{S1_{E,Kr}(\text{center})} = \frac{\alpha + R_{Kr}(xyz)}{\alpha + R_{Kr}(\text{center})} = \frac{\alpha + 1 - \frac{S2_{E,Kr}(xyz)}{S2_{E,Kr}(\text{center})}(1 - R_{Kr}(\text{center}))}{\alpha + R_{Kr}(\text{center})} \quad (155)$$

where we have used equation 154 in the last step. Therefore, all we need to measure the strength of the field effect on  $^{83m}\text{Kr}$  S1 data is the recombination during a  $^{83m}\text{Kr}$  event at the center of the detector, given by  $R_{Kr}(\text{center})$ . As mentioned in section 7.2.1, NEST does not simulate the physics of  $^{83m}\text{Kr}$  events well, but it has been tuned to simulate the physics of  $\text{CH}_3\text{T}$  events. As such, we once again turn to the  $\text{CH}_3\text{T}$  data to determine the value of  $R_{Kr}(\text{center})$ . First, we write the ratio of the efficiency corrected  $^{83m}\text{Kr}$   $S2_E$  pulse area at the center

of the detector to the efficiency corrected  $\text{CH}_3\text{T}$   $S2_E$  pulse are at the center of the detector in terms of the S2 gain factor ( $g_2$ ), recombination during a  $^{83m}\text{Kr}$  event ( $R_{Kr}$ ), recombination during a  $\text{CH}_3\text{T}$  event ( $R_{H3}$ ), number of ions produced during a  $^{83m}\text{Kr}$  event ( $N_{ion-Kr}$ ), and number of ions produced during a  $\text{CH}_3\text{T}$  event ( $N_{ion-H3}$ ), given by

$$\frac{S2_{E,Kr}(\text{center})}{S2_{E,H3}(\text{center})} = \frac{g_2(1 - R_{Kr}(\text{center}))N_{ion-Kr}}{g_2(1 - R_{H3}(\text{center}))N_{ion-H3}}. \quad (156)$$

This can be rewritten as an expression for the recombination of  $^{83m}\text{Kr}$  at the center of the detector given by

$$R_{Kr}(\text{center}) = 1 - \frac{S2_{E,Kr}(\text{center})}{S2_{E,H3}(\text{center})} \frac{N_{ion-H3}}{N_{ion_{Kr}}} (1 - R_{H3}(\text{center})) \quad (157)$$

where the gain factor  $g_2$  does not depend on energy, and therefore can be removed from the equation. The number of ions for both  $^{83m}\text{Kr}$  events and  $\text{CH}_3\text{T}$  events is given by equations 140 and 141, with the assumption  $E = 41.55$  keV for  $^{83m}\text{Kr}$  and  $E = 2.5$  keV for  $\text{CH}_3\text{T}$ , and the recombination at the center of the detector of  $\text{CH}_3\text{T}$  events ( $R_{H3}$ ) can be determined from NEST.

Using equations 155 and 157 we can convert the field effect measured in the  $^{83m}\text{Kr}$   $S2_E$  data to an inferred field effect in  $^{83m}\text{Kr}$  S1 data. The result of this is shown in Figure 77. A  $\chi^2$  fit to the expected  $\text{CH}_3\text{T}$  and  $^{83m}\text{Kr}$  energy spectra returns an average reduced  $\chi^2$  of 1.31, with a reduced  $\chi^2$  of  $248/124=2.00$  for  $\text{CH}_3\text{T}$  alone (Figure 78), and a reduced  $\chi^2$  of  $16.2/26=0.622$  for  $^{83m}\text{Kr}$  alone using the best fit parameters of  $g1 = 0.1$  and  $EE = 0.89$ . (Figure 79) It is likely that the complicated nature of the  $^{83m}\text{Kr}$  decay (detailed in Appendix ??) introduces

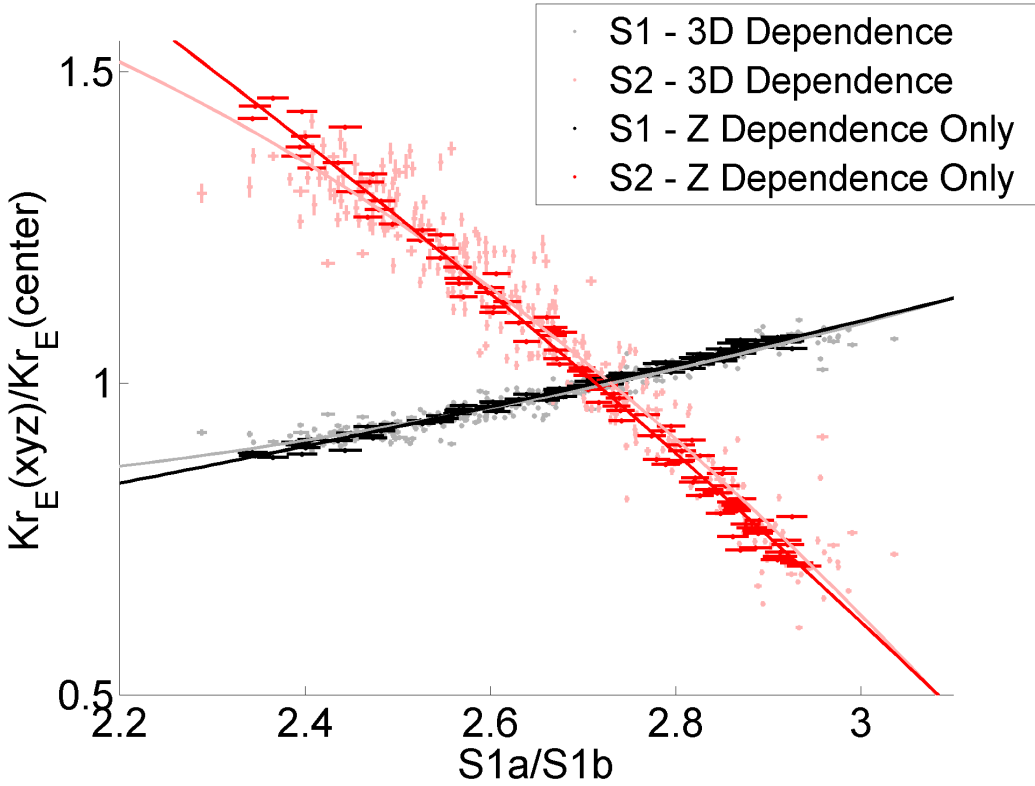


Figure 77: The Z (black) and three dimensional (grey) relationship of the  $^{83m}\text{Kr}$  S1a/S1b ratio to the  $^{83m}\text{Kr}$  S1 field effect. The black and grey data points are not measured, but instead inferred from the Z (dark red) and three dimensional (light red) relationship of the  $^{83m}\text{Kr}$  S1a/S1b ratio to the  $^{83m}\text{Kr}$  S2<sub>E</sub> field effect.

intricacies which are not account for in equations 155 and 157. In the next section we will seek to improve this result with a direct measurement of the S1a/S1b to S1 field effect relationship before turning to a  $\chi^2$  minimization method in section 7.2.9 to determine the optimal field effect to S1a/S1b relationships.

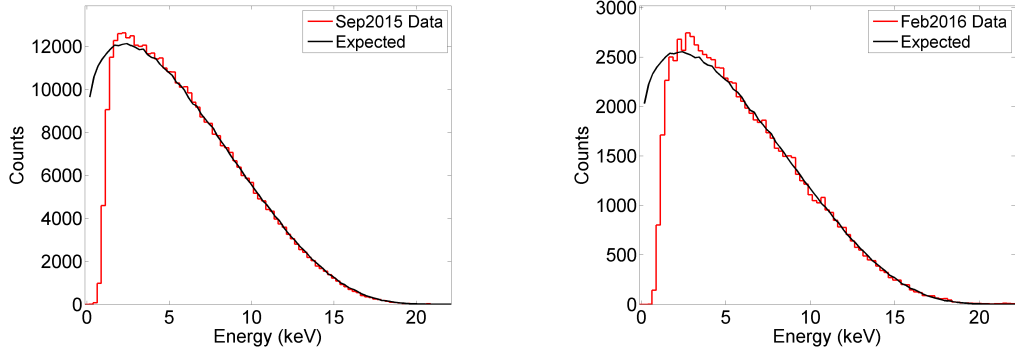


Figure 78: The energy spectrum of the efficiency corrected CH<sub>3</sub>T data (red) after utilizing the S1 field effect measurements from this section in September 2015 (left) and February 2016 (right). The expected energy spectrum is shown in black.

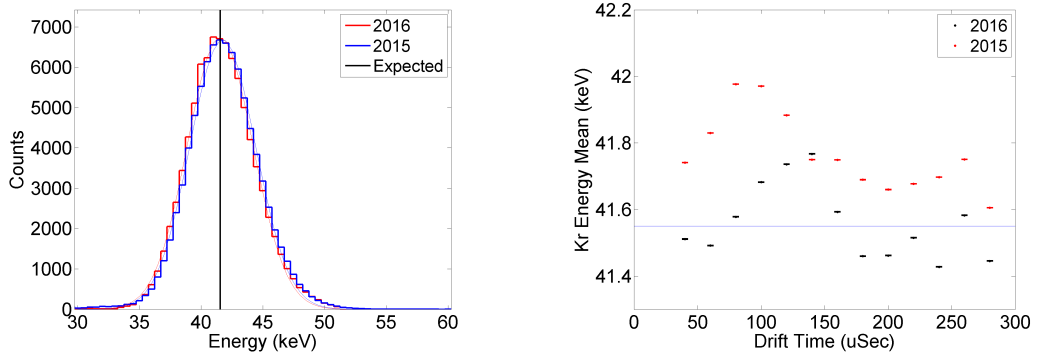


Figure 79: (Left) The energy spectrum of efficiency corrected <sup>83m</sup>Kr data in September 2015 (red) and February 2016 (blue) after utilizing the S1 field effect measurements from this section in KrypCal. (Right) The Z dependence of the <sup>83m</sup>Kr energy peaks in September 2015 (red) and February 2016 (black) and the expected energy (blue).

### 7.2.7 Measuring the S1a/S1b Ratio to S1 Field Effect Relationship with the S1a Signal

The relative light yield of the <sup>83m</sup>Kr 32.1 keV decay, <sup>83m</sup>Kr 9.4 keV decay, and <sup>57</sup>Co 122 keV decay has been measured as a function of the light yield at an applied

electric field divided by the light yield at zero electric field by Manalaysay, et al. in reference [48]. (Figure 80) We can combine NEST predictions for the light yield of the 122 keV  $^{57}\text{Co}$  line with the ratio of the light yield of the 32.1 keV  $^{83m}\text{Kr}$  line to the 122 keV  $^{57}\text{Co}$  line from reference [48] to convert the relative light yield measurements to absolute light yield measurements. This results in an empirical formula for the absolute light yield of the  $^{83m}\text{Kr}$  32.1 keV decay as a function of electric field given by

$$\frac{\gamma}{E} = 55.2[1 - 0.0004895 \times F \times \ln(1 + 1/(8.9e-4 \times F))] \quad (158)$$

where  $\gamma$  is the number of photons,  $E$  is the energy of the decay, and  $F$  is the applied electric field in units of V/cm.

Using equation 158 we can directly measure the strength of the field effect in the  $^{83m}\text{Kr}$  S1 data and relate it to the S1a/S1b ratio. We begin by using the electric field to S1a/S1b relationships shown in Figure 95, as well as the electric field measured by Lucie's field maps to estimate the electric field in the detector in September 2015. The average of the three electric field maps is taken as the measurement of the electric field, and the difference in each of the three electric field maps is taken as a systematic error. The electric field map is converted to a map of the expected light yield at 32.1 keV using equation 158, assuming no detector inefficiency effects are present. The three dimensional spatial dependence of the light yield provides a direct measurement of the strength of the field effect in the S1a data, given by  $\gamma(xyz)/\gamma(\text{center})$ . Note that the strength of the field effect in the S1a data can help us derive the strength of the field effect in the combined S1 data, but the two are not equivalent. Normalizing the field effect in the S1a

data to the center of the detector, as shown in equation 159, produces  $S1a_F$  data which has spatial variation due to detector inefficiency effects only.

$$S1a_F = S1a \frac{\gamma(\text{center})}{\gamma(xyz)} \quad (159)$$

We measure the detector inefficiency effects in the  $S1a_F$  data by dividing the detector into three dimensional voxels with X and Y width of 7 cm and Z width of 47  $\mu$ Sec. A Gaussian distribution is fit to the  $S1a_F$  spectrum in each voxel, and the Gaussian mean is used to determine the spatial dependence of the  $S1a_F$  data due to detector inefficiency effects alone. Since the detector inefficiency effects are not dependent on the energy of an event, the spatial variation measured in the  $S1a_F$  data is equivalent to the spatial variation in the combined  $S1$  data due to detector inefficiency effects alone. Therefore, we can use the spatial variation measured in the  $S1a_F$  data to produce detector inefficiency corrected combined  $S1_E$  data as shown in the equation

$$S1_E = S1 \frac{S1a_F(\text{center})}{S1a_F(xyz)}. \quad (160)$$

Any residual spatial variation in the detector inefficiency corrected combined  $S1_E$  data is due to field effects in the combined  $^{83m}\text{Kr}$   $S1$  data alone. We measure the strength of these field effects by again dividing the detector into three dimensional voxels with X and Y width of 7 cm and Z width of 47  $\mu$ Sec. A Gaussian distribution is fit to the  $S1_E$  spectrum in each voxel, and the Gaussian mean is used to determine the spatial dependence of the  $S1a_E$  data due to field effects alone. At the same time, we use separate Gaussian distribution fits to the  $S1a$  and  $S1b$  data in each voxel to measure the spatial dependence of the  $S1a/S1b$  ratio. Finally, we relate the  $S1a_E$  Gaussian mean to the  $S1a/S1b$  ratio of each voxel and fit a second order

polynomial which describes the strength of the field effect in the  $^{83m}\text{Kr}$  combined S1 signal to the data. (Figure 81)

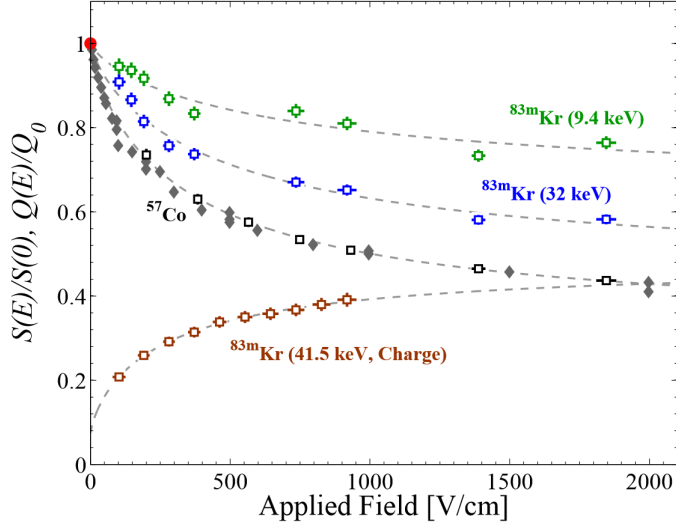


Figure 80: Relative light yield of the  $^{83m}\text{Kr}$  and  $^{57}\text{Co}$  decays defined as the light yield at an applied field divided by the light yield at zero field. Historical data for the  $^{57}\text{Co}$  relative light yield is shown by the grey diamond points. Dashed lines correspond to fit parameters to the data.

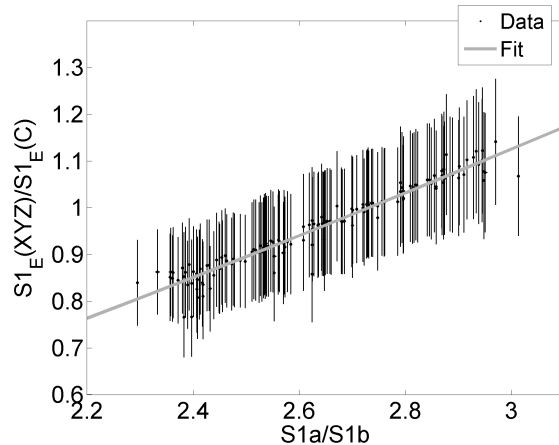


Figure 81: The strength of the S1 field effect measured in this section (grey) compared to the strength of the S1 field effect measured in section 7.2.9 (blue). The large error bars on the data are due to systematic uncertainties in the field maps detector inefficiency corrections.

We can use the direct measurement of the S1a/S1b ratio to S1 field effect relationship measured in this section with the direct measurement of the S1a/S1b ratio to S2 field effect relationship measured in section 7.2.5 to remove the field effects in  $^{83m}Kr$  data and produce detector inefficiency corrections via the methods in section 7.3. The result of this is shown in Figure 82 and Figure 83. A  $\chi^2$  fit to the expected CH<sub>3</sub>T and  $^{83m}Kr$  energy spectra returns an average reduced  $\chi^2$  of 2.22, with a reduced  $\chi^2$  of 1196/124=1.58 for CH<sub>3</sub>T alone, and a reduced  $\chi^2$  of 74.2/26=2.85 for  $^{83m}Kr$  alone using the best fit parameters of  $g1 = 0.100$  and  $EE = 0.76$ . The large systematic errors in the S1a/S1b ratio to field effect relationships, introduced by uncertainties in the field maps and systematic errors in the detector inefficiency corrections, lead to poorly optimized energy spectra when the two direct measurement results are combined. Therefore, we turn to a  $\chi^2$  minimization method in section 7.2.9 to determine the optimal S1 field effect to S1a/S1b relationship and S2 field effect to S1a/S1b relationship.

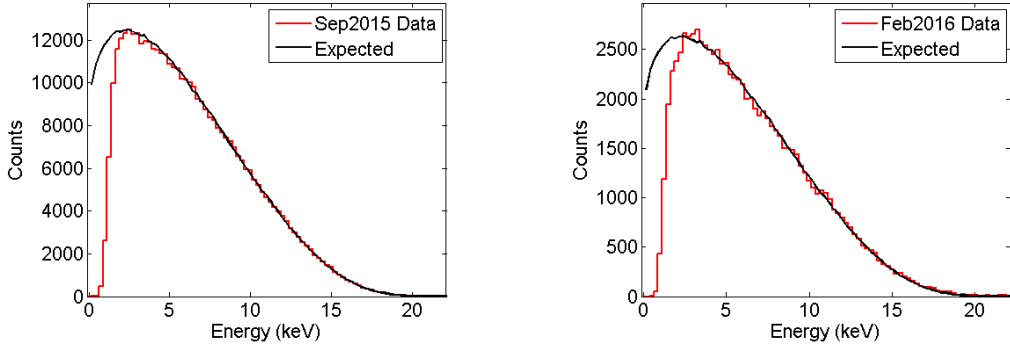


Figure 82: The energy spectrum of the efficiency corrected CH<sub>3</sub>T data (red) after utilizing the S1 field effect measurements from this section and the S2 field effect measurements from section 7.2.5 in September 2015 (left) and February 2016 (right). The expected energy spectrum is shown in black.

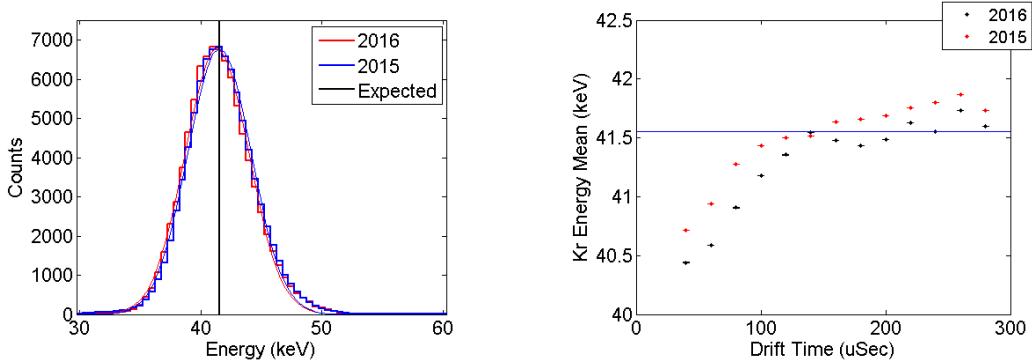


Figure 83: (Left) The energy spectrum of efficiency corrected <sup>83m</sup>Kr data in February 2016 (red) and September 2015 (blue) after utilizing the S1 field effect measurements from this section and the S2 field effect measurements from section 7.2.5 in KrypCal. (Right) The Z dependence of the <sup>83m</sup>Kr energy peaks in September 2015 (red) and February 2016 (black).

### 7.2.8 Expectation for G1

The process described in section 7.2.7 also yields an expectation for the value of  $g_1$  in Run04. First, we measure the mean of the S1a distribution at the center.

This is equivalent to measuring the inefficiency corrected S1a<sub>E</sub> data given by

$$S1a_E = S1a \frac{S1a_F(\text{center})}{S1a_F(xyz)} \quad (161)$$

since we normalize the detector inefficiency effects to the center of the detector. Combining this measurement with equation 158, which predicts the number of photons produced by a 32.1 keV decay at the center of the detector, provides a prediction for the gain factor  $g_1$  given by

$$g_1 = \frac{S1a(\text{center})}{\gamma(\text{center})}. \quad (162)$$

The result of this prediction is  $g_1 = 0.108 \pm 0.010$ , where systematic errors from the field map measurement and the parameters in equation 158 have been included in the result. Note that this prediction is only one sigma below the optimal value of  $g_1$  found in the following section.

### 7.2.9 Measuring the S1a/S1b Ratio to S1 Field Effect Relationship with $\chi^2$ Fitting Methods

Although field induced variation in the recombination of a  $^{83m}\text{Kr}$  event can introduce a spatial and time dependence in the  $^{83m}\text{Kr}$  S1 and S2 signals, the total energy signal given (with gain factors  $g_1$  and  $g_2$ ) by

$$E = \left( \frac{1}{73} \right) \left( \frac{S1_E}{g_1} + \frac{S2_E}{g_2} \right) \quad (163)$$

should be insensitive to field variations. We can take advantage of this fact to determine the optimal S1a/S1b to S1 field effect relationship corresponding to the

directly measured S1a/S1b to S2 field effect relationship measured in section 7.2.5. Unfortunately, we do not have knowledge of the strength of the field effect in the  $^{83m}\text{Kr}$  S1 signal, so we can not remove the field effect from the data to produce the efficiency-only corrected  $S1_E$  signal. Likewise, without efficiency corrected data we can not measure the gain factors  $g_1$  and  $g_2$  to produce a combined energy spectrum. The only tools that we have at our disposal are a measurement of the strength of the field effect in the  $^{83m}\text{Kr}$  S2 signal and its relationship to S1a/S1b, as well as the ability to produce efficiency only corrected  $^{83m}\text{Kr}$   $S2_E$  data based on to the spatial variation of field effect corrected  $^{83m}\text{Kr}$   $S2_F$  data. In this section we turn to a  $\chi^2$  minimization approach which will float the S1 field effect to S1a/S1b relationship, produce inefficiency corrections based on the field removed  $S1_F$  and  $S2_F$  signals, and then float the gain factors  $g_1$  and  $g_2$  to produce an optimized combined energy spectrum.

We begin by eliminating one of the three parameters associated with the second order polynomial which describes the S1 field effect to S1a/S1b relationship. We choose to normalize the spatial variation induced by the nonuniform electric field to the center of the detector, so the strength of the field effect as measured by  $\frac{S1_{E,Kr}(xyz)}{S1_{E,Kr}(\text{center})}$  must equal one at the center of the detector. Therefore, we can relate one of the coefficients ( $a, b$ , and  $c$ ) in the second order polynomial

$$\frac{S1_{E,Kr}(xyz)}{S1_{E,Kr}(\text{center})} = a \left( \frac{S1a}{S1b} \right)^2 + b \left( \frac{S1a}{S1b} \right) + c \quad (164)$$

to the other two, such that

$$c = 1 - a \left( \frac{S1a_c}{S1b_c} \right)^2 - b \left( \frac{S1a_c}{S1b_c} \right) \quad (165)$$

where  $S1a_c$  and  $S1b_c$  represent the values of  $S1a$  and  $S1b$  at the center of the detector. Next, we scan over a range of  $a$  and  $b$  values and produce the  $\frac{S1_{E,Kr}(xyz)}{S1_{E,Kr}(center)}$  to  $\frac{S1a}{S1b}$  relationship for each pair of  $a$  and  $b$  values. We follow the procedure described in section 7.3 and use the S1 field effect to S1a/S1b relationship from each pair of  $a$  and  $b$  values, in conjunction with the S2 field effect S1a/S1b relationship measured in 7.2.3, to produce efficiency-only corrections for CH<sub>3</sub>T data and <sup>83m</sup>Kr data from September 2015 and February 2016. These corrections are used to produce S2<sub>E</sub> and S1<sub>E</sub> data for all four data sets. We then scan over a range of  $g_1$  and extraction efficiency (EE) values and use the S2<sub>E</sub> and S1<sub>E</sub> data to produce a combined energy spectrum (for each source) for each combination of  $a,b,g_1$ , and EE based on equation 163. Note that  $g_2 = SE \times EE$ , where  $SE$  is the single electron size at the time of each data set.

To evaluate the performance of each  $a,b,g_1$ , and  $EE$  combination we must develop models for the expected energy spectra of CH<sub>3</sub>T and <sup>83m</sup>Kr data in September 2015 and February 2016. The <sup>83m</sup>Kr events consist of a monoenergetic 32.1 keV decay and a monoenergetic 9.4 keV decay. The expected energy spectrum is a Gaussian distribution centered around the sum of these two monoenergetic decays at 41.55 keV. The width of the Gaussian distribution depends on a number of factors, including the detector's efficiency for collecting S1 and S2 light, as well as the spatial dependence of the recombination of <sup>83m</sup>Kr events induced by the nonuniform electric field. While we can measure most of these parameters, we would have to feed them into NEST to determine the final width of the Gaussian distribution. Since NEST does not simulate <sup>83m</sup>Kr events well, we can only use the mean of the Gaussian distribution as a figure of merit for the <sup>83m</sup>Kr energy spectrum.

Tritium is a beta decay with an energy spectrum that has a broad peak at 2.5 keV and a smoothly falling distribution out to 18 keV. As with  $^{83m}\text{Kr}$ , this spectrum is smeared based on a number of parameters. Unlike  $^{83m}\text{Kr}$ , the smearing in  $\text{CH}_3\text{T}$  data can be accurately determined by NEST so we can compare the energy spectrum from data to simulations on a bin by bin basis.

For each  $a,b,g_1$ , and  $EE$  combination a reduced  $\chi^2$  for the  $\text{CH}_3\text{T}$  and  $^{83m}\text{Kr}$  data is measured using the difference between the expected energy spectra and measured energy spectra. During the  $^{83m}\text{Kr}$   $\chi^2$  calculation, the energy spectrum is from each point in time is divided into drift time bins so that the spatial dependence of the energy spectrum is included in the  $\chi^2$  measurement. The  $^{83m}\text{Kr}$  data has very high statistics, and only the mean of a Gaussian fit to the data is of interest, so the variance used in the  $\chi^2$  measurement is dominated by systematic error. We use the standard deviation of the  $^{83m}\text{Kr}$  energy spectrum over the duration of Run03 to evaluate the size of this systematic error, and find  $\sigma = 0.2395$ . During the  $\text{CH}_3\text{T}$   $\chi^2$  calculation, the energy spectrum is divided into energy bins so that the entire beta spectrum (above 3.5 keV to avoid the detector threshold) is included in the  $\chi^2$  measurement. The variance of the  $\text{CH}_3\text{T}$  data is based on statistics alone, due to finer binning and lower statistics of the data. We choose to define a total reduced  $\chi^2$  (to be minimized in the  $\chi^2$  fit) as the average of the reduced  $\chi^2$  for the  $^{83m}\text{Kr}$  and  $\text{CH}_3\text{T}$  data, so that each source carries the same amount of weight in the fit. A minimum average reduced  $\chi^2$  of 0.8413 is found for the  $a = 0.065, b = 0.02, g_1 = 0.0980$ , and  $EE = 0.0808$  combination. The corresponding reduced  $\chi^2$  of the  $^{83m}\text{Kr}$  and  $\text{CH}_3\text{T}$  energy spectra separately are  $12.17/26=0.4682$  ( $p=0.99$ ) and  $150.6/124=1.2143$  ( $p=0.05$ ), respectively. Note that (as we will see in section 7.4) the extraction efficiency needed to produce these results is consistent with our

expectations, and the results produce  $^{83m}\text{Kr}$  energy peaks (unbinned in drift time) that are within one sigma of the expected 41.55 keV in both September 2015 and February 2016.

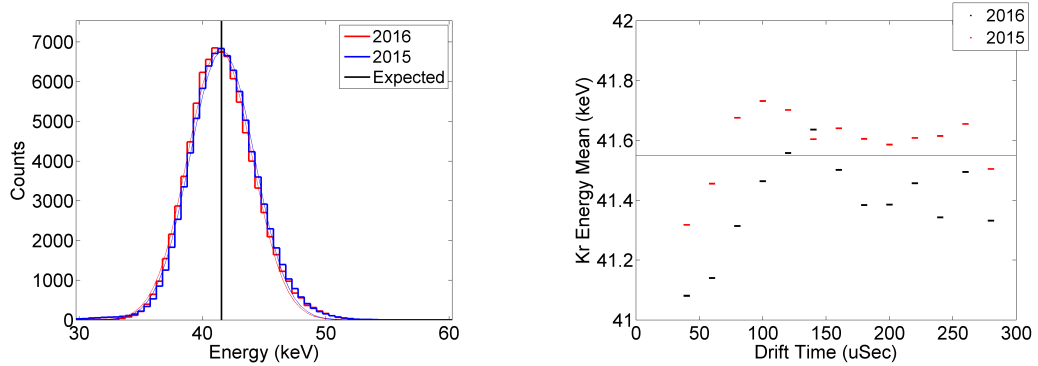


Figure 84: (Left) The energy spectrum of  $^{83m}\text{Kr}$  data in February 2016 (red) and September 2015(blue) after determining the S1 field effect to S1a/S1b relationship from the version 2.22 reduced  $\chi^2$  method. The energy spectrum is expected to be a Gaussian distribution centered around the black line. (Right) The Z dependence of the  $^{83m}\text{Kr}$  energy peaks in September 2015 (red) and February 2016 (black).

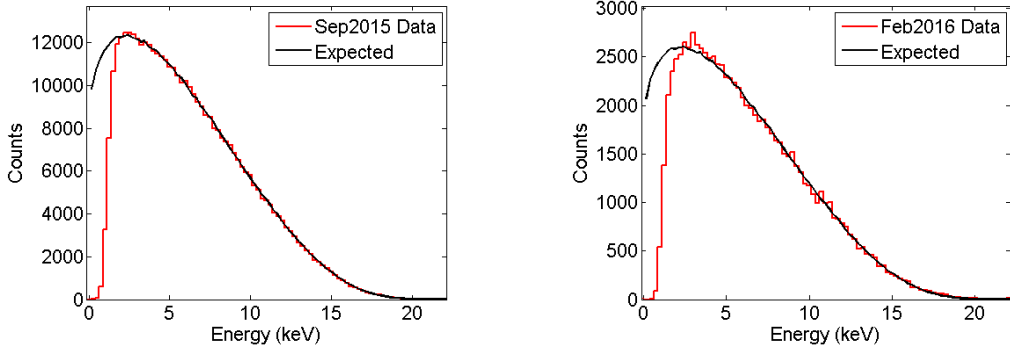


Figure 85: (Left) The energy spectrum of CH<sub>3</sub>T data in September 2015 (left) and February 2016 (right) after determining the S1 field effect to S1a/S1b relationship from the reduced  $\chi^2$  method. The expected CH<sub>3</sub>T energy spectrum for each data set is shown in black.

### 7.2.10 Summary of S1a/S1b Ratio to Field Effect Measurements

We have directly measured the strength of the field effect in <sup>83m</sup>Kr S2 data by removing detector inefficiency effects from the data with the help of CH<sub>3</sub>T data. We have also directly measured the strength of the field effect in <sup>83m</sup>Kr S1 data using the expected light yield of the <sup>83m</sup>Kr S1 data 32.1 keV decay. Combining these two direct measurement techniques does not produce satisfactory energy spectra. Instead, we turn to  $\chi^2$  optimization methods to find the optimal S1 field effect to S1a/S1b relationship to pair with the direct S2 field effect measurement, as well as the optimal S2 field effect to S1a/S1b relationship to pair with the direct S1 field effect measurement. We find that the optimal S1 field effect found by a  $\chi^2$  optimization for the directly measured S2 field effect agrees very closely with our expectations from recombination physics. This promising result is bolstered by the improvements in the corrected data discussed in section 7.4. We choose to use the S2 field relationship measured in section 7.2.5 and the corresponding optimal

S1 field effect relationship measured in section 7.2.9 for our KrypCal work.

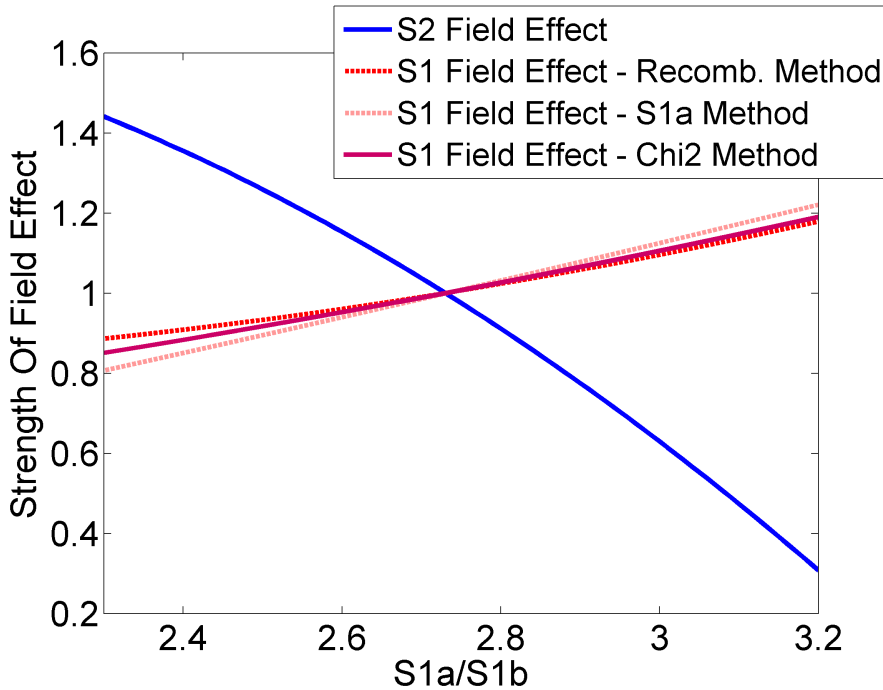


Figure 86: The S1a/S1b to field effect relationships measured in this work. The method to measure each line is indicated by the color in the legend. Red shades indicate measurements of the strength of the field effect in  $^{83m}\text{Kr}$  S1 data, and blue shades indicate the strength of the field effect in  $^{83m}\text{Kr}$  S2 data. Solid lines represent measurements that are used in KrypCal, and dashed lines represent measurements that are supplementary cross checks.

### 7.3 Producing Detector Inefficiency Corrections in KrypCal

Now that we have related the strength of the field effect in both  $^{83m}\text{Kr}$  S2 and  $^{83m}\text{Kr}$  S1 data to the S1a/S1b ratio we can make use of these relationships to produce detector inefficiency-only corrections during every  $^{83m}\text{Kr}$  calibration. This process is very similar to (and in some ways, the reverse of) the process to measure the field effect in  $^{83m}\text{Kr}$  S2 data. Nevertheless, we will describe the process here for completeness and clarity.

### 7.3.1 Mapping S1a/S1b

For a  $^{83m}\text{Kr}$  calibration at any point in time, we begin by measuring the Z and XY dependence of the S1a/S1b ratio using the methods of section 7.2.4 and 7.2.5. We first divide the detector into drift times bins with a width chosen such that each bin has roughly 300 events. A Gaussian distribution is fit to the S1a and S1b spectrum of each bin to determine the mean pulse areas versus Z. A second order polynomial is fit to the ratio of the Gaussian means versus Z and is used to determine the S1a/S1b at any drift time in the detector. The XY dependence of the S1a/S1b signal is found in a similar manner. We first remove the Z dependence of the S1a/S1b data by normalizing the polynomial fit found above to the detector center (defined by taking the mean drift time value of all  $^{83m}\text{Kr}$  events above 4  $\mu\text{seconds}$  drift time). We then divide the detector into square, two dimensional XY bins with lengths defined such that each bin has roughly 300 events, and fit a Gaussian distribution to the S1a and S1b data of each bin. The mean of the Gaussian distribution from each bin is used to construct an S1a/S1b XY dependence map, with a spline interpolation and extrapolation being used to determine the XY dependence between and outside of the bins. If the  $^{83m}\text{Kr}$  data set has enough statistics (more than 100,000 S1a/S1b events after cuts) a three dimensional S1a/S1b map is also constructed. The detector is divided into three dimensional voxels with dimensions chosen such that each voxel has roughly 200 events. A three dimensional map of S1a/S1b ratio is produced by fitting a Gaussian distribution to the S1a and S1b pulse area spectrum in each voxel. A spline interpolation is used to determine the S1a/S1b ratio between the three dimensional voxels, and the S1a/S1b Z dependence map is used to extrapolate outside of the

range of the voxels.

### 7.3.2 Removing the field effect from $^{83m}\text{Kr}$ Data

We use the  $^{83m}\text{Kr}$  S2 field effect to S1a/S1b relationship and S1 field effect to S1a/S1b relationship measured in sections 7.2.3 and 7.2.9 to convert the Z, XY, and three dimensional maps of S1a/S1b into field effect maps for both S1 and S2 data. The strength of the field effect is measured by  $\frac{S1_E(xyz)}{S1_E(\text{center})}$  and  $\frac{S2_E(xyz)}{S2_E(\text{center})}$ , so that dividing by the strength of the field effect normalizes the raw  $^{83m}\text{Kr}$  S1 and S2 signals to the center of the detector and produces the field effect-only corrected  $S1_F$  and  $S2_F$  signals, as shown in equations 166 and 167. (Figure 92)

$$S1_F = S1 \times \frac{S1_E(\text{center})}{S1_E(xyz)} \quad (166)$$

$$S2_F = S2 \times \frac{S2_E(\text{center})}{S2_E(xyz)} \quad (167)$$

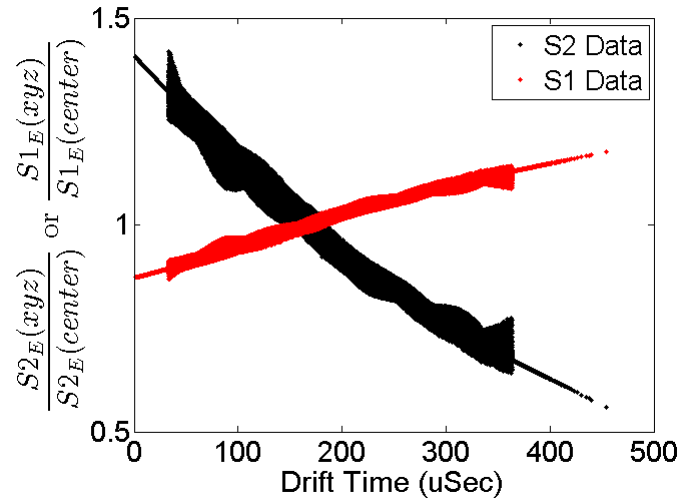


Figure 87: The three dimensional field effect in  $^{83m}\text{Kr}$  S2 (black) and S1(red) data versus drift time. The wide regions are areas in which the three dimensional S1a/S1b maps are interpolated with a spline function, and the narrow regions are areas in which the three dimensional S1a/S1b maps are extrapolated based on the S1a/S1b Z dependence map.

### 7.3.3 Measuring Detector Inefficiencies

After removing the field effects from the  $^{83m}\text{Kr}$  data we are ready to measure the residual spatial pulse area variation due to detector inefficiencies alone. We first measure the Z dependence of the  $S_{2F}$  and  $S_{1F}$  pulse areas by slicing the detector into drift time bins with widths defined such that each bin has roughly 300 events. A Gaussian distribution is fit to the  $S_{2F}$  and  $S_{1F}$  spectra of each bin to determine the location of the spectra maximums. (Figure 88 and Figure 89) In the case of the  $S_{2F}$  signal, a cubic interpolation is used to determine the  $S_{2F}$  Z dependence between each drift time bin, and a linear extrapolation based on the first and last 20% of Gaussian distribution data points is used to determine the  $S_{2F}$  Z dependence above and below the span of the drift time bins. A detector inefficiency correction for the Z direction is defined by taking the ratio of the  $S_{2F}$  pulse area at a height of 4  $\mu\text{seconds}$  (just below the liquid surface) to the  $S_{2F}$  pulse area as a function of Z as described in the equation

$$S_{2\text{-efficiency-correction}} = \frac{S_{2F}(z = 4)}{S_{2F}(z)}. \quad (168)$$

In the case of the  $S_{1F}$  signal, a second order polynomial is used to determine the  $S_{1F}$  Z dependence between and outside of each drift time bin. A detector inefficiency correction for the Z direction is defined by taking the ratio of the  $S_{1F}$  pulse area at the center of the detector ( $z_c$  as defined by the average drift time of

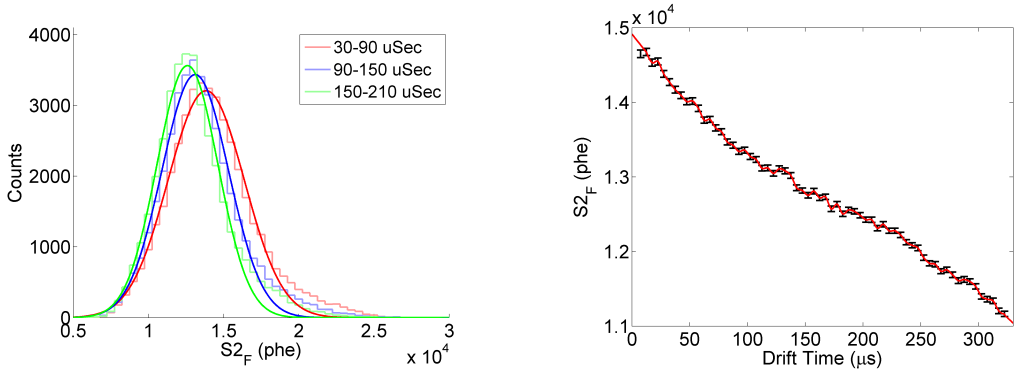


Figure 88: (Left) Gaussian distribution fits to the field corrected  $S2_F$  data that are used to determine the drift time dependence of the  $S2_F$  pulse area. For illustrative purposes, a drift time bin width of 60  $\mu$ seconds was chosen for this plot. (Right) The Z dependence of the  $S2_F$  pulse area after field effects are removed. Black points indicate the maximum of Gaussian distribution fits for each drift time bin, and red points indicate the interpolation and extrapolation of that data.

$^{83m}\text{Kr}$ ) to the  $S1_F$  pulse area as a function of Z as described in the equation

$$S1_{\text{z-efficiency-correction}} = \frac{S1_F(z_c)}{S1_F(z)}. \quad (169)$$

The XY dependence of the field removed  $S2_F$  and  $S1_F$  signals are found by dividing the z inefficiency corrected ( $S2_F \times S2_{\text{z-efficiency-correction}}$  and  $S1_F \times S1_{\text{z-efficiency-correction}}$ ) data into two dimensional XY bins with lengths defined such that each bin has roughly 300 events, and then fitting Gaussian distributions to the data of each bin. The mean of the Gaussian distribution from each bin is used to construct  $S2_F$  and  $S1_F$  XY dependence maps, with a spline interpolation and extrapolation being used to determine the XY dependence between and outside of the bins. (Figure 90) A detector inefficiency correction for the XY direction is defined by taking the ratio of the z inefficiency corrected  $S2_F$  (or  $S1_F$ ) pulse area at the center of the detector to the z inefficiency corrected  $S2_F$  (or  $S1_F$ ) pulse area

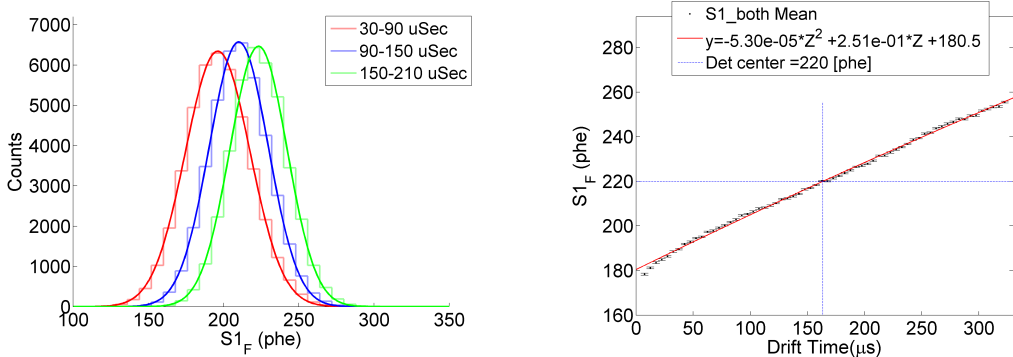


Figure 89: (Left) Gaussian distribution fits to the field corrected S1<sub>F</sub> data that are used to determine the drift time dependence of the S1<sub>F</sub> pulse area. For illustrative purposes, a drift time bin width of 60  $\mu$ seconds was chosen for this plot. (Right) The Z dependence of the S1<sub>F</sub> pulse area after field effects are removed. Black points indicate the maximum of Gaussian distribution fits for each drift time bin, and red points indicate the polynomial fit to that data.

as a function of XY in cm, as shown below

$$S2_{xy\text{-efficiency-correction}} = \frac{S2_{z\text{-efficiency-correction}} \times S2_F(x_c, y_c, z)}{S2_{z\text{-efficiency-correction}} \times S2_F(xyz)} \quad (170)$$

$$S1_{xy\text{-efficiency-correction}} = \frac{S1_{z\text{-efficiency-correction}} \times S1_F(x_c, y_c, z)}{S1_{z\text{-efficiency-correction}} \times S1_F(xyz)}. \quad (171)$$

where  $x_c$  and  $y_c$  are the x and y center of the detector in uncorrected coordinates determined by taking the average position of the  $^{83m}\text{Kr}$  events in each direction.

To apply these S1 and S2 efficiency corrections to data at any time, we must interpolate between the corrections in time. The S2<sub>E</sub> XY, S1<sub>E</sub> Z, and S1<sub>E</sub> XY efficiency corrections are not expected to change rapidly in time, so a simple nearest neighbor interpolation is used to apply these efficiency corrections to data sets at any point in time. However, the S2<sub>E</sub> Z dependence is expected to change rapidly in time due to the sudden changes in xenon purity introduced by detector

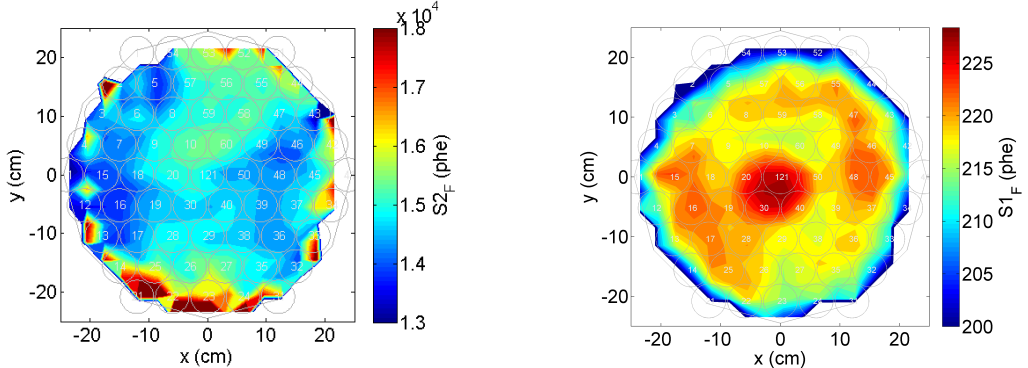


Figure 90: (Left) Two dimensional map of the XY dependence in  $^{83m}\text{Kr}$   $S2_F$  data determine by fitting a Gaussian distribution to XY bins of the data and tracking the mean of each fit.(Right) Two dimensional map of the XY dependence in  $^{83m}\text{Kr}$   $S1_F$  data determine by fitting a Gaussian distribution to XY bins of the data and tracking the mean of each fit.

operations. To account for this, we find the  $^{83m}\text{Kr}$  calibration taken immediately before and after a particular data set which the detector efficiency corrections are being applied to. A weighted average of the  $^{83m}\text{Kr}$   $S2_E$  Z dependence splines, with weights based on the time between each  $^{83m}\text{Kr}$  calibration data set and the data set being corrected, is used to defined a time interpolate  $S2_E$  Z dependence correction. Multiplying the raw  $S2$  and  $S1$  signals of any data set by the time-interpolated Z and the XY correction factors results in inefficiency corrected  $S2_E$  and  $S1_E$  signals (with field effects still present).

$$S2_E = S2 \times S2_{\text{xy-efficiency-correction}} \times S2_{\text{z-efficiency-correction}} \quad (172)$$

$$S1_E = S1 \times S1_{\text{xy-efficiency-correction}} \times S1_{\text{z-efficiency-correction}} \quad (173)$$

#### 7.3.4 Additional Output from KrypCal: Electron Lifetime

The  $S2_F Z$  dependence is not expected to be exponential in a nonuniform drift field due to the drift velocity dependent absorption cross section. Nonetheless, it is still useful to define a electron lifetime to track the purity of the detector's xenon over time. Two approaches have been taken in this regard. The first approach is to treat the  $S2_F Z$  dependence as approximately exponential anyway and quote the exponential decay constant as the lifetime, regardless of the quality of the fit. Due to the increasing strength of the field this approximation worsens over time. (Figure 91) The second approach to measuring the electron lifetime is to define a pseudo-lifetime from the  $S2_F Z$  dependence by fitting an exponential to the  $S2_F$  mean just below the liquid surface (at 4  $\mu$ seconds) and just above the cathode (at 320  $\mu$ seconds). While this approach avoids any issues with poor fits, it also neglects the  $S2_F Z$  dependence in the bulk of the detector. Note that the actual corrections use a spline fit to the  $S2_F Z$  dependence, and therefore avoid any issues in defining an exponential lifetime.

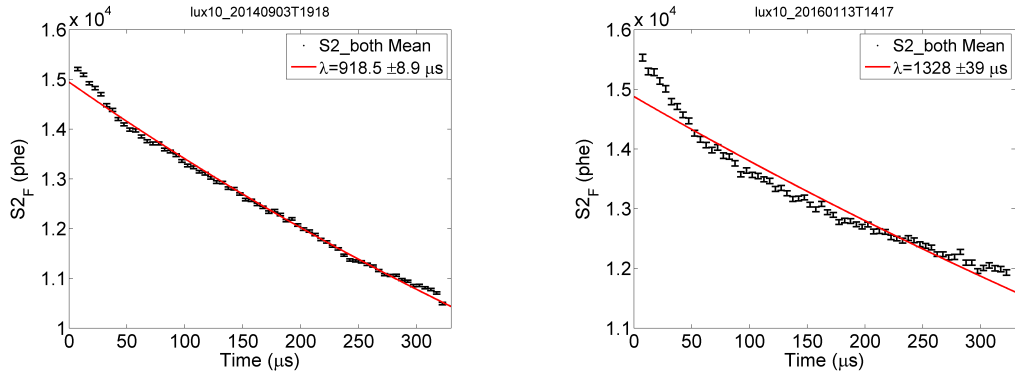


Figure 91: (Left) A reasonable exponential fit to the  $S2_F$  Z dependence in September 2014 (Right) A poor exponential fit to the  $S2_F$  Z dependence in January 2016. The higher field variation leads to a worse fit due to the drift velocity dependence of the absorption cross section.

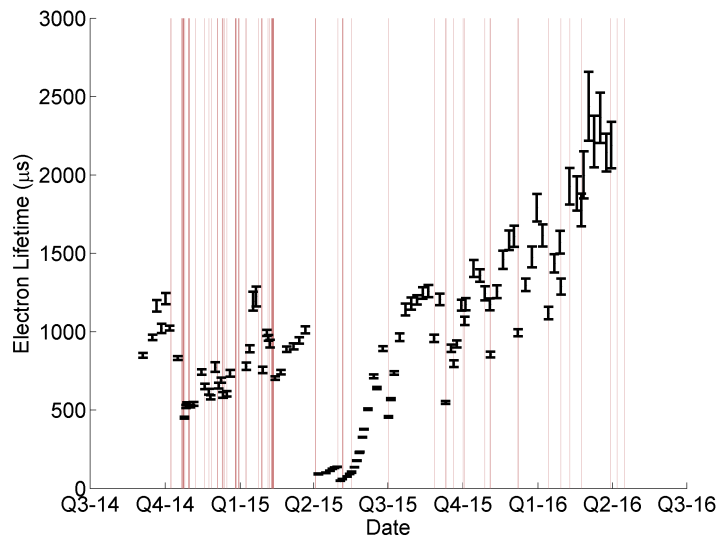


Figure 92: The electron lifetime over Run04 found by fitting an exponential to the  $S2_F$  Z dependence. Red areas indicate circulation outages. At high lifetimes the  $S2_F$  Z dependence is less exponential, leading to larger errors on the measurement.

### 7.3.5 Additional Output from KrypCal: Single Electron Size

Changes in the detector pressure, temperature, and liquid levels can cause the single electron size in the detector to vary over time. These variations introduce variations in the size of  $g_2$ , so it is necessary to track the single electron size in each  $^{83m}\text{Kr}$  calibration data set. In particular, we are interested in the single electron size at the center of the detector, since the field effects do not impact the result and the detector inefficiency effects are normalized to the center.

We select a population of clean events by requiring 100 samples between the first S1 of a  $^{83m}\text{Kr}$  event and the single electron associated with it. We then take two approaches to measure the single electron size at the center of the detector. In the first approach, we measure the single electron size by fitting a skew Gaussian distribution to the single electron pulse area spectrum within the radius at which the single electron size begins to decay at the edges of the detector. (Figure 93) In Run04, this radial limit is  $r < 17$  cm. In the second approach, we slice the detector into XY bins with widths determined such that each bin has roughly 100 single electron events. A skew Gaussian distribution is fit to the single electron spectrum of each bin, and a XY map of the single electron size is constructed. The value of the single electron size at the center of the detector is found with a spline interpolation of the XY dependence map. (Figure 94) These two methods agree within 1%.

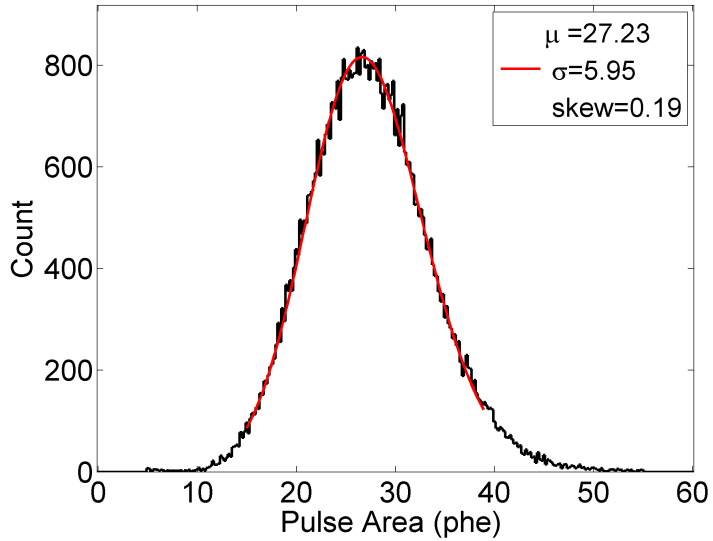


Figure 93: The result of our first approach for measuring the single electron size at the center of the detector. We perform this measurement for every  $^{83m}\text{Kr}$  data set. In this particular example from September 03, 2014 the single electron size is found to be  $27.23 \pm 0.044$ .

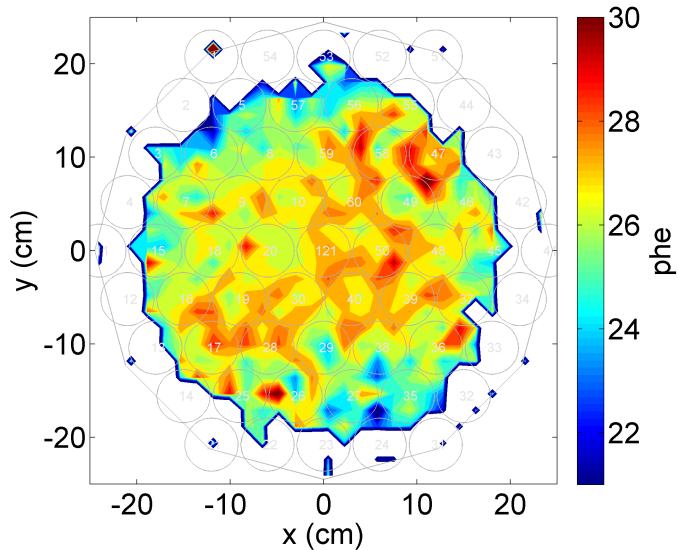


Figure 94: The XY dependence of the single electron size used in our second approach for measuring the single electron size at the center of the detector. We perform this measurement for every  $^{83m}\text{Kr}$  data set. In this particular example from September 03, 2014 the single electron size is found to be  $27.40 \pm 0.31$ .

### 7.3.6 Additional Output from KrypCal: Electric Field Maps

Due to the time variation of the electric field in Run04 it is clearly important to measure the electric field in each  $^{83m}\text{Kr}$  calibration data set. To accomplish this, we relate Scott Hertel's RvZ field maps in September 2014 and September 2015 to the RvZ dependence of the S1a/S1b ratio during the same points in time. (Figure 95) Although the measured S1a/S1b to electric field relationship is similar between the two datasets, the estimate of the field differs depending on which relationship is used. We choose to use the average result of the two relationships for the reported field strength, and take the difference between them as a systematic error. (Figure 96)

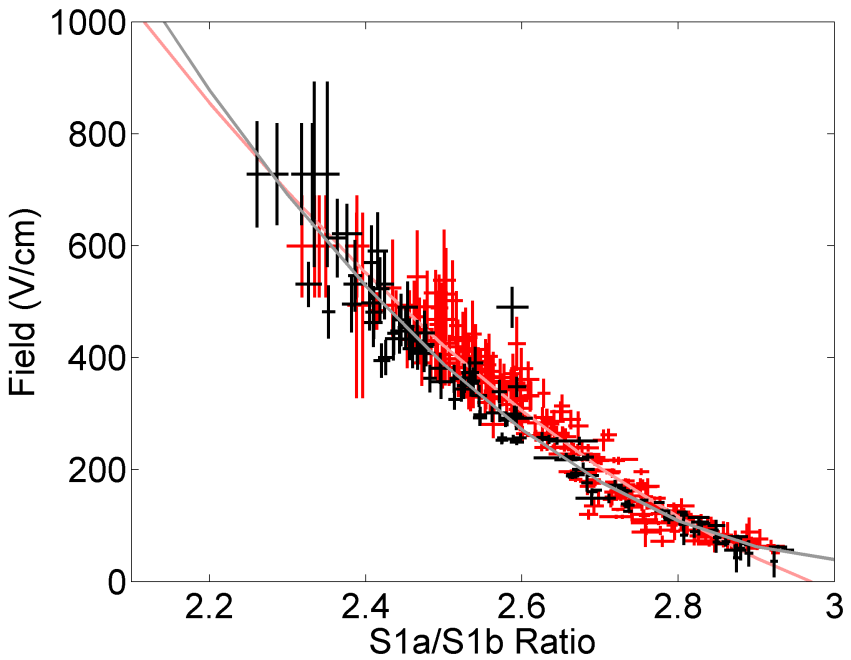


Figure 95: The S1a/S1b to field strength relationship measured in September 2014 (red) and September 2015 (black).

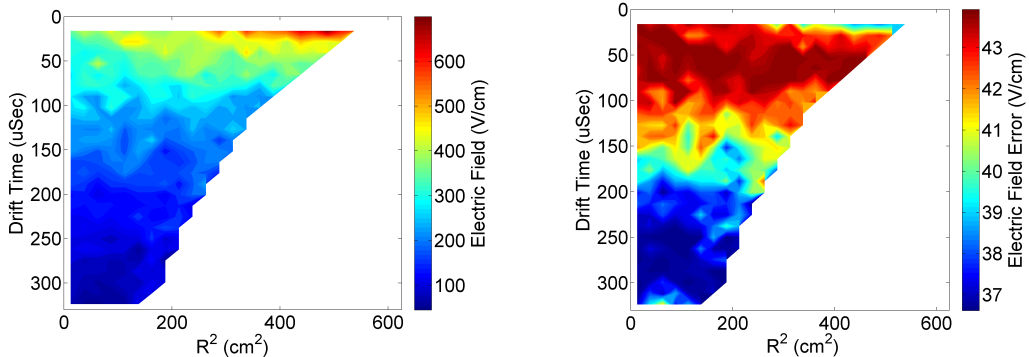


Figure 96: (Left)  $R^2vZ$  map of the electric field on September 03, 2014 as measured by KrypCal (Right)  $R^2vZ$  map of the systematic error in the electric field measurement on September 03, 2014.

## 7.4 Results of the KrypCal Corrections

In this section we will cover a number of metrics which have been used to determine how well the KrypCal corrections are working in Run04. A version of KrypCal which does not acknowledge the spatial and time dependent field in Run04 (similar to what we did in Run03) has been produced for comparison of each metric.

### 7.4.1 Energy Spectra

Version 2.22 of the  $\chi^2$  method presented in section 7.2.9 finds an average total reduced  $\chi^2$  of 0.8413 for the  $\text{CH}_3\text{T}$  and  $^{83m}\text{Kr}$  energy spectra, with a reduced  $\chi^2$  of  $150.6/124=1.2143$  ( $p=0.05$ ) for  $\text{CH}_3\text{T}$  alone and a reduced  $\chi^2$  of  $12.17/26=0.4682$  ( $p=0.99$ ) for  $^{83m}\text{Kr}$  alone. The resulting  $^{83m}\text{Kr}$  energy spectra (unbinned in drift time) from September 2015 and February 2016 are shown in figure 97. The Gaussian means differ from the expected 41.55 keV by less than one sigma, and the reduced  $\chi^2$  based on the Z dependence of the Energy spectra returns a p-value of 0.99.

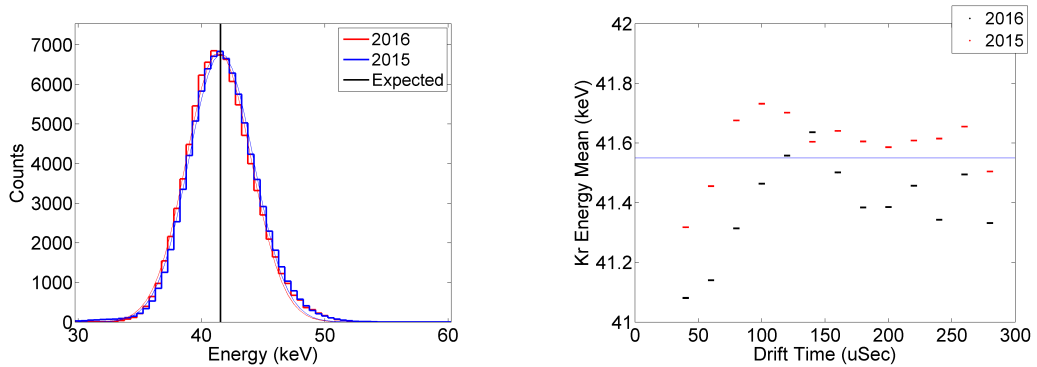


Figure 97: (Left) The energy spectrum of  $^{83m}\text{Kr}$  data in September 2014 (red) and September 2015(blue) after determining the S1 field effect to S1a/S1b relationship from the version 2.22 reduced  $\chi^2$  method. The energy spectrum is expected to be a Gaussian distribution centered around the black line. (Right) The Z dependence of the  $^{83m}\text{Kr}$  energy peaks in September 2014 (red) and September 2015 (black).

The  $\text{CH}_3\text{T}$  energy spectra from calibrations in September 2014, November 2014, February 2015, September 2015, and February 2016 are shown in figure 98. The fractional difference between the expected  $\text{CH}_3\text{T}$  spectrum and the  $\text{CH}_3\text{T}$  is shown below each energy spectrum. Fractional residuals of up to  $3 \sigma$  are comparable to our  $\text{CH}_3\text{T}$  results from Run03.

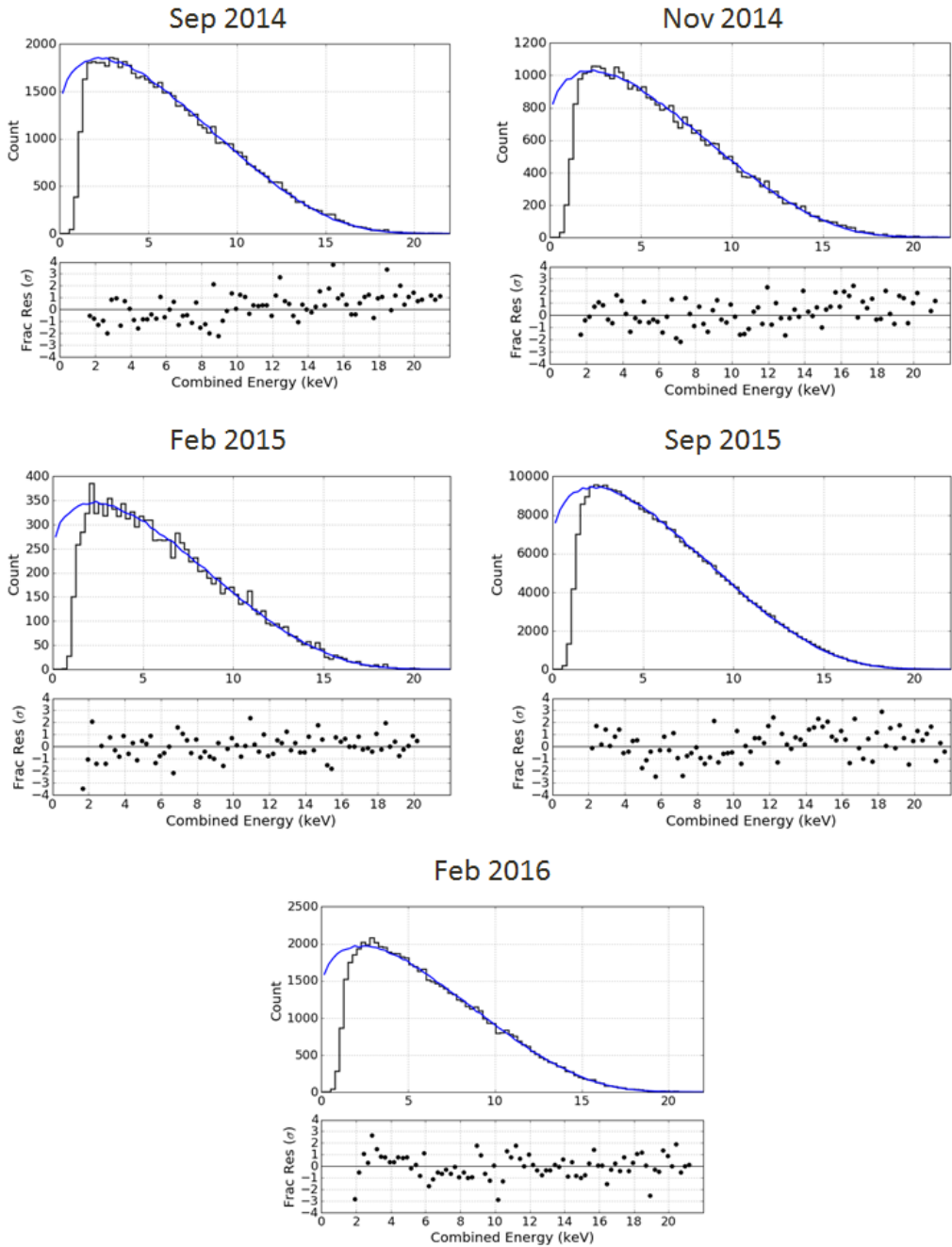


Figure 98: The September 2014, November 2014, February 2015, September 2015, and February 2016 CH<sub>3</sub>T energy spectra resulting from KrypCal 2.22 corrections.

A version of  $^{83m}\text{Kr}$  which does not acknowledge the spatial and time dependent

field in Run04 produces the  $^{83m}\text{Kr}$  energy spectra shown in Figure 99 and the  $\text{CH}_3\text{T}$  energy spectra shown in Figure 100. This version of KrypCal produces corrections that normalize the  $^{83m}\text{Kr}$  S1 and S2 signals everywhere in the detector, regardless of whether the variation is induced by field effects or detector inefficiency. An optimal value of  $g_1 = 0.100 \pm 0.001$  and extraction efficiency of  $\text{EE} = 1.08 \pm 0.030$  is found by an energy spectrum  $\chi^2$  fit. This optimal value of the extraction efficiency is 40%-80% higher than our expectations based on Guschin data and our extraction field strength, and exceeds 100%. Even with the unreasonably high extraction efficiency, the  $^{83m}\text{Kr}$  and  $\text{CH}_3\text{T}$  energy spectra produce an worse average reduced  $\chi^2$  of 1.12 for the  $^{83m}\text{Kr}$  and  $\text{CH}_3\text{T}$  energy spectra when compared to the expected energy spectra, with a reduced  $\chi^2$  of  $10.06/26=0.3869$  for  $^{83m}\text{Kr}$  alone, and a reduced  $\chi^2$  of  $230.2/124=1.8562$  for  $\text{CH}_3\text{T}$  alone.

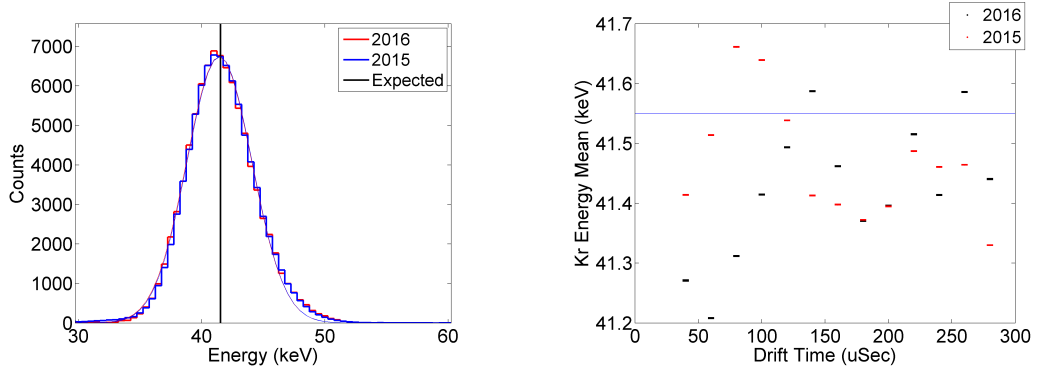


Figure 99: (Left) The energy spectrum of  $^{83m}\text{Kr}$  data in February 2016 (red) and September 2015(blue) using a version of KrypCal that does not properly account for field effects. The energy spectrum is expected to be a Gaussian distribution centered around the black line. (Right) The Z dependence of the  $^{83m}\text{Kr}$  energy peaks in September 2015 (red) and February 2016 (black) using the same version of KrypCal.

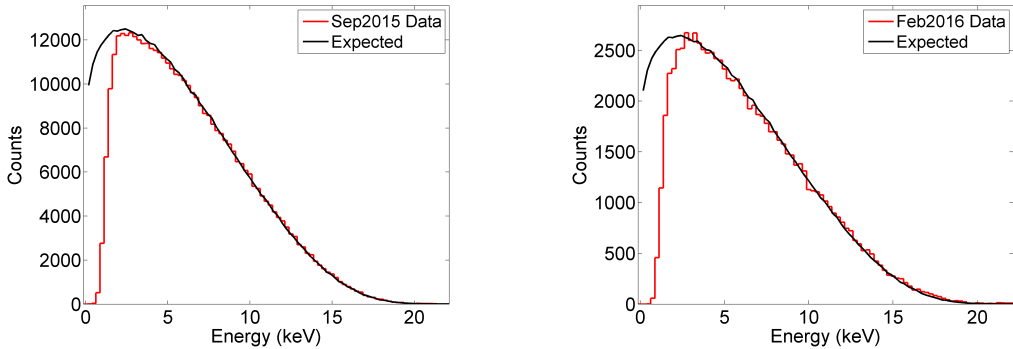


Figure 100: (Left) The energy spectrum of CH<sub>3</sub>T data in September 2015 (left) and February 2016 (right) using a version of KrypCal that does not properly account for field effects. The expected CH<sub>3</sub>T energy spectrum for each data set is shown in black.

#### 7.4.2 Energy Threshold

The Run04 energy threshold calculated by comparing the expected CH<sub>3</sub>T energy spectrum to the measured CH<sub>3</sub>T energy spectrum in September 2014, November 2014, February 2015, September 2015, and February 2016 is shown in Figure 101. The 50% efficiency measurements are shown in Table 6. The average detector threshold of  $1.19 \pm 0.64$  keV is consistent with libNEST expectation of  $1.29 \pm 0.17$  keV.

Date	50% Threshold (keV)
September 2014	$1.11 \pm 1.07$
November 2014	$1.17 \pm 0.38$
February 2015	$1.25 \pm 0.23$
September 2015	$1.22 \pm 0.22$
February 2016	$1.21 \pm 0.52$

Table 6: The energy threshold calculated from the CH<sub>3</sub>T spectrum on different dates.

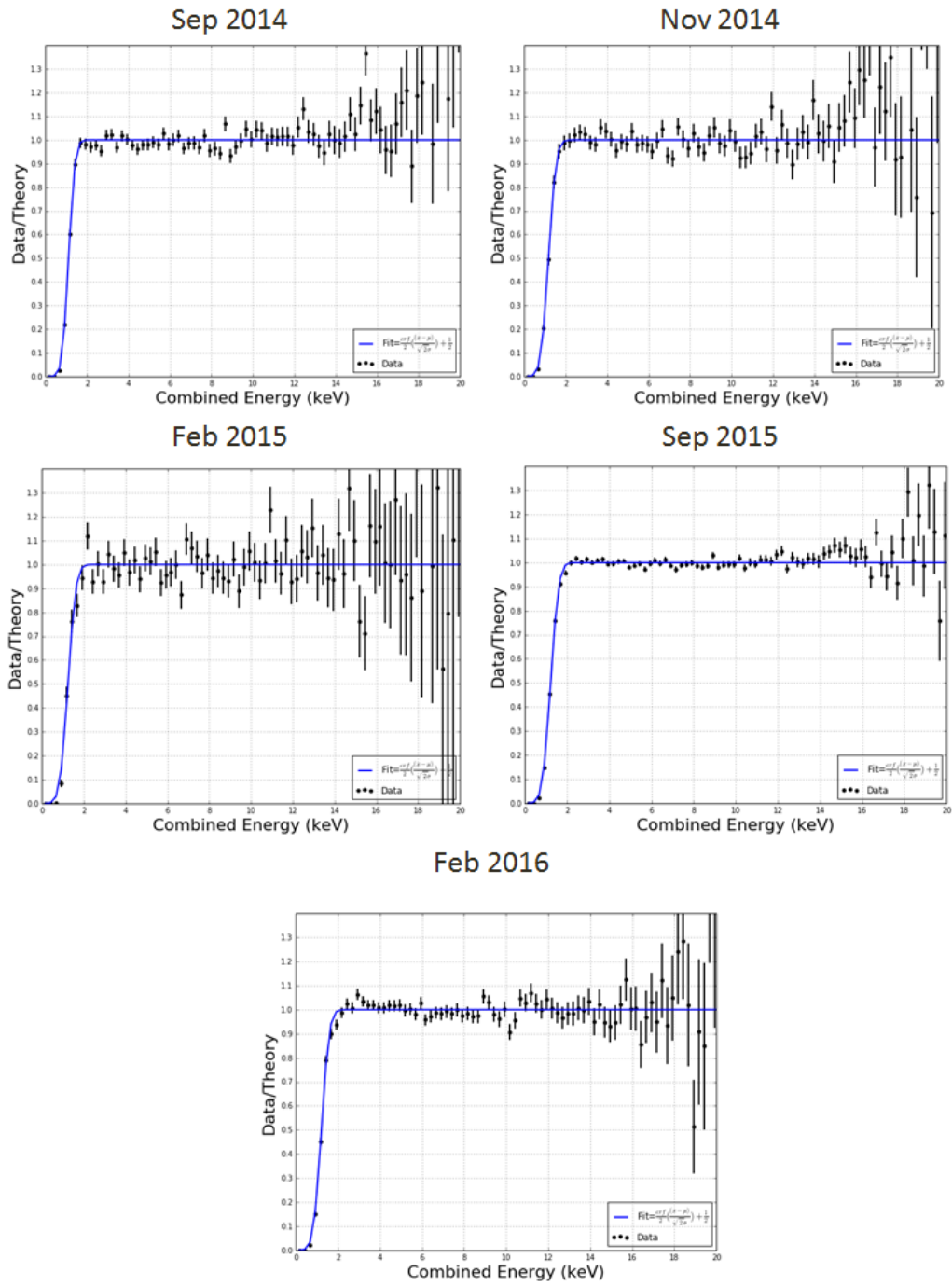


Figure 101: The September 2014, November 2014, February 2015, and September 2015 energy thresholds resulting from KrypCal 2.22 corrections.

### 7.4.3 G1 and EE

Version 2.22 of the  $\chi^2$  method presented in section 7.2.9 finds best fit values of  $g_1 = 0.098 \pm 0.001$  and  $EE = 0.808 \pm 0.022$ . This is consistent with our expectations of an extraction efficiency between 0.6 and 0.8, based on our extraction field models and the Run04 liquid level, and is much better than the  $g_1 = 0.100 \pm 0.001$  and  $EE = 0.108 \pm 0.030$  result found in section 7.4.1. (Figure 102) Likewise, the best fit value of  $g_1$  is within one sigma of our expectation of  $g_1 = 0.108 \pm 0.010$  found in section 7.2.8.

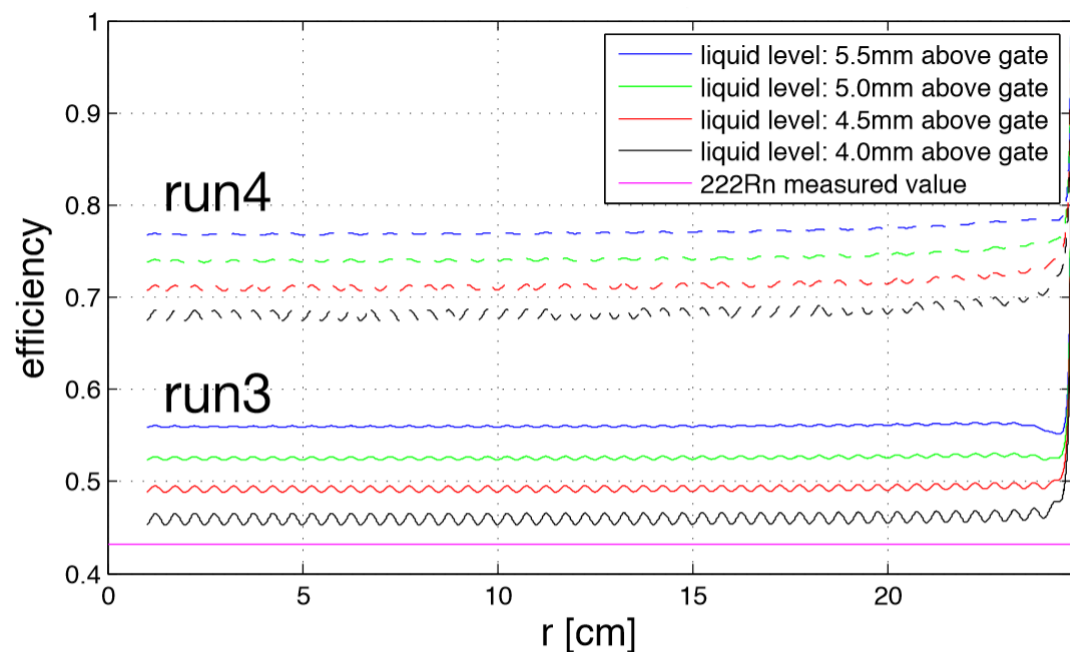


Figure 102: The expected extraction efficiency based on Scott's RvZ field map. The expectation is derived from a Guschin curve, and is dependent on the height of the liquid above the gate. The exact liquid level in Run04 is currently unknown, so a range of possible values is depicted.

#### 7.4.4 Lifetime Estimates

The nonuniform field in the LUX detector produces higher recombination of  $^{83m}\text{Kr}$  events in the bottom of the detector. This results in an attenuation of the  $^{83m}\text{Kr}$  S2 signal that is directly proportional to drift time. This effect mimics the attenuation of the  $^{83m}\text{Kr}$  S2 signal produced by impurities capturing charge as it drift to the top of the detector. As a result, when field effects are not properly accounted for in a  $^{83m}\text{Kr}$  calibration the electron lifetime is drastically underestimated, resulting in an over correction of all S2 signals in the detector. This problem is rectified in the latest version of KrypCal, which measures higher values of electron lifetime after the field effects have been properly separated from the detector inefficiency effects.

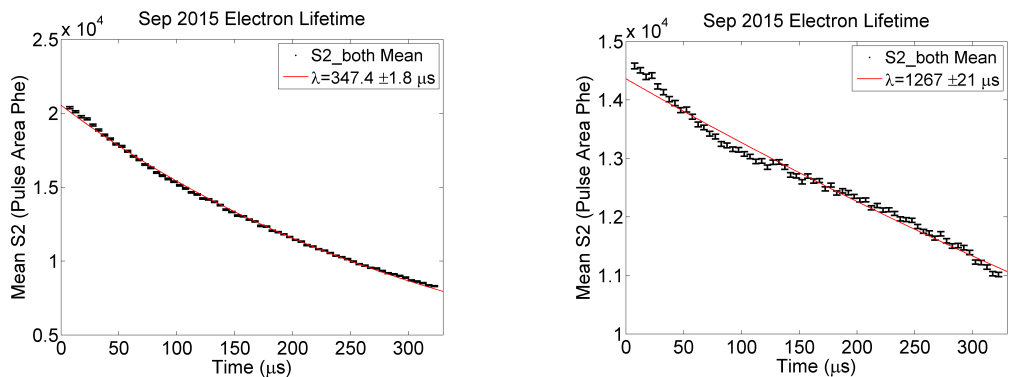


Figure 103: (Left) The electron lifetime measurement for a particular data set when field effects are not properly accounted for. (Right) The electron lifetime measurement for the same data set when field effects are properly separated from detector inefficiency effects.

### 7.4.5 Energy Resolution

The energy spectra of xenon activation peaks found in neutron generator calibration data sets is shown in Figure 104. Using KrypCal 2.22 corrections, we find an energy peak at each of the expected xenon activation lines. An unreasonably high extraction efficiency of 108% is required for the xenon activation peaks to appear at their correct energies, and the resolution of the peaks is worsened. For reference, the energy resolution of each of the xenon activation peaks, as well as for the  $^{83m}\text{Kr}$  peaks are included in Table 7 (version which does not account for field effects properly) and Table 8 (version which does account for field effects properly). Together, these energy spectra results confirm improved energy reconstruction and energy resolution ranging from 1.36 keV to 275 keV.

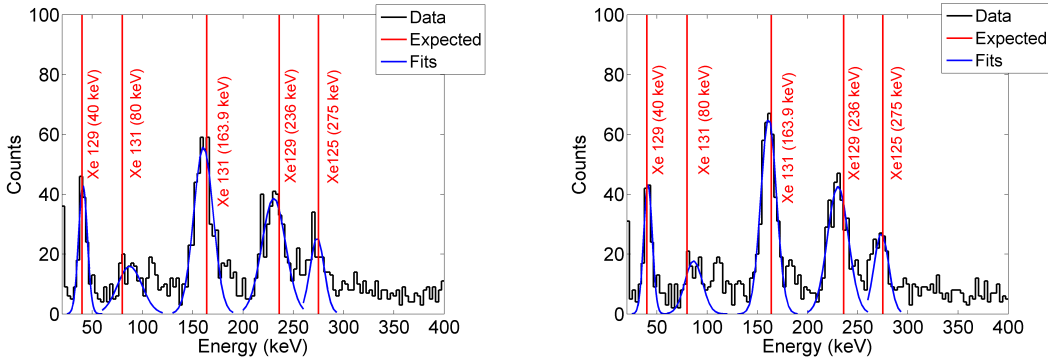


Figure 104: (Left) The xenon activation energy spectra from October 2015 resulting from corrections which do not properly account for field effects. (Right) The xenon activation energy spectra from the same data sets resulting from corrections which do properly account for field effects.

Source	Mean (keV)	Sigma (keV)	Energy Resolution
$^{129}\text{Xe}$ (40 keV)	$40.8 \pm 0.55$	$4.33 \pm 0.55$	$0.106 \pm 0.014$
$^{131}\text{Xe}$ (80 keV)	$87.3 \pm 4.49$	$12.1 \pm 5.51$	$0.139 \pm 0.064$
$^{131}\text{Xe}$ (164 keV)	$160.6 \pm 0.52$	$9.56 \pm 0.55$	$0.060 \pm 0.003$
$^{129}\text{Xe}$ (236 keV)	$230.5 \pm 1.17$	$11.7 \pm 1.35$	$0.051 \pm 0.006$
$^{125}\text{Xe}$ (275 keV)	$273.6 \pm 2.05$	$6.93 \pm 2.68$	$0.025 \pm 0.010$
Sep2014 $^{83m}\text{Kr}$ (41.55 keV)	$41.42 \pm 0.024$	$2.64 \pm 0.024$	$0.0638 \pm 0.0006$
Sep2015 $^{83m}\text{Kr}$ (41.55 keV)	$41.46 \pm 0.023$	$2.63 \pm 0.023$	$0.0635 \pm 0.0006$

Table 7: The mean, width, and energy resolution of Gaussian fits to the the DD and  $^{83m}\text{Kr}$  energy peaks based on a version of KrypCal which does not account for field effects properly.

Source	Mean (keV)	Sigma (keV)	Energy Resolution
$^{129}\text{Xe}$ (40 keV)	$40.9 \pm 0.54$	$4.25 \pm 0.53$	$0.104 \pm 0.013$
$^{131}\text{Xe}$ (80 keV)	$86.4 \pm 1.24$	$8.65 \pm 1.45$	$0.100 \pm 0.017$
$^{131}\text{Xe}$ (164 keV)	$161.2 \pm 0.43$	$7.78 \pm 0.44$	$0.048 \pm 0.003$
$^{129}\text{Xe}$ (236 keV)	$230.3 \pm 0.83$	$10.3 \pm 0.90$	$0.045 \pm 0.004$
$^{125}\text{Xe}$ (275 keV)	$273.6 \pm 1.58$	$7.24 \pm 2.14$	$0.027 \pm 0.008$
Sep2014 $^{83m}\text{Kr}$ (41.55 keV)	$41.40 \pm 0.022$	$2.62 \pm 0.022$	$0.0630 \pm 0.0005$
Sep2015 $^{83m}\text{Kr}$ (41.55 keV)	$41.60 \pm 0.021$	$2.62 \pm 0.021$	$0.0632 \pm 0.0005$

Table 8: The mean, width, and energy resolution of Gaussian fits to the the DD and  $^{83m}\text{Kr}$  energy peaks based on a version of KrypCal which does account for field effects properly.

#### 7.4.6 Nuclear Recoil Band

Nuclear recoils are much less sensitive to field variation effects in the detector, so if we were to see a significant spatial dependence in the NR band it would indicate a flaw in the corrections. As expected, the results of the KrypCal 2.22 NR band calibration in October 2014 show very little spatial dependence in the NR band. (Figure 105) The result of the same calibration using a version of KrypCal which does not properly account for field effects is also shown in Figure 105. The underestimate of the electron lifetime and subsequent over correction of the S2 data produces a non-physical z dependence in the NR band.

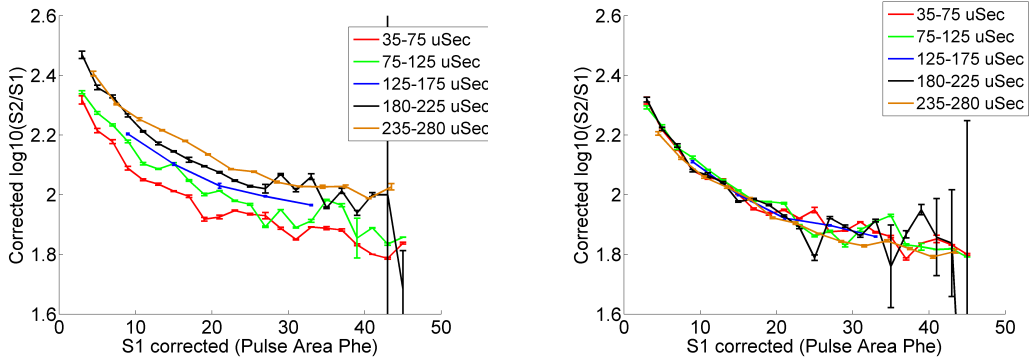


Figure 105: (Left) The Z dependence of the NR band mean using a version of KrypCal which does not properly account for field effects. (Right) The Z dependence of the NR band mean from the same datasets using a version of KrypCal which does properly account for field effects.

#### 7.4.7 Electron Recoil Band

The electron recoil band that results from KrypCal 2.22 corrections should have significant spatial and time dependence due to the recombination variation induced by the nonuniform electric field remaining in the data.

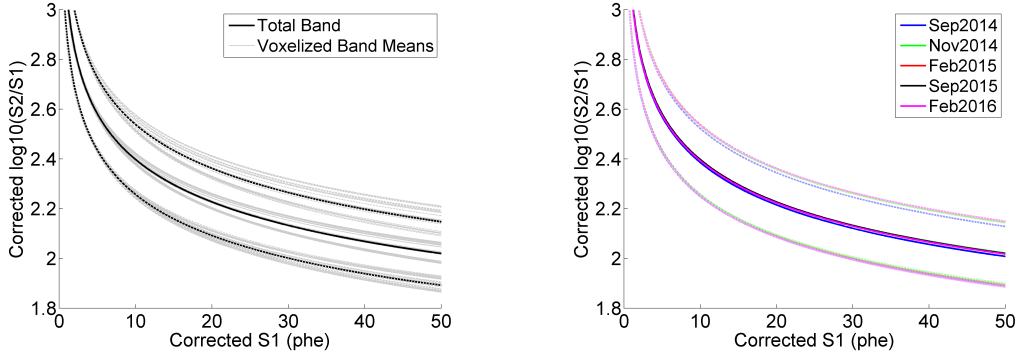


Figure 106: (Left) The spatial variation of the KrypCal 2.22 corrected ER band from September 2015. The black band represents the total, unbinned ER band and the grey bands represent the ER band from each voxel. (Right) The time dependence of the total, unbinned ER band as measured by the KrypCal 2.22 corrected data at four points in time.

The corrected ER band calibration data from September 2015 was divided into three dimensional voxels with a Z height of  $86 \mu\text{seconds}$  and an X and Y width of 16 cm. We see a 16% spatial variation of the ER band in September 2015 (at  $S1=20 \text{ phd}$ ), which is close to the libNEST prediction of a 13% spatial variation (at  $S1=20 \text{ phd}$ ). We also observe a  $\sim 1\%$  variation in time for the total ER band over the duration of Run04. (Figure 106) The relative size of the spatial and time dependence of the ER band is consistent with expectations, since the spatial dependence of the electric field is stronger than the time dependence of the electric field.

The variation in the ER band, although expected, is not ideal for detector calibrations since we would like to know what the ER band is at all points in time. To achieve this goal, we have related the ER band power law parameters to the  $S1a/S1b$  ratio in voxels from September 2015. We observe the polynomial relationships shown in Figure 107. We then use these measured relationships to

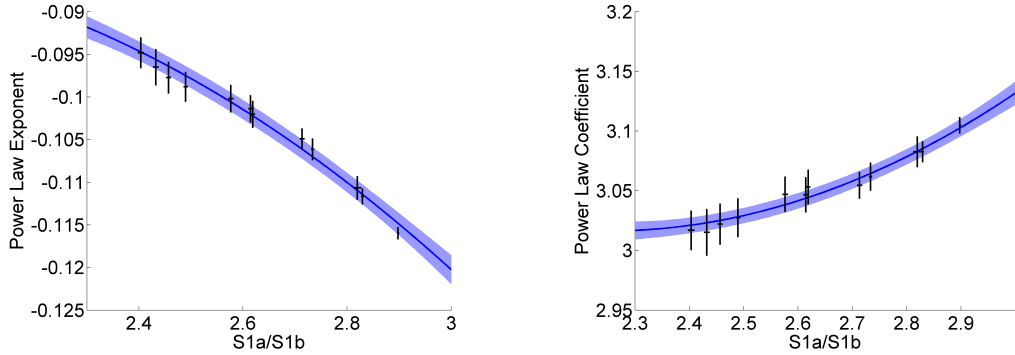


Figure 107: (Left) The measured relationship between S1a/S1b and the ER band power law exponent. (Right) The measured relationship between S1a/S1b and the ER band power law coefficient. The light blue region indicates one  $\sigma$  uncertainties on each fit.

reconstruct the ER band from the February 2015, September 2015, and February 2016 ER band calibrations from measurements of S1a/S1b alone. Each of the inferred bands are at most 3% different than the ER band measured in data, and all of the inferred bands have  $\chi^2$  results that return  $p=1$ . Although the spatial dependence of the Monte Carlo bands is not shown, the spatial dependence of each ER band calibration is reproduced within 2% with p-values close to 1.

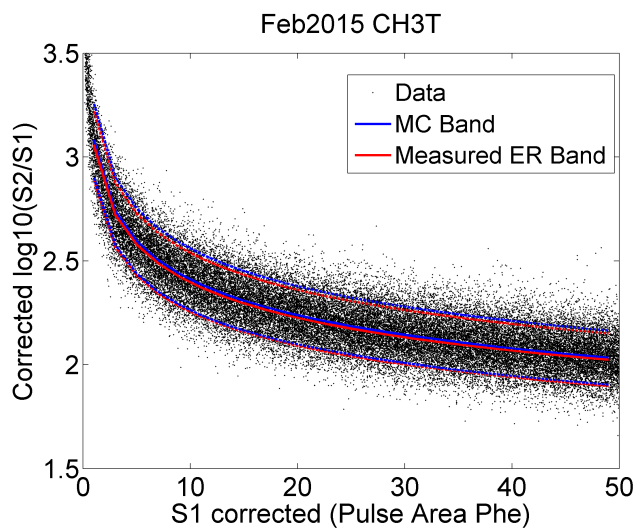


Figure 108: Monte Carlo data for the February 2015 ER band generated from S1a/S1b using the relationship found in Figure 107. A fit to the Monte Carlo data is shown in blue, and a fit to the actual calibration data (not shown) is shown in red.

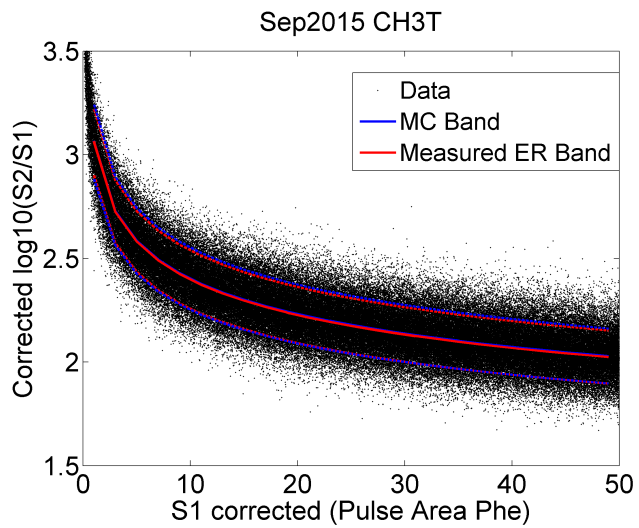


Figure 109: Monte Carlo data for the September 2015 ER band generated from S1a/S1b using the relationship found in Figure 107. A fit to the Monte Carlo data is shown in blue, and a fit to the actual calibration data (not shown) is shown in red.

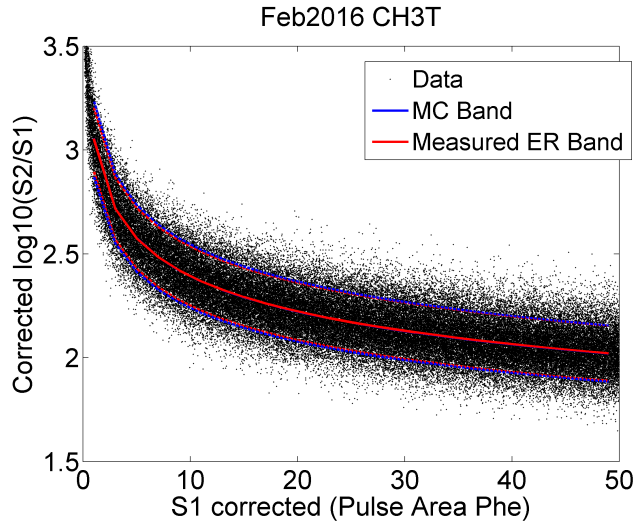


Figure 110: Monte Carlo data for the February 2016 ER band generated from S1a/S1b using the relationship found in Figure 107. A fit to the Monte Carlo data is shown in blue, and a fit to the actual calibration data (not shown) is shown in red.

## 7.5 Conclusions

LUX Run04 data is complicated by a nonuniform electric field in the detector. The variation of the electric field in space and time produces variation in the recombination of S1 and S2 events as a function of energy, time, space, and recoil type. If this recombination variation is not properly separated from detector inefficiency effects in  $^{83m}\text{Kr}$  data, the KrypCal corrections produce data which has poor energy reconstruction with unreasonably high extraction efficiency estimates, worsened energy resolution, and widened ER bands. We have developed multiple methods to relate the strength of the field effect in S1 and S2 data to the  $^{83m}\text{Kr}$  S1a/S1b ratio. These two relationships can be used to separate the field effects from detector inefficiency effects prior to producing KrypCal corrections from  $^{83m}\text{Kr}$  calibrations taken at any point in time. This process results in better energy reconstruction

with g1 and extraction efficiency values close to our expectations, improved energy resolution, and improved ER band width. However, since the field effects remain in the corrected data, a spatial and time dependence remain in the corrected S1 and S2 signal, leading to complications in calibrating the corrected ER band over time.

## References

- [1] Georges Aad, Tatevik Abajyan, Brad Abbott, Jalal Abdallah, S Abdel Khalek, AA Abdelalim, O Abdinov, R Aben, B Abi, M Abolins, et al. Search for dark matter candidates and large extra dimensions in events with a jet and missing transverse momentum with the atlas detector. *Journal of High Energy Physics*, 2013(4):1–51, 2013.
- [2] Mark Gerald Aartsen, R Abbasi, Yasser Abdou, M Ackermann, J Adams, JA Aguilar, M Ahlers, D Altmann, J Auffenberg, X Bai, et al. Search for dark matter annihilations in the sun with the 79-string icecube detector. *Physical review letters*, 110(13):131302, 2013.
- [3] MG Aartsen, R Abbasi, Yasser Abdou, M Ackermann, J Adams, JA Aguilar, M Ahlers, D Altmann, J Auffenberg, X Bai, et al. Icecube search for dark matter annihilation in nearby galaxies and galaxy clusters. *Physical Review D*, 88(12):122001, 2013.
- [4] A Abramowski, F Acero, F Aharonian, AG Akhperjanian, G Anton, A Barnacka, U Barres De Almeida, AR Bazer-Bachi, Yvonne Becherini, J Becker, et al. Search for a dark matter annihilation signal from the galactic center halo with hess. *Physical Review Letters*, 106(16):161301, 2011.
- [5] L Accardo, M Aguilar, D Aisa, B Alpat, A Alvino, G Ambrosi, K Andeen, L Arruda, N Attig, P Azzarello, et al. High statistics measurement of the positron fraction in primary cosmic rays of 0.5–500 gev with the alpha magnetic spectrometer on the international space station. *Physical review letters*, 113(12):121101, 2014.
- [6] M Ackermann, Marco Ajello, A Albert, L Baldini, G Barbiellini, K Bechtol, R Bellazzini, B Berenji, RD Blandford, ED Bloom, et al. Fermi lat search for dark matter in gamma-ray lines and the inclusive photon spectrum. *Physical Review D*, 86(2):022002, 2012.

- [7] M Ackermann, Marco Ajello, A Allafort, WB Atwood, L Baldini, G Barbarelli, D Bastieri, K Bechtol, R Bellazzini, B Berenji, et al. Measurement of separate cosmic-ray electron and positron spectra with the fermi large area telescope. *Physical Review Letters*, 108(1):011103, 2012.
- [8] C Afonso, JN Albert, J Andersen, R Ansari, É Aubourg, P Bareyre, JP Beaulieu, G Blanc, X Charlot, F Couchot, et al. Limits on galactic dark matter with 5 years of eros smc data. *Astronomy & Astrophysics*, 400(3):951–956, 2003.
- [9] DS Akerib, HM Araújo, X Bai, AJ Bailey, J Balajthy, P Beltrame, EP Bernard, A Bernstein, TP Biesiadzinski, EM Boulton, et al. Tritium calibration of the lux dark matter experiment. *Phys. Rev. D*, 93:072009, 2016.
- [10] DS Akerib, X Bai, S Bedikian, E Bernard, A Bernstein, A Bolozdynya, A Bradley, D Byram, SB Cahn, C Camp, et al. The large underground xenon (lux) experiment. *Nuclear Instruments and Methods in Physics Research Section A: Accelerators, Spectrometers, Detectors and Associated Equipment*, 704:111–126, 2013.
- [11] Charles Alcock, RA Allsman, David R Alves, TS Axelrod, Andrew C Becker, DP Bennett, Kem H Cook, N Dalal, Andrew John Drake, KC Freeman, et al. The macho project: microlensing results from 5.7 years of large magellanic cloud observations. *The Astrophysical Journal*, 542(1):281, 2000.
- [12] Richard Arnowitt, Bhaskar Dutta, and Bo Hu. Dark matter, muon g-2 and other susy constraints. In *Beyond the Desert 2003*, pages 25–41. Springer, 2004.
- [13] J Balajthy. April 2015 ch4 injection results. [https://docs.google.com/presentation/d/16VfGTd51YoIk9AkkJypX6qpJ5SujgQQt8d0YEjFinCo/edit#slide=id.gae573feed\\_0\\_5](https://docs.google.com/presentation/d/16VfGTd51YoIk9AkkJypX6qpJ5SujgQQt8d0YEjFinCo/edit#slide=id.gae573feed_0_5), 2015. Accessed: 2016-06-14.
- [14] J Balajthy and C Hall. Simulations of ch3t diffusion into plastic parts of the lux detector. lux document database. <http://teacher.pas.rochester.edu:8080/wiki/pub/Lux/LuxDB00000481>, 2013. Accessed: 2016-06-14.
- [15] Varouzhan Baluni. Cp-nonconserving effects in quantum chromodynamics. *Physical Review D*, 19(7):2227, 1979.
- [16] KG Begeman, AH Broeils, and RH Sanders. Extended rotation curves of spiral galaxies: Dark haloes and modified dynamics. *Monthly Notices of the Royal Astronomical Society*, 249(3):523–537, 1991.

- [17] Maria Beltran, Dan Hooper, Edward W Kolb, Zosia AC Krusberg, and Tim MP Tait. Maverick dark matter at colliders. *Journal of High Energy Physics*, 2010(9):1–17, 2010.
- [18] CL Bennett, M Halpern, G Hinshaw, N Jarosik, A Kogut, M Limon, SS Meyer, L Page, DN Spergel, GS Tucker, et al. First year wilkinson microwave anisotropy probe (wmap) observations: Preliminary maps and basic results. *The Astrophysical Journal Supplement Series*, 148(1):1, 2003.
- [19] Gianfranco Bertone, Dan Hooper, and Joseph Silk. Particle dark matter: Evidence, candidates and constraints. *Physics Reports*, 405(5):279–390, 2005.
- [20] T. Biesiadzinski. Evolution of the observed detector wall. [http://teacher.pas.rochester.edu:8080/wiki/pub/Lux/LuxDB00000406/TB\\_field-wall\\_update\\_150519.pdf](http://teacher.pas.rochester.edu:8080/wiki/pub/Lux/LuxDB00000406/TB_field-wall_update_150519.pdf), 2015. Accessed: 2016-06-14.
- [21] Amitai Yisrael Bin-Nun. Gravitational lensing with a large deflection angle as a probe of general relativity and the galactic center. *Publicly accessible Penn Dissertations*, 2010.
- [22] Tremaine Binney. *Galactic Dynamics*. Princeton University Press, 2 edition, 2008.
- [23] P Brás. *Finding a needle in a haystack: Background studies and WIMP detection efficiency in LUX*. PhD thesis, Universidade De Coimbra, 2015.
- [24] Hsin-Chia Cheng, Jonathan L Feng, and Konstantin T Matchev. Kaluza-klein dark matter. *Physical Review Letters*, 89(21):211301, 2002.
- [25] Daniel JH Chung, Edward W Kolb, and Antonio Riotto. Superheavy dark matter. *Physical Review D*, 59(2):023501, 1998.
- [26] Douglas Clowe, Maruša Bradač, Anthony H Gonzalez, Maxim Markevitch, Scott W Randall, Christine Jones, and Dennis Zaritsky. A direct empirical proof of the existence of dark matter. *The Astrophysical Journal Letters*, 648(2):L109, 2006.
- [27] PEBS Collaboration. Positron fraction. [http://www1b.physik.rwth-aachen.de/~pebs/?PEBS\\_physics:Positron\\_fraction](http://www1b.physik.rwth-aachen.de/~pebs/?PEBS_physics:Positron_fraction), 2010. Accessed: 2016-06-14.
- [28] Planck Collaboration et al. Planck 2015 results. xiii. cosmological parameters. arxiv preprint. *arXiv*, 1502, 2015.

- [29] The PAMELA Collaboration. The cosmic-ray positron energy spectrum measured by pamela. *Physical Review Letters*, 111(1):081102, 2013.
- [30] C.E. Dahl. *The physics of background discrimination in liquid xenon, and first results from Xenon10 in the hunt for WIMP dark matter*. PhD thesis, Princeton University, 2009.
- [31] Joyce Dever, Bruce Banks, Kim de Groh, and Sharon Miller. Degradation of spacecraft materials. *Handbook of environmental degradation of materials*, pages 465–501, 2005.
- [32] A. Dobi. *Measurement of the Electron Recoil Band of the LUX Dark Matter Detector With a Tritium Calibration Source*. PhD thesis, University of Maryland, 2014.
- [33] A. Dobi. Tritium beta shape. <http://teacher.pas.rochester.edu:8080/wiki/pub/Lux/LuxDB00000402/TritiumBetaShape.pdf>, 2015. Accessed: 2016-06-14.
- [34] Tadayoshi Doke, Akira Hitachi, Shinzou Kubota, A Nakamoto, and Tan Takahashi. Estimation of fano factors in liquid argon, krypton, xenon and xenon-doped liquid argon. *Nuclear Instruments and Methods*, 134(2):353–357, 1976.
- [35] Battaner E. and Florido E. The rotation curve of spiral galaxies and its cosmological implications. *Fund. Cosmic Phys.*, 21:1–154, 2000.
- [36] John Ellis, John S Hagelin, Dimitri V Nanopoulos, K Olive, and Mark Srednicki. Supersymmetric relics from the big bang. *Nuclear Physics B*, 238(2):453–476, 1984.
- [37] Evalyn I Gates, Geza Gyuk, and Michael S Turner. The local halo density. *The Astrophysical Journal Letters*, 449(2):L123, 1995.
- [38] H Goldberg. Constraint on the photino mass from cosmology. *Physical Review Letters*, 50(19):1419, 1983.
- [39] S. Hertel. Describing september 2014 with an axisymmetric field model. <http://teacher.pas.rochester.edu:8080/wiki/pub/Lux/LuxDB00000446>, 2014. Accessed: 2016-06-14.
- [40] Wayne Hu. Cmb introduction. <http://background.uchicago.edu/~whu/intermediate/map1.html>, 2001. Accessed: 2016-06-14.

- [41] D. Javorsek, II, E. Fischbach, and V. Teplitz. New Experimental Bounds on the Contributions to the Cosmological Density Parameter  $\Omega$  from Strongly Interacting Massive Particles. *The Astrophysical Journal*, 568:1–8, March 2002.
- [42] Gerard Jungman, Marc Kamionkowski, and Kim Griest. Supersymmetric dark matter. *Physics Reports*, 267(5):195–373, 1996.
- [43] Marc Kamionkowski and Michael S Turner. Distinctive positron feature from particle dark-matter annihilations in the galactic halo. *Physical Review D*, 43(6):1774, 1991.
- [44] J Knapp, D Heck, SJ Sciutto, MT Dova, and M Risso. Extensive air shower simulations at the highest energies. *Astroparticle Physics*, 19(1):77–99, 2003.
- [45] EW Kolb and MS Turner. The early universe, 1994.
- [46] Hannu Kurki-Suonio. Lecture notes in cosmological perturbation theory. <http://theory.physics.helsinki.fi/~cpt/Cosmo12.pdf>, Fall 2015. Accessed: 2016-06-14.
- [47] JD Lewin and PF Smith. Review of mathematics, numerical factors, and corrections for dark matter experiments based on elastic nuclear recoil. *Astroparticle Physics*, 6(1):87–112, 1996.
- [48] A Manalaysay, T Marrodán Undagoitia, A Askin, L Baudis, A Behrens, AD Ferella, A Kish, O Lebeda, R Santorelli, D Vénos, et al. Spatially uniform calibration of a liquid xenon detector at low energies using k83mr. *Review of Scientific Instruments*, 81(7):073303, 2010.
- [49] Stephen J. Parke. Determining the neutrino mass hierarchy. In *Third NO-VE International Workshop on Neutrino Oscillations in Venice : Fifty years after the neutrino esperimental discovery : Venezia, February 7-10, 2006, Istituto Veneto di Scienze, Lettere ed Arti, Campo Santo Stefano*, pages 115–125, 2006.
- [50] Sergio Pastor. Light neutrinos in cosmology. *Physics of Particles and Nuclei*, 42(4):628–640, 2011.
- [51] M. Persic, P. Salucci, and F. Stel. The universal rotation curve of spiral galaxies - I. The dark matter connection. *Monthly Notices of the Royal Astronomical Society*, 281:27–47, July 1996.
- [52] P. Phelps. *The LUX Dark Matter Experiment: Detector Performance and Energy Calibration*. PhD thesis, Case Western Reserve University, 2014.

- [53] Til Piffl, C Scannapieco, J Binney, Matthias Steinmetz, R-D Scholz, MEK Williams, RS de Jong, G Kordopatis, G Matijević, O Bienaymé, et al. The rave survey: the galactic escape speed and the mass of the milky way. *Astronomy & Astrophysics*, 562:A91, 2014.
- [54] S Pires, J-L Starck, and A Refregier. Light on dark matter with weak gravitational lensing. *arXiv preprint arXiv:0908.4157*, 2009.
- [55] Alexandre Refregier. Weak gravitational lensing by large-scale structure. *Ann.Rev.Astron.Astrophys*, 41:645–668, 2003.
- [56] RG Hamish Robertson. Direct determination of neutrino mass. In *Journal of Physics: Conference Series*, volume 173, page 012016. IOP Publishing, 2009.
- [57] Barbara Sue Ryden. *Introduction to cosmology*, volume 4. Addison-Wesley San Francisco USA, 2003.
- [58] Pasquale D Serpico. Astrophysical models for the origin of the positron “excess”. *Astroparticle Physics*, 39:2–11, 2012.
- [59] Chung-Lin Shan. Determining ratios of wimp-nucleon cross sections from direct dark matter detection data. *Journal of Cosmology and Astroparticle Physics*, 2011(07):005, 2011.
- [60] JJ Simpson. Measurement of the  $\beta$ -energy spectrum of h 3 to determine the antineutrino mass. *Physical Review D*, 23(3):649, 1981.
- [61] David N Spergel, Licia Verde, Hiranya V Peiris, E Komatsu, MR Nolta, CL Bennett, M Halpern, G Hinshaw, N Jarosik, A Kogut, et al. First year wilkinson microwave anisotropy probe (wmap) observations: determination of cosmological parameters. *The Astrophysical Journal Supplement Series*, 148(1):175, 2003.
- [62] FW Stecker. The cosmic  $\gamma$ -ray spectrum from secondary particle production in cosmic-ray interactions. *Astrophysics and Space Science*, 6(3):377–389, 1970.
- [63] S. Stephenson. Position corrections. [http://teacher.pas.rochester.edu:8080/wiki/pub/Lux/AnalysisMeeting150818/20150818\\_PositionCorrection\\_ScottStephenson.pdf](http://teacher.pas.rochester.edu:8080/wiki/pub/Lux/AnalysisMeeting150818/20150818_PositionCorrection_ScottStephenson.pdf), 2015. Accessed: 2016-06-14.
- [64] Matthew Szydagis, Adalyn Fyhrie, Daniel Thorngren, and Mani Tripathi. Enhancement of nest capabilities for simulating low-energy recoils in liquid xenon. *Journal of Instrumentation*, 8(10):C10003, 2013.

- [65] W. To. Collections of presentations and documentations of the grid conditioning and the radial field. <http://teacher.pas.rochester.edu:8080/wiki/bin/view/Lux/LuxDB00000387>, 2015. Accessed: 2016-06-14.
- [66] L. Tvrnikova. Run04 3d electric field fits. [http://teacher.pas.rochester.edu:8080/wiki/pub/Lux/LuxDB00000428/160112\\_MH\\_6x7.pdf](http://teacher.pas.rochester.edu:8080/wiki/pub/Lux/LuxDB00000428/160112_MH_6x7.pdf), 2015. Accessed: 2016-06-14.
- [67] David Tytler, David Kirkman, John M O'Meara, Nao Suzuki, Adam Orin, Dan Lubin, Pascal Paschos, Tridivesh Jena, Wen-Ching Lin, Michael L Norman, et al. Cosmological parameters sigma8, the baryon density, and the uv background intensity from a calibrated measurement of h i lyman-alpha absorption at  $z = 1.9$ . *The Astrophysical Journal*, 617(1):1, 2004.
- [68] Jan van Paradijs and Johan AM Bleeker. X-ray spectroscopy in astrophysics. In *X-Ray Spectroscopy in Astrophysics*, volume 520, 1999.
- [69] P Venkataramaiah, K Gopala, A Basavaraju, SS Suryanarayana, and H Sanjeeviah. A simple relation for the fermi function. *Journal of Physics G: Nuclear Physics*, 11(3):359, 1985.
- [70] Alexey Vikhlinin, A Kravtsov, W Forman, C Jones, M Markevitch, SS Murray, and L Van Speybroeck. Chandra sample of nearby relaxed galaxy clusters: Mass, gas fraction, and mass-temperature relation. *The Astrophysical Journal*, 640(2):691–709, 2006.
- [71] Xiang-Ping Wu, Tzihong Chiueh, Li-Zhi Fang, and Yan-Jie Xue. A comparison of different cluster mass estimates: consistency or discrepancy? *Monthly Notices of the Royal Astronomical Society*, 301(3):861–871, 1998.
- [72] F. Zwicky. Republication of: The redshift of extragalactic nebulae. *General Relativity and Gravitation*, 41:207–224, January 2009.